Pulsed positive corona discharges : fundamental study and application to flue gas treatment

Pulsed Positive Corona Discharges

Fundamental Study and Application to Flue Gas Treatment

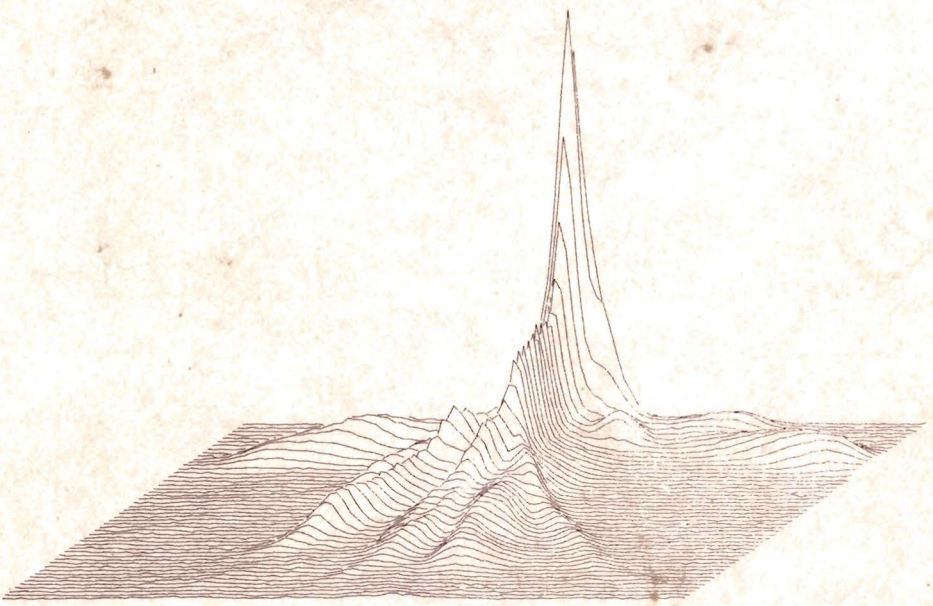

Y.L.M. Creyghton

Pulsed Positive Corona Discharges

Fundamental Study and Application to Flue Gas Treatment

Pulsed Positive Corona Discharges

Fundamental Study and Application to Flue Gas Treatment

PROEFSCHRIFT

ter verkrijging van de graad van doctor aan de Technische Universiteit Eindhoven, op gezag van de Rector Magnificus, prof.dr. J.H. van Lint, voor een commissie aangewezen door het College van Dekanen in het openbaar te verdedigen op dinsdag 20 september 1994 om 16.00 uur

door

Yves Lodewijk Maria Creyghton

geboren te Nijmegen

druk: wibro dissertatiedrukkerij, helmond

Dit proefschrift is goedgekeurd
door de promotoren:

prof.dr. W.R. Rutgers
en
prof.dr. L.H.Th. Rietjens

co-promotor:

dr.ir. E.M. van Veldhuizen

CIP-DATA KONINKLIJKE BIBLIOTHEEK, DEN HAAG

Creyghton, Yves Lodewijk Maria

Pulsed positive corona discharges : fundamental study and application to flue gas treatment / Yves Lodewijk Maria Creyghton. - [S.l. : s.n.]. - Ill., fig. foto's, tab.
Thesis Eindhoven. - With ref. - With summary in Dutch.
ISBN 90-9007232-2
NUGI 812
Subject headings: flue gas cleaning / corona / pulsed power.

These investigations have been supported by KEMA Nederland BV,
the Netherlands Technology Foundation (STW) and the European Commission
(Joule program).

Aan Isabelle

Contents

page:

Summary

There is a growing interest for gas cleaning by electrical techniques. A possible application is the pulsed corona *deNO$_x$* process in which various products of dissociation of oxygen and water (e.g. *O*, *O$_3$*, *OH*, *HO$_2$*) react selectively with the harmful gases *NO* and *NO$_2$* (*NO$_x$*) to form acids. Upon the addition of ammonia the acids are converted to solid salt particles. These particles are removed from the gas stream by conventional techniques (e.g. electrostatic precipitators or bag filters). Features which make this novel *deNO$_x$* process attractive in comparison to presently applied methods (e.g. catalytic reduction) are: estimated investment costs are low, re-heating of flue gas is not necessary, *SO$_2$* is removed simultaneously by a thermal reaction with ammonia, the by-products (ammonium sulphate and ammonium nitrate) can be sold because they are useful as a soil-fertilizer, HV pulse parameters can be controlled for optimum reactor operation under variable gas conditions.

The main objective of this work is to understand the influence of HV pulse parameters (e.g. rise time, maximum voltage, pulse duration) on the *deNO$_x$* process by means of electrical and optical measurements and by means of numerical simulations of the pulsed discharge as well as the chemical kinetics. In order to test the validity of the discharge model, experiments have been performed with *N$_2$*-*O$_2$* mixtures. Measurements of the energy cost for *NO$_x$* removal have been performed using simulated flue gas and flue gas supplied by a natural gas burner.

A gated image intensifier and CCD camera have been used to obtain time-resolved pictures of discharge light emission (~30 ns time resolution). The pictures reveal the discharge to consist of numerous streamers (discharge filaments) with an average number density along the wire of ~600 per meter. The streamer number density appears to be independent on the anode radius and the maximum of the pulsed voltage. Three time-phases of the streamer discharge are distinguished: (i) Primary streamers propagate at high speed ($>2\cdot10^5$ m/s) from the anode to the cathode. (ii) After arrival of primary streamers at the cathode, secondary streamers are seen as re-illuminating and prolonging parts of the residual dark primary streamer channels. (iii) A decay phase is characterized by secondary streamers with diminishing light emission intensity and constant length. The optical radii (measured at 50% of the emission intensity maximum) of primary and secondary streamers are respectively ~200 μm and ~150 μm.

Simultaneous voltage, current and local light emission measurements yield average values and probability distributions of the streamer inception time lag, the streamer inception voltage and the dissipated energy per pulse. The spread in the inception time lags of streamers produced at different positions along the wire during the same HV pulse, is very small when compared to streamer inception time lags. This result demonstrates that streamer formation along the wire is influenced by the first formed streamer(s).

With increasing HV pulse repetition rate and also when HV pulses are superimposed on a positive bias voltage, the dissipated energy per pulse decreases because the negative ion concentration increases close to the anode-wire. The influence of negative ions has two causes: (a) a lowering of the average streamer inception voltage as a result of detachment, (b) a lowering of the field close to the anode-wire as a result of space charge. It appears that the streamer inception voltage can be raised by increasing the wire radius or by decreasing the voltage rise time. For different anode-wire radii, the measured minimum value of the streamer inception voltage is close to the value which can be calculated with the Raether-Meek criterion. The addition of water vapour to dry air causes a large reduction of the dissipated energy per pulse, probably because very stable hydrated negative ions are formed.

Delay time measurements of local light emission signals have been used to determine the streamer velocity. When streamers propagate from the anode-wire toward the low field region, the streamer velocity strongly decreases in a region close to the wire, it remains approximately constant in the mid-gap region and it increases again when approaching the cathode. When the applied voltage is raised or when the O_2 concentration in a N_2-O_2 mixture is lowered, the streamer velocity increases in the entire gap.

Measurements of the intensity ratio of N_2^+*(391.4 nm)* and N_2*(337.1 nm)* emission lines have been used to determine the maximum field strength in the discharge. The measured maximum field strength in primary streamers is in the range 500-1000 Td. The changes in the maximum field strength in primary streamers as a function of their position in the gap, the applied voltage and the O_2 concentration are qualitatively very similar to changes in the streamer velocity. The maximum field strength in the secondary streamer is just below the ionization threshold. It appears from measurements of the rotational structure of the N_2*(337.1 nm)* emission line that the neutral gas temperature in the secondary streamer is close to the ambient gas temperature.

Schlieren photography is used to visualize temperature gradients in the discharge. The photographs show that after the maximum of the discharge current pulse (with a decay time constant of ~100 ns) gas-dynamic expansion of residual streamer channels to a radius of about 1 mm occurs within a period of ~2 μs. The photographs also show that energy dissipation is highest in those parts of the residual streamer channels where also secondary streamer emission occurred. The main part of the dissipated energy is transferred to the gas with a characteristic time of ~100 μs.

The model for chemical kinetics indicates that among the various chemical reactive particles produced in the discharge, positive ions and electronic excited molecules
are the most essential for the formation of oxidants. The primary streamer model shows that electrons in the fast propagating primary streamer head possess an average energy in the range 10-20 eV, which is very efficient for ionization and production of excited molecules. Electrons in the primary streamer channel, which dissipate most of the energy, possess an average electron energy ($\sim$1 eV) which is too low for efficient production of oxidants. Calculated values of the primary streamer velocity and the maximum field strength in primary streamers are in good quantitative agreement with experimental data, measured in the mid-gap region.

A reduction of the energy cost per removed NO_x molecule is expected from the addition of oxygen and/or water vapour which increases the concentration of oxidants in the streamer head and decreases energy dissipation in the streamer channel as a result of attachment of free electrons. The chemical kinetics model shows that NO_x oxidation is mainly limited by the reduction of NO_2 to NO. The energy consumption for NO_x removal can be lowered by adding gases which favour the oxidation of NO_2 (e.g. ammonia).

The significance of the oxidation-reduction equilibrium of NO_2 is confirmed by measurements of NO and NO_2 concentrations. A lowering of the gas temperature and an increase of the water vapour concentration cause a reduction of the energy cost per removed NO_x molecule in spite of an increase of the NO_2 concentration. A considerable improvement of the NO_x removal efficiency is obtained limiting the HV pulse duration to the average transit time of primary streamers. This result indicates that the average number of oxidants per quantity of dissipated energy is higher in the primary streamer phase than in the secondary streamer phase.

Pulsed corona discharges can also be applied to oxidize various other contaminants which are present with low concentrations (100-1000 ppm) in effluent gases (e.g. volatile organic compounds and dioxines). The properties of the pulsed corona discharge which have been investigated are also of interest for the optimization of these applications.

Samenvatting

Elektrische technieken voor gasreiniging zijn sterk in opkomst. Een mogelijke toepassing is het $deNO_x$ proces waarbij een gepulste corona-ontlading diverse produkten produceert door dissociatie van zuurstof en waterdamp (bijvoorbeeld O, O_3, OH, HO_2) die selectief reageren met de schadelijke gassen NO en NO_2 (NO_x). Hierbij worden zuren gevormd die onder toevoeging van ammoniakgas worden omgezet in vaste zoutdeeltjes. Deze deeltjes worden met gebruikelijke technieken uit het gas verwijderd (bijvoorbeeld met elektrostatische stofvangers of doekfilters). Eigenschappen die dit nieuwe $deNO_x$ proces aantrekkelijk maken in vergelijking met nu toegepaste methoden (bijvoorbeeld katalytische reductie) zijn: de verwachte investeringskosten zijn laag, opnieuw opwarmen van rookgas is niet nodig, SO_2 wordt simultaan verwijderd in een droog proces door een thermische reactie met ammoniakgas, er bestaat een markt voor de bijprodukten (ammoniumsulfaat en ammoniumnitraat) omdat deze als kunstmest kunnen worden gebruikt, parameters van HS pulsen kunnen onder variabele gascondities aangepast worden voor een optimaal functioneren van de reactor.

Het hoofddoel van dit werk is kennis te vergaren over de invloed van parameters van HS pulsen (bijvoorbeeld de stijgtijd, het spanningsmaximum en de pulsduur) op het $deNO_x$ proces door middel van elektrische en optische metingen en door middel van numerieke simulaties van de gepulste ontlading en de chemische kinetiek. Om de geldigheid van het ontladingsmodel te testen zijn metingen uitgevoerd met N_2-O_2 mengsels. Metingen van het energieverbruik voor de verwijdering van NO_x zijn uitgevoerd met gesimuleerd rookgas en met het rookgas van een aardgasbrander.

Een beeldversterker en een CCD camera zijn gebruikt voor tijdopgeloste opnamen (~30 ns resolutie) van het door de ontlading geëmitteerde licht. De opnamen laten zien dat de ontlading bestaat uit vele streamers (ontladingsfilamenten) met een gemiddeld aantal van ~600 per meter draad. Het aantal streamers aan de draad blijkt onafhankelijk te zijn van de draadradius en de maximum waarde van de spanningspuls. Drie tijdsfasen van de streamerontlading worden onderscheiden: (i) Primaire streamers propageren met hoge snelheid ($>2 \cdot 10^5$ m/s) van de anode naar de kathode. (ii) Nadat primaire streamers aan de kathode zijn aangekomen worden secundaire streamers waargenomen in de vorm van opnieuw oplichtende en zich uitbreidende delen van de donkere primaire streamerkanalen. (iii) Tenslotte bestaat er een vervalfase die wordt gekarakteriseerd door secundaire streamers met afnemende intensiteit en constante lengte. De optische radii (gemeten bij 50% van de maximum intensiteit) van primaire en secundaire streamers zijn respectievelijk ~200 μm en ~150 μm.

Simultane spanning-, stroom- en lokale lichtemissiemetingen geven gemiddelde waarden en kansverdelingen van de streamerinceptietijd, de streamerinceptiespanning en de gedissipeerde energie per puls. De strooïng in inceptietijden van streamers, die op verschillende plaatsen langs de draad gevormd zijn tijdens één HS puls, is zeer klein ten opzichte van de inceptietijden zelf. Dit resultaat toont aan dat de vorming van streamers langs de draad beïnvloedt wordt door de eerst gevormde streamer(s).

Met toenemende herhaalfrequentie van HS pulsen en ook wanneer HS pulsen worden gesuperponeerd op een constante positieve spanning, neemt de gedissipeerde energie per puls af omdat bij de anodedraad de concentratie van negatieve ionen toeneemt. De invloed van negatieve ionen heeft twee oorzaken: (a) een verlaging van de gemiddelde streamerinceptiespanning als gevolg van detachment, (b) een verlaging van het elektrische veld dicht bij de anodedraad als gevolg van ruimtelading. De streamerinceptiespanning blijkt verhoogd te kunnen worden door een toename van de draadradius of door een afname van de HS pulsstijgtijd. Voor verschillende radii van de anodedraad, ligt de gemeten minimum waarde van de streamerinceptiespanning dicht bij waarde die met het Raether-Meek criterium berekend kan worden. De toevoeging van waterdamp aan droge lucht leidt tot een grote afname van de gedissipeerde energie per puls die mogelijk veroorzaakt wordt door de vorming van zeer stabiele gehydrateerde negatieve ionen.

Metingen van tijdverschillen tussen lokale emissiesignalen zijn gebruikt voor het bepalen van de streamersnelheid. Wanneer streamers propageren vanaf de anodedraad naar het gebied met lage veldsterkte, neemt de streamersnelheid sterk af in het gebied dicht bij de draad, in het centrale gebied tussen de elektroden blijft ze bij benadering constant en bij het naderen van de kathode neemt ze weer toe. Wanneer de aangelegde spanning wordt verhoogd of wanneer de O_2 concentratie in een N_2-O_2 mengsel wordt verlaagd neemt de streamersnelheid in het gehele ontladingsgebied toe.

Metingen van de intensiteitsverhouding van $N_2^+(391.4\ nm)$ en $N_2(337.1\ nm)$ emissielijnen zijn gebruikt voor het bepalen van de maximum veldsterkte. De gemeten maximum veldsterkte in primaire streamers ligt in het bereik 500-1000 Td. De veranderingen in de maximum veldsterkte in streamers als functie van de positie in het ontladingsgebied, de aangelegde spanning of de O_2 concentratie komen kwalitatief sterk overeen met veranderingen in de streamersnelheid. De maximum veldsterkte in de secundaire streamer ligt beneden de drempelwaarde voor ionisatie. Uit metingen van de rotatiestructuur van de $N_2(337.1\ nm)$ emissielijn blijkt dat de temperatuur van het neutrale gas in de secundaire streamer nauwelijks hoger is dan de omgevingstemperatuur.

Schlierenfotografie is gebruikt om kleine temperatuurverschillen in de ontlading zichtbaar te maken.

De foto's laten zien dat volgend op het maximum van de ontladingsstroom (die een vervaltijd van ~100 ns bezit) gasdynamische expansie van het gas optreedt binnen een tijd van ~2 μs waarna de achterblijvende streamerkanalen een radius van ~1 mm bezitten. De foto's laten ook zien dat relatief veel energie gedissipeerd wordt in die gedeelten van de achterblijvende streamerkanalen waar ook emissie van secundaire streamers plaatsvond. Het grootste deel van de gedissipeerde energie wordt met een karakteristieke tijd van ~100 μs aan het gas overgedragen.

Het model voor chemische kinetiek geeft aan dat onder de diverse chemisch reactieve deeltjes die de ontlading produceert, positieve ionen en geëxciteerde moleculen essentieel zijn voor de vorming van oxydanten. Het model van de primaire streamer laat zien dat elektronen in de snel propagerende streamerkop een gemiddelde elektronenenergie bezitten in het bereik 10-20 eV, dat zeer efficient is voor ionisatie en productie van geëxciteerde moleculen. Elektronen in het kanaal van de primaire streamer, die het grootste deel van de energie dissiperen, bezitten een gemiddelde energie (~1 eV) die te laag is voor efficiënte produktie van oxidanten. Berekende waarden van de streamersnelheid en de maximum veldsterkte in streamers komen quantitatief goed overeen met experimentele waarden, gemeten in het centrale gebied tussen de elektroden.

Een verlaging van het energieverbruik per NO_x molecule wordt verwacht van toevoeging van zuurstof of waterdamp omdat hierdoor de concentratie oxidanten in de streamerkop toeneemt en de energiedissipatie in het streamerkanaal afneemt als gevolg van attachment van vrije elektronen. Het model voor chemische kinetiek laat zien dat NO_x oxidatie voornamelijk beperkt wordt door reductie van NO_2 naar NO. Het energieverbruik voor verwijdering van NO_x wordt verlaagd door toevoeging van gassen die de oxidatie van NO_2 bevorderen (bijvoorbeeld ammoniakgas).

Het belang van het oxidatie-reductie evenwicht van NO_2 wordt bevestigd door metingen van NO en NO_2 concentraties. Afkoeling van het gas of verhoging van de waterdampconcentratie leiden, ondanks een toename van de NO_2 concentratie, tot een verlaging van het energieverbruik per verwijderd NO_x molecule. Een aanzienlijke verlaging van het energieverbruik voor NO_x verwijdering is verkregen door het verkorten van de HS pulsduur tot de gemiddelde oversteektijd van primaire streamers. Dit resultaat geeft aan dat in de primaire streamerfase het gemiddeld aantal geproduceerde oxydanten per hoeveelheid gedissipeerde energie hoger is dan in de secundaire streamerfase.

Gepulste corona ontladingen kunnen ook toegepast worden voor het oxideren van diverse overige schadelijke stoffen die in lage concentraties aanwezig zijn in afvalgassen (bijvoorbeeld vluchtige organische stoffen en dioxynes). De eigenschappen van de gepulste corona ontlading die onderzocht werden zijn eveneens van belang voor de optimalisatie van deze toepassingen.

Chapter 1 Introduction

1.1 Objectives

The work described in this thesis has been performed as a part of the Coal & Electricity program at the faculty of Electrical Engineering of the Eindhoven University of Technology. The major topic of this program is the clean use of coal in the production of electricity. The historical problems that arise when extracting and burning coal (safety hazards, air pollution) have contributed to a general climate of antagonism toward coal. Nevertheless, coal is still considered today one of the main fossil fuels (Landrieu and Turpin, 1989; Patterson, 1993) and huge resources of coal are still available in the world. One of the most serious drawbacks of coal combustion is the release of ash particles, nitrogen oxides NO_x and sulphur dioxide SO_2 in the atmosphere. In industrial areas with dense traffic and under unfortunate geographical and meteorological conditions, these gases contribute to the *photochemical smog* phenomenon. Moreover, NO_x and SO_2 can be transported over several hundreds of kilometres before being deposited or washed from the air as acids in rain or snow. Throughout the 1980s *acid rain* was one of the most controversial environmental issues in Europe. In the 1990s it has been replaced by the CO_2 greenhouse effect but it remains a serious continental problem.

During the last two decades, coal-fired electrical power plants and other stationary sources of NO_x and SO_2 emissions in the USA, Japan and Europe have been equipped with systems for emission control. At present, still considerable efforts are put in the development of new promising techniques for the denitrification and desulphurization of combustion gases (abbreviated as $deNO_x$ and $deSO_2$). These efforts are encouraged by the emission standards which become more stringent but also by the high costs of the currently used systems.

Early laboratory experiments which showed the possibility to control NO_x by corona discharge treatment, have been performed in Japan (Masuda and Wu, 1987). The results have been improved using short (sub-microsecond) high voltage pulses instead of a constant voltage and with pulses of positive polarity rather than negative ones. In Italy, promising results demonstrating both NO_x and SO_2 removal, have been obtained in a pilot plant, treating a small fraction (100 m^3/hr) of the flue gas of a coal-fired electrical power plant (Civitano, 1993). The pulsed corona discharge can also be used for other stationary sources of NO_x and SO_2, e.g. cement kilns and incineration plants.

Although an overwhelming amount of literature data exists on the subject of corona discharges, rather few data are available for corona discharges initiated by

fast rising high voltage (HV) pulses. In view of optimization of the pulsed corona induced *deNO$_x$* process, this thesis describes detailed studies of different aspects of pulsed positive corona discharges under various HV pulse conditions.

The general characteristics and the terminology of corona discharges will be presented in **1.2**. Section **1.3** provides information about sources and consequences of NO_x and SO_2 emissions and will be followed by a discussion of the presently available techniques for emission control in **1.4**. The pulsed corona induced *deNO$_x$* process and its integration in an electrical power plant will be described in **1.5**.

1.2 General aspects of corona discharges and applications

By the term *corona discharge* one generally refers to the electrical discharge phenomena in the vicinity of conductors of small radius of curvature such as sharp points and thin wires. These phenomena have been called coronas because of some similarity between them and the glow or corona surrounding the sun which is seen during a total eclipse of the sun. Corona discharges can occur for instance around HV power transmission lines where they are sometimes perceived as a crackling acoustic noise. Due to their transient (time-varying) electrical properties, corona discharges along HV lines are also responsible for electromagnetic "noise", emitted on a wide range of radio broadcast bands. The discharge volume of coronas can generally be subdivided in an *ionization region*, where electrons and ions are produced, and a much larger *drift region*, where electrons do not gain sufficient energy from the electric field to cause ionizing collisions. In gases containing electronegative molecules (for instance O_2 in air), the electrons will be rapidly attached to form negative ions and the electron density in the drift region will be rather low when compared to the ion density. In the drift region, momentum transfer of positive or negative ions to the neutral gas causes a gas motion which is known as electric wind or corona wind.

Electrical coronas are by no means a product of man only. They occur also frequently in natural circumstances. The primary processes preceding the formation of the bright filamentary discharge channels of lightning during thunder storms are undoubtedly corona discharge phenomena in strongly asymmetrical electric fields of clouds. However, the details of the physical processes leading to formation and separation of charge within clouds are still a question of debate (Raizer, 1987). Usually, corona phenomena are weakly luminous. Light phenomena around sharp objects at the top of high buildings or at the masts of ships (St. Elmo's Fire) are also definitely corona discharges but in the daytime they are often too weak to be perceived by eye.

The visual appearance of corona discharges, observed in a well-darkened

environment, may be *glow*-like, filamentary or a combination of these two forms. The filaments, called *streamers*, can be characterized as ionizing waves which, by means of their own electric space charge field, can propagate in regions where the geometric electric field is below the field needed for ionization. Upon arrival of a streamer at the opposite electrode, its weakly conductive channel can be transformed into the highly conductive arc channel and consequently lead to the *breakdown* of the applied voltage. Often the glow and streamer discharge phenomena remain located in the high electric field region near a single curved electrode, called the *active electrode*, the other electrode being at a too far distance.

Streamer phenomena are not a property of corona discharges alone. Also in case of a uniform static electric field, in between two parallel flat electrodes, streamer development is possible and it will then usually lead to the formation of one or more arcs or sparks (sparks are arcs of short duration). In corona discharges, however, streamer phenomena are often observed without arc formation and this fact is possibly the historical reason for electrical coronas also being called *partial discharges*.

The density of electrons and ions in a corona discharge is generally more than a factor 10^4 lower than the neutral gas density. Therefore, corona discharges can be categorized in the class of weakly ionized plasmas, the term plasma referring to the state of a gas where charged particles (electrons and ions) play a predominant role. However, the energy of the electrons is generally much higher than the energy of other particles (ions, neutrals) in the discharge. While free electrons reach sufficient energy to ionize and dissociate molecules, the neutral gas remains often at near ambient temperature and pressure. This non-equilibrium property of the electrons is an essential feature of the corona discharge and for this reason the discharge has also been qualified as a *cold discharge* or as a *non-thermal plasma*. The properties of fully thermalized arcs, which may be initiated by corona streamers, are completely different: The energy delivered by the electrical power supply is used to heat all particles, including the neutral gas.

In order to distinguish between the various types of coronas it is possible to use a classification according to *external conditions* under which these coronas are produced. For example, a corona is called either *positive* or *negative* depending on the polarity that is applied to the active electrode. The terms *DC-*, *AC-* and *pulsed corona* are used to designate corona discharges which are supplied by a constant voltage, an alternating voltage or a pulsed voltage respectively. Corona discharges are also often qualified in terms of their *external features*, for example as glow corona or as streamer corona. Occasionally the features of the current in the external circuit are used to characterize corona discharges. This current can be continuous or pulsating even when a DC supply voltage is used. In the vast literature on the subject several terms are used to designate the impulsive character

of DC coronas, e.g. *intermittent coronas* and *impulsive coronas*. We will use here the term *self-repetitive corona* in order to avoid any confusion with the *pulsed corona*, produced with externally generated HV pulses.

Corona discharges are applied in various industrial processes and products. Many of these applications are based upon the possibility to produce corona discharges in air at normal pressure (1 bar) which is, for electrical discharges in general, a relatively high pressure. Industrial applications such as electrostatic painting and printing devices (copiers, laser printers) use the corona discharge as an effective means for electrical charging. Also the chemical activity of corona discharges is widely used in industry. Coronas are used for surface treatment of polymers and assimilated materials in order to increase their adhesive properties (e.g. the manufacturing of electronic, photographic and magnetic supports). The non-thermal property of corona discharges is particularly useful in chemical applications where the gas temperature is preferably kept low while the radicals, produced by electron impact dissociation, initiate chemical reactions. An example of such an application is the generation of ozone O_3 where reverse reactions such as $O + O_3 \rightarrow 2\,O_2$ are suppressed by reducing the gas temperature (Sälge, 1983). Ozone is one of the strongest oxidizing agents, mainly used for the treatment of drinking water. Presently it is introduced as an alternative for bleaching by chlorine compounds.

An electrostatic application with large environmental impact is the electrostatic precipitator (ESP) which has been used successfully for several decades to remove dust particles (also ash and soot) from the exhaust gases of stationary sources, e.g. electrical power plants and cement kilns. The electrode geometry usually consists of a wire electrode positioned centrally between two vertical parallel plates (Fig. 1.1).

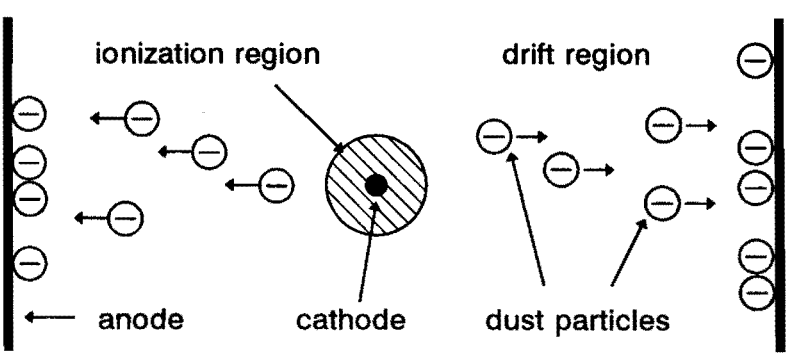

Fig. 1.1 The principle of an electrostatic precipitator with negative corona.

The principle of the ESP involves several steps: ion production, particle charging, particle migration, dust layer collection and dust layer removal by mechanical rapping. In case of a negative wire-electrode a uniform corona discharge provides optimum conditions for particle charging. Streamer phenomena which occur in positive coronas are undesirable because they disturb the discharge uniformity thereby reducing the collection efficiency (McLean, 1988).

With high dust resistivity, say $>10^{10}$ Ωm, a voltage drop across the dust layer can result in breakdown within this layer, causing collected dust to re-enter into the drift region. This phenomenon is known as *back-corona*. ESP's have been initially operated with a DC supply voltage and improvements of the particle collection efficiency have been sought by raising the applied voltage. However, the associated increase in dust layer current enhanced the problem of back corona and power losses. Recently the performance of ESP's has been much improved by the use of HV pulses which are superimposed on a DC bias voltage (Nelson and Salasoo, 1987; Verhaart, 1992). The HV pulses are used for the ion production while particle charging, particle migration and dust layer formation are assured by the DC bias voltage which can be kept below the ionization threshold. Back corona is avoided, the average current is very low and energy consumption is reduced. The use of HV pulses offers a flexibility which allows for optimum working conditions even in case of a plant with variable gas flow conditions and variable dust particle size. Collection efficiencies over 99% are achieved by using HV pulse widths in the range of 50 μs to 1 ms.

1.3 NO_x and SO_2 emissions: effects, sources and regulations

The most notorious role of NO_x in air pollution in and around cities is its contribution to the formation of photochemical smog. Nitrogen oxides react with oxygen and hydrocarbons (from vehicle exhaust) under influence of UV light to produce a variety of harmful compounds, for example organic nitrocompounds and ozone[(1)]. Some of these compounds reduce visibility, others such as ozone cause eye irritation, impaired lung function and damage to trees and crops. NO_2 and O_3 are relatively insoluble and therefore able to penetrate deep into the lungs. Both NO_2 and O_3 interfere with oxygen transport by haemoglobin (having a poisoning effect similar to that of CO). SO_2 emissions, known for producing sulphur compounds with obnoxious odours, are also destructive to living organisms.

(1) Ozone plays different roles in environmental issues: (a) Natural stratospheric ozone is critically important for absorbing UV radiation from the sun. (b) Increased ozone concentration in ambient air is a sign of air pollution. (c) Ozone is a useful industrial product that can replace chlorine compounds for bleaching and decontamination without harmful by-products.

Compared with other gaseous pollutants, SO_2 is highly soluble in water and therefore it will, when inhaled, be absorbed in the upper respiratory system. Obviously, the effects depend very much on the concentration and the exposure time. Exposure to SO_2 levels of the order of 1 ppm (1 part per million) during several hours leads to constriction of the airways.

The ultimate fate of NO, NO_2 and SO_2 in the atmosphere is oxidation, either in the gas phase forming nitric acid HNO_3 and sulphuric acid H_2SO_4 or in the liquid phase forming nitrate NO_3^- and sulphate SO_4^{2-} dissolved in water. In the presence of cloud drops the liquid phase oxidation of SO_2 is by far the most important, but liquid phase oxidation of NO_x is likely to be of small importance when compared to gas phase oxidation (Seinfeld, 1986). Deposition of nitrates and sulphates is known as acid rain but acid deposition is a more correct term because also dry deposition occurs.

A number of noticeable effects have been ascribed to acid rain: The dying off of trees in Germany and North America, the acidification of lakes in the Scandinavian countries and Canada, not to mention the corrosion defacing many historical buildings made of sandstone, limestone or marble. Clean air contains small concentrations of NO, NO_2 and SO_2 from natural sources, e.g. volcanos and physical and chemical atmospheric processes (Seinfeld, 1986). The natural acidity of rain results in a pH value of ~5.6. If the pH of rain is less than 5.0, we can be fairly certain that man-made influences are present. The specific interactions of acid deposition with lake fauna, soils and different vegetation types are still incompletely understood, but there is little doubt that acid deposition places severe stress on ecosystems (Park, 1987; Harter, 1989; Ulrich, 1990).

NO_x and SO_2 are formed when fossil fuels (coal, oil) are burned. During the combustion NO_x is initially formed as NO. *Thermal NO* is formed by the oxidation of atmospheric nitrogen and *fuel NO* is formed by the oxidation of nitrogen-containing compounds in the fuel. A part of the formed NO is oxidized to NO_2 in the combustion zone and in the flue gas ducts. The NO_x in the resulting flue gas usually consists of 90 to 95% NO and 5 to 10% NO_2. Other oxides of nitrogen, such as N_2O and N_2O_5, may also be present in combustion gases but their concentrations are generally less than 1% of the N_xO_y total. Typical concentrations of NO_x in the flue gas of a coal-fired electrical power plants are in the range 500-1000 ppm. SO_x emissions from the combustion of coal or oil consist of approximately 99% SO_2 and 1% SO_3. Since SO_3 emissions represent but ~1% of total SO_x emissions, usually only SO_2 emissions are considered. The SO_2 concentration in the flue gas of a power plant burning bituminous coal with 1 wt. % (percentage in weight) sulphur is approximately 700 ppm (Vernon, 1993). The sulphur content in different types of coal is generally in the range 1-3% but some types of coal contain more than 5% sulphur (Davidson, 1993). Typical concentrations of SO_2 in the flue gas of a coal-

fired electrical power plant are in the range 500-2000 ppm.

The burning of fossil fuels in electrical power plants is of course by no means the only source of NO_x and SO_2 in the atmosphere. In most of the industrialized countries, vehicle exhausts are the major source of NO_x. Large differences exist between countries with respect to the contribution of coal-combustion to their total SO_2 emissions. In many countries, refineries and steel industry contribute to the total SO_2 emission as much as electrical power plants.

The health-related and acid rain related problems each occur at a different geographical scale. This difference has consequences for the effects of possible counter-measures against NO_x and SO_2 emission. The local health-related effects may be reduced by building high chimneys and by reducing the emissions of main sources in industrial areas with unfortunate geographical and meteorological circumstances for the dispersion of gases. However, the acid rain related problems can be brought under control only if the total emission is reduced. Moreover, because of the continental scale of the acid rain problem international cooperation is a prerequisite.

The most important international agreements on limiting NO_x and SO_2 emissions are (a) the United Nations Economic Commission for Europe (UNECE) Convention on Long-range Transboundary Air Pollution (1979) and its protocols, and (b) the European Communities legislation on limitation of emissions from large combustion plants. Signatories of the UNECE convention are required to exchange information on control technologies and approaches. NO_x emissions should have been frozen in each country before 1994 to 1978 levels. SO_2 emissions should have been reduced by at least 30% before 1994, compared to 1980 levels. A set of international regulations concerning emissions of particulates (fly ash), NO_x and SO_2, called the Large Combustion Plants Directive was agreed in 1988. The agreed directive incorporates two regulatory instruments for emission control:

1) Emission standards to be applied to new combustion plants with a capacity over 100 MW from 1990
2) National targets for the reduction of total emissions from combustion plants over 50 MW existing before July 1987

Countries may choose whether to treat plants built between July 1987 and 1990 as new plants subject to emission standards or as existing plants contributing to targeted emissions. According to this directive the emission limits of NO_x and SO_2 for new coal-fired plants with a capacity larger than 500 MW are 650 and 400 mg/Nm^3 (i.e. 320 ppm NO_2 and 140 ppm SO_2)[(1)] respectively. Also in the USA and Japan strict emission standards are in force.

(1) 1 Nm^3 is 1 m^3 at normal pressure and temperature (NPT: p = 1.013 bar and T = 293 K). At NPT 1 mg/m^3 NO = 0.75 ppm NO, 1 mg NO_2 = 0.49 ppm NO_2, 1 mg/m$_3$ SO_2 = 0.35 ppm SO_2.

Existing techniques for abatement of NO_x and SO_2 from stationary sources have been widely applied in the USA, Japan and Germany and in some smaller countries among which Switzerland and the Netherlands (Ando, 1989). In these countries a considerable decrease of SO_2 emissions has already been achieved in the period 1970-1990. Also NO_x emissions started to decrease in this period in spite of increased road traffic. In the Netherlands the emission of SO_2 decreased from 1100 kton/year in 1965 to 208 kton/year in 1990 (Boonekamp, 1992). The emissions of NO_x and SO_2 in 1990 for different sectors in the Netherlands are given in Table 1.1.

In many countries in the world power plants are devoid of any environmental control techniques. A considerable reduction of NO_x and SO_2 emissions can still be achieved in East European countries where often high-sulphur coals are used. Probably in no country NO_x and SO_2 emissions are increasing as much as in China, after the USA the second largest consumer of energy in the world. Energy consumption in China increased in the period 1970-1990 by 220% (the annual growth rate is more than 6%) and relies heavily on coal with a high sulphur content, sometimes up to 5% (Levine et al., 1992). A clean coal programme set up in Japan will promote the transfer of clean coal technology and expertise to China and other countries in Asia (Kimura, 1991).

Sector	NO_x emission (%)	SO_2 emission (%)
Transport	56	15
Power plants	13	22
Refineries	4	33
Others (industrial)	15	29
Others (non-industrial)	12	1
Total	100% = 554 kton/year	100% = 208 kton/year

Table 1.1 The emissions of NO_x and SO_2 by various sectors in the Netherlands in 1990 (Boonekamp, 1992).

Because of the large resources of fossil energy still available in the world, the known environmental impacts of burning fossil fuels and the absence of emission control techniques in many countries, there is a growing pressure for the world-wide introduction of strict emission standards and for the development of more efficient and cheaper techniques for NO_x and SO_2 control.

1.4 NO_x and SO_2 emission control: available techniques and new developments

In principle three methods exist for reducing NO_x and SO_2 emissions from stationary sources: (1) pre-combustion methods, (2) combustion modification and (3) post-combustion methods (flue gas treatment).

Pre-combustion methods

The possibilities to reduce SO_2 emissions by cleaning coal prior to combustion have been reviewed in detail by Couch (1991). Physical coal cleaning techniques, removing inorganic sulphur (mostly FeS_2), are well-established and widely used. However, about 50% of the sulphur contained in coal is organic (Davidson, 1993). A promising development is *coal gasification integrated with combined-cycle power generation* (IGCC). In the gasification process the sulphur and nitrogen in coal are transformed mainly to H_2S (hydrogen sulphide) and NH_3 (ammonia). These compounds are removed from the synthesis gas before combustion by means of a catalytic process, the so-called Claus process. A IGCC demonstration project (presently the largest in the world) has been built at Buggenum in the Netherlands. The reduced environmental impact of this plant has been reviewed by Jones (1992). Using coal with 1 wt. % sulphur content, the annual average SO_2 removal efficiency is expected to be 98%.

Combustion modification techniques

Low NO_x burners of different manufactors are described by Hjalmarsson and Soud (1990). Generally, the burners are designed to achieve two combustion stages through the way air and fuel are introduced. The first stage is either oxygen or fuel deficient and the air or fuel required to complete the combustion process is introduced in a second stage. The formation of thermal *NO* is suppressed by the lower flame temperature. By means of a combination of combustion modification techniques a reduction up to about 70% of the NO_x emission of a coal fired power plant can be achieved. However, this reduction is often insufficient to satisfy emission standards.

Flue gas treatment ($deNO_x$ and $deSO_2$)

A variety of $deNO_x$ and $deSO_2$ processes is available. The processes are usually installed in separate vessels after the boiler. It is common to distinguish between *dry* and *wet* processes, i.e. processes producing a dry or a wet by-product. At

present, one of the most advanced processes for $deNO_x$ is a dry catalytic process, called *selective catalytic reduction* (SCR). For flue gas desulphurization (FGD) mainly the *wet limestone-gypsum process* is used.

In SCR ammonia (NH_3) is added to chemically reduce NO_x to N_2 and H_2O in the presence of a catalyst. Generally, 70-85% of NO_x is removed using a stoichiometric ratio ($[NH_3]/[NO_x]$) of 0.7 to 0.9. The optimum temperature for this process is 300-400 °C. The process is therefore often located not too far from the boiler where the flue gas temperature is still high enough and before the ESP for fly ash removal.

The *wet limestone-gypsum process* produces $CaSO_4$ (gypsum) as a useful and saleable by-product. The process is based upon the selective absorption of SO_2 by a mixture of $CaCO_3$ (limestone) and water which is sprayed into the flue gas. A low flue gas temperature (50-60 °C) is required to obtain sufficient solubility of SO_2. The process is usually capable of removing 90% or more of the SO_2. Common problems with the wet limestone-gypsum process are the necessity of gas reheating for adequate dispersion of the flue gas in the atmosphere and the treatment of waste water. Generally the process is installed downstream of the ESP in order to obtain gypsum with a minimum of ash particles.

The investment and operation costs of combined $deNO_x$-$deSO_2$, using SCR and a wet FGD process together, increase the price of electricity by about 20-30% (Ando, 1989). This fact and the strict emission rules for large combustion plants, encourage research laboratories to investigate new promising techniques for $deNO_x$ and $deSO_2$. The International Energy Agency has a sister agency, called IEA Coal Research, whose publications are an essential source of information about developments in the field of $deNO_x$ and $deSO_2$ technology (e.g. Hjalmarsson and Soud, 1990). Some of the new processes, which transform NO_x and/or SO_2 in useful by-products and which are generally operated downstream of an ESP, are briefly discussed below.

The *activated carbon process* uses activated carbon in a moving bed absorber for simultaneous reduction of NO_x and SO_2. In a first stage, SO_2 is oxidized to H_2SO_4 which is adsorbed on the carbon. In presence of ammonia, the carbon acts also as a catalyst for NO_x reduction. In a second stage, SO_2 is recovered by heating the carbon to a temperature of 400-500 °C. The SO_2-rich off-gas can be used to produce elemental sulphur in a catalytic Claus process. A 350 MWe plant is currently in operation in Germany. Removal efficiencies of over 95% for SO_2 and 70% for NO_x have been achieved.

The *wet gas sulphuric acid process* (WSA) uses a catalytic converter which oxidizes SO_2 to SO_3 at 400-420 °C. SO_3 reacts with water to form sulphuric acid, H_2SO_4. After passing the converter, the flue gas is cooled down to the dew-point of sulphuric acid (~100 °C) that is subsequently collected as a by-product. The process is combined with conventional SCR for NO_x removal. In a demonstration project

in Denmark a 300 MWe power plant is in operation using this system. Typically 95% of SO_2 can be removed.

In the *electron beam (e-beam) process*, the flue gas is irradiated by a beam of mono-energetic electrons downstream of the ESP for fly ash removal. The initial energy of the electrons (300-800 keV) is sufficient to ionize a large number of molecules, thereby creating secondary electrons with an energy of the order of 100 eV. The secondary electrons, in turn, cause ionizing collisions. Apart from ions (e.g. N_2^+, O_2^+), also radicals, like O and OH, are formed by dissociation of oxygen and water. These radicals react selectively with NO_x and SO_2 to form nitric acid HNO_3 and sulphuric acid H_2SO_4. Upon the addition of ammonia NH_3 the acids are transformed to the solids ammonium nitrate NH_4NO_3 and ammonium sulphate $(NH_4)_2SO_4$. The solid particles are collected downstream of the reactor with a second ESP. Ammonium sulphate and nitrate are useful by-products that can be sold as a high quality fertilizer. Frank and Hirano (1993) reviewed pilot plant investigations of the e-beam process. Demonstrations with flue gas flow rates in the range 20.000-25.000 Nm^3/m have been performed in the USA, Japan, Germany and recently in Poland.

1.5 The pulsed corona deNO$_x$ process

1.5.1 Differences between pulsed corona and e-beam processes

The pulsed corona and e-beam $deNO_x$ processes have much in common. Both processes are initiated by electrons producing ions and radicals which transform the pollutants into acids. In both processes, the addition of ammonia converts the acids to salts that can be removed from the gas stream by means of an ESP or bag filter. However, also essential differences exist. In particular the properties of electrons (spatial and energy distributions) are very different. In a streamer corona discharge electrons are produced in thin discharge channels while in e-beam irradiated gas the spatial distribution of electrons is rather uniform. In the streamer corona discharge electrons are produced with an initial average energy of about 10 eV. In the e-beam process, the initial energy of the electrons which are injected into the gas, is in the range 300-800 keV. Secondary electrons, formed by ionizing collisions with the neutral gas, possess an energy of the order of 100 eV (Mätzing, 1989, 1991). It is obvious that in the e-beam process the relative number of electrons with an energy of more than 10 eV is much higher than in a corona discharge.

The differences between the pulsed corona and e-beam process with respect to the electron energy distribution, will probably have large consequences for the relative concentrations of radicals formed by dissociation and ionization. The

electron energy needed for dissociation and ionization of major gas components in flue gas, is given in Table 1.2. The cross sections for dissociative attachment to O_2, CO_2 and H_2O are peaked with a maximum value at energies in between 4 and 12 eV. The cross sections for ionization are marked by a well determined energy threshold which is larger than 12 eV. The energy of the main part of the electrons in the e-beam process is too high for dissociative attachment.

Molecule	N_2	O_2	CO_2	H_2O
Dissociation (eV)	9.8 (1)	6.7 (2)	4.4, 8.2 (2)	6.5, 8.6, 11.8 (2)
Ionization (eV) (1)	15.6	12.1	13.8	12.6

(1) Corresponding to cross section thresholds (Kieffer, 1973)
(2) Corresponding to cross section maxima (Christophorou, 1984)

Table 1.2 Electron energy for dissociation and ionization of molecules in flue gas.

1.5.2 The main chemical reactions

The oxidation of NO, NO_2 and SO_2 in an e-beam or pulsed corona reactor is in principle comparable to oxidation of these gases in the atmosphere. In atmospheric chemistry the OH radical, formed by photodissociation of water, plays a key role in the transformation of NO_x and SO_2 to nitric and sulphuric acids. Even ammonia is present in the atmosphere as a result of biological processes. Many reactions with NO, NO_2, SO_2, NH_3, O_3 and OH radicals in humid atmospheric air, have been investigated in order to understand the chemistry of acid rain formation (Seinfeld, 1986). The main differences between the chemical reactions in the atmosphere and those in a reactor are the concentration of the reactants and the temperature of the gas. Even in a strongly polluted environment, the concentrations of NO, NO_2, SO_2, NH_3 and O_3 are generally below 0.25 ppm (Seinfeld, 1986). In a pulsed corona or e-beam reactor for $deNO_x$-$deSO_2$, the densities of these gases are about three orders of magnitude higher. Moreover, increasing the energy density in a reactor, the number of oxidizing radicals per NO and SO_2 molecule can be made high also. Consequently, the characteristic time of many reactions in a reactor will be much shorter than the time of the same reactions in the free atmosphere.

JAERI results (Tokunaga and Suzuki, 1984)

Systematic investigations of e-beam induced NO, NO_2 and SO_2 removal, as function of absorbed energy and with different gas mixtures, have been performed

at the Japan Atomic Energy Research Institute (JAERI) and have been published by Tokunaga and Suzuki (1984). The experiments in simple gas mixtures in particular show the influence of *back-reactions* in the NO_x chemistry. In the case of e-beam irradiation of N_2-O_2-NO_2 mixtures, NO is formed by the reaction: $O + NO_2 \rightarrow NO + O_2$. The same reaction limits the conversion of NO to NO_2 in N_2-O_2-NO mixtures.

The main results, obtained with a mixture consisting of 80% N_2, 12% O_2 and 8% H_2O, are briefly discussed below. The concentrations of the major gas components were little changed by the addition of minor concentrations of NO, SO_2 and NH_3. The gas temperature in the experiments was 100 or 120 °C.

The initial NO concentration has a significant influence on the percentage of NO that can be oxidized. At an energy density of 1 Mrad (10 kJ/kg, ~2.8 Wh/Nm^3) an initial NO concentration of 100 ppm is almost completely oxidized, but with an initial NO concentration of 500 ppm, only ~70% is oxidized. When the relative concentration of water vapour is increased, both NO and NO_2 concentrations decrease. OH radicals, formed by dissociation of H_2O, react selectively with NO and NO_2 to form HNO_2 and HNO_3.

The presence of water vapour appears to be essential for SO_2 removal. Even at high irradiation doses of N_2-O_2-SO_2 mixtures, almost no decrease of the SO_2 concentration is measured. A remarkable result is the improved NO_x removal efficiency with SO_2 addition. At an energy density of 2 Mrad, without SO_2, an initial NO concentration of 235 ppm decreases to 50 ppm while about 150 ppm NO_2 is formed, thus only 35 ppm NO_x is removed. When also 1050 ppm SO_2 is added, the NO concentration decreases to ~40 ppm and the NO_2 concentration decreases to ~125 ppm, thus about 70 ppm NO_x is removed.

The best results, regarding both removal efficiency and energy consumption, have been obtained when also NH_3 is added. The NH_3 concentration in the gas may be expressed in the stoichiometric ratio for salt formation, SR:

$$SR = \frac{[NH_3]}{[NO_x] + 2[SO_2]} \tag{1.1}$$

However, even in absence of irradiation a thermal reaction occurs between NH_3 and SO_2. Almost all SO_2 is removed with $[NH_3] = 2 \cdot [SO_2]$. The reaction rate increases strongly with temperature (Tokunaga, 1993). Fig. 1.2 shows the influence of NH_3 addition on measured NO and NO_2 concentrations as a function of energy consumption. NO_x is never completely removed, even with high stoichiometric NH_3 addition ($SR > 1$) and with high relative water vapour concentration.

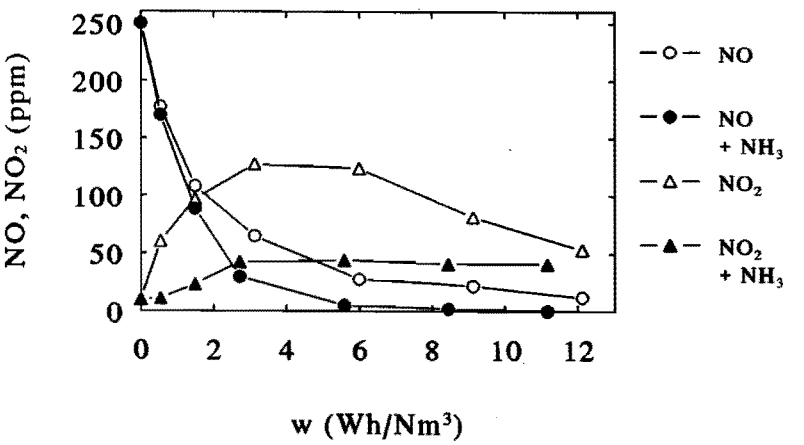

Fig. 1.2 The influence of the addition of 750 ppm NH_3 on the removal of NO and NO_2 by e-beam irradiation (79.9-80% N_2, 12% O_2, 8% H_2O, 250 ppm NO, 250 ppm SO_2, gas temperature = 120°C, Tokunaga and Suzuki, 1984).

Numerical studies of chemical kinetics

Data compilations for atmospheric chemistry (e.g. Baulch et al. 1980, 1982, 1984; Atkinson, 1985) are of high interest for chemical kinetics studies. Person and Ham (1985) incorporated 150 chemical reactions in their model for e-beam treatment. The calculations indicate that the *OH* radical is mainly produced via the formation of H_2O^+ ions. One of the main reactions is:

$$H_2O^+ + H_2O \rightarrow H_3O^+ + OH \qquad (1.2)$$

According to the calculations, the presence of CO_2 in flue gas has no large influence on the chemical kinetics. Comparing calculated removal efficiencies with the experimental results of Tokunaga and Suzuki (1984), Person and Ham (1985) obtained a good agreement with results obtained at low water vapour concentration. However, the calculations seriously underpredict the NO_x and SO_2 removal at high humidity. Mätzing (1989, 1991) extended the list of reactions to a total number of 739, incorporating reactions with negative ions and electronic excited molecules. Also some *heterogeneous reactions* (gas-liquid and gas-solid reactions) were included in order to simulate e-beam results obtained with high humidity and ammonia addition. It was recognized that still insufficient data are available on the heterogeneous reaction mechanisms.

Calculations of chemical kinetics in the pulsed corona induced $deNO_x$-$deSO_2$ process have been performed at the Institute for High Temperatures in Moscow (Alekseev at al., 1993). The rate coefficients, which have been used in the calculations, are similar to those used by Mätzing (1989) for the e-beam induced process. Alekseev et al. (1993) made a detailed analysis of dominant gas-phase chemical reactions. Table 1.3 shows a list of reactions that play a principal role in the pulsed corona process. Also the main electron-molecule collision processes have been indicated.

Formation of primary ions, radicals and excited states:

ionization	$e^- + N_2$	→	$N_2^+ + 2\,e^-$
charge transfer	$N_2^+ + O_2$	→	$N_2 + O_2^+$
cluster formation	$O_2^+ + n \cdot H_2O$	→	$O_2^+(H_2O)_n$
dissociation	$e^- + N_2$	→	$2\,N + e^-$
dissociative attachment	$e^- + H_2O$	→	$OH + H^-$
dissociative ionization	$e^- + H_2O$	→	$OH + H^+ + 2\,e^-$
electronic excitation	$e^- + N_2$	→	$N_2^* + e^-$

Formation of secondary radicals and radical loss:

$H_2O^+ + H_2O$	→	$H_3O^+ + OH$	(R.1)
$H_2O^+ + e^-$	→	$OH + H$	(R.2)
$N_2^* + O_2$	→	$N_2 + 2\,O$	(R.3)
$N_2^* + H_2O$	→	$N_2 + OH + H$	(R.4)
$O + O_2 + M$	→	$O_3 + M$	(R.5)
$O + OH$	→	$H + O_2$	(R.6)
$H + O_2$	→	HO_2	(R.7)
$OH + HO_2$	→	$H_2O + O_2$	(R.8)
$O_3 + O$	→	$2\,O_2$	(R.9)
$NH_3 + OH$	→	$NH_2 + H_2O$	(R.10)
$NH_2 + O$	→	$NH + OH$	(R.11)

Table 1.3 Essential electron-molecule collision processes and gas-phase chemical reactions in the e-beam or pulsed corona $deNO_x$-$deSO_2$ process, N_2^* refers to the electronic excited metastable $N_2(A_3\Sigma_u^+)$, M refers to any major gas component in three-body reactions (N_2, O_2, CO_2 or H_2O).

NO_x oxidation: (Table 1.3 continued)

$NO + OH + M$	→	$HNO_2 + M$	(R.12)
$NO + HO_2$	→	$NO_2 + OH$	(R.13)
$NO + O + M$	→	$NO_2 + M$	(R.14)
$NO + O_3$	→	$NO_2 + O_2$	(R.15)
$NO + N$	→	$N_2 + O$	(R.16)
$NO + NH_2$	→	$N_2 + H_2O$	(R.17)
$NO_2 + O$	→	$NO + O_2$	(R.18)
$NO_2 + OH + M$	→	$HNO_3 + M$	(R.19)

SO_2 oxidation:

$SO_2 + OH + M$	→	$HSO_3 + M$	(R.20)
$HSO_3 + O_2$	→	$SO_3 + HO_2$	(R.21)
$SO_3 + H_2O$	→	H_2SO_4	(R.22)

Salt formation:

$NH_3 + HNO_3$	→	NH_4NO_3	(R.23)
$NH_3 + H_2SO_4$	→	NH_4HSO_4	(R.24)
$NH_3 + NH_4HSO_4$	→	$(NH_4)_2SO_4$	(R.25)

The *OH* radical is essential for the transformation of NO_2 to HNO_3 (R.19) and for the transformation of SO_2 to SO_3 via reactions (R.21 and R.22). SO_3 reacts so rapidly with water vapour to form H_2SO_4 (R.22) that any process in which SO_3 is formed can be considered equivalent to the formation of H_2SO_4. Reaction R.21 can be the cause for the experimentally demonstrated support of NO_x removal by SO_2 because the HO_2 radical, formed by this reaction, is effective for *NO* removal via reaction R.13. Moreover, R.13 produces a new *OH* radical that promotes the oxidation of both NO_2 and SO_2. The main effect of ammonia addition is the substitution of *OH* by the NH_2 radical (R.10) that effectively reduces *NO* to N_2 and H_2O (R.17).

The importance of reaction R.17 has been confirmed recently by mass spectroscopy experiments at JAERI where ammonia has been labelled as the isotope $^{15}NH_3$ (Tokunaga et al., 1993). Also proof of a significant influence of reaction R.16 was given by means of mass spectrometry, using isotope labelled ^{15}NO as input and detecting the resulting $^{29}N_2$. In simulated flue gas, 23% of 400 ppm ^{15}NO was decomposed to form $^{29}N_2$ (Tokunaga et al., 1993).

1.5.3 The efficiency of NO_x and SO_2 removal in laboratory experiments

A number of quantities are currently used to evaluate the performance of *deNO_x-deSO_2* processes with respect to energy consumption. In e-beam investigations one uses often the number of molecules removed per 100 eV dissipated energy, a quantity that is called the *G-value*. For the production of a gas in a plasma reactor (e.g. ozone) it is common to use the *energy yield* (g/kWh). Sometimes, this quantity is also used for the energy efficiency of an oxidation process. An alternative quantity, the *energy cost*, i.e. the dissipated energy per removed pollutant, can be expressed in units of electron volts per molecule (eV/molec.). This quantity is used here and the conversion between this quantity and other quantities is given in Appendix A.

In order to determine the *energy cost* W_m experimentally, it is sufficient to measure the difference between the concentrations of pollutants at the inlet and outlet of the reactor Δn, and the energy density (or energy consumption) w:

$$W_m(eV/molec.) = \frac{897 \cdot w(Wh/Nm^3)}{\Delta n(ppm)} \tag{1.3}$$

Usually, W_m depends on the energy density w and the initial concentration of pollutants (see for example Fig. 1.2). This fact complicates the comparison of experimental results obtained with different reactors for *deNO_x-deSO_2*. Nevertheless, we will use the *energy cost* for a rough comparison of laboratory investigations of the process.

Early laboratory tests of SO_2 oxidation in the presence of corona discharges have been performed by Matteson et al. (1972). A mixture of humid air with 1.6% H_2O (70% relative humidity at 20 °C) and 500-3000 ppm SO_2 was treated with a positive DC corona in a wire-cylinder geometry. At an energy density of ~500 Wh/Nm^3, 90% of an initial SO_2 concentration of 1000 ppm was removed, i.e. $W_m \approx 500$ eV/molec.

NO_x removal from exhaust gases by treatment in a corona discharge has probably been demonstrated first by Masuda and co-workers in Japan (Masuda et al., 1981). Originally, Masuda's experiments were aimed at the improvement of the e-beam induced *deNO_x* process by means of the additional presence of an electric field. An increase of the removal efficiency was only obtained under conditions where the electric field strength was high enough for the production of a corona discharge.

Also the possibility to remove NO_x and fly ash in a single process, has been investigated in Masuda's laboratory (Ohtsuka, 1985). In an ESP operated with a DC negative voltage, an appreciable reduction of NO_x was achieved only with an average electric field exceeding the usual level for ESP operation (0.5-1 kV/mm).

NO_x removal experiments were pursued in Masuda's laboratory with pulsed

coronas of both polarities (Masuda and Wu, 1987; Masuda and Nakao, 1990). In air at 20 °C, using HV pulses with a duration of about 300 ns (at ~50% of the voltage maximum), a NO_x removal efficiency of 80% was achieved with an energy consumption of 20 Wh/Nm^3 (complete removal of 200 ppm NO, formation of 40 ppm NO_2), i.e. $W_m \approx 100$ eV/molec. With positive HV pulses more energy per pulse was transferred to the gas than with negative HV pulses (at the same absolute value of the maximum voltage) but the energy cost appeared to be approximately the same for HV pulses of both polarities.

The simplicity of the power supply for DC coronas justified prolonged investigations of both NO_x and SO_2 removal by DC corona treatment. Scheuermann and Bloss (1988) performed experiments with DC corona discharges in simulated flue gas (75% N_2, 15% CO_2, 5% O_2, 5% H_2O). The best results were obtained at low temperature and with ammonia addition (T=60 °C, 340 ppm NH_3). At an energy density of 190 Wh/Nm^3, an initial concentration of 320 ppm NO was reduced practically to zero with 60 ppm NO_2 formation (~80% removal efficiency). The energy cost, $W_m \approx 660$ eV/molec., was high when compared to results obtained with pulsed coronas.

Although tests of SO_2 removal by short HV pulses have been performed (Mizuno et al., 1986) the experimental data can not be used to determine the energy cost. High removal efficiencies have been obtained with positive HV pulses that were super-imposed on a DC bias (below corona onset).

Vogtlin and Penetrante (1993) investigated the removal of NO and NO_x with pulsed positive corona and a closed loop gas flow system. In a gas mixture consisting of 70% N_2, 15% CO_2, 5% O_2 and 10% H_2O (T=114 °C) almost 100% of the initial 720 ppm NO was removed at an energy consumption of 22 Wh/Nm^3, corresponding to W_m=28 eV/NO. About 45% of the initial 900 ppm NO_x was removed at an energy consumption of 39 Wh/Nm^3, corresponding to W_m=80 eV/NO_x. The influence of adding octane to the gas mixture was investigated. The experiments with octane were performed at a relative high NO_x concentration of 1500 ppm. With 1200 ppm octane, 550 ppm NO_x was removed at 40 Wh/Nm^3, corresponding to W_m=65 eV/NO_x. With 4500 ppm octane, 500 ppm NO_x was removed at 24 Wh/Nm^3, corresponding to W_m=40 eV/NO_x.

The minimum energy cost that has been achieved in pulsed corona experiments is still high when compared to the minimum energy cost achieved in e-beam experiments. In the experiments of Tokunaga and Suzuki (1994), at an energy consumption of 5.5 Wh/Nm^3, an initial concentration of 250 ppm NO was almost completely removed while 50 ppm NO_2 was formed (see Fig. 1.2). This result corresponds to an energy cost of 25 eV/NO_x. Even much better results have been obtained with repeated e-beam pulses (called multi-stage irradiation) of a mixture consisting of 80% N_2, 6% O_2, 14% CO_2, 150 ppm NO_x, 500 ppm SO_2, and

$SR(NH_3) \approx 1$ (Tokunaga et al., 1993). The initial NO_x concentration of 150 ppm has been reduced to 30 ppm at an energy consumption of 2 Wh/Nm^3, corresponding to an energy cost $W_m = 15$ eV/NO_x. It is not possible to make a proper comparison between the results obtained with e-beam treatment and pulsed positive corona treatment because of the differences in the initial concentrations of NO_x and the different additives. Experiments under identical gas conditions (composition, temperature and average gas residence time) are needed in order to make such a comparison.

1.5.4 Integration in an electrical power plant

The possible integration of a pulsed corona $deNO_x$-$deSO_2$ process in an electrical power plant is schematically shown in Fig. 1.3.

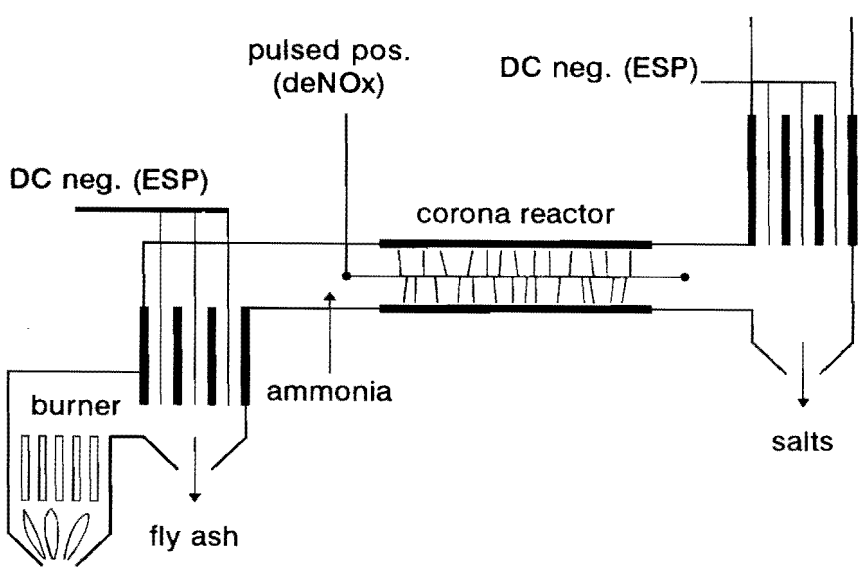

Fig. 1.3 Flue gas cleaning in an electrical power plant with advanced corona technology.

The simultaneous removal of NO_x and SO_2 from flue gas of coal-fired electrical power plants, has been investigated by the Italian national electricity board ENEL (Dinelli et al. 1990; Civitano and Sani, 1993; Civitano, 1993). In experiments at the Marghera power plant near Venice, a small fraction of the flue gas is treated in a corona reactor that has been installed downstream of an ESP for fly ash removal. The flue gas consists of 73% N_2, 6% O_2, 13% CO_2, 8% H_2O, 240 ppm NO_x and 650 ppm SO_2 (Dinelli et al., 1990). Results described by Civitano (1993) have been obtained with a reactor that treats a gas flow rate of 100 Nm^3/h. At a flue gas temperature of ~80 °C and with 1300 ppm NH_3 added upstream of the reactor, practically 100% SO_2 and 50% NO_x are removed at an energy consumption of 12 Wh/Nm^3, corresponding to an energy cost per NO_x molecule of 90 eV. The "NH_3 slip", i.e. the remaining NH_3 concentration at the outlet of the reactor, is below 1 ppm. This is essential in fulfilling emission standards for NH_3 emission. Since NH_3 has been added with $[NH_3]=2 \cdot [SO_2]$, probably all NH_3 has been chemically bound with sulphate. A chemical analysis of the solid particles that are formed in the process shows that these particles consist of ammonium nitrate and ammonium sulphate with high purity (Civitano, 1993). Also the size distribution has been determined. Practically all particles possess a diameter in the range 0.1-1 μm that is suitable for efficient removal in an ESP or bag filter.

Advantages of the pulsed corona $deNO_x$-$deSO_2$ process, when compared to a combination of selective catalytic reduction for $deNO_x$ and the wet limestone-gypsum process for $deSO_2$, are:

1) NO_x and SO_2 are removed *simultaneously* in a single reactor with low capital costs.
2) It is a *dry* method, i.e. there is no need for waste water treatment.
3) The electrode structure is *uncomplicated* and similar to those used in conventional ESP's.
4) The *pressure drop* in the reactor is small compared to the pressure drop in catalytic converters for $deNO_x$, thereby avoiding power consumption in electrical fans.
5) *Re-heating* of flue gas before release in the atmosphere is not necessary.
6) The *by-product* is useful and can be taken up by the soil-fertilizer market.

The following points need more investigation before the pulsed corona process can be accepted as a mature $deNO_x$-$deSO_2$ technology:

1) The process has not yet been fully optimized regarding *energy consumption.* The energy cost per pollutant can depend on gas parameters (flue gas composition including additives, temperature, residence time), voltage parameters (polarity, rise

time, peak voltage, pulse width, bias voltage) and electrode structure (wire radius, presence of dielectric barrier).

2) The capital and operating costs of *pulsed power supplies* depend on the required shape of the HV pulse. For this reason it is important to investigate the influence of pulse parameters on the effectiveness of the $deNO_x$-$deSO_2$ process. Different techniques for the production of fast rising and short HV pulses are available. A recent development in this field is magnetic pulse compression technique (Keet, 1992; Neau et al., 1993). In laboratory experiments, one frequently uses HV transformers to charge a capacitor with a rectified AC high voltage. Energy stored in the capacitor is transferred to the corona reactor using a synchronous rotating spark gap as switch. In continuous operation, switches are the most critical elements in pulsed power supplies with respect to life time. The requirement of reliable and efficient power switches for pulsed corona applications stimulates the development of new switches, such as speudospark gaps. Accelerators for e-beam generation are not devoid of problems similar to those encountered in the development of pulsed power supplies for pulsed coronas. Common problems with the commercial introduction of the e-beam induced $deNO_x$-$deSO_2$ process are the high investment costs of accelerators and the limited life time of the foil-windows which transmit the electrons to the gas.

3) Shielding against *electromagnetic radiation* from the electrical circuit is necessary in order to satisfy Electromagnetic Compatibility (EMC) regulations. The EMC-requirement of pulsed power supplies has its analogy in the e-beam process where shielding against X-rays is a necessity.

4) Besides NH_3 also other *additives* like H_2O_2 (Civitano, 1993) are proposed in order to lower the energy cost per removed pollutant. The influence of these additives on the gas composition and the composition of solid products downstream of the reactor, must be investigated. Obviously, toxic by-products should be avoided.

5) Experience with *pilot plants* is needed to solve scaling problems and to demonstrate reliable operation in practice.

A study was recently commissioned by the Japanese Ministry of International Trade and Industry to perform technical and economic assessments of conventional SCR and FGD, the pulsed corona and the e-beam processes for electrical power plants. The committee concluded that the pulsed corona process is cheaper than conventional and e-beam processes because of much lower investment costs and in spite of the high energy consumption (Masuda, 1993).

For a proper comparison of the pulsed corona technique with conventional and other innovative methods for $deNO_x$-$deSO_2$, an ensemble of features of the process is important. Progress can be made in an empirical way, varying the external parameters of the process and measuring their influence on energy consumption, the NO_x and SO_2 concentrations at the outlet of the reactor, the composition of solid by-products and their usefulness.

Pulse parameters (rise time, peak voltage, pulse length, bias voltage) are known to have a strong influence on the percentage of pollutants that can be removed from a gas stream and on the energy consumption per removed pollutant. It is expected that process optimization regarding both removal efficiency and energy cost is possible by an appropriate choice of pulse parameters. However, the cause of the influence of pulse parameters is not well understood yet. Therefore, a detailed investigation of the main physical and chemical processes is needed. This investigation can reveal fundamental limitations as well as unexpected possibilities. In this work, emphasis has been given to the investigation of the physical processes and in particular to the influence of voltage pulse parameters on streamer properties.

Chapter 2 Streamer Properties and Models

The aim of the present chapter is to review the main properties of streamers and to investigate these properties by means of models. The principle of streamer formation and essential parameters of streamer models are introduced in **2.1.** Streamer formation in positive, negative, DC and pulsed coronas is briefly discussed in **2.2.** The remaining part of the chapter deals with streamers formed in pulsed positive corona discharges.

In order to estimate the electric field and charged particle distributions in the fast propagating streamer front and the densities of chemical reactive dissociation products, the use of elaborate numerical procedures is inevitable. Because the numerical modelling of the electron-molecule kinetics, the streamer discharge and the streamer-induced chemical kinetics constitute an immense task, cooperation has been started with institutes where much experience in the field of numerical modelling is available. Models for both the streamer discharge and streamer induced chemical kinetics have been realized at the Institute of High Temperatures (IVTAN) in Moscow. Electron transport coefficients, which serve as input data of the streamer model, have been calculated at the University Paul Sabatier in Toulouse. Basic equations, input data and numerical modelling results are presented in **2.3.** Section **2.4** presents an analytical model for streamer propagation which is used to calculate the initial charge distribution deposited by a streamer when it propagates across the electrode gap. This simple analytical model has been extended with a numerical part which accounts for the properties of the residual streamer channel, once the primary streamer has crossed the electrode gap. The first results of simulations of chemical kinetics in a streamer are presented in **2.5.**

2.1 Electron avalanches and streamers

Streamer formation is most clearly demonstrated examining the development of an avalanche of electrons in an uniform field. Both experimental and theoretical studies of electron avalanches and streamers in uniform fields are reviewed.

2.1.1 Drift and diffusion of an electron avalanche

Fig. 2.1 shows schematically the formation of an avalanche of electrons which is formed after the release of initial electrons at the cathode surface by a short

pulse of ultraviolet light. The electrons gain energy from the electric field and lose energy by a variety of collision processes (e.g. elastic scattering, excitation to rotational and vibrational degrees of freedom, electronic excitation, ionization). At the *critical field strength* E_{crit} (~2.5 kV/mm at normal pressure and temperature (NPT), see appendix **A**), electron gain processes (ionization, detachment from negative ions) are exactly balanced by electron loss processes (recombination, attachment). At $E > E_{crit}$ the growth of the number of electrons at the head of an electron avalanche is, at least initially, exponential:

$$N_e(x) = N_{e0} \cdot \exp(\alpha' x) \,, \quad x = w_d t \tag{2.1}$$

N_{e0} is the initial number of electrons at the cathode and w_d is the electron drift velocity. The net ionization coefficient α' is usually equal to the difference between the coefficients α and η representing respectively collisional ionization and electron attachment (forming negative ions): $\alpha' = \alpha - \eta$. The net ionization coefficient may also account for detachment (see **2.3.3**).

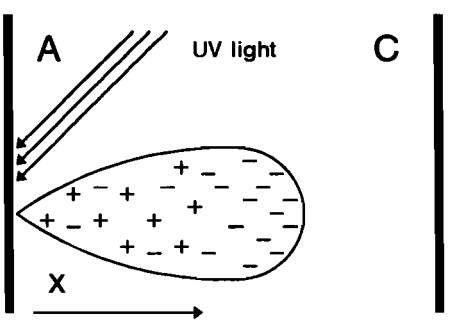

Fig. 2.1 The drift and diffusion of an electron avalanche in a parallel-plate discharge gap.

The change of the local electron density as a function of time t in the avalanche can be expressed by a continuity equation which includes ionization, attachment, convection and diffusion:

$$\frac{\partial n_e}{\partial t} = \alpha' w_d n_e - \frac{\partial (w_d n_e)}{\partial x} + \frac{\partial}{\partial x}\left(D \frac{\partial n_e}{\partial x} \right) \tag{2.2}$$

where n_e is the electron density. Diffusion is the tendency of the electrons to spread as a result of their random motion and is characterized by a diffusion coefficient D (unit: $m^2 s^{-1}$). The electron transport coefficients α, η, w_d and D depend on the ratio of the field strength E and the neutral gas density n: the *reduced field strength* E/n.

It is convenient to express E/n in the unit Townsend (Td), although this is not a SI unit: 1 Td = 10^{-21} Vm^2, $(E/n)_{crit}$ = 100-110 Td. Until recently, however, it has been common practice to use E/p (where p is the gas pressure at 20 °C) rather than E/n: E/n (Td) = 3.03 E/p (V · cm^{-1} · Torr^{-1}). In this work E/n (Td) and n (m^{-3}) are used except when data are reviewed which have originally been expressed in E/p. When E/n does not depend on time nor on position (i.e. electrodes are a far distance and space charge distortion is negligible), the solution for Eq. 2.2 is (Huxley and Crompton, 1974, Chap. 11):

$$n_e(x,t) = \frac{n_{e0} \exp(\alpha' w_d t)}{\sqrt{4\pi D t}} \exp\left(-\frac{(x - w_{CM} t)^2}{4Dt}\right) \tag{2.3}$$

where w_{CM} is the centre-of-mass drift velocity of the electron avalanche that is close to but, in general, not equal to the drift velocity w_d (Huxley and Crompton, 1974, Chap. 7). In the presence of a strong electric field diffusion can be anisotropic (Huxley and Crompton, 1974, Chap 11.), that is two parameters then characterize the diffusive motion, the transverse diffusion coefficient D_T (perpendicular to the electric field) and the longitudinal diffusion coefficient D_L (parallel to the electric field).

From Eq. 2.3 follows that the diffusion radius r_D, defined as the distance normal to the electric field at which the electron density is e times less than the maximum, increases according to (characteristic diffusion law):

$$r_D = \sqrt{4 D_T t} = \sqrt{\frac{4 D_T x}{w_d}} = \sqrt{\frac{4 x}{E} \cdot \frac{D_T}{\mu_e}} \tag{2.4}$$

where D_T is the transversal diffusion coefficient and μ_e the electron mobility. The ratio D_T/μ_e is an estimate of the average electron energy (Nernst-Townsend relation, Huxley and Crompton, 1974, Chap. 3):

$$\frac{D_T}{\mu_e} = \frac{F}{q_e} \frac{1}{2} m_e \langle w_e^2 \rangle = \frac{F}{q_e} \varepsilon_a \tag{2.5}$$

where F is the Townsend energy factor, w_e represents the thermal electron velocity and $\langle\ \rangle$ averaging over the electron energy distribution. For the Maxwell electron energy distribution function (Eq. 2.31 in **2.3.3**) the Townsend factor F is 2/3. Frost and Phelps (1962) named the ratio D_T/μ_e the characteristic electron energy, a term that is now widely used.

Townsend (1910, 1915) was one of the first to investigate electron avalanches both experimentally and theoretically. One of the main findings of Townsend are the *similarity laws* according to which the electron transport coefficients, expressed

in the form α/n, η/n, w_d and D_T/μ_e, are sole functions of the reduced field strength E/n, thus independent on the quantities E and n separately. The significance of the similarity laws is that electron transport coefficients, determined for example with electron avalanche experiments at low gas density, can also be used at different gas densities.

Townsend obtained an accurate quantitative account of current measurements, on the hypothesis that free electrons are not only generated by ionizing collisions in the gas but also at the cathode by incident positive ions. He was able to show that the current is given by an equation of the form (with $\eta = 0$, $\alpha' = \alpha$):

$$i = i_0 \frac{e^{\alpha d}}{1 - \gamma/\alpha \, (e^{\alpha d} - 1)} \tag{2.6}$$

where i_0 is the current in absence of collisional ionization in the gas and γ the secondary ionization coefficient. The ratio γ/α is the number of electrons released at the cathode per positive ion produced in the discharge. In case of electronegative gases ($\eta \neq 0$) a modified form of Eq. 2.6 exists (e.g. Kuffel, 1984) that is, however, not of interest for the present discussion. Townsend's breakdown criterion is obtained from Eq. 2.6 by setting the denominator to zero so that the current becomes limited only by the external electrical circuit:

$$e^{\alpha d} = 1 + \frac{\alpha}{\gamma} \tag{2.7}$$

This mathematical criterion gave an adequate theoretical basis to the empirical Paschen law, according to which the static breakdown voltage V_b is a sole function of the product αd.

2.1.2 The original streamer concept

The streamer concept emerged in the years 1935-1940, through the work in Raether's group at the University of Hamburg and the work in Loeb's group at the University of California (Berkeley). It was put forward as an alternative for Townsend's breakdown criterion (Eq. 2.7). Discrepancies between the Townsend theory and experiments with parallel-plate gaps appeared in particular at high values of the product of gas pressure and gap distance, $pd > \sim 200$ Torr cm. The main difficulties encountered by the Townsend theory have been summarized by Meek (1940):

1) Measured breakdown voltages appeared to be lower than predicted (deviation from the Paschen law) and independent on cathode material.

2) Measured breakdown times appeared to be much shorter than expected from the electron drift velocity corresponding to the applied field (at $E/n = 110$-120 Td, w_d in dry air is $\sim 10^5$ m/s giving in a 10 mm gap a transit time of $\sim 10^{-7}$ s).
3) The theory was unable to explain the weakly luminous and narrow discharge channels that were observed preceding the much brighter arc discharges in both uniform and non-uniform fields.
4) It seemed impossible to extend the Townsend criterion (derived for a discharge in between parallel plates) to positive corona discharges where the cathode is often at too far distance to play a significant role in providing secondary electrons.

Raether (1940) and Loeb and Meek (1940) used Wilson cloud chambers to visualize electron avalanches. The cloud chamber technique uses the fact that ions, left behind by electron avalanches, act as condensation centres for saturated water vapour to form droplets that can be photographed. Some of Raether's (1940) results are discussed here. HV pulses with different durations, obtained by discharging cables with different lengths, were applied directly following the generation of initial electrons at the cathode by a short light pulse. The development of the avalanche was studied at fixed E/n with variable pulse duration and at fixed pulse duration with variable E/n. Below the static breakdown voltage V_b, the observed avalanche properties (speed and diffusional spreading) were in agreement with theory (Eqs. 2.3 and 2.4). At small overvoltage, i.e. $(V-V_b)/V_b \ll 1$, anode-directed streamers (ADS) and cathode-directed streamers (CDS) were observed. The main observations in air, with saturated water vapour were ($T = 20$°C, $p \approx 300$ Torr, $[H_2O] = 6\%$, $E/p \approx 35$ V cm^{-1} Torr^{-1}, $d = 36$ mm):

1) A transition from the initial electron avalanche to the ADS is seen as:
   - Abrupt broadening of the (optical) diameter
   - Increased velocity (from $\sim 10^5$ m/s to $\sim 10^6$ m/s)
   - Increased light emission intensity
2) A CDS develops usually in the path of the original avalanche and reaches a velocity comparable to the ADS velocity.
3) The product of the ionization coefficient and the avalanche length is, at the moment when the avalanche-to-streamer transition occurs, constant for different values of E/n: $\alpha' x \approx 20$.
4) A spark develops after both streamers have reached the electrodes inside the residual ionized plasma channel which is left by the streamers.

Streamer formation and propagation have been explained by Raether (1940) and Meek (1940) mainly on the basis of field distortion by space charge. Fig. 2.2 shows schematically the principle of streamer formation and propagation. The head

of the electron avalanche and the positive ions, which are left behind the avalanche, form a sort of dipole. The dipole field E_1 adds up vectorially to the external applied (geometric) field E_0 resulting in a field E. When E_1 reaches a value comparable to E_0 the normal development of the avalanche is strongly disturbed. The electric field is enhanced in front of the head of the electron avalanche while the electric field is reduced in between the avalanche head and the positive ions which are left behind. Still further back in the avalanche, the electric field between the positive ions and the cathode is enhanced again.

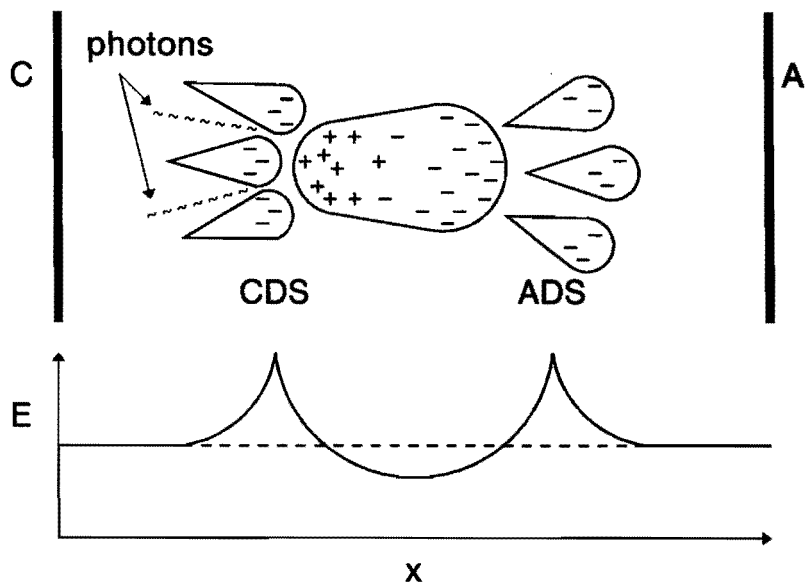

Fig. 2.2 Schematic representation of streamer formation and propagation in an uniform electric field.

The ADS is in fact a "modified" electron avalanche which, as a result of the space charge field, increased its velocity and light emission intensity. When a strong space charge field and initial electrons are present at the cathode side of the initial electron avalanche, a CDS can be formed. The CDS propagates as a result of secondary avalanches which neutralize the positive charge concentration of the previous avalanches, leaving a new positive ion concentration behind at a shorter distance from the cathode. The CDS propagates in a direction opposite to the electron drift velocity. Some mechanism generating initial electrons, which act as starting points for secondary avalanches in front of the CDS, is required. In the original streamer theory it has been postulated that initial electrons are generated by photo-ionization. This item will be discussed in **2.1.3.**

The ADS and CDS are also called respectively negative and positive streamers according to the polarity of the net space charge in their fronts. Three fundamental differences exist between the ADS and the CDS:

1) In the ADS the electron drift velocity is directed outward from the region with the high electric space charge field and parallel to diffusion flow. In the CDS these directions are anti-parallel.
2) In the ADS, the axial component of the drift velocity is parallel to the direction of propagation. In the CDS these directions are anti-parallel.
3) Initial electrons in front of the CDS (generated by any process) are necessary for its propagation. Initial electrons in front of the ADS may influence its propagation but are not a necessity.

The above qualitative picture of streamer formation has been placed on an approximate quantitative basis by Meek (1940), representing the space charge field at the head of the electron avalanche by the field of a charged conducting sphere:

$$E_1 = \frac{q_e.N_e(x)}{4\pi\varepsilon_0 r^2} = \frac{q_e.e^{\alpha' x}}{4\pi\varepsilon_0 r^2} \tag{2.8}$$

If the diffusion radius of the avalanche r_D (Eq. 2.4) is substituted for the sphere radius r in Eq. 2.8, one obtains, rearranging terms:

$$\alpha' x = \ln\left(\frac{16\pi\varepsilon_0 D_T}{q_e^2 \mu_e}\right) + \ln\left(\frac{E_1}{E_0}\right) + \ln(x) \tag{2.9}$$

According to Meek (1940) *a streamer will develop when the radial field about the positive space charge in an electron avalanche attains a value of the order of the external applied field* (geometric field). This criterion implies that in Eq. 2.9 $\ln(E_1/E_0) \approx 0$. Using the experimental value $D_T/\mu_e \approx 2.5$ eV at E/n = 110-120 Td (Rees, 1964), Meek's streamer criterion becomes:

$$\alpha' x = 22.7 + \ln(x) \tag{2.10}$$

with x in the unit meter. For electrode gaps in the range 0.01-0.1 m Meek's criterion reduces to $\alpha' x \approx 18\text{-}20$, close to Raether's empirical criterion $\alpha' x \approx 20$ that could be inferred only approximately from the cloud track pictures. It is emphasized, however, that also Meek's criterion may be inaccurate because it is based on a rough estimation of the space charge field. Note that space charge effects can significantly influence the avalanche development before a streamer is formed. When $N_e \approx 10^6$ the space charge distortion will be $E_1/E_0 \approx 1\%$ which corresponds at

$E/n = 110$ Td to a change of about 5% in α'. Usually, the *Raether-Meek criterion* for streamer formation is written as:

$$\alpha' x = 18\text{-}20\ , \quad N_e = e^{\alpha' x} \approx 10^8 \tag{2.11}$$

The gas density n does not appear explicitly in this criterion. At fixed E_0/n, the diffusion radius (Eq. 2.4) at the moment of the avalanche-to-streamer transition decreases with increasing gas density n according to:

$$r_D = \frac{1}{n} \cdot \sqrt{\frac{4\,\alpha' x \cdot D_T/\mu_e}{\alpha'/n \cdot E_0/n}} \sim \frac{1}{n} \tag{2.12}$$

According to Eqs. 2.12 and 2.8, the reduced space charge field augments with n:

$$\frac{E_1}{n} \sim \frac{1}{n\, r_D^{\,2}} \sim n \tag{2.13}$$

The diffusion radius at the moment of the avalanche-to-streamer transition in dry air at $p = 1$ bar can be evaluated from Eq. 2.12. One obtains with $n = 2.45 \cdot 10^{25}$ m^{-3}, $E_0/n = 120$ Td, $D_T/\mu_e = 2.5$ eV (Rees, 1964), $(\alpha\text{-}\eta)/n = 1\text{-}4 \cdot 10^{-23}$ m^2 (Dutton, 1975, p. 722): $r_D = 250\text{-}500$ μm.

2.1.3 The nature of secondary electrons

The range of the product pd (gas pressure times gap distance) for applicability of the streamer theory has frequently been questioned. Although it was initially believed that the streamer mechanism of breakdown prevails upon the Townsend mechanism at $pd > 200$ Torr cm (Meek, 1940), Llewellyn-Jones and his colleagues at Swansea (1952, 1966) demonstrated experimentally that the *generalized Townsend criterion* (Eq. 2.7 with γ/α representing also secondary electrons released at the cathode by incident photons and metastables) can account for measured breakdown voltages up to $pd = 760$ Torr cm without recourse to space charge effects and photo-ionization in the gas. Their experiments were performed with carefully polished parallel electrodes and a very stable voltage source. The purpose of these experiments was to show that the apparent departure of Paschen's law at high pd values was due to poor experimental conditions.

Photo-ionization

In experimental investigations of ionizing radiation (e.g. Przybylski, 1962; Teich, 1967; Penney and Hummert, 1970), essentially two quantities have been measured: (a) the ratio of a photo-ion current and discharge current i_p / i_d and (b) the absorption coefficient of ionizing radiation. Penney and Hummert (1970) used a positive corona discharge in point-plate geometry in air, oxygen and nitrogen (see Fig. 2.3). A low gas pressure (p=0.1-18 Torr) was used for different reasons: (a) the discharge is located in the vicinity of the point, (b) absorption is limited so that measurements of i_p/i_d as a function of distance d_s to the point-source are possible and (c) a direct proportionality exists between i_p and i_d. The intensity of photo-ionizing radiation has been expressed by means of the quantity:

$$\psi = \frac{i_p}{i_d} \cdot \frac{1}{pL\ \theta} \quad (Torr^{-1}\ cm^{-1}\ sr^{-1}) \tag{2.14}$$

where pL is the product of the gas pressure times length of the ion collector and θ is the solid angle of emitted radiation that is intercepted by the collector. The measurements showed that ψ depends on the product pd_s and not on these quantities separately. The insensitivity of measured ψ to pressure changes (at constant pd_s) indicates that the spectra of ionizing radiation are almost unaffected by the gas density.

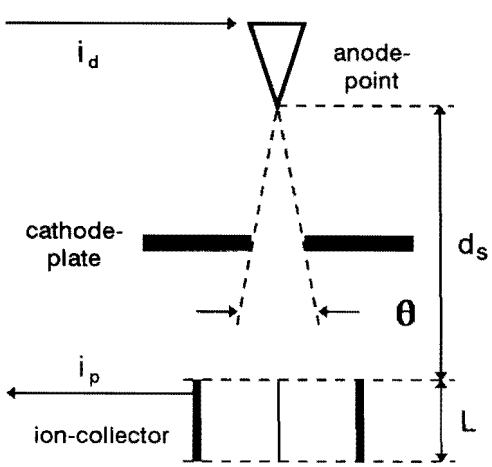

Fig. 2.3 Schematic view of Penney and Hummert's (1970) experiment for measuring the photo-ion current.

A possible mechanism for photo-ionization in N_2-O_2 mixtures is direct ionization of O_2 (ionization threshold 12.1 eV, required wavelength $\lambda < 102.5$ nm) by photons emitted from excited states of N_2 (ionization threshold 15.6 eV). Only a few transitions from excited states of N_2 generate photons with $\lambda < 102.5$ nm, for example the spectral system $b^1\Pi_u \rightarrow X^1\Sigma_g^+$. Because N_2 strongly absorbs radiation with

$\lambda < 98$ nm (Carter, 1972), only a small wavelength range ($98 < \lambda < 102.5$ nm) exists where direct photo-ionization of O_2 by emission of N_2 is possible. In this range the absorption coefficient of oxygen decreases strongly with increasing wavelength: $k_{max}(98\text{ nm}) = 2$ Torr^{-1}cm^{-1}, $k_{min}(102.5\text{ nm}) = 3.5 \cdot 10^{-2}$ Torr^{-1}cm^{-1} (Hudson, 1971).

Zheleznyak et al. (1982) calculated the dependence of the quantity ψ in a N_2-O_2 mixture on the product $p(O_2)\, d_s$ assuming that ionization of O_2 by photons from excited states of N_2 is the dominant process. According to this theory, the quantity ψ depends on $p(O_2)\, d_s$ as:

$$\psi = \frac{\omega}{\alpha} f_q \, \phi \,, \quad with$$

$$\phi = \frac{\exp\left(-k_{min}\, p(O_2) d_s\right) - \exp\left(-k_{max}\, p(O_2) d_s\right)}{4\pi\, p(O_2) d_s \, \ln(k_{max}/k_{min})} \tag{2.15}$$

The photo-ionization efficiency ω/α is the ratio of the number of photo-ions and the number of ions produced in the discharge, in absence of quenching and absorption. This ratio is not known with high accuracy. In a review of various experimental investigations, Teich (1967) shows a table with values of ω/α in the range 0.01-0.1. The dimensionless factor f_q accounts for collisional (non-radiative) quenching of excited states and the factor ϕ accounts for the effective absorption of photons with different wavelengths. The quenching factor f_q is calculated as:

$$f_q = \frac{p_q}{p(O_2) + p_q} \tag{2.16}$$

According to measurements of Teich (1967) the quenching pressure p_q is ~30 Torr, thus f_q is 0.165 at atmospheric pressure (760 Torr).

The quantity ψ, calculated according to Eq. 2.15 with $\omega/\alpha = 0.01$, is shown in Fig. 2.4 together with experimental data as a function of $p(O_2)\, d_s$. In both the calculated and the measured data, the effective absorption coefficient (i.e. the slope of $\log\psi$) is clearly seen to decrease with increasing $p(O_2)\, d_s$. It shows that photo-ionizing radiation with the highest absorption coefficient is "outfiltered" (absorbed) at small distance from the radiative source and that radiation which is less absorbed dominates at larger distance. The experimental data of Teich (1967) show that the ratio ω/α decreases with increasing field strength.

Although Eq. 2.15 gives a good quantitative account of experimental data of the effective absorption of photo-ionizing radiation in a N_2-O_2 mixture, it can not be said that the specific mechanism of photo-ionization in this mixture is well understood. Spectral studies of light emitted by avalanches or streamers at wavelengths of about 100 nm are not known. Also other photo-ionization mechanisms may be important. A possible maintaining mechanism for the CDS is

for example photodetachment. The detachment of electrons from negative ions requires a moderate photon energy (about 0.4 eV for O_2^-, $\lambda < 3100$ nm) where there is little absorption in the neutral gas. In the case of a positive corona discharge, where a negative charge density is built up close to the anode, photodetachment may play a significant role. Moreover, in a pure gas (with a single type of molecule) direct photo-ionization seems impossible because the energy of the highest excited electronic states is below the ionization potential.

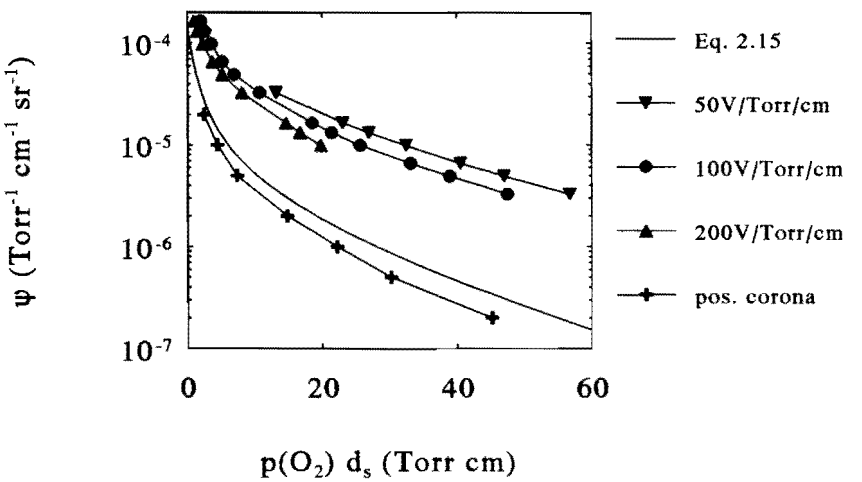

Fig. 2.4 *The influence of $p(O_2)d_s$ on ψ (Eqs. 2.14, 2.15) in N_2-O_2 mixtures, (▽, ○, △) Teich (1967), avalanches in uniform field at p=2-50 Torr, (+) Penney and Hummert (1970), positive corona at p=0.1-18 Torr.*

Wagner's experiments

A step forward in the understanding of mechanisms providing secondary electrons in high pressure discharges was made by Wagner (1966, 1967). Wagner used an image intensifier camera operated in the streak mode to observe the avalanche-to-streamer transition preceding breakdown in uniform fields. Less sensitive than Wilson cloud chambers, this camera offers the possibility to record one spatial dimension of the discharge (generally in the direction of the applied field) as a function of time. Fig. 2.5 shows Wagner's interpretation of a typical streak photograph with two different stages in streamer development. An essential element of this interpretation is the formation of a secondary electron avalanche at the cathode, by photons emitted at the end of the primary avalanche stage. On arrival of the secondary electron avalanche in the region of the CDS, the streamer is accelerated (stage II). The result is very meaningful because it demonstrates that,

in a streamer discharge, secondary electron production in the gas and at the cathode can be simultaneously in effect.

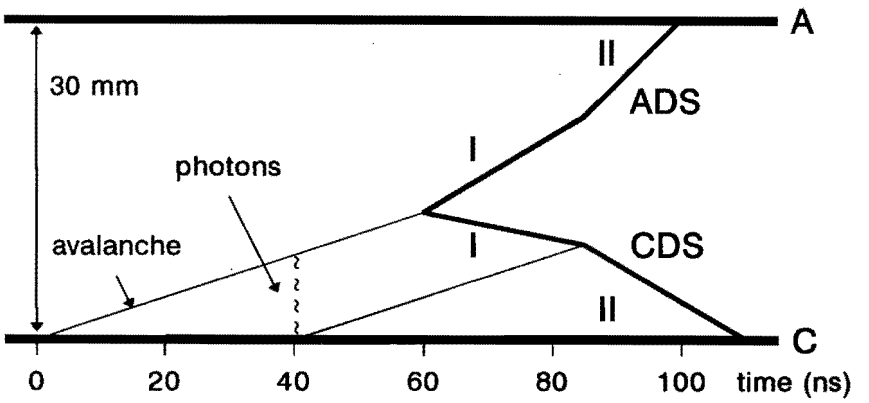

Fig. 2.5 Interpretation of streak photographs showing streamer formation (Wagner, 1967, dry air, p=390 Torr, E/p=47 V cm^{-1} Torr^{-1}, $(V-V_b)/V_b$=25%).

Wagner (1966) was able to confirm the Raether-Meek criterion (Eq. 2.11) taking into account the initial number of electrons at the cathode N_{e0}, that was controlled with an accuracy of about a factor 2. Under a variety of conditions (N_2-CH_4 mixtures, $(V-V_b)/V_b$=20-60%) the product $\alpha' x$ at the onset of streamers, observed from a sudden increase in velocity of the ADS, was in the range 19-20. Some remarkable observations of Wagner (1967) are:

1) Both ADS and CDS velocities are increased by increasing the gas pressure. According to Eq. 2.13 an increase of the gas pressure (density) causes higher space charge fields and therefore higher velocities are expected.
2) Streamer velocities in N_2 mixtures (e.g. N_2 - O_2, N_2 - CH_4) are generally higher than in pure N_2. This observation supports the idea that radiation from the highest excited states of N_2 (ionization potential: 15.6 eV) ionizes the other molecules (ionization potentials of O_2 and CH_4 are 12.2 and 13.0 eV respectively).
3) Both ADS and CDS velocities are increased when 5-10% water vapour is added to dry air. However, the velocities decrease again when more water vapour is added (p=100 Torr, E/p=58 - 61 V cm^{-1} Torr^{-1}). This observation can be understood assuming that water vapour (ionization potential: 12.6 eV) strongly absorbs ionizing radiation thereby augmenting the concentration of secondary electrons but also limiting the range of the photoionizing radiation. When photo-ionizing radiation is mainly absorbed at very small distance from the position where this radiation is produced, it can be ineffective for streamer propagation. A strong increase in the

effective absorption coefficient of ionizing radiation by adding water vapour to air has been measured by Przybylski (1962) and by Teich (1967), see Fig. 2.6.

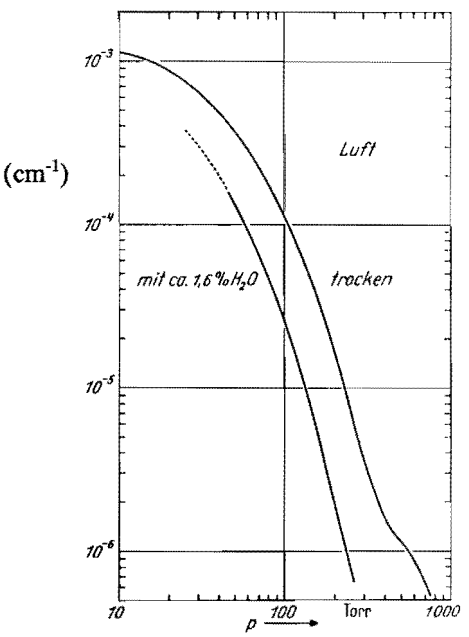

Fig. 2.6

Influence of humidity on absorption of photoionizing radiation. Measurements of the quantity $4\pi p\psi$ in a homogeneous electric field by Teich (1967).

The experiments of Wagner served as comparison with numerical calculations of Davies et al. (1971) and Kline (1974, 1975). In these calculations the streamer radius R_s is treated as an input parameter and one-dimensional continuity equations for charged particles are solved together with the Poisson equation to account for the space charge field distortion (see **2.3.2**).

Davies et al. (1971) obtained fair agreement with the experiment of Wagner in N_2 with 10% CH_4 taking no photo-ionization, only secondary electron emission at the cathode into account. However, even better agreement with this experiment (quantitatively for streamer velocities and qualitatively for the light emission intensity) was obtained by Kline (1974) neglecting secondary electron emission at the cathode and including photo-ionization in the gas. The photo-ionization efficiency ω/α was treated as an adjustable parameter and the absorption of ionizing radiation (determining its range) was taken from experimental data of Penney and Hummert (1970) for N_2. Including also secondary electron emission at the cathode, the results were shown to be independent on γ/α (the ratio of the number of secondary electrons released at the cathode per electron-positive ion pair produced in the discharge) for $\gamma/\alpha < 2 \cdot 10^{-5}$. Kline (1975) made also numerical simulations of Wagner's (1967) experiments of streamer formation in dry air. The inclusion of gas photo-ionization in the model appeared to be necessary in order to obtain a good agreement between calculated and measured streamer velocities.

It is concluded that even for uniform field gaps a general theoretical or empirical boundary value *pd* (or *nd*) for the onset of space charge effects does not exist. In experiments, electrode roughness may play a significant role in lowering this boundary value. The generation of secondary electrons in the gas, so important for CDS propagation, can be due to several mechanisms including gas photo-ionization and electron emission at the cathode under influence of incident ions, photons or metastables. Although quantitative data of these processes are limited, it is evident from Wagner's experiments and the models simulating these experiments, that both mechanisms can contribute to the production of secondary electrons in a streamer discharge in air. In the presence of a gas that strongly absorbs the photo-ionizing radiation (e.g. H_2O) secondary electron emission at the cathode can often be neglected. In a gas where photo-ionizing radiation reaches the cathode surface (e.g. N_2) streamer propagation can be strongly influenced by electron emission from the cathode.

2.2 Streamers in corona discharges

2.2.1 Early observations

In the book written by Loeb (1965) one will find a review of the progressive evolution of the understanding of electrical coronas which has taken place since the end of the last century. One of the first detailed investigations of voltage breakdown in wire-cylinder geometry was carried out in Townsend's laboratory in 1914. In 1928, Geiger and Müller, investigating coronas in wire-cylinder tubes, discovered that these tubes can be used to detect ionizing radiation. The possibility to measure the intensity of ionizing radiation greatly stimulated the interest in the study of these coronas. Loeb and Leigh (1937) investigated the light emitted by positive point-plate coronas in air. Their studies revealed the corona to consist of *many minute but finite transient streamers randomly propagated at great speed from the point and indicating - by the blue spectrum - high field gradients*. Around 1938, when oscilloscopes with sufficient time resolution became available, systematic current and photographic studies of DC coronas in point-plate gaps were performed in Loeb's laboratory. Loeb initially believed that the basic understanding of the mechanism of spark breakdown could be best obtained from further corona research: *The reason why the coronas should furnish the basis for such understanding lies in the fact that discharge propagation results in and also from inhomogeneities in electric fields produced by cumulative ionization and the difference between electron and positive ion mobilities* (Loeb and Kip, 1939). However, shortly after that, also Loeb and Meek (1940) published cloud track photographs of the avalanche-to-

streamer transition in parallel-plate gaps, reproducing Raether's (1939) earlier photographs, and recognized that the corona streamers and Raether's streamers in uniform field gaps, as well as their proposed mechanism, were nearly the same.

2.2.2 Types of corona discharges

Properties of corona discharges in point-plate gaps are briefly reviewed in order to discuss the basic differences between negative, positive, DC and pulsed corona discharges. As a background of the experiments presented in Chapter **5** the discussion is limited to coronas in air at atmospheric pressure with gap distance in the range 10-200 mm and point radius in the range 0.1-10 mm. Information has been drawn from the books of Loeb (1965), Nasser (1971) and reviews of corona discharges by Goldman and Goldman (1978) and Sigmond and Goldman (1982).

DC positive coronas

The *existence region* of DC coronas is the voltage range from the *corona onset voltage* (the minimum voltage at which a corona current can be measured) to the static breakdown voltage. When a positive voltage across a point-plate geometry is gradually raised, the first ionizing events which are observed are weakly luminous cathode-directed or positive streamers, usually referred to as *onset streamers*. The current pulses associated with onset streamers occur irregularly in time and are called *burst pulses*. One of the causes of the irregular character of onset streamers and burst pulses is the statistically varying number of initial electrons in the critical volume (the volume where $\alpha' > 0$). In the *Geiger-counter regime*, i.e. at voltages close to onset, the repetition rate of burst pulses is proportional to the number of ions created per unit time in the critical volume.

When the voltage is raised further, streamer occurrence becomes more frequent until suddenly all streamer activity stops and a steady thin glow appears very close to the anode. The glow, referred to as *Hermstein glow* (Loeb, 1965, p. 86), occurs in a quasi uniform field that exists between the anode surface and a negative space charge layer. The glow gives rise to a continuous but fluctuating current. The fact that this glow mode is only observed in electronegative gases confirms the role of the negative space charge layer.

At still higher voltage again positive streamers (CDS) occur but these are brighter and advance further in the gap than the onset streamers. Because of their role in the breakdown mechanism, these streamers are sometimes referred to as *breakdown* or *pre-breakdown streamers*. With a proper choice of gap distance and voltage, the self-repetitive streamers of positive DC coronas in point-plate geometries exhibit a very high reproducibility in both space and time. The streamers

follow exactly the path of previous streamers along the symmetry axis of the gap with a frequency in the range 1-100 kHz. These properties of the self-repetitive positive DC coronas have proven to be very useful with respect to diagnostic methods (e.g. spectroscopy, see **4.2.1**, and Schlieren photography, see **4.3.1**). Marode (1975) used an image intensifier camera in the streak mode to make photographs of single streamers during repetitive streamer production. The streak photographs clearly show that a small region at the streamer front is luminous while the streamer channel remains dark.

With a relatively large anode surface, for example a wire electrode, the glow corona may exist simultaneously with streamers developing at other locations. The most striking differences between the glow and streamer discharge modes are schematically shown in Fig. 2.7. In the glow mode the ionization processes remain located in the vicinity of the anode-point. In the streamer mode, the propagating streamer heads constitute ionization regions which can, in principle, reach each arbitrary position of the discharge gap. The quasineutral plasma channels, left behind by propagating streamer heads, constitute drift regions where electrons are attached to form negative ions.

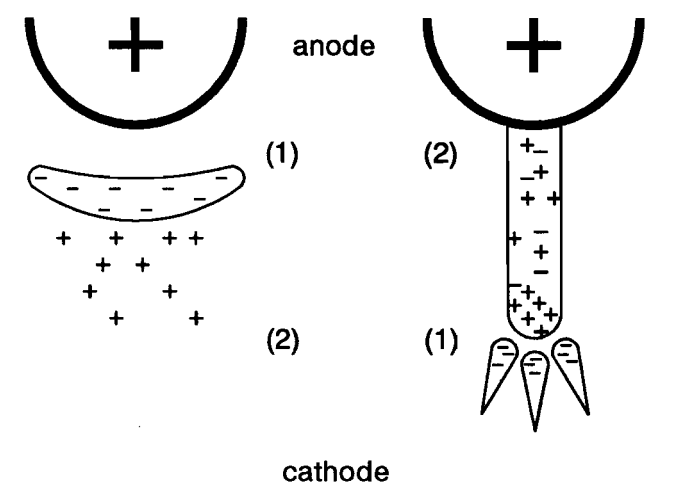

Fig. 2.7 Basic discharge modes in positive DC coronas, (left) glow, (right) streamer, (1) ionization region, (2) drift region.

The regular frequency of positive streamers in a point-plate geometry can be understood as follows: After the formation of each streamer, the positive and

negative ions which are left in the vicinity of the anode-point reduce locally the electric field. A new streamer can be formed only when the electric field has been partly restored as a result of drift, diffusion and recombination of ions. The transit time of positive streamers in a 10 mm gap can be as short as 100 ns. The transit time for positive ions from the anode to the cathode is much longer, on the order of 1 ms. However, the relative slow ion motion has a large influence on the electric field distribution in the gap which is essential for streamer formation. The detailed theoretical analysis of this discharge mode is very difficult because of the coexistence and interplay of discharge phenomena with very different characteristic time and spatial scales. The fact that repetitive DC corona streamers propagate often along exactly the same path may be due to a local increase of temperature and the resulting increase of the reduced field strength E/n. Photodetachment is probably an important process for the generation of secondary electrons from negative ions.

DC negative coronas

When the voltage across a negative point-plate gap in air is gradually increased the first ionization phenomena produce regular current pulses. These pulses have been first studied in great detail by Trichel in 1938 and are now known as the *Trichel pulses*. The frequency of the Trichel pulses starts with about 2 kHz near onset and it may attain a few MHz before the current becomes continuous.

During both the pulsed mode and the continuous current mode, the visual structure of the discharge has the general features of a glow discharge: Light is emitted in a thin negative glow (thickness < 50 μm) and in a positive column (extending only a few mm into the gap), separated by a Faraday dark space. Negative streamers (ADS) are not observed and ionization processes remain located in a small region near the negative point.

Pulsed coronas

The discharge structure of pulsed positive coronas has been investigated by Nasser around 1960 in Berlin. The main results have been obtained with sub-microsecond HV pulses applied to point-plate gaps in ambient air (gap distance: 25-150 mm) and have been published in Nasser's book (1971). Nasser observed both positive streamers (CDS) produced at a positive point and negative streamers (ADS) produced at a negative point. The streamers were made visible by means of the Lichtenberg technique. When a sensitive photographic film is placed parallel to the plate electrode, at some distance from the point, streamers propagating from the high applied field region close to the point toward the low applied field region at the cathode, hit the film and continue to propagate over the film surface. After

suitable processing of the film, the positions where streamers arrived are seen as bright spots and the surface streamers are seen as beautiful branched tree-like patterns, known as Lichtenberg figures, see Fig. 2.8. The branches never cross each other because of electrostatic repulsion. The number of streamer branches in the gas is determined from the number of spots on the film. The streamer velocity as a function of gap distance has been obtained by varying the HV pulse length and the distance between the point electrode and the film.

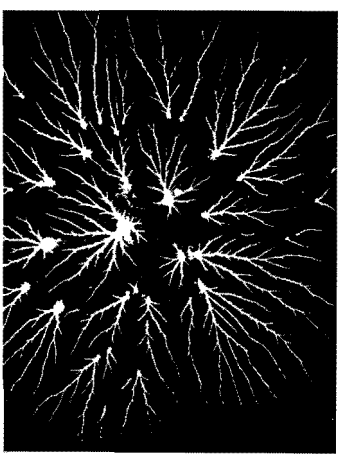

Fig. 2.8 Lichtenberg figure (photograph in positive point-plate 25 mm gap at 15 mm from the point, taken by Nasser, 1977, p. 308).

Nasser's study of positive pulsed coronas in particular establishes a large existence region for positive streamers (10-90 kV in a 150 mm point-plate gap). The most striking feature of the positive streamers is their strong branching. In a 25 mm gap and with a voltage of 30 kV, a single streamer may branch into about 40 branches at 10 mm distance and into as many as 200 streamers at the cathode.

With a negative pulsed voltage, negative streamers (ADS) are observed. To start negative streamers a higher pulsed voltage is required and the existence region for negative streamers is smaller than for positive streamers. Negative streamers propagate much less in radial and axial directions as their positive counterparts at the same pulsed voltage. Also branching of negative streamers is much less. Under the experimental conditions used by Nasser (1971), the number of streamer branches at the anode-plate of a 25 mm gap never exceeds 10. The velocity of negative streamers advancing in the low field region was found to increase while the velocity of positive streamers was found to decrease.

Basic differences between DC and pulsed coronas

In contrast to the pulsed coronas, the electric field distribution in DC coronas is always significantly affected by the collection of ions near the active electrode.

The glow discharge modes in both positive and negative DC coronas and the repetitive streamer mode in positive DC coronas are strongly dependent on field distortion caused by ion drift.

It is obvious that in a corona discharge operated with short sub-microsecond HV pulses and moderate repetition rate (< 1 kHz) the drift of ions is strongly limited when compared to DC coronas. In dry air at atmospheric pressure, the mobilities of positive and negative ions are in the range $1\text{-}4\cdot10^{-4}$ m^2 V^{-1} s^{-1} (Davies, 1987). At the critical field strength (~2.5 kV/mm) the ion drift velocity does not exceed 10^3 m/s, thus during a time of about 1 μs ions are displaced over not more than 1 mm.

On the other hand, if the repetition rate of a pulsed corona discharge is high, space charge effects resulting from ion drift can have a similar influence as in DC coronas. A higher repetition rate will increase the average ion density and the ion collection efficiency will be higher by increasing the duty cycle (the ratio of pulse width and the period between pulses), exactly as in electrostatic precipitators.

2.2.3 Streamer formation in a pulsed discharge

It is possible to extend the Raether-Meek criterion for streamer formation (Eq. 2.11) to non-uniform fields. The product $\alpha' x$ in this criterion can be replaced by the *ionization integral*:

$$N_e(r) = \exp\left[\int_{r_s}^{r} \alpha'(r')dr'\right] \approx 10^8 \qquad (2.17)$$

where r_s is the position of the initial electron that starts the avalanche. A problem that will be encountered when one attempts to evaluate this integral in a corona discharge is that the field distribution E/n in the gap may differ from the geometric field distribution as a result of space charge. However, in a pulsed corona discharge with low repetition rate it can be assumed that the ion charge density is too low to modify significantly the field distribution. The voltage required for streamer formation can thus be calculated with the ionization integral (Eq. 2.17) assuming that α' depends on the geometric field only. Fig. 2.9 shows schematically the critical volume in a wire-cylinder corona geometry. The outer radius of the critical volume r_{crit} is the radial distance from the central axis of the wire where $\alpha' = 0$. The inner radius of the critical volume r_i is the minimum distance from the anode where an avalanche may start and grow out to a number of 10^8 electrons just before arriving at the anode surface. In terms of Eq. 2.17, r_i is the minimum value of the starting position of the avalanche r_s so that at the anode the number of electrons in the avalanche is: $N_e(r_a) = 10^8$.

The minimum voltage required for streamer inception $V_{i,min}$ can be determined by recalculating $N_e(r_a)$ with $r_s = r_{crit}$ for stepwise increasing voltage levels until the condition $N_e(r_a) = 10^8$ is satisfied.

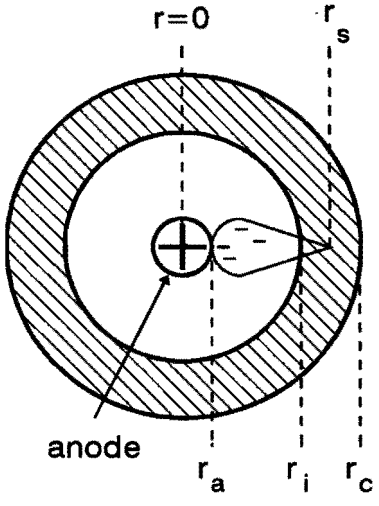

Fig. 2.9 The critical volume for streamer formation in a wire-cylinder gap.

Fig. 2.10 (a) shows the inner and outer radius of the critical volume as a function of time calculated for a positive HV pulse with 40 ns rise time applied to a wire-cylinder corona geometry. For this particular case, the minimum streamer inception voltage has been determined at ~17 kV. Fig. 2.10 (b) shows the growth rate of the critical volume. Assuming that the rate of production of initial electrons within the critical volume is a constant, the streamer inception probability is directly proportional to this growth rate.

Usually, when during a fast rising HV pulse the minimum (static) streamer inception voltage is reached, a corona discharge is formed after a statistically varying period which is called the *inception time lag*. This time lag is often decomposed into two components, a *statistical time lag*, associated with the statistically varying number of initial electrons inside the critical volume, and a *formative time lag*, which corresponds to the time needed for the formation of an avalanche with a critical size, i.e. 10^8 electrons (Kuffel and Zaengl, 1984).

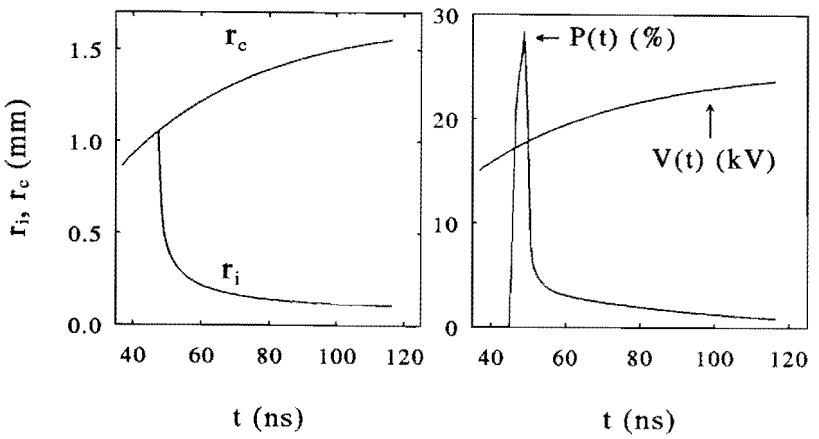

Fig. 2.10 *(left) Inner radius r_i and outer radius r_c of the critical volume for streamer formation in air, (right) growth rate of the critical volume (wire-cylinder geometry, $E(r)=V(t)/(r \cdot \ln[r_{cyl}/r_a])$, anode wire radius $r_a=0.3$ mm, cylinder radius $r_{cyl}=35$ mm, $V(t)=V_p(1 - \exp[-t/t_r])$ with $V_p=25$ kV, $t_r=40$ ns, $\alpha(E/n)$ for dry air is given in* **2.3.3**.

Detachment from negative ions (e.g. O_2^-) is probably the primary source of initial electrons in air (Somerville and Tedford, 1978). A negative ion density is always built up as a result of natural ionization sources (e.g. cosmic rays and natural radioactivity. The detachment rate in air depends strongly on humidity because of the formation of hydrated negative ions, e.g. $O_2^-(H_2O)_n$, which are very stable against detachment (Pack and Phelps, 1966). Due to the complexity of the processes in which negative ions are involved, e.g. detachment, charge transfer, clustering and de-clustering of water molecules (see **2.3.3**), it seems very difficult to make even a rough estimate of the detachment rate in a repetitive streamer discharge in humid air or flue gas.

2.3 Numerical streamer model

2.3.1 Modelling approach

As a first approach, the modelling task has been subdivided into separate models for electron-molecule kinetics (presented in this section), the streamer discharge (this section and **2.4**) and streamer-induced chemical kinetics (**2.5**).

In order to use the numerical streamer model for the study of streamer properties a good knowledge of elementary processes (e.g. ionization, attachment, photo-ionization) is essential. The coefficients for these processes which serve as input data of the streamer model are often available for pure gases but there are few data available for the complex flue gas mixtures consisting of four major components: N_2, O_2, H_2O and CO_2. Therefore, the numerical streamer model has been applied, in a first stage, to dry air (which can be considered as a simple mixture consisting of 80% N_2 and 20% O_2). In a second stage the model has been applied to N_2-O_2 mixtures with variable O_2 content. Varying the O_2 content in a N_2-O_2 mixture is motivated by the following arguments:

1) In comparison to N_2, the flue gas components O_2, CO_2 and H_2O all have the distinctive feature of being electronegative gases which are responsible for electron loss by dissociative attachment. The attachment coefficients of these gases are peaked at values of E/n close to the critical field strength (~100 Td). N_2-O_2 mixtures with variable O_2 content can thus be used in both calculations and experiments for a fundamental study of the influence of electron attachment on streamer properties.
2) Quantitative data for photo-ionization in N_2-O_2 mixtures are available but the influence of CO_2 and H_2O on the photo-ionization mechanism is only qualitatively known (see **2.1.3**).
3) Spectroscopic measurements can be analyzed using coefficients for collisional de-activation of excited states of N_2 and N_2^+. These coefficients are available for N_2 and O_2 but not for CO_2 and H_2O (see **4.2**).

In order to provide insight in the influence of the gas composition on the electron transport coefficients, this section also includes results obtained by solving the Boltzmann equation. These results are used for a (qualitative) discussion of differences between dry air, humid air and flue gases. The solution of the Boltzmann equation is also used in section **2.5** to calculate rate coefficients for the production of chemical reactive dissociation products. A simplified model for streamer propagation in air is presented in section **2.4**. This model is extended to include the discharge phase which follows the arrival of primary positive streamers at the cathode.

The separation of the Boltzmann equation (describing electron-molecule kinetics) and the discharge model equations is based upon two basic assumptions:

1) It is assumed that the macroscopic properties of electrons are independent on space and time variables and are thus sole functions of E/n. This assumption is referred to as *local equilibrium* or *hydrodynamic approach*.

2) The electron energy distribution function (which is the key variable in the solution of the Boltzmann equation) depends almost completely on collisions of electrons with the neutral background gas. This assumption which implies that for example the Coulomb interaction between electrons is neglected, is usually correct at low ionization degree: $n_e / n < 10^{-5}$.

The separation of the streamer discharge and the chemical kinetics models is based upon the assumption that changes in the gas composition have a negligible influence on the concentrations of the major neutral gas components N_2, O_2, CO_2 and H_2O. Results of calculations of chemical kinetics (section **2.5**) indeed show that the densities of all particles which are produced in the discharge (electrons, ions, vibrational and electronic excited molecules, dissociation fragments and chemical reaction products) remain low when compared to the gas density (less than 0.1 %).

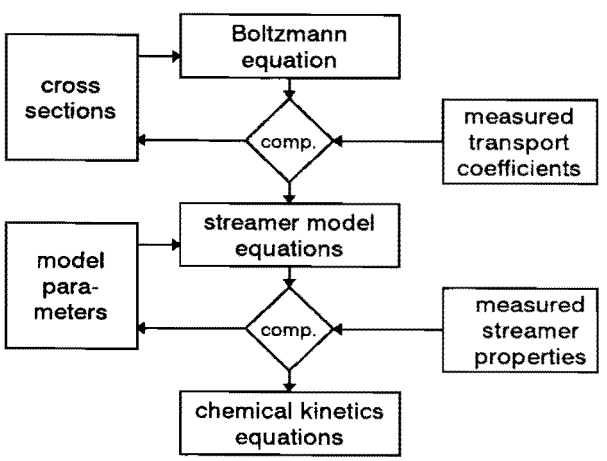

Fig. 2.11
Numerical models used for the calculation of streamer properties. Input parameters are optimized by comparison of calculated data and measured data.

The Boltzmann calculations require a reliable and complete set of cross sections for momentum transfer, excitation (rotational, vibrational and electronic), attachment and ionization in the gases N_2, O_2, CO_2 and H_2O. Some of the cross sections are only approximately known and are therefore adjusted using the comparison of calculated and measured electron transport coefficients in pure gases as a guide. It is proposed to use a similar approach for the evaluation of uncertain input parameters of the one-dimensional numerical streamer model, such as the streamer radius and photo-ionization parameters, see Fig. 2.11. These input parameters can be varied so as to obtain the best possible agreement between measured and calculated streamer properties. Measurable streamer discharge properties, which serve as comparison with model predictions, are: (a) the streamer-

induced current in the external circuit, (b) the streamer inception voltage, (c) the streamer propagation velocity and (d) the relative line intensities of the emission spectrum. The experimental techniques for measuring these properties are described in the Chapters 3 and 4 of this thesis.

2.3.1 Basic equations of the numerical streamer model

The validity of the hydrodynamic approach has been examined by Wu and Kunhardt (1988) modelling streamers in a uniform field in N_2 at 1 bar. They compared their results of a hydrodynamic model for streamer formation in N_2 ($n=2.45\cdot10^{25}$ m^{-3}) with Monte-Carlo simulations where no assumption of local equilibrium is made (Kunhardt and Tzeng, 1988). The fact that the results of the macroscopic hydrodynamic model compare very well with the results of the microscopic Monte-Carlo model (simulating the individual electron-molecule collision processes without the use of macroscopic variables as α/n, η/n and w_e) gives evidence that the hydrodynamic approach is valid.

A one-dimensional (1-D) model has been realized in which the streamer is assumed to possess cylindrical symmetry. The densities of the charged particles on the central axis (x-axis) of the streamer can be calculated solving the continuity equations:

$$\frac{\partial n_e}{\partial t} + \frac{\partial (w_e n_e)}{\partial x} - \frac{\partial}{\partial x} D_L \frac{\partial n_e}{\partial x} = (\alpha - \eta) w_e n_e + \delta w_n n_n - \beta_{ei} n_p n_e + S_{ph} \tag{2.18}$$

$$\frac{\partial n_p}{\partial t} = \alpha w_e n_e - \beta_{ei} n_p n_e - \beta_{ii} n_p n_n + S_{ph} \tag{2.19}$$

$$\frac{\partial n_n}{\partial t} = \eta w_e n_e - \beta_{ii} n_p n_n - \delta w_n n_n \tag{2.20}$$

In this set of equations, n_e, n_p and n_n are the densities of respectively electrons, positive ions and negative ions, w_e and w_n are the drift velocities of electrons and negative ions and D_L is the longitudinal diffusion coefficient. The coefficients α, η and δ account for ionization, attachment and detachment, β_{ei} and β_{ii} are coefficients for electron-ion and ion-ion recombination and S_{ph} is the photo-ionization rate. Because of the comparatively low ion mobility, the drift and diffusion of ions have been neglected (in dry air at $E/n=40$ Td, $\mu_e=5\cdot10^{-2}$ m^{2}V^{-1}s^{-1} and $\mu_i=2.3\cdot10^{-4}$ m^{2}V^{-1}s^{-1}, Davies, 1987).

It is possible to solve the continuity equations in a 2-D model (using cylindrical coordinates) together with the Poisson equation for the electric field:

$$\nabla \cdot \boldsymbol{E} = \frac{(n_p - n_e - n_n)\, q_e}{\varepsilon_0} \tag{2.21}$$

2-D models, in which the radial distribution of charged particles is calculated self-consistently, have already been realized to simulate streamer formation in an uniform electric field (Wang and Kunhardt, 1990; Kennedy and Wetzer, 1994). However, these models require much more computation time than 1-D models. Probably for this reason the simulated discharge period has often been limited to about 1 ns (streamer length < 1 mm). In order to calculate properties of streamers in electrode gaps of the order of 100 mm, we have preferred to use a 1-D model with an approximation of the Poisson equation which accounts for the influence of the finite streamer radius on the space charge electric field. The method we have adopted to calculate the space charge electric field in the 1-D model was first proposed by Davies et al. (1964) and is known as the method of disks, see Fig. 2.12.

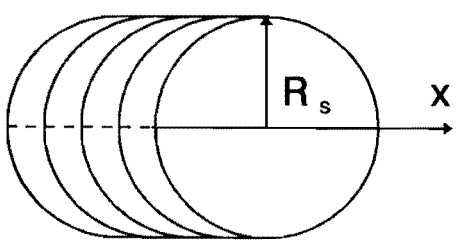

Fig. 2.12 Illustration of the method of disks (Davies et al., 1964) which is used to calculate the field distortion.

The streamer is represented by a cylinder with radius R_s, made up by a series of disks with a uniform charge distribution in each disk. The electric field on the streamer axis is obtained by the superposition of the contributions of the disks. The field at any point along the axis of the streamer is given by (Davies et al., 1964):

$$E(x) = E_g(x) + \frac{1}{2\varepsilon_0} \int_{-x}^{0} \rho\,(x+x') \left(-1 - \frac{x'}{\sqrt{x'^2 + R_s^2}} \right) dx' + \frac{1}{2\varepsilon_0} \int_{0}^{d_g - x} \rho\,(x+x') \left(1 - \frac{x'}{\sqrt{x'^2 + R_s^2}} \right) dx' \tag{2.22}$$

where $E_g(x)$ is the geometric field, the gap extends from $x=0$ to d_g and $\rho(x)$ is the net linear charge density:

$$\rho(x) = \pi R_s^2 \, (n_p - n_e - n_n) \tag{2.23}$$

The electric field in the discharge gap does not only depend on geometric applied electric field and the charge distribution $\rho(x)$ in the streamer but also on the image charges which are induced in the conducting electrodes. The influence of the image charges can be properly taken into account in the boundary conditions of $\rho(x)$ in Eq. 2.22.

The method of disks will unavoidably cause an inherent error in the calculation of the axial electric field which is due to the assumption of a uniform radial charge distribution in each disk. A detailed comparison of the field calculated according to Eq. 2.22 and the exact solution of the Poisson equation (Eq. 2.21) by Davies et al. (1967), showed that Eq. 2.22 provides a reasonable estimate of the space charge electric field. Gallimberti and Gleijeses (1978) adapted the method of disks assuming that the net charge density is not radially uniform but distributed according to a Gaussian curve with a half width which is the same for each disk. It is not expected, however, that this modification gives more accurate results. Recent 2-D streamer models show that the constant density contours of the net (positive) charge in the streamer possess a hemispherical shape. Thus the net positive charge density (n_p-n_e-n_n) is concentrated at the boundary of the streamer whereas the densities of n_p, n_e and n_n individually are highest in the center of the streamer.

In the numerical streamer model, realized at IVTAN (Moscow), the system of equations (Eqs. 2.18-2.20) is solved using the Flux Corrected Transport (FCT) method which has originally been developed by Boris and Book (1973) to model shock fronts in fluids and which has been applied before to model streamers by Morrow (1985, 1988, 1991) and Gallimberti (1987, 1988). The numerical FCT algorithms are identical to those proposed by Morrow and Cram (1985) and will therefore not be described here. A small modification of the FCT algorithms, proposed by Wu and Kunhardt (1987) to reduce numerical diffusion, has also been included. The expression for the space charge electric field (Eq. 2.22) is represented by a simple matrix equation which depends only on electrode geometry and the computational mesh (Morrow and Cram, 1984). The time step Δt of the calculation is limited by the calculation of the electron drift and diffusion terms in Eq. 2.18 and the size of the computational mesh Δx. For the drift term, numerical stability is obtained if the Courant condition applies: $C = w_e \, \Delta t / \Delta x \leq 1$. For the diffusion term, stable solutions are obtained if the Von Neumann condition applies: $S = 2 \, D_L \, \Delta t \, / \, (\Delta x)^2 \leq 1$. Because the mesh size Δx in the streamer head region must be very small (in order to limit numerical diffusion), and S depends on $(\Delta x)^{-2}$, the Von Neumann condition imposes a maximum value for Δt.

For the fast moving streamer head with large spatial gradients, a non-uniform and moving spatial mesh is necessary. A fine uniform mesh is used across the region where the streamer head propagates, and an expanding mesh away from this region towards the electrodes. Because for any change in the mesh, the coefficients of the matrix, which is used to solve Eq. 2.22, must be recalculated, the mesh is not adapted after every time step. When the streamer reaches the end of the fine mesh region, the mesh is rezoned, so that the streamer head is at the start of the new fine mesh region. The adopted size of the fine mesh is 5 μm over a length of 1.2 mm. The mesh expands smoothly towards the cathode region and towards the streamer channel where the mesh size is 150 μm. In order to obtain non-oscillating solutions the stiffness coefficient (the ratio of neighbouring intervals of the mesh) is made less than 10%. A fine mesh is also used in the anode region to resolve the anode fall. Streamer propagation over 100 mm (corresponding to a streamer transit time of at least 100 ns) can be calculated in about 6 hours on a PC (486 processor with 50 MHz clock frequency). This computation time is short enough to study the influence of uncertain model input parameters (e.g. the streamer radius and photoionization parameters) by means of systematic parameter variations.

2.3.3 Basic processes and input data

Attachment, detachment and ion conversion

A crucial point in the modelling of streamers is the need for reliable data for electron gain (ionization, detachment) and electron loss (attachment, electron-positive ion recombination). Experimental attachment coefficients are much more uncertain than ionization coefficients, principally because the difference between attachment followed by detachment and no attachment at all is often difficult to determine experimentally (Wen, 1989). In dry air, the following reactions play a significant role:

1)	three-body attachment	$e^- + O_2 + M$	$\rightarrow$	$O_2^- + M$
2)	dissociative attachment	$e^- + O_2$	$\rightarrow$	$O^- + O$
3)	electron detachment	$O^- + M$	$\rightarrow$	$O + M + e^-$
4)	ion conversion	$O^- + O_2\,(+ M)$	$\rightarrow$	$O_2^- + O + (M)$

The three-body attachment process, in which the third body M can be any particle (including electronic excited molecules), is important at high pressure. The dissociative attachment process (threshold 4.4 eV) produces temporary O^- ions which undergo either detachment (thereby providing an additional source of electrons in the discharge) or conversion to negative ions which are more stable

than O^- (e.g. O_2^-). In experimental studies of ionization and attachment in dry air often no account has been made for the influence of detachment and ion conversion on the measured effective ionization and attachment coefficients. This fact is probably responsible for the large scatter in measured coefficients in air which appears from the data review of Dutton (1975). More recently Gallagher et al. (1983), reviewing electron transport data in electronegative gases, concluded that even in pure oxygen the picture of electron gain and loss at $E/n > 50$ Td is still confuse because ionization, attachment, detachment and ion conversion occur. Although many investigations indicate that O^- is the primary source of detachment, also detachment from O_2^- and O_3^- is possible. The picture of detachment in oxygen and dry air can be clarified only with more work incorporating identification of the specific ions present, their concentrations, energy distributions and the reactions in which they participate.

In gas mixtures with O_2, CO_2 and H_2O a large number of other reactions involving negative ions can occur. An impressive number of interesting data about these reactions can be found in the early work of Phelps et co-workers. Pack and Phelps (1966) showed that H_2O is 7 times as effective a third body in the three-body attachment process as the O_2 molecule. Moruzzi and Phelps (1966) demonstrated the role of clustering of water molecules:

$$\begin{aligned} &O_2^- + H_2O + M \rightarrow (H_2O) \cdot O_2^- + M \\ &(H_2O)_{n-1} \cdot O_2^- + H_2O + M \rightarrow (H_2O)_n \cdot O_2^- + M \end{aligned} \qquad (2.24)$$

The clustered hydrated ions $O_2^-(H_2O)_n$ and $O^-(H_2O)_n$ with $n=1$ to 5, which were identified by mass spectrometry, showed very little evidence of detachment.

The electron swarm studies of Verhaart in humid air (Verhaart, 1982) and flue gas (Verhaart, 1989) indicate that the conversion from unstable to stable hydrated negative ions is a very fast process so that in case of an electron electron avalanche at low pressure (in absence of space charge effects) these gases behave as a normal attaching gas where the effective ionization coefficient equals the difference between the real ionization coefficient and the real attachment coefficient: $\alpha' = \alpha - \eta$. In electron avalanches in dry air at $E/n = (E/n)_{crit} = \sim 110$ Td ($p=778$ Torr), the characteristic time for detachment turns out to be 83 ns whereas the time for ion conversion is 32 ns. In humid air ($p_{H2O}=11.25$ Torr, $[H_2O]=1.5\%$) only a very small current due to detachment is measured and the characteristic time for ion conversion is only 3 ns (Verhaart and van der Laan, 1984).

Fig. 2.13 shows experimental data for the (effective) ionization frequency ($\nu_i = \alpha \cdot w_e$) and the (effective) attachment frequency ($\nu_a = \eta \cdot w_e$) in both dry and humid air (2% H_2O) at atmospheric pressure ($p=1$ bar, $T=273$ K), obtained by

Davies (1987). Three-body attachment dominates at low values of the electric field strength ($E/n < 20$ Td) and at moderate electric fields ($50 < E/n > 100$ Td) the two-body attachment process dominates. As a result, a local minimum in the attachment coefficient exists in the range $E/n = 20$-50 Td. The data of Davies in particular show that even a low concentration of water vapour can have a significant influence on the attachment frequency. At $E/n < 20$ Td, water vapour increases the attachment frequency by increasing three-body attachment. For $50 < E/n < 100$ Td the attachment frequencies in dry and humid air are practically equal. However, at $E/n > 100$ Td, water vapour again increases the measured effective attachment frequency, probably as a result of the formation of hydrated negative ions (Eq. 2.24a).

The data of Davies (1987) are in agreement with the observations made by Verhaart and van der Laan (1984) who measured separately the net ionization coefficient α-η and coefficients for ion conversion and detachment. They found that adding 1.5% H_2O to dry air at $p = 778$ Torr increases significantly the effective ionization coefficient because detachment is suppressed by the formation of stable negative ions. A possible influence of the addition of water vapour on the net ionization coefficient (the difference between the real ionization and attachment coefficient, α-η) was found to be beyond the detection limit.

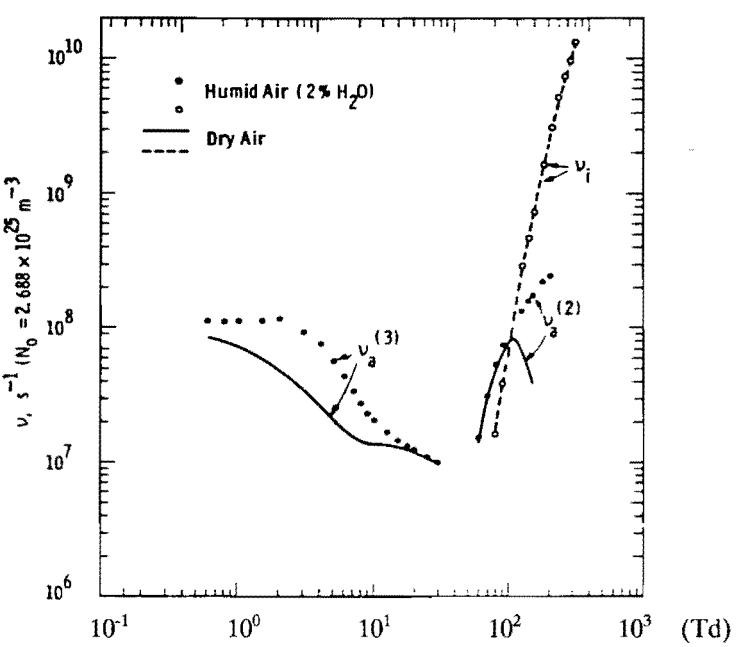

Fig. 2.13 Ionization frequency ν_i and attachment frequency ν_a in dry and humid air. (2) Two-body and (3) three-body attachment process (Davies, 1987).

The theoretical analysis of detachment in (humid) air or flue gases is difficult because it should take a processes into account for which no accurate experimental data are available. Detachment rates generally increase with temperature (Smirnov, 1982). Metastable electronic excited molecules, possessing enough energy to detach electrons from O_2^- (such as $O_2(a^1\Delta_g)$ with 0.977 eV), can play a significant role (Aleksandrov, 1978). In the presence of water vapour also clustering and declustering of hydrated negative ions should be taken into account: the energy required to detach an electron from an hydrated negative ion increases with the cluster size n, however, the energy required for dissociation of the cluster of water molecules (declustering) decreases with increasing n.

In the propagating streamer head, detachment can play a role (even at high water vapour concentration) because the characteristic time of new plasma generation in front of the streamer head (δ_h / v_s = 0.1 ns) is short compared to the time needed for conversion from unstable to stable negative ions (~1 ns). The influence of detachment on streamer properties was investigated by Kline (1975) and more recently by Kennedy and Wetzer (1994) using a numerical models for streamer formation in a uniform field in atmospheric air. Kline's calculations demonstrate that detachment influences the initial stage of electron avalanches. However, because most of the electrons are produced at the maximum electric field in the streamer where ionization dominates all other electron gain and loss processes (detachment, attachment, recombination) the calculated maximum field strength, the maximum electron density, the streamer velocity and the streamer-induced current are almost insensitive to assumed attachment, detachment and ion conversion coefficients.

Detachment has not been taken into account in the numerical calculations. The influence of detachment on the streamer-induced current will be evaluated by means of a simplified streamer model in section **2.4**.

Solution of the Boltzmann equation

The dynamics of an assembly of electrons can usually be characterized by an electron velocity distribution function $F(r, w, t)$. The time evolution of this function is described by the Boltzmann equation:

$$\frac{\partial F}{\partial t} + \boldsymbol{w}.\nabla_r F + \boldsymbol{a}.\nabla_w F = C(F) \qquad (2.25)$$

where $\boldsymbol{w}$ is the electron velocity vector and $\boldsymbol{a}$ ($=q_e \boldsymbol{E}/m_e$) the acceleration vector. The collision operator C represents the gain and loss of electrons in the velocity-space element $dwdr$ due to both elastic collisions (momentum exchange) and inelastic collisions (excitation, ionization etc.). The possible influence of detachment

and recombination on the electron energy distribution function has been neglected. Solutions of the Boltzmann equation are generally complicated because $F(r, w, t)$ depends on six velocity-space variables and time. In the hydrodynamic approach (local equilibrium), the simplifying assumption $F(r, w, t) = n_e(r, t) \cdot f(w)$ can be made which casts the Boltzmann equation into a form amenable to numerical solution. Usually, the electron velocity distribution function is expanded into a series of Legendre polynomials P_k (Huxley and Crompton, 1974, Chap. 4):

$$f(w) = f_0(w) + \sum_{k=1}^{\infty} f_k(w)\, P_k(\cos\theta) \tag{2.26}$$

where θ is the scattering angle of an electron with respect to the field direction. The isotropic part of the velocity distribution function $f_0(w)$ is related to the energy distribution function $f_0(\epsilon)$ by $\sqrt{\epsilon}\, f_0(\epsilon)\, d\epsilon = 4\,\pi\, w^2 f_0(w)\, dw$ and $f_0(\epsilon)$ is normalized by:

$$\int_0^{\infty} \sqrt{\varepsilon}\, f_0(\varepsilon)\, d\varepsilon = 1 \tag{2.27}$$

From the electron energy distribution function, the electron transport coefficients w_e and D_T can be calculated as (Huxley and Crompton, 1974, p. 182):

$$w_e = \frac{E}{3n}\sqrt{\frac{2}{m_e}} \int_0^{\infty} \frac{\varepsilon}{\sigma_m(\varepsilon)} \frac{df_0}{d\varepsilon}\, d\varepsilon \tag{2.28}$$

$$D_T = \frac{1}{3n}\sqrt{\frac{2}{m_e}} \int_0^{\infty} \frac{\varepsilon}{\sigma_m(\varepsilon)} f_0(\varepsilon)\, d\varepsilon \tag{2.29}$$

In Eqs. 2.28 and 2.29, $\sigma_m(\epsilon)$ is the effective momentum transfer cross section that includes both elastic and inelastic collisions. Kinetic rate coefficients can be calculated as:

$$k_i = \sqrt{\frac{2}{m_e}} \int_0^{\infty} \sqrt{\varepsilon}\, \sigma_i(\varepsilon)\, f_0(\varepsilon)\, d\varepsilon \quad (m^3 s^{-1}) \tag{2.30}$$

where σ_i are cross sections for ionization, attachment, dissociation and excitation (the ionization coefficient $\alpha/n = k_{ion}/w_e$ (m^2), the ionization frequency $\nu_i = n\, k_{ion}$).

In the conventional solution of the Boltzmann equation, the series of Legendre polynomials P_k in Eq. 2.26 is truncated after the first two terms. This two-term approximation is valid subject to the restriction that electrons gain or lose only a

small fraction of their energy between collisions. With the introduction of multi-term numerical Boltzmann solutions (using more than two terms of the expansion in Legendre polynomials) and the use of efficient Monte-Carlo simulation codes (which avoid entirely the use of the Boltzmann equation) there has been considerable interest in clarifying the circumstances under which the two-term solution is no longer adequate. In N_2 at electric fields higher than 1500 Td, errors in the calculation of the diffusion coefficient resulting from the use of a two-term approximation are more than 25% (Phelps and Pitchford, 1985). In pure water vapour at 1000 Td this error is 50% (Ness and Robson, 1988). Since the electric field in a streamer reaches values on the order of 1000 Td, we present results using a multi-term method which has been developped at the University Paul Sabatier (Toulouse). The method of solution of the Boltzmann equation has been described by Yousfi et al. (1985). Comparisons of this method with other multi-term methods show that it is attractive with respect to computation time as well as accuracy (Ségur et al., 1984, 1986).

Even at low ionization degree ($n_e/n < 10^{-4}$) the Coulomb interaction between electrons can have a considerable influence on the electron energy distribution function. Yousfi et al. (1992) included this interaction in the Boltzmann equation for various values of E/n and n_e/n. Their results clearly show that for conditions in a streamer discharge ($E/n > 10$ Td and $n_e/n < 10^{-5}$) the Coulomb interaction can be neglected.

The applied set of cross sections for N_2, O_2 and CO_2 of Yousfi et al. (1988) is essentially based on the sets collected at the Joint Institute for Laboratory Astrophysics (JILA) by Kieffer (1973), Phelps and Pitchford (1985) and Phelps (1985). Yousfi et al. (1993) completed this set with cross sections for H_2O. At low electron energy, the elastic scattering cross section in H_2O is very large (typical for polar molecules). Theoretical cross sections for rotational excitation (Itikawa, 1972) and experimental cross sections for vibrational excitation (Seng and Linder, 1976) have been adjusted by comparison of calculated electron transport data with new experimental data in N_2-H_2O mixtures (Friedrich and Yousfi, 1991). The cross sections obtained from this fitting procedure must be considered as a coherent and not separable set(1).

Three-body attachment cross sections in dry air have been obtained by fitting of the magnitude of cross sections given by Phelps (1985) and using the comparison of experimental and calculated attachment coefficients. Cross sections for three-body attachment with CO_2 and H_2O as third body are assumed to be proportional to the experimental rate constants given by Christophorou et al. (1984, p. 583).

(1) This set has not been published. Overviews of cross sections (including clear figures) have been published by Hunter and Christophorou (1984) for N_2, O_2 and CO_2 and by Ness and Robson (1988) and Elford (1991) for H_2O.

For $M = N_2, O_2, CO_2$ and H_2O, these constants are respectively: k_3 = 0.05, 2, 3 and 14 · 10^{-36} m^6s^{-1}. However, assuming a direct proportionality between cross sections and measured rate constants may lead to considerable errors because the measured rate constants depend not only on cross sections but also on the electron distribution function. A similar procedure for obtaining cross sections was followed by Phelps (1987) to calculate via the solution of the Boltzmann equation net ionization and attachment coefficients in dry and humid air.

The Boltzmann equation has been solved by Yousfi for the gas mixtures given in Table 2.1. Flue gas B has the typical composition of the flue gas emitted by a coal-fired electrical power plant. For this gas mixture experimental electron transport coefficients are available (Verhaart, 1989). Also calculations for air with 10% water vapour have been made because $deNO_x$ experiments (section **5.5**) have been performed using this gas mixture.

gas	N_2 (%)	O_2 (%)	CO_2 (%)	H_2O (%)	n (m^{-3})	T (K)
N_2-O_2 mixtures	90, 80, 60, 40	10, 20, 40, 60	0	0	$2.5 \cdot 10^{25}$	293
humid air	72	18	0	10	$1.87 \cdot 10^{25}$	373
flue gas B	74	5	15	6	$1.87 \cdot 10^{25}$	373

Table 2.1 Gas mixtures used in solutions of the Boltzmann equation.

Fig. 2.15 shows the influence of the O_2 concentration in a N_2-O_2 mixture on the electron energy distribution functions (eedf's) at E/n = 100 Td. Also the Maxwell eedf is shown for comparison:

$$f(\varepsilon)_M = 2.07 \cdot \varepsilon_a^{-\frac{3}{2}} \exp[-1.5\varepsilon/\varepsilon_a] \tag{2.31}$$

where the average electron energy ϵ_a is given by the Boltzmann solution $f_0(\epsilon)$:

$$\varepsilon_a = \int_0^\infty \varepsilon \sqrt{\varepsilon}\, f_0(\varepsilon)\, d\varepsilon \tag{2.32}$$

The main differences between the Boltzmann eedf and the Maxwell eedf are due to resonant vibrational excitation of N_2 with a maximum cross section at 2 eV. Fig. 2.15 clearly shows that with decreasing N_2 concentration more electrons pass the "vibrational excitation energy barrier" at 2 eV. In spite of the changes in the eedf the calculated attachment coefficient in N_2 - O_2 mixtures was found to be almost directly proportional to $[O_2]$ for $[O_2]$ = 10 - 60%.

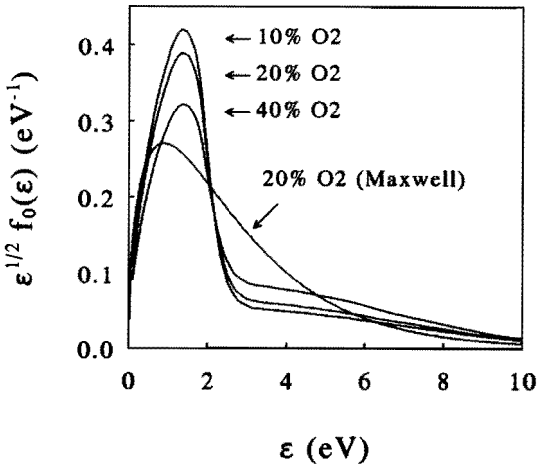

Fig. 2.15 Electron energy distributions in N_2-O_2 mixtures at E/n=100 Td. For air also a Maxwell distribution is shown (ϵ_a = 2.7 eV).

In Fig. 2.16 calculated eedf's in dry air and flue gas B are compared for characteristic values of *E/n* in streamers, given in Table 2.2 (in the streamer channel *E/n* is about 20 Td and in the streamer head *E/n*>500 Td, see **2.3.4**). Although flue gas B contains more CO_2 (15%) than H_2O (6%), the main differences between the eedf's in air and flue gas B are due to the presence of water vapour. In particular at low electron energy, cross sections for elastic scattering, rotational excitation and vibrational excitation in H_2O are large when compared to the corresponding cross sections of CO_2.

E/n (Td)	DT/μe (eV) dry air	D_T/μ_e (eV) flue gas B	ϵ_a (eV) dry air	ϵ_a (eV) flue gas B
4	0.5	0.04	0.7	0.06
20 (streamer channel)	1.6	1.1	1.0	0.8
100 (critical)	2.1	2.0	2.7	2.7
500 (streamer head)	**5.6**	**5.6**	**9.6**	**9.4**

Table 2.2 Typical values for the electric field E/n, the characteristic electron energy D_T/μ_e and the average electron energy ϵ_a of streamers in dry air and in flue gas B, calculated by solving the Boltzmann equation.

At $E/n=4$ Td, the main electron energy loss process in dry air is vibrational excitation of the lower levels of N_2 (energy threshold at 0.2 eV). In flue gas B, however, the energy of the main part of the electrons remains below the vibrational bending energy threshold of H_2O at 0.198 eV and therefore rotational excitation of H_2O molecules is the dominant process.

At $E/n=20$ Td, the resonant vibrational excitation of N_2 at 2 eV influences strongly the eedf's in both air and flue gas B. In flue gas B, the energy of a significant part of the electrons remains below the vibrational stretching thresholds (at 0.435 and 0.466 eV) of H_2O. Differences from Maxwell's distribution are large in air as well as in flue gas.

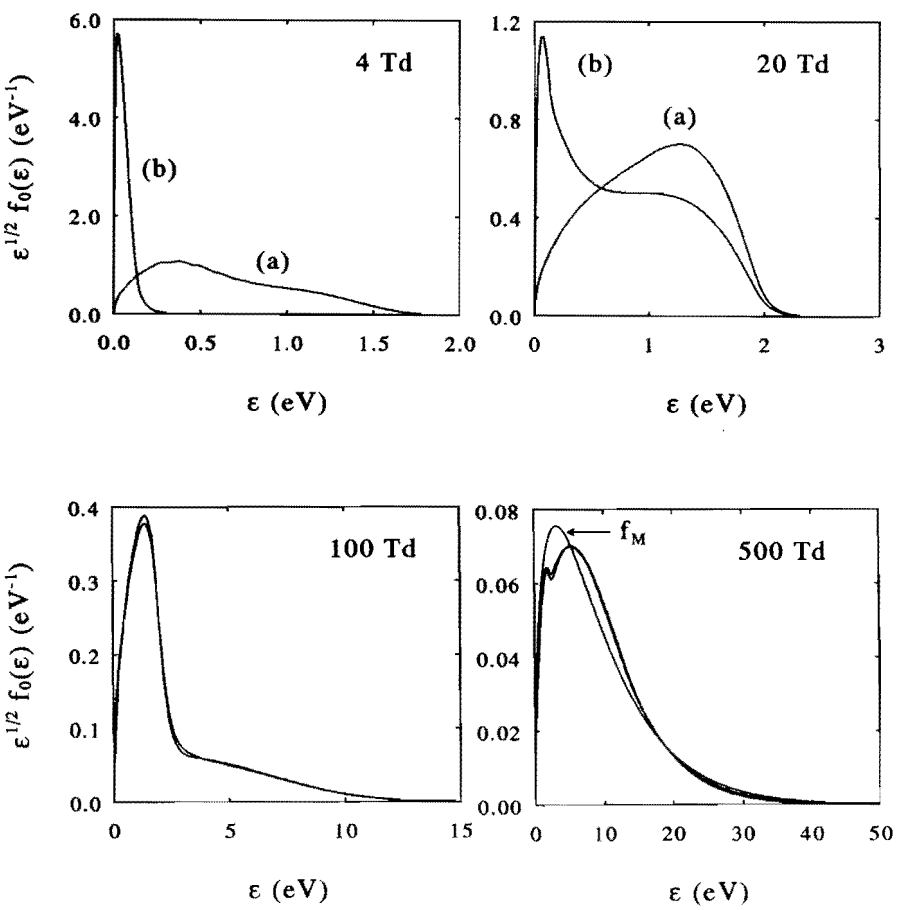

Fig. 2.16 Calculated eedf's in (a) dry air and (b) flue gas B for different E/n. For E/n=500 Td, f_0 is compared with the Maxwell distribution f_M (Eq. 2.41).

At the critical field strength, $E/n = 100$ Td, the electron distribution functions in dry air and flue gas B are very similar because both are dominated by the same energy loss process: resonant vibrational excitation of N_2. The eedf's differ much from the Maxwellian shape (see also Fig. 2.15). Only a small fraction of the electrons participates in ionizing collisions (the ionization thresholds for N_2, O_2, CO_2 and H_2O are respectively 15.6, 12.2, 13.7 and 12.6 eV).

At $E/n = 500$ Td, the eedf's in dry air and flue gas are very similar and also close to the Maxwell distribution. Resonant vibrational excitation of N_2 is now seen to decrease the number of electrons at the low energy part of the distribution function.

Fig. 2.17 shows calculated values of the ionization frequency ν_i, the attachment frequency ν_a, the drift velocity w_e and the ratios D_T/μ_e and D_L/μ_e as a function of E/n for dry air, flue gas B and air with 10% water vapour. The ionization frequency is almost insensitive to changes in the gas composition. However, significant differences occur in the attachment frequency. The local minima of the attachment frequency in air, flue gas B and air with 10% water vapour are respectively $\sim 10^7$, $\sim 1.5 \cdot 10^7$ and $\sim 10^8$ s^{-1}. The differences in the attachment frequency are partly due to differences in the drift velocity, see Fig. 2.17 (b). The position of the local minimum in the attachment frequency is in dry air, flue gas B and air with 10% water vapour respectively ~30, ~40 and ~50 Td.

In flue gases in general the critical field strength $(E/n)_{crit}$ can be higher or lower than in dry air. The presence of the gases CO_2 and H_2O tends to increase the attachment coefficient but, in principle, it is also possible that $(E/n)_{crit}$ is lower than in dry air as a result of the comparatively low O_2 concentration. The calculated critical field strength $(E/n)_{crit}$ in air, flue gas B and air with 10% water vapour is respectively ~110, ~115 and ~135 Td, thus the difference in $(E/n)_{crit}$ between dry air and flue gas B appears to be very small.

Fig. 2.17 (c) shows calculated values of D_T/μ_e and D_L/μ_e. As a result of the large number of rotational transitions of water vapour with low electron energy threshold, the characteristic electron energy at low E/n is much lower in flue gas than in air. In flue gas at E/n close to 1 Td, D_T/μ_e approaches the neutral gas temperature (T_{gas} = 300 K = $2.5 \cdot 10^{-2}$ eV).

Fig. 2.17 (page 59)

Electron transport coefficients in air, flue gas B (containing 6% H_2O) and air with 10% H_2O, (a) ionization and attachment frequency, (b) drift velocity, (c) D/μ_e.

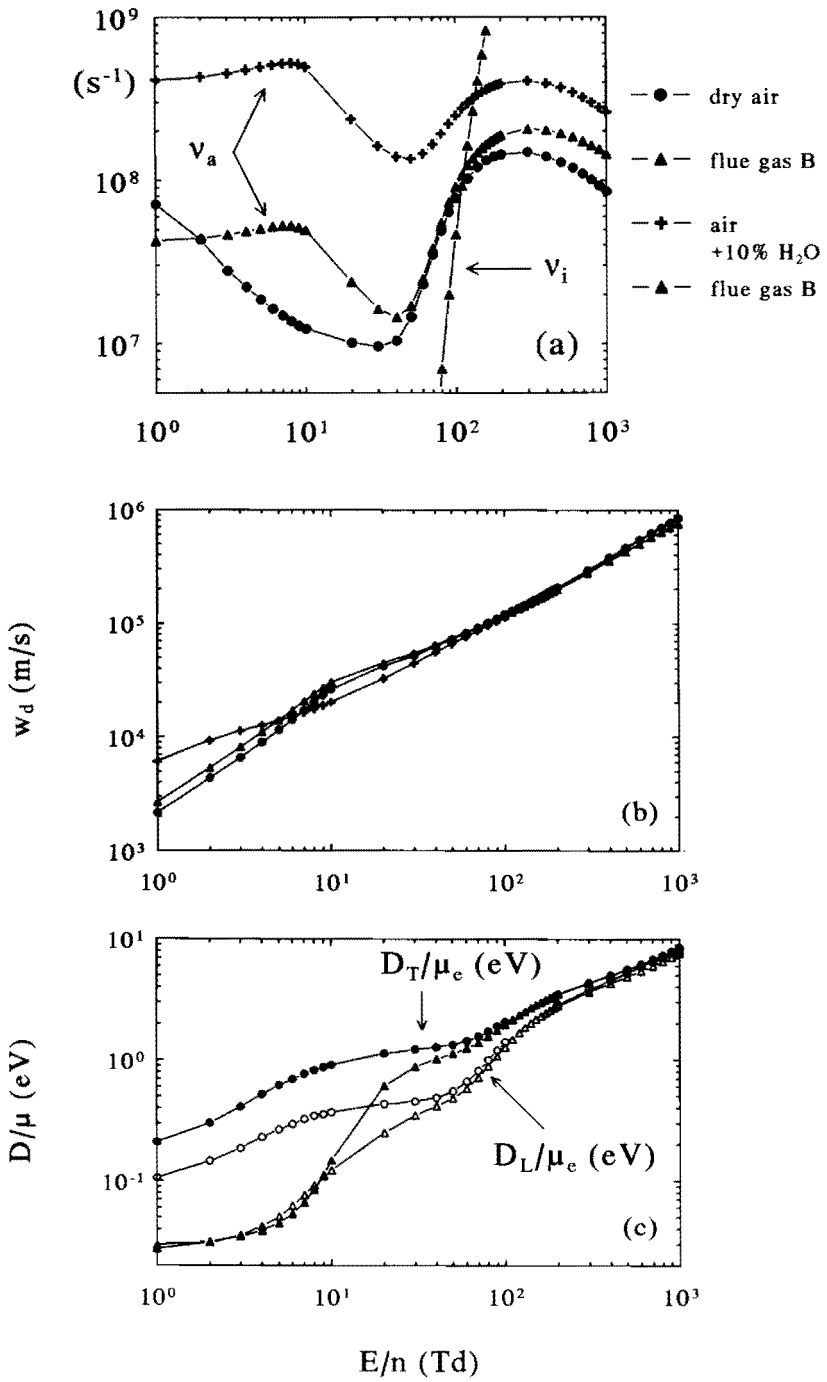
10^9
(s^{-1})
10^8
10^7
ν_a
ν_i
(a)
10^0
10^1
10^2
10^3
dry air
flue gas B
air
+10% H_2O
flue gas B
10^6
10^5
10^4
10^3
w_d (m/s)
(b)
10^1
10^0
10^{-1}
D/μ (eV)
D_T/μ_e (eV)
D_L/μ_e (eV)
(c)
E/n (Td)

In Fig. 2.18 calculated ionization and attachment coefficients in flue gas B are compared with experimental data of Verhaart (1989). Calculated ionization coefficients are close to measured data. It is also shown that ionization coefficients in air and flue gas are practically the same. However, there is a considerable difference between calculated and measured attachment coefficients. It is improbable that this difference is caused by detachment because the differences appear also at $E/n < 100$ Td where the detachment rate is very low (Wen, 1989). A possible influence on the experimental attachment coefficient can be due to the presence of H_2O clusters. Experiments of Vostrikov et al. (1987), using crossed electron and molecular beams, show that the formation of these clusters has a signifant influence on cross sections for dissociative attachment: with increasing cluster size the width of the cross section peak becomes wider, its magnitude lower and it shifts to higher electron energy. The size dependence of electron attachment to water clusters has also been theoretically studied (e.g. Barnett et al., 1988).

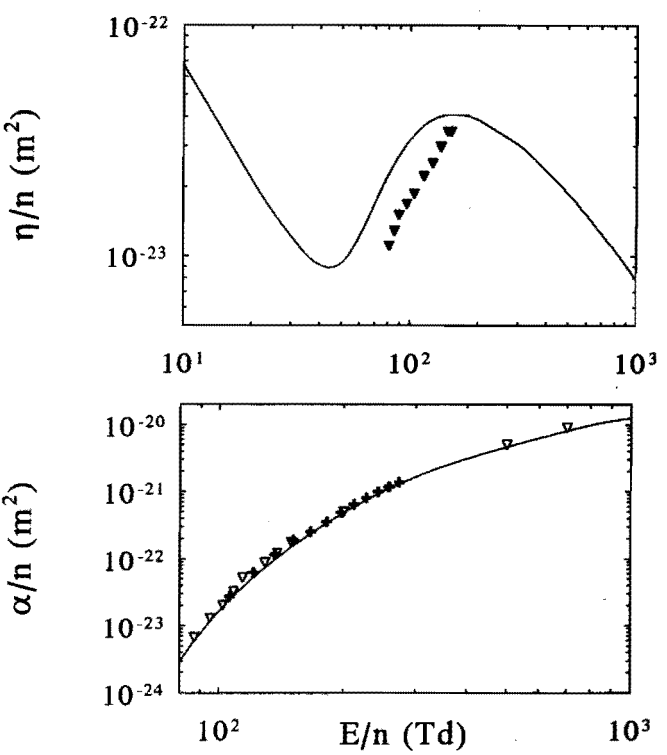

Fig. 2.18 Comparison of calculated and measured α/n and η/n.

Data used in the numerical streamer model

Electron transport coefficients for N_2-O_2 mixtures which have been calculated by solving the Boltzmann equation, have been represented by analytical functions in the numerical code. Differences in the electron drift velocity for different O_2 concentrations are negligible. The following approximation of the drift velocity has been made:

$$w_e = 3.2 \cdot 10^3 \, [E/n]^{0.8} \quad (m/s) \tag{2.33}$$

The ionization coefficient is given by the expression:

$$\frac{\alpha}{n} = 5 \cdot 10^{-20} \left(1 + \frac{b}{[E/n]^3} \right) \exp\left(\frac{-1010}{[E/n]} \right) \quad (m^2) \tag{2.34}$$

with for $[O_2]$ = 10%, 20% and 40%: $b = 4 \cdot 10^6$, $7 \cdot 10^6$ and $1 \cdot 10^7$.
The two-body attachment coefficient is represented by the function:

$$\frac{\eta_2}{n} = 4.3 \cdot 10^{-23} \, \frac{[O_2]}{20} \, \exp\left[-1.05 \, | 5.3 - \ln[E/n] |^3 \right] \quad (m^2) \tag{2.35}$$

The three-body attachment coefficient in dry air is given by:

$$\frac{\eta_3}{n^2} = 1.6 \cdot 10^{-47} \, [E/n]^{-1.1} \quad (m^5) \tag{2.36}$$

The three-body attachment coefficient in N_2-O_2 mixtures is written as:

$$\frac{\eta_3}{n^2} = \left(\frac{\eta_3}{n^2} \right)_{air} \frac{[O_2]^2}{20^2} \quad (m^5) \tag{2.37}$$

The net ionization frequency, calculated according Eqs. 2.23-2.27, is shown in Fig. 2.19.
The diffusion coefficient D_L has been interpolated from the data shown in Fig. 2.17 (c).

The ion-ion recombination coefficient in dry air is given by (Smirnov, 1982):

$$\beta_{ii} = 2 \cdot 10^{-12} \cdot \left(\frac{T}{300} \right)^{-1.5} \quad (m^3/s) \tag{2.38}$$

where T is the gas temperature in K.

The electron-positive ion recombination coefficient depends on the type of ion and the average electron energy:

$$\beta_{ei} = \beta_{ei}^{0} \cdot \left(\frac{300}{T_e} \right)^{0.5} \tag{3.38a}$$

where T_e (K) = $1.2 \cdot 10^4$ ϵ_a (eV). For N_2^+ and O_2^+, β_{ei}^0 is respectively $3.5 \cdot 10^{-13}$ and $1.9 \cdot 10^{-13}$ (McGowan and Mitchell, 1984). In the calculations we have used a constant value, based on the average energy of electrons in the streamer channel ($\epsilon_a = 1$ eV): $\beta_{ei} = 5 \cdot 10^{-14}$ m^3/s.

The photo-ionization source term in Eq. 2.18 has been calculated as:

$$S_{ph}(x) = A \int_0^d \alpha \, w_e \, n_e \, g \, (|x-x'|) \, dx' \tag{2.39}$$

$$\text{with} \quad A = \frac{\omega}{\alpha} f_q \, n(O_2) \, , \quad g \, (x) = \frac{1}{2} \left[\phi(|x-x'|) - \phi \left[\sqrt{|x-x'|^2 + R_s^2} \right] \right]$$

The factors ω/α (~ 0.1), f_q and ϕ have been discussed in section **2.1.3**. The factor g in Eq. 2.39 accounts for the influence of the streamer radius R_s on the volume where secondary avalanches can be formed (Bityurin et al., 1992). Fig. 2.20 shows the probability for the formation of a photo-ion (in a sheath of 1 mm) per ion produced in the discharge as a function of the relative distance $|x-x'|$ to the photon source. Increasing $n(O_2)$ from 20% to 40% the factor A in Eq. 2.39 is little changed (from $3.3 \cdot 10^{-3}$ to $3.6 \cdot 10^{-3}$). The main changes are due to absorption: by increasing the relative oxygen concentration, photons penetrate less far into the gas.

A streamer radius R_s of 100 μm has been used as standard condition in the calculations. This value is close to the streamer radius calculated in 2-D models: Wang and Kunhardt (1990), modelling streamer formation in a uniform field in N_2 at atmospheric pressure, showed that the streamer radius (defined as the radial distance from the streamer axis where n_e is 1% of the maximum) is ~100 μm for the CDS and ~200 μm for the ADS. Note that these values are close to the diffusion radius of an electron avalanche at the moment of the avalanche-to-streamer transition which has been estimated using the Raether-Meek criterion in **2.1.2**. The fact that the radius of the CDS is less than that of the ADS can be understood from the main difference between the CDS and the ADS: in the CDS the electron drift velocity is directed toward the region with the high electric space charge field and in the ADS outward from this region.

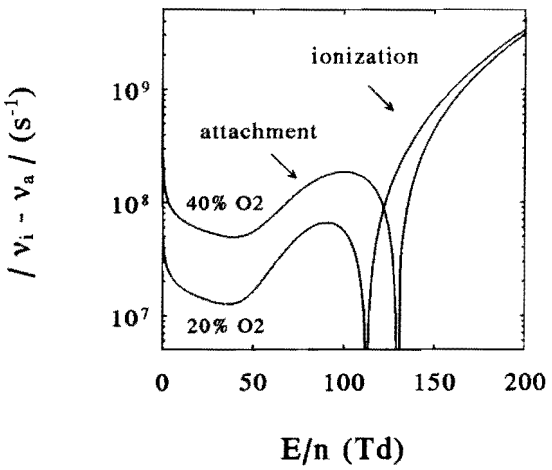

Fig. 2.19
The net ionization frequency $|\nu_i - \nu_a|$ for N_2-O_2 mixtures with $[O_2]$=20% and 40% according to Eqs. 2.33-2.37.

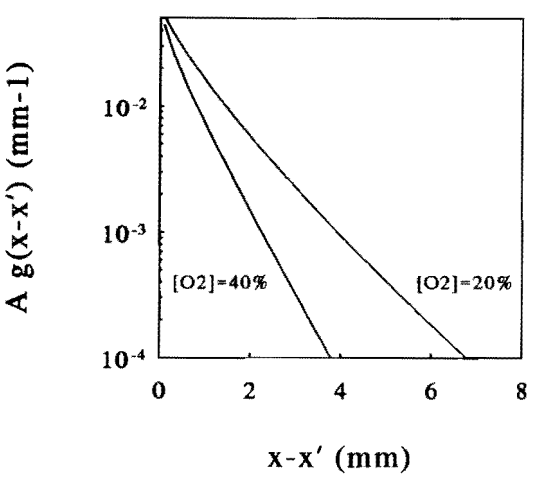

Fig. 2.20
The quantity A g($|x-x'|$) as a function of $|x-x'|$ with $n(O_2)$=20% and $n(O_2)$=40% (Eq. 2.39).

2.3.4 Results of the numerical streamer model

Two different versions of the numerical streamer model have been realized at IVTAN. The first version is referred to as code I. In a second version, referred to as code II, changes saving computation time have been introduced. Diffusion and recombination have not been taken into account in code I but were introduced in code II. The models have been applied to experimental conditions of experiments (see Table 3.1). The geometric electric field is that of a wire-cylinder configuration: $E(r,t) = V(t)/(ln[r_{cyl}/r_w] \cdot r)$ with wire radius r_w=0.3 mm and cylinder radius r_{cyl}=35 mm. The neutral gas density n is $2.45 \cdot 10^{25}$ m^{-3}.

Field and charged particle density distributions in streamers

Fig. 2.21 shows the distributions of the electric field and the electron density of a streamer propagating in dry air. The voltage varies as function of time as: $V(t) = 30 \cdot (1 - \exp[-t\ (\text{ns})/40])$ kV. The value of the initial electron density has no influence on the calculated results for $n_{e0} < 10^{12}$ m^{-3}. As standard value $n_{e0} = 10^{11}$ m^{-3} has been adopted. At the moment when the streamer starts to propagate ($t_{inc} = 24$ ns) the streamer inception voltage V_{inc} is 14 kV. Note that this value is lower than the value that has been calculated with the Raether-Meek criterion, $V_{inc} = 17$ kV (Fig. 2.10 in **2.2.3**). Shortly after streamer formation, the electron density starts to grow in the whole gap to a value of $\sim 10^{13}$ m^{-3} because of the assumed photo-ionization mechanism. The electron density in the streamer head is initially 10^{20} m^{-3} and decreases by about a factor 3 before reaching the cathode. The maximum electric field in the streamer head reaches ~700 Td when it is at ~5 mm from the anode. When approaching the cathode, the electric field in the streamer head still reaches 500 Td. The electric field in the streamer channel is, except from the region close to the anode, in the range 20-40 Td thus close to the minimum in the attachment rate (Fig. 2.19). The streamer propagation velocity, initially $\sim 10^6$ m/s at the anode, slows down to about 30% of this value in the cathode region. The changes in the streamer velocity are thus more pronounced than the changes in the maximum value of E/n in the streamer head.

Fig. 2.22 shows the propagation of a streamer in a mixture consisting of 60% N_2 and 40% O_2. Initially, when the streamer head is close to the anode, the maximum electric field and the maximum electron density are comparable to data in air. However, during propagation to the cathode, the electric field and the electron density in the streamer head region decrease much stronger than in air. In this case, when the peak value of the electric field is below 400 Td, the streamer slows down and stops to propagate. Note that when streamer propagation stops, the maximum field strength in the streamer head is still larger than the critical field strength (110 Td). The differences with calculated data in air may partly be due to the influence of oxygen on the ionization rate (see Fig. 2.19). However, the main differences in the calculated electric field and electron density, when compared to the calculated data in air, are due to the decreased number of photo-ions in front of the streamer (see Fig. 2.20). The electric field in the streamer channel is close to values in air.

Fig. 2.23 shows results which have been calculated with code II. The voltage has been maintained constant (V=30 kV) and recombination and diffusion have been included. The maximum field strength in the streamer head region (~1500 Td) is about two times higher than the maximum field strength in streamers which have been simulated with code I. Also the density of electrons and the streamer

propagation velocity are higher. The streamer transit time (the time needed for the streamer to propagate from anode to cathode) is 50 ns using code I and it is 20 ns using code II. Repeated calculations showed that the significant differences between the results obtained with code I and code II can not be explained by the effect of rise time or by the inclusion of diffusion and recombination in code II. The inclusion of the diffusion term was found to have a negligible influence on the calculated results. Wang and Kunhardt (1990) modelling streamers in a uniform electric field in N_2 and Morrow (1991) modelling streamers in a non-uniform electric field in SF_6, arrived at the same conclusion.

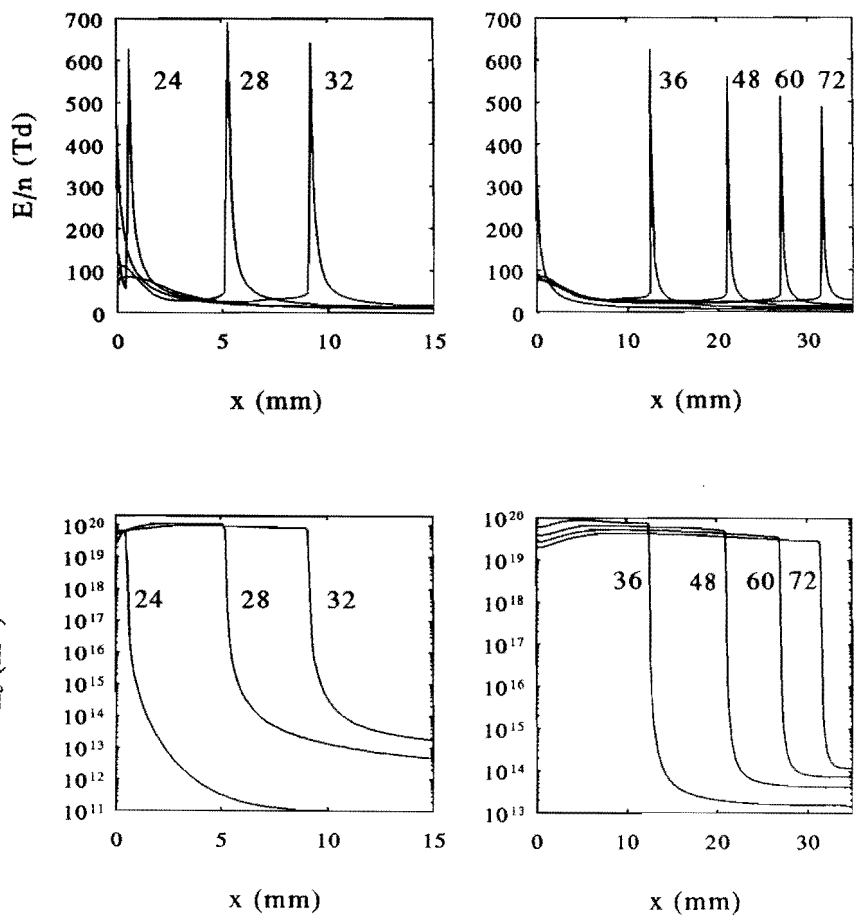

Fig. 2.21 Time evolution of the electric field E/n and the electron density n_e of a streamer propagating in dry air (80% N_2, 20% O_2), $V(t)=30 \cdot (1 - exp[-t(ns)/40])$, calculated with code I. Time is given in ns units.

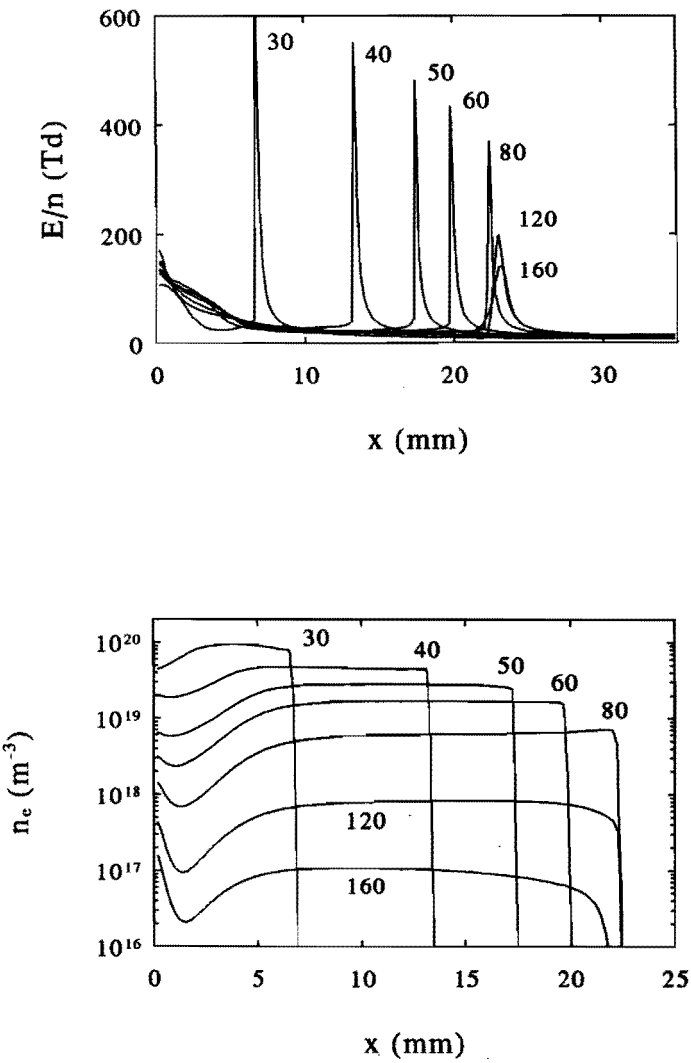

Fig. 2.22 Time evolution of the electric field E/n and the electron density n_e of a streamer propagating in a mixture consisting of 60% N_2 and 40% O_2, V(t)=30 · (1 - exp[-t (ns)/40]), calculated with code I. Time is given in ns units.

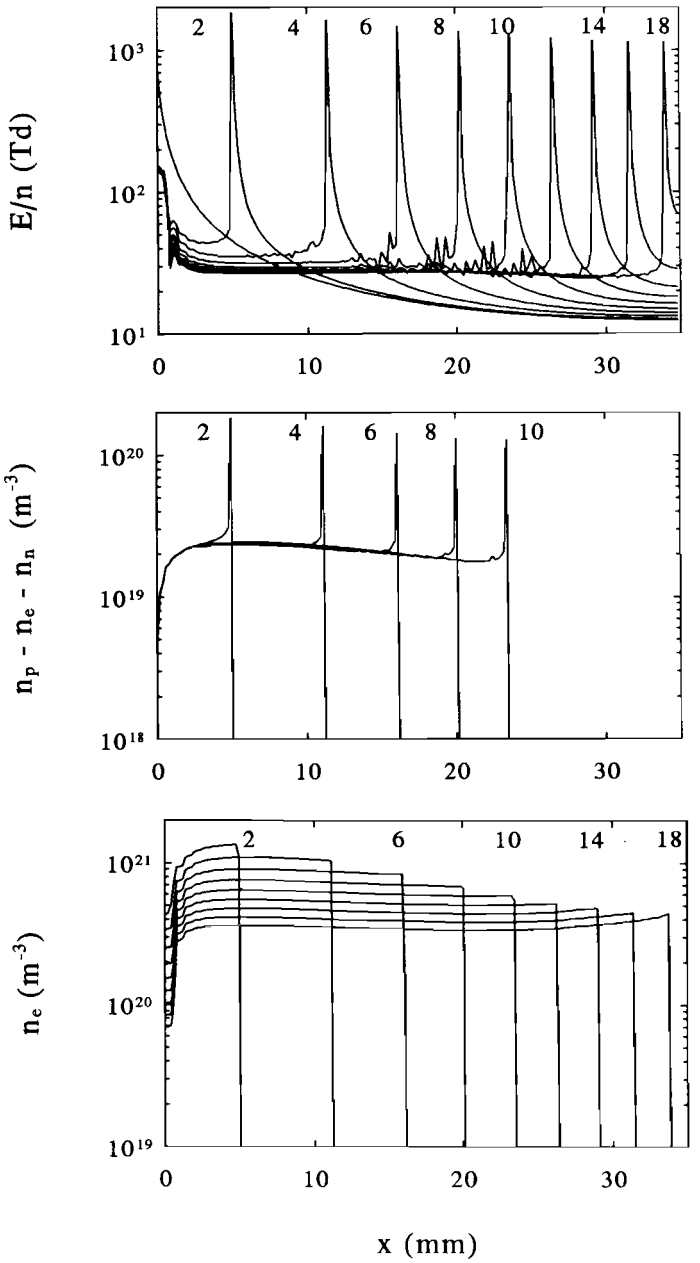

Fig. 2.23 Time evolution of the electric field E/n, the net positive charge density n_p - n_e - n_n and the electron density n_e of a streamer propagating in dry air (80% N_2, 20% O_2), V=30 kV, calculated with code II. Time is in ns units.

The streamer radius R_s is an essential model input parameter. Fig. 2.24 shows the influence of R_s on electric field and electron density distributions in the streamer head at 10 mm distance from the anode. When the streamer radius is made smaller, the electric field maximum increases but also the field gradient becomes steeper. At a distance larger than 0.1 mm from the streamer head the electric field is lowered with a smaller value of R_s. Similar changes appear in the electron density.

The streamer radius has also influence on the streamer velocity. With smaller streamer radius, the streamer velocity decreases: for R_s = 100, 50 and 25 μm, v_s = 0.9, 0.8 and 0.7 mm/ns. This decrease in streamer velocity is a consequence of the lower density of initial electrons in front of the streamer (at a distance larger than 0.1 mm from the position of the maximum electric field). It is interesting to recognize that the maximum drift velocity of electrons in the streamer head is inversely proportional to the streamer velocity: for R_s = 100, 50 and 25 μm, $w_{e,max}$ = 0.57, 0.77 and 0.91 mm/ns. Nevertheless, the maximum drift velocity and the streamer velocity are of the same order and approximately equal for R_s = 50 μm.

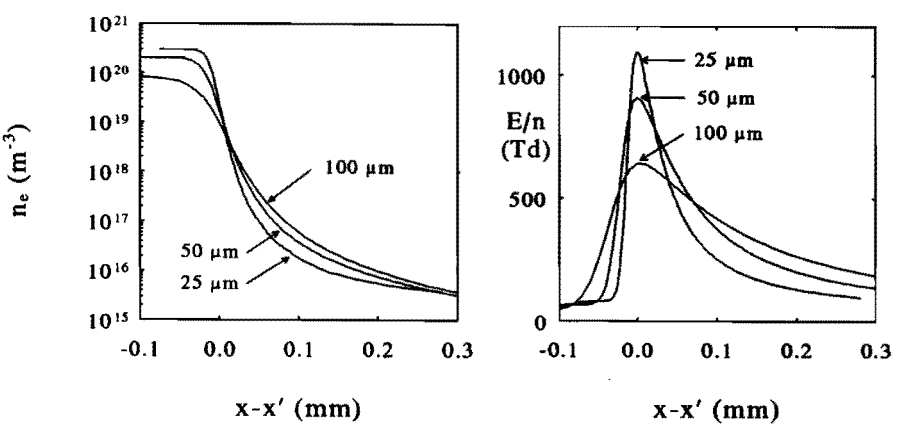

Fig. 2.24 Influence of the streamer radius R_s on the electric field and electron density distributions in the streamer head (streamer at 10 mm from anode, conditions similar to those used for Fig. 2.21).

The gradient of the electric field in front of the streamer head depends on the (three-dimensional) shape of the net positive charge distribution. Using Eq. 2.22, this field is calculated only in an approximate manner. As a result of this gradient, the growth of electrons in avalanches in front of the streamer head is higher than exponential. The gradient in the electric field with opposite sign, which exists at the boundary of the plasma region, is even much higher. When electrons arrive in this region, where the electric field drops down to a value which is far below the critical

field strength, their growth ceases abruptly. The high gradient of the electric field at the boundary of the plasma depends on the characteristic shielding length (Debye length) which in turn depends on the average electron energy or temperature ($\epsilon_a = kT_e$) and the electron density n_e as:

$$\lambda_D = \sqrt{\frac{\varepsilon_0 \, kT_e}{q_e^2 \, n_e}} \tag{2.40}$$

Typical values for the plasma boundary region in the streamer are: kT_e = 10 eV (at E/n=500 Td), $n_e = 10^{19}$ m^{-3} so that λ_D = 10 μm. As a result of the high gradient of the electric field, electrons may be out of local equilibrium. In order to verify the local equilibrium assumption the characteristic time of electric field changes τ_E, "seen" by an electron in the field E, is evaluated as:

$$\tau_E = E \cdot \left(\frac{\partial E}{\partial t}\right)^{-1} = \frac{E}{|v_s| + |w_e|} \cdot \left(\frac{\partial E}{\partial x}\right)^{-1} \tag{2.41}$$

where v_s and w_e are respectively the streamer velocity and the electron drift velocity. From the electric field and electron density distributions, which are shown in Fig. 2.24, it is possible to derive for R_s = 25 μm at E=1000 Td: $\partial E / \partial x$ = 4000 Td/mm. The characteristic time of electric field changes τ_E is according to Eq. 2.41 (v_s = 0.7 mm/ns, w_e=0.9 mm/ns): ~0.1 ns. For local equilibrium, the time τ_E is required to be large when compared to the time needed to obtain a steady state electron energy distribution function τ_{ss} (the energy relaxation time). Braun (1990) calculated the energy relaxation time in air with a Monte-Carlo method: τ_{ss} p = 0.01 ns. The local equilibrium assumption appears to be valid because the characteristic time of field changes is about a factor 10 larger than the energy relaxation time.

Calculation of measured streamer properties

Streamer properties have been calculated which can be compared with experiments (current, inception voltage, streamer velocity and light emission, see Chapter 5).The current which is caused by moving charges in a non-uniform geometric field can be calculated according to the Ramo-Shockley theorem of electrostatics (recently discussed by Wetzer and van der Laan, 1992):

$$i(t) = \sum_j \frac{q_j \, \boldsymbol{w}_j \cdot \boldsymbol{E}_g}{V} \tag{2.42}$$

where q_j and w_j are the charge and drift velocity of particle j, and E_g is the

geometric electric field. Note that the space charge electric field does not appear explicitly in the current expression: the space charge field influences the current only via the drift velocity w_j. Current pulses have been calculated with code I and code II, see Fig. 2.25. The higher streamer velocity calculated with code II causes a shorter rise time of the current. The characteristic (exponential) decay times calculated with code I and II are respectively ~21 ns and ~14 ns. The difference is mainly due to electron-ion recombination which was not included in code I.

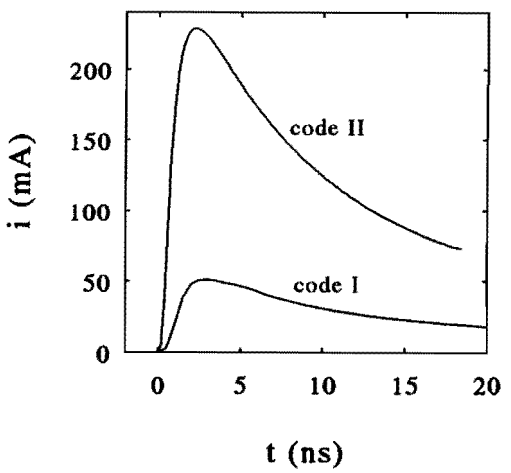

Fig. 2.25 Calculated streamer current pulses, conditions are similar to those used for Fig. 2.21 and 2.23.

The formative time lag of a streamer corresponds to the time needed for the formation of an electron avalanche with the critical number 10^8 (see **2.2.3**). Because of the finite time required for streamer formation, it is expected that the rate of rise of voltage influences the minimum streamer inception voltage. Fig. 2.26 shows calculated data of the streamer inception voltage as a function of V_m for different anode-radii. The voltage rate of rise has been been varied by changing the maximum voltage V_m at fixed rise time t_r. An increase of the voltage rate of rise by a factor 2 causes an increase in the minimum streamer inception voltage of about 2 kV.

Fig. 2.27 (a) shows calculated values of the streamer propagation velocity for different values of V_m in air. Fig. 2.27 (b) shows the influence of the relative oxygen concentration in a N_2-O_2 mixture. The streamer velocity increases with increasing voltage and it decreases with increasing oxygen concentration.

Calculated characteristics of the light emitted by streamers are presented in **4.2.5** of Chapter **4**. A further discussion of the calculated results of the numerical model is given in **2.4.4**.

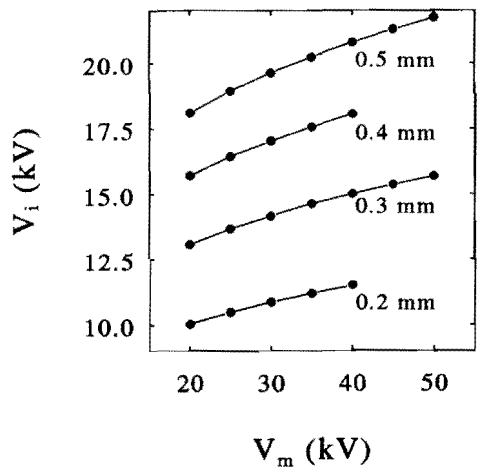

Fig. 2.26

The calculated influence of the anode-radius r_a and maximum voltage V_m on the streamer inception voltage, code I, dry air, $V(t) = V_m \cdot (1 - \exp[-t\ (ns)/100])$.

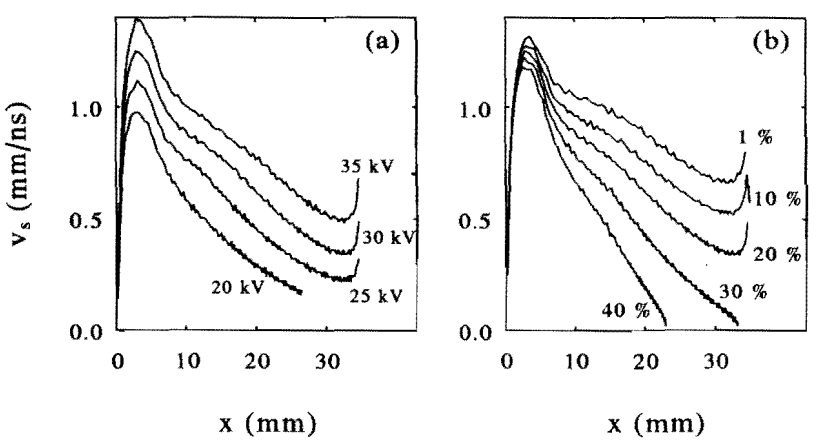

Fig. 2.27 *Streamer propagation velocity, calculated with code I,*
$V(t) = V_m \cdot (1 - \exp[-t\ (ns)/40])$,
(a) 80% N_2, 20% O_2, V_m=20, 25, 30 and 35 kV,
(b) V_m=25 kV, N_2-O_2 mixtures with $[O_2]$=1, 10, 20, 30 and 40%.

2.4 Stability field and secondary streamer

2.4.1 Stability field

On streak camera photographs of Wagner (1967) positive streamers are seen to propagate in an uniform electric field in air, even after switching off the voltage pulse. A similar effect has been observed by Marode applying a short HV pulse to a point-plate gap in air (in: Goldman and Goldman, 1978, p. 251). Apparently positive streamers are able to propagate in a zero electric field. At the same time, however, their propagation velocity decreases and their light emission weakens.

Phelps and Griffiths (1976) measured in a parallel-plate gap (90-120 mm) the minimum field required for propagation of positive streamers in air. Streamers were generated at a sharp pin, mounted coaxially in a circular hole of the plane anode. The field was non-uniform only close to the pin, in a very small part of the gap. Observations of streamers were made by eye in total darkness. Measurements were made of the minimum electric field needed for the most vigorous streamers to reach the cathode. Gradually increasing the voltage the onset of streamer crossing was observed to be quite abrupt indicating that a critical value for stable streamer propagation in air exists. This critical value has been referred to as *stability field* E_s by others (e.g. Gallimberti, 1979). Phelps and Griffiths (1976) measured E_s in air as a function of gas pressure and humidity but the data were not normalized to the neutral gas density. After normalization it appears that the reduced stability field $(E/n)_s$ increases linearly with n and also linearly with water vapour concentration (for n = 1 - 2.5·10^{25} m^{-3} and $[H_2O]$ = 0 - 10 %):

$$\frac{E_s}{n} = \left[20 + 12.5 \cdot \frac{n - n_0}{n_0} \right] \cdot (1 + [H_2O]/6) \quad (Td) \tag{2.43}$$

where $[H_2O]$ is the water vapour concentration in %. The stability field in dry atmospheric air (T = 293 K, $n = n_0$ = 2.5·10^{25} m^{-3}) is: E_s = 500 V/mm, $(E/n)_s$ = 20 Td. According to Eq. 2.43, $(E/n)_s$ increases by adding 10% water vapour to ~50 Td. Phelps and Griffiths found that the stability field in a 1 m gap is 5.5% higher than in a 90 mm gap. The weak dependence on gap distance and the linear dependence of E_s on humidity has recently been confirmed by Allen and Boutlendj (1991).

It is interesting to note that the empirical field strength for stable streamer propagation is close to the value of the electric field where the attachment frequency in dry and humid air possesses a local minimum (see Figs. 2.13, 2.17, 2.19). Moreover, the calculated electric field strength in the streamer channel (see

Figs. 2.21-2.23) appears to be also close to this value. The fact that the electric field strength in the streamer channel is a little below the value corresponding to the minimum of the net attachment frequency is essential for the spatial and temporal stability of this electric field. This can be argued as follows: the electric field in the streamer channel $(E/n)_{ch}$ depends on the local current density according to:

$$\left(\frac{E}{n}\right)_{ch} = \frac{j_e}{q_e\ \mu_e\ n_e\ n} \tag{2.44}$$

As a result of attachment, the electron density n_e will decrease and thus $(E/n)_{ch}$, according Eq. 2.44, will increase. This field increase causes, however, a decrease of the attachment rate ν_a so that the field $(E/n)_{ch}$ stabilizes at a value where the dependence of ν_a on E/n is weak, i.e. close to the value of E/n where ν_a has a minimum. On the other hand, if the electric field in the streamer channel exceeds the value of E/n where a minimum in ν_a exists, an initial increase of the electric field will lead to stronger attachment and thus to a further increase of the field. The instability which then follows is observed close to the anode in the calculated results of the numerical model (Fig. 2.21-2.23). This instability is also likely to occur in the *secondary streamer* which is seen in air as a partial re-illumination of the dark residual streamer channel after the primary streamer crossed the electrode gap, see **2.4.3.**

2.4.2 Analytical streamer model

The stability field plays an essential role in Gallimberti's (1972, 1979) analytical model for positive streamers in air. In this model, the electron avalanches which are formed continuously in front of the positively charged streamer tip are represented by a single equivalent electron avalanche, see Fig. 2.28.

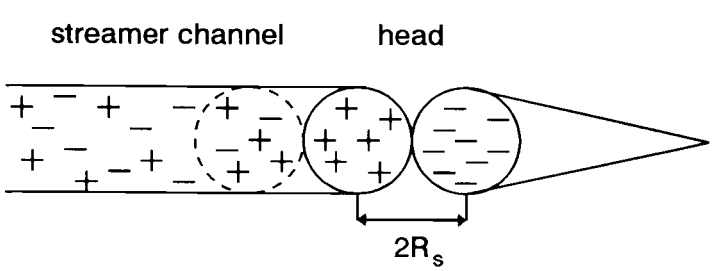

Fig. 2.28 Schematic representation of Gallimberti's (1972) analytical streamer model.

Similar to Meek's derivation of the criterion for streamer formation (see **2.1.2**), the concentrations of positive ions and electrons are represented by spherical regions with radius R_s. The propagation of the streamer head is described in steps $\Delta x = x_{i+1} - x_i = 2R_s$. The number of positive ions at x_i and t_n is equal to the number of electrons in the previous avalanche at x_i and t_{n-1}:

$$N_p(t_n, x_i) = N_e(t_{n-1}, x_i) \tag{2.45}$$

The number of positive ions in the streamer head region $N_p(x_i)$ is calculated by solving a simple energy balance equation. After each step $\Delta x = 2R_s$, the energy losses W_l (e.g. excitation and ionization) must be balanced by the gain of potential energy ΔW_{pot}:

$$\Delta W_{pot} = W_{pot}(x_{i+1}) - W_{pot}(x_i) = W_l \tag{2.46}$$

The potential energy consists of two terms:

$$W_{pot}(x_i) = q_e N_p(x_i) V_g(x_i) + \frac{\beta N_p(x_i)^2}{R_s} \tag{2.47}$$

$$with \quad \beta = \frac{0.5\, q_e^2}{4\pi\varepsilon_0}$$

V_g is the geometric potential. In Eq. 2.47 the first right hand term represents the potential energy of N_p positive ions in the geometric field, the second right hand term accounts for the intrinsic electrostatic energy of the ions due to their own space charge field. In Eq. 2.46 the energy loss term W_l is assumed proportional to the number of ions which has been produced after each step:

$$W_l = \gamma N_p(x_i) \tag{2.48}$$

Using Eqs. 2.47 and 2.48 the balance equation 2.46 can be written as:

$$q_e E_g \left[(N_p + \Delta N_p) \cdot (x + \Delta x) - N_p x \right] - \frac{\beta}{R_s} \left[(N_p + \Delta N_p)^2 - N_p^2 \right] = \gamma N_p \tag{2.49}$$

where $\Delta N_p = N_p(x_{i+1}) - N_p(x_i)$. Stability implies that N_p is independent on x, i.e. $\Delta N_p = 0$. Imposing this condition, the term which contains the coefficient β vanishes in the balance equation and one obtains an expression for the stability field $E_s = E_g(\Delta N_p = 0)$:

$$E_s = \frac{\gamma}{2q_e R_s} \tag{2.50}$$

Assuming $R_s \approx 50$ μm and using the empirical stability field value in dry air at $p = 1$ bar ($E_s = 500$ V/mm) the coefficient γ is according to Eq. 2.50 ~50 eV per positive ion. It is reasonable that γ is much larger than the ionization potential (15.6 eV for N_2) because it represents the total energy loss, per positive ion produced in the streamer head, including the energy loss due to excitation (vibrational and electronic) and dissociation. For $\Delta N_p \ll N_p$ Eq. 2.49 reduces to:

$$\Delta N_p = \frac{q_e R_s^2}{\beta} (E_g - E_s) \quad i.e.$$
$$\frac{\Delta N_p}{\Delta x} = \frac{\gamma}{4\beta} \frac{E_g - E_s}{E_s} \tag{2.51}$$

The number of positive ions in the streamer head region increases when $E_g > E_s$ and decreases when $E_g < E_s$. At constant applied voltage an analytical solution exists:

$$N_p(x) = N_p(0) + \frac{\gamma}{4\beta} \frac{[V - V_g(x) - E_s x]}{E_s} \tag{2.52}$$

where $N_p(0)$ is the initial number of ions at the anode when the streamer starts to propagate. A condition for the maximum streamer length is obtained from Eq. 2.52 assuming that the streamer continues to propagate until $N_p(x)$, after reaching a maximum, is reduced to its initial value $N_p(0)$:

$$V - V_g(x_{max}) - E_s x_{max} = 0 \tag{2.53}$$

The length of streamers not reaching the cathode, but stopping to propagate in the low geometric field region of a corona configuration, can be calculated assuming $V_g(x_{max}) \ll V$. Condition 2.53 states that the maximum streamer length is then approximately:

$$x_{max} \approx V/E_s \tag{2.54}$$

This expression is confirmed by observations of Nasser (1968) who used the Lichtenberg technique to visualize streamers in a positive pulsed corona discharge in point-plate geometry (see **2.2.2**). In dry air at 1 bar the maximum length of streamers increases linearly with voltage and the value of E_s derived from these experiments is ~480 kV/m (~19.2 Td).

Fig. 2.29 shows the calculated number of electrons and positive ions in the streamer head as a function of its distance to the anode, for typical conditions of experiments (presented in the following chapters). The initial number of electrons is, corresponding to the Raether-Meek criterion, assumed to be 10^8. As long as the streamer propagates in the region where $E_g > E_s$, the potential energy gained from the geometric field is larger than the energy losses due to electron-molecule collisions. The surplus of energy is stored in the form of an increasing number of charges in the head region. The stored potential energy is consumed during streamer propagation in the region of the gap where $E_g < E_s$. According to Eq. 2.53 the minimum voltage needed for a streamer to cross the gap is, under conditions of the example in Fig. 2.10, V=17.5 kV. This value is close to the minimum streamer inception voltage which according to the Raether-Meek criterion (Eq. 2.17) is ~17 kV. Thus the existence region for streamers not reaching the cathode is small for the geometric field conditions used in the calculations for Fig. 2.29.

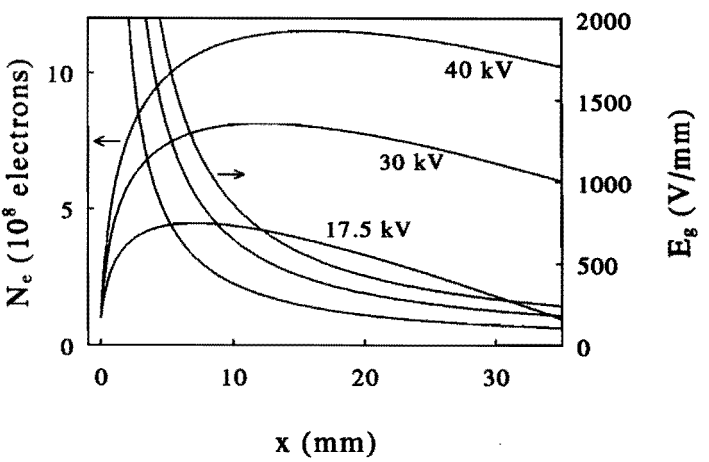

Fig. 2.29 The number of electrons in the streamer front calculated according to Eq. 2.51, wire-cylinder geometry with wire-radius r_w=0.3 mm, cylinder radius r_{cyl}=35 mm, $E_g(x) = V / ln[r_{cyl}/r_w] / x$.

According to Gallimberti (1987) the analytical streamer propagation model, that is based on energy conservation in the streamer head region, only applies in weakly electronegative gases. The condition for "weakly electronegative behaviour" is that the average free path of an electron before attachment λ_{att} is much larger than the characteristic dimension of the streamer head region δ_h:

$$\lambda_{att} = \frac{1}{\eta} > \delta_h \qquad (2.55)$$

The characteristic dimension of the streamer head δ_h is the size of the region where both n_e and E are close to their maximum values ($> \sim 10\%$ of the n_e and E maxima). When λ_{att} becomes comparable to the head size, the charge separation between the positive ions in the streamer head and the electrons drifting away in the streamer channel starts to be inhibited by the high attachment rate. In dry air δ_h is on the order of 10-50 μm and in the streamer channel (where $E/n \approx 20$ Td) $\lambda_{att} \approx 3$ mm thus the condition for applicability of this model (Eq. 2.55) is well satisfied.

Gallimberti (1987) shows by numerical calculations of positive streamers in air-SF_6 mixtures that the assumption of a stability field (the minimum geometric field required for stable streamer propagation) loses its validity in air-SF_6 mixtures with increasing SF_6 concentration. SF_6 is a strongly electronegative gas with a net attachment coefficient increasing monotonously with decreasing E/n (Gallagher et al., 1983). The effect of the addition of 1% SF_6 in weakly electronegative dry air is dramatic: the electric field in the streamer channel raises from ~20 Td to ~120 Td while the maximum value of the electric field in the streamer head region is reduced. When the percentage SF_6 in air is further increased toward pure SF_6 the field in the streamer channel increases to the critical field strength of SF_6: $(E/n)_{crit}$ = 360 Td. In air with 1% SF_6, E/n in the streamer channel reaches 120 Td and λ_{att} is ~0.5 mm, thus about 10 times larger than the streamer head size. In pure SF_6, E/n in the streamer channel is 360 Td and λ_{att} is ~10 μm, thus condition 2.55 is not satisfied.

2.4.3 The secondary streamer

Essential observations of the discharge phase following the primary streamer and preceding arc formation have been made in Loeb's laboratory (Hudson and Loeb, 1961; Loeb, 1965, p. 152-168) using a system of two photomultipliers to detect the light emitted by advancing streamers in a point-plate gap in air. The oscillograms clearly show that the primary positive streamer, propagating from the anode to the cathode, is followed by a second light emitting wave which also starts in the anode region but which propagates with lower speed and extends less far in the gap than the primary streamer. Hudson's measurements were probably the first obtained using an oscilloscope and photomultipliers with sufficient time resolution to separate light emission signals from primary and secondary streamers in time. Because the time-integrated emission intensity of the secondary streamer is often much higher than that of the primary streamer, in earlier investigations (where recording techniques with less sensitivity were applied) probably one *only* saw secondary streamers. Nasser, visualizing positive streamers of a pulsed corona discharge, showed that the range of potential over which streamers cross the gap

before causing a spark is remarkably large (Nasser and Loeb, 1963; Nasser, 1968). Marode (1972) used a streak camera to visualize primary and secondary streamers and also performed measurements of the discharge current during both phases. The maximum electron density in the residual streamer channel was estimated at $\sim 10^{21}$ m^{-3} by Bastien and Marode (1979) using measurements of Stark broadening of H_α and H_β emission lines. The most essential observations of the discharge phase following the arrival of primary positive streamers at the cathode are:

1) Primary streamer arrival does not obligatory lead to arc formation.
2) At voltages close to breakdown the fast growth of current, which is associated with arc formation, may start after the current through the residual channel of the primary streamer has decayed almost to zero (time delays between the primary streamer and arc formation up to ~1 ms are possible).

A step forward in modelling the streamer-to-arc transition has been made by Marode and Bastien (Marode et al., 1979; Bastien and Marode, 1985). According to their models, the main mechanism leading to spark formation and current growth, after the initial decay of the current through the residual channel, is the increase of E/n as a result of the decrease of the gas density n (gas heating). The model of Marode et al. (1979) is limited to a radial treatment of the discharge channel. Hydrodynamic equations are solved to show that the transfer of a small fraction (2-5%) of the dissipated energy to the thermal energy of the gas is sufficient to cause a cylindrical shock wave (at a short time scale of ~100 ns the main part of the dissipated energy is in the form of vibrational excited states of N_2). For a positive streamer with a current maximum of ~100 mA the maximum calculated decrease of the neutral density is ~10%. The model of Bastien and Marode (1985) describes properties of the residual streamer channel as a function of position along the central axis of the streamer. In this model the radial hydrodynamic expansion is represented by an analytical function in correspondence with the radial treatment of the streamer channel made by Marode et al. (1979).

In principle it is possible to extend the numerical model of the primary propagating streamer to the discharge phase after its arrival at the cathode, thus integrating the primary and secondary streamer in a single calculation. The results of the primary streamer model presented in Figs. 2.19, 2.20 and 2.21, clearly show that a domain with high electric field and low electron density is formed close to the anode before arrival of the primary streamer at the cathode. There is little doubt that secondary streamer propagation corresponds to the extension of such a high field domain when, after primary streamer arrival, the potential which is concentrated at the primary streamer head has been redistributed along the residual plasma channel.

Braun et al. (1992) developed a 2-D model for streamer development in a dielectric barrier discharge in air (1 mm plane parallel gap between the cathode and a dielectric covering the anode). Close to the anode, the positive streamer head possesses a radius (defined as the halfwidth of the radial electron density distribution) of about 100 μm. The calculations show in particular that in a very short time the high electric field region at the streamer head, when approaching the cathode, becomes very thin in axial direction and wider in radial direction, i.e. a cathode layer is formed. The maximum field strength is ~800 Td when the streamer is at small distance from the cathode. Only after ~0.1 ns the thin cathode layer with a maximum field strength of ~4000 Td and a thickness of ~10 μm is formed. Odrobina and Černák (1992, 1993), modelling the streamer-cathode interaction in a short positive point-plate gap in N_2, show that ions contribute significantly to the current during the cathode layer formation. By their calculations, current spikes which have been measured when positive streamers "make contact" with the cathode (Marode, 1972; Inoshima et al., 1990) are explained on the basis of ion drift without recourse to electron release at the cathode by field emission, photoionization or ion bombardment. This work exemplifies the considerable progress which has been made recently in the numerical modelling of the streamer-cathode interaction. However, a full model for the complete sequence of primary streamer propagation, cathode-layer formation and the secondary streamer phenomenon has probably not been published yet.

In the following the simple analytical streamer model of Gallimberti (1972) is extended with the calculation of the electric field and charged particle distributions in the streamer channel before as well as after arrival of the primary streamer at the cathode. The purpose of this model is to study the properties of the secondary streamer and to calculate the current and energy dissipation during the primary streamer propagation phase and during the subsequent discharge phase. The initial density of electrons formed in the gas where the streamer propagates is calculated by dividing N_e (Eq. 2.52) by the cell volume: $\Delta x\, \pi R_s^2 \approx 10^{-12}$ m^3 for R_s = 50 μm. The following assumptions are made:

1) The streamer velocity is proportional to the electron drift velocity at the maximum field strength and enough photo-electrons are produced in front of the streamer to guarantee its propagation.
2) The streamer channel is quasi-neutral (n_p - n_e - n_n = 0) and the decay of the charged particle densities in the streamer channel can be calculated neglecting drift and diffusion terms in the continuity equations (Eqs. 2.18 - 2.21).
3) After arrival of the positive streamer, the cathode plays the (passive) role of an electron source with a current density depending only on the properties of the residual streamer channel.

ad 1) The first assumption is in agreement with the results of the numerical streamer model presented in Fig. 2.24 which show that the majority of the electrons in the streamer head is produced in an electric field which is very close to the maximum electric field. The electrostatic potential of the streamer head is calculated as:

$$V_{sp} = \frac{N_p q_e}{4\pi\varepsilon_0 R_s} \tag{2.56}$$

In order to calculate the maximum field strength in the streamer head region it is possible to use the electric field expression for a charged sphere: $E_{sp}(x) = V R_s / x^2$. However, a better approximation is obtained by using an analytical expression for the electric field along the symmetry axis of a tip-plate configuration with a hemispherical shaped tip (see Eq. 3.3 in section **3.1**). This expression accounts for the influence of image charges in the plate electrode which significantly influence the electric field distribution when the streamer tip approaches the cathode plate electrode.

ad 2) The potential difference across the streamer channel is:

$$V_{ch} = V - V_{sp} - V_g(x_h) \tag{2.57}$$

where x_h is the position of the streamer head. According to numerical calculations of the formation of the cathode-layer which is formed after streamer arrival the potential drop in this layer is ~1 kV (Braun et al., 1992). Thus when the streamer head potential is much larger than 1 kV, it can be assumed that this potential is almost completely redistributed along the residual streamer channel. The current density in the streamer channel is assumed to be independent on the axial coordinate:

$$\frac{\partial j_e}{\partial x} = \frac{\partial (q_e n_e w_e)}{\partial x} = 0 \tag{2.58}$$

This assumption can generally be made in plasmas without high spatial gradients or temporal oscillations of the electric field strength. The numerical calculations of electric field distributions in the streamer channel (Fig. 2.21 - 2.23) show that the electric field in the streamer channel is remarkably constant in both space and time. There are no fast moving and high spatial gradients of the electric field as occur in the propagating streamer head.

The decay of the charged particle densities along the streamer channel can be calculated with sufficient small time steps Δt in first order approximation as:

$$\begin{aligned}
\Delta n_p &= \left(\alpha w_e n_e - \beta_{ei} n_e n_p - \beta_{ii} (n_n + n_m) n_p \right) \Delta t \\
\Delta n_n &= \left(\eta_2 w_e n_e - \beta_{ii} n_n n_p - \delta w_n n_n - \theta w_n n_n \right) \Delta t \\
\Delta n_m &= \left(\eta_3 w_e n_e - \beta_{ii} n_m n_p + \theta w_n n_n \right) \Delta t \\
n_e &= n_p - n_n - n_m
\end{aligned} \tag{2.59}$$

In this set of equations n_n represents unstable O^- formed by dissociative attachment and n_m stable O_2^- and $O_2^-(H_2O)_n$ ions formed by three-body attachment, charge transfer and clustering with water molecules. The coefficients α, η_3, η_2, β_{ei}, β_{ii}, representing ionization, two-body attachment, three-body attachment, electron-ion and ion-ion recombination, have been given in **2.3.3**. The coefficients θ and δ account for respectively ion conversion and detachment. The ion conversion coefficient in humid air is taken from the work on electron avalanches of Verhaart and van der Laan (1984):

$$\frac{\theta}{n} = (1 + 7 \cdot [H_2O]) \cdot 10^{-23} \quad (m^2) \tag{2.60}$$

where $[H_2O]$ is the absolute humidity in %. This expression is in agreement with experimental data of Wagner (1971) which have been used in calculations of Kline (1974), for $E/n = 100$ Td and $[H_2O] = 2\%$ ($\theta = 1.5 \cdot 10^{-22}$ m^2):

$$\frac{\theta}{n} = 9.1 \cdot 10^{-21} \exp\left(\frac{-405}{E/n} \right) \quad (m^2) \tag{2.61}$$

For the detachment coefficient an expression is used which fits the experimental data of Wagner (1971) and which has been applied before by Sigmond (1984):

$$\frac{\delta}{n} = 3.6 \cdot 10^{-18} \exp\left(\frac{-940}{E/n} \right) \quad (m^2) \tag{2.62}$$

Under the assumption of a constant current density in the streamer channel (Eq. 2.58):

$$V = \Delta x \sum_k E(x_k) = \Delta x \, j_e \sum_k \frac{1}{q_e \, \mu_e(x_k) \, n_e(x_k)} \tag{2.63}$$

Since the electron mobility depends weakly on E/n in comparison to n_e, for small time steps $\Delta t = t_n - t_{n-1}$ the electric field distribution can be recalculated from the electron density distribution at $t = t_n$ (calculated by Eqs. 2.59) as:

$$j_e(t_n) \approx \frac{V_{ch}}{\Delta x \sum_k \frac{1}{q_e\ \mu_e(x_k,t_{n-1})\ n_e(x_k,t_n)}} \tag{2.64}$$

$$E(x_i,t_n) \approx \frac{j_e(t_n)}{q_e\ \mu_e(x_i,t_{n-1})\ n_e(x_i,t_n)} \tag{2.65}$$

where subscripts i and k relate to space steps Δx and subscripts n to time steps Δt.

Gas heating and vibrational relaxation are described by the system of equations (Marode, 1985):

$$\begin{aligned} \frac{5}{2}\frac{kT_g}{dt} &= f_T\left(q_e n_e w_e \frac{E}{n}\right) + \frac{\varepsilon_v - \varepsilon_{v0}}{\tau_{VT}} \\ \frac{d\varepsilon_v}{dt} &= f_V\left(q_e n_e w_e \frac{E}{n}\right) - \frac{\varepsilon_v - \varepsilon_{v0}}{\tau_{VT}} \end{aligned} \tag{2.66}$$

(for molecules with 2 atoms the heat capacitance under constant volume is: $C_v = 5/2\ R = 5/2\ k\ N_A$). This first equation expresses the fact that the neutral gas is heated by direct energy transfer and delayed energy transfer from the vibrational energy reservoir. From the dissipated power (the term in between brackets) only a small fraction f_T is used for direct heating (momentum transfer, rotational excitation) and a much larger fraction f_V is used for vibrational excitation. The coefficients f_T and f_V have been determined from a solution of the Boltzmann equation for electron-molecule kinetics in dry air (Aleksandrov et al. 1981):

$$\begin{aligned} f_T &= \frac{1 + 0.02\ E/n}{1 + 0.4\ E/n} \\ f_E &= \frac{(E/n)^3}{4{\cdot}10^5 + (E/n)^3} \\ f_V &= 1 - f_T - f_E \end{aligned} \tag{2.67}$$

where f_E expresses the energy loss due to electronic excitation, dissociation and ionization. Because in air vibrational excitation of O_2 can be neglected when compared to vibrational excitation of N_2, the equilibrium value of the vibrational energy ϵ_{v0} can be expressed as:

$$\varepsilon_{v0} = \frac{\omega_v}{\exp(\omega_v/T_g) - 1} \tag{2.68}$$

where ω_v is the vibrational quantum of N_2 (ω_v=3360 K). Note that for low gas temperatures the equilibrium value of the vibrational energy is negligibly small (T_g < 450 K, ϵ_{v0} < 2K).

It is in general difficult to estimate the vibrational relaxation time constant τ_{VT}. The understanding of the detailed mechanism of vibrational relaxation in air requires a model taking into account both the vibrational-vibrational (VV) and vibrational-translational (VT) energy transfer involving a large number of vibrational excited states of both N_2 and O_2. In an electrical discharge in air, the situation is even more complicated because also the vibrational relaxation caused by collisions with dissociation fragments (*N*, *O*, *CO*) should also be taken into account (Mnatsakanyan and Naidis, 1986). However, when water vapour is present at a concentration higher than 0.1%, the dominant process for depopulation of the vibrational excited states of N_2 is VV energy transfer to H_2O followed by fast VT relaxation of H_2O (Finzi et al., 1977). Laser-induced fluorescence investigations of $N_2(v=1)$ de-excitation by H_2O yield: $\tau_{VT} \cdot p(H_2O)$ = 1-10 μs atm (Finzi et al., 1977; Bass and Hottman, 1980). In humid atmospheric air with ~2% water vapour the vibrational relaxation time is thus expected to be in the range 50-500 μs. Here we use τ_{VT}=100 μs as a standard condition.

The contributions of the electrons in the streamer head and the electrons in the streamer channel to the total current which the streamer induces in the external circuit are calculated separately:

$$i_h = \frac{q_e V_s N_e(x_h) E_g(x_h)}{V}$$

$$i_c = \frac{\pi R_s^2 \Delta x \, q_e \sum_j w_e(x_j) n_e(x_j) E_g(x_j)}{V} \tag{2.69}$$

Similar procedures for the calculation of distributions of the electric field and charge particle densities in the residual streamer channel as delineated above were followed by Sigmond (1984) and Bastien and Marode (1985). Sigmond (1984) started the calculation of the secondary streamer assuming initial constant charge distributions in the primary residual streamer channel. Bastien and Marode (1985) omitted the influence of recombination, detachment and ion conversion.

Model calculations have been performed using Eq. 2.52 to calculate the initial electron density in the streamer head, Eq. 2.59 to calculate the decay of charged

particles in the streamer channel and Eqs. 2.64 and 2.65 to calculate the electric field distribution in the streamer channel. The spatial step Δx was 100 μm (R_s=50 μm, γ=50 eV/ion) and the time step was during primary streamer propagation $\Delta t = \Delta x / v_s$ and after primary streamer transit Δt=2 ns. The model calculations have been applied to the same conditions as used in the numerical streamer model (wire-cylinder geometry with r_w=0.3 mm, r_{cyl}=35 mm, n=2.45·10^{25} m^{-3}, V=30 kV). Figs. 2.30 - 2.32 show results obtained with calculations where recombination, detachment and conversion (in dry air) have been included.

Fig. 2.30 (a) shows the electric field distribution in the gap before primary streamer crossing which happens at t=52 ns and Fig. 2.30 (b) shows the electric field distribution after this moment. The maximum field strength and the velocity of the primary streamer initially increase where $E_g > E_s$, decrease where $E_g < E_s$ and increase again when the streamer approaches the cathode. The final increase of the maximum field strength is entirely due to the influence of the streamer tip-cathode distance on the electrostatic field distribution (Eq. 3.3). The secondary streamer is clearly shown by the calculated results as a plateau where the electric field is constant in time and close to the critical value for ionization. This electric field plateau is separated from the low field domain in the residual primary streamer channel by a steep gradient. Shortly after primary streamer arrival at the cathode (at t=52 ns) the electric field increases everywhere in the gap except in the high field plateau. At t=60 ns the gradient of the electric field is less steep then before streamer arrival. Propagation of the secondary streamer corresponds to the extension of the high field plateau while the field in the low field domain decreases and the gradient separating the high and low field domains becomes steeper again.

Fig. 2.31 (a) shows the electron density n_e in the residual streamer channel. The low and high electron density domains correspond respectively to high and low electric field domains. The changes in the electron density as a function of time are dominated by two- and three-body attachment. Initially, also electron-positive recombination has a major effect. However, this effect is greatly offset by a depletion of positive ions by ion-ion recombination. The strong ion-ion recombination results in a negative ion density which is about an order of magnitude lower than the electron density. In dry air, detachment contributes considerably to the formation of free electrons. This is clearly demonstrated in Fig. 2.31 (b) showing that the addition of 2% H_2O to dry air results in a noticeable reduction of n_e.

Fig. 2.31 (c) and (d) show the O^- ion density (n_n) and the O_2^- ion density (n_m). Dissociative attachment, forming unstable negative O^- ions occurs in the secondary streamer but is almost absent in the primary streamer channel where negative ions are mainly stable O_2^-. Conversion of O^-, forming hydrated clusters like $O^-(H_2O)_n$, strongly suppresses detachment.

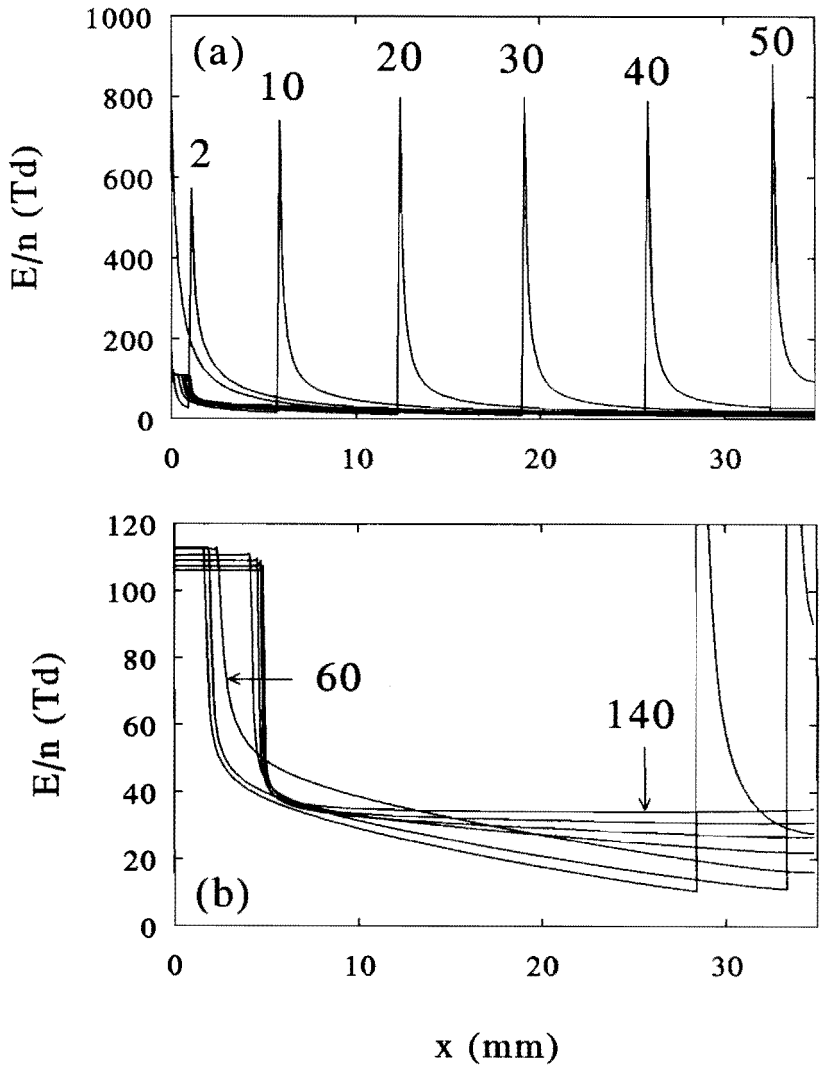

Fig. 2.30 Electric field distribution in (a) primary streamers and (b) secondary streamers (conditions: see text, time unit: ns).

Fig. 2.32 shows the time-dependence of the gas temperature and the vibrational temperature distributions in the gap. The calculated gas temperature increases by several tens of degrees while the increase of the vibrational temperature is much larger. In particular in the secondary streamer at $E/n = 100$ Td ($\epsilon = \sim 2.7$ eV) strong vibrational excitation is observed.

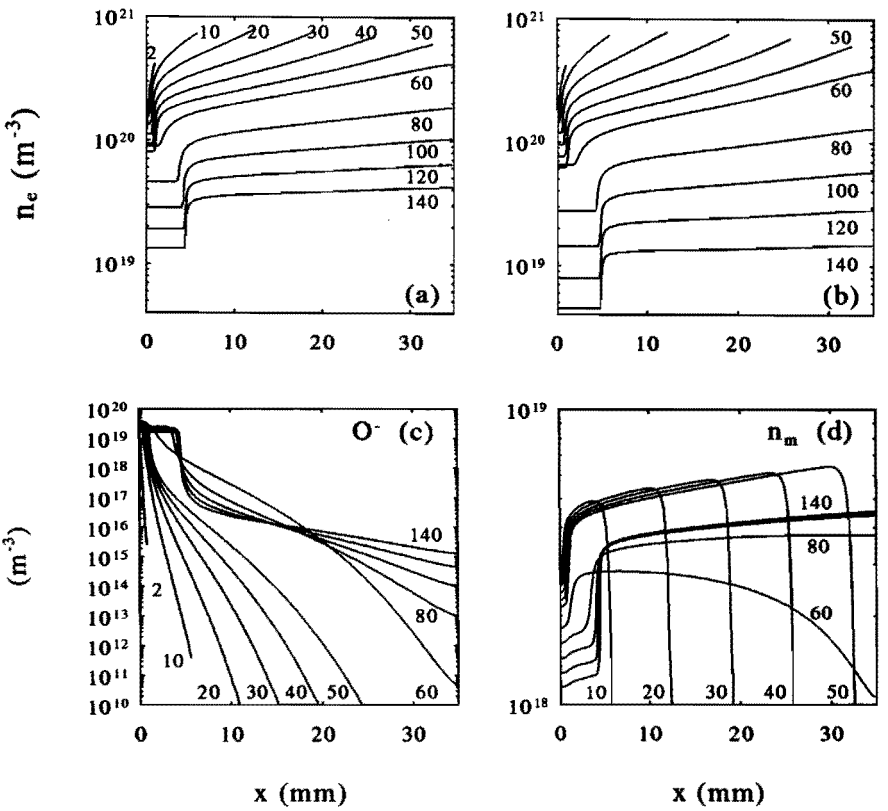

Fig. 2.31 Density distributions of (a) electrons in dry air, (b) electrons in air with 2% H_2O, (c) unstable negative ions and (d) the stable negative ions in dry air.

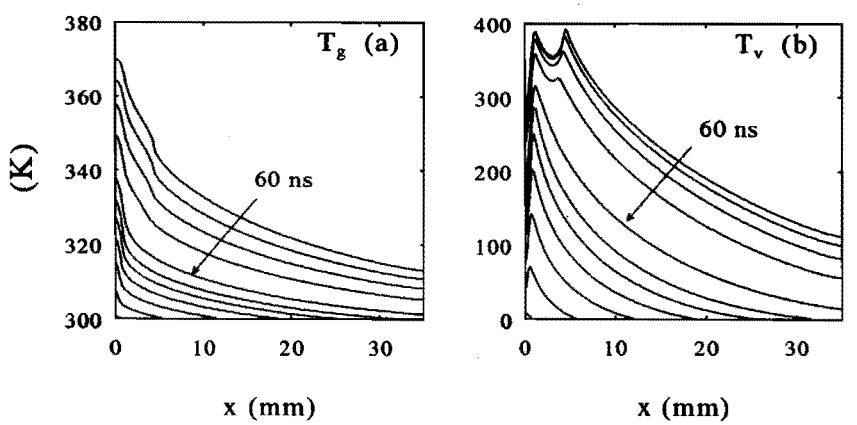

Fig. 2.32 Distribution of (a) gas temperature T_g and (b) vibrational temperature T_v

The calculated gas temperature may have been seriously underestimated because a part of the energy consumed in electronic excitation, dissociation and ionization (represented by the term f_E in Eq. 2.67) can be transferred to the gas in a time which is short compared to the typical duration of the discharge current pulse and also exothermal chemical reactions may cause significant gas heating. More accurate knowledge of the energy transfer to the translational energy of the heavy species in the gas by electronic de-excitation and molecular dissociation and chemical reactions is needed in order to include these processes in the energy balance equation (Eq. 2.66).

Fig. 2.33 shows calculated positive streamer corona current pulses for four different conditions:

1) Standard condition (also used for Fig. 2.30-2.32): dry air with constant gas density. Attachment, ion conversion and electron detachment are included.
2) Humid air with 2% H_2O (limiting detachment, see Eq. 2.60)
3) No recombination ($\beta_{ei} = \beta_{ii} = 0$)
4) Varying gas density: $n(t) = n_0 \cdot (1 - \exp[-t\ (\mu s)])$, $n_0 = 10^{25}$ m^{-3}

The vibrational energy is transferred to the gas after a time of the order of 100 μs (τ_{VT}). Thus vibrational relaxation is not expected to influence much on E/n during the discharge current pulse with a typical width of 200 ns. Condition (4) has been used in order to investigate the influence of a much larger increase of the gas temperature on the current. A large increase in gas temperature will cause a radially propagating shock wave with a typical time constant of ~1 μs (R_s divided by the sound velocity).

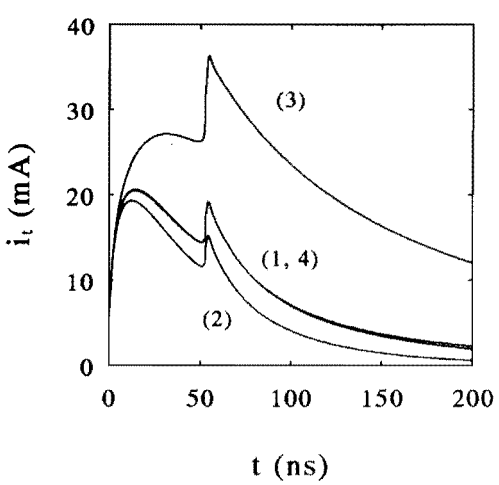

Fig. 2.33 Streamer-induced current pulses, for conditions see text.

The calculated current pulses show a peak immediately after the moment of primary streamer arrival which is due to the redistribution of the potential of the streamer head along the streamer channel. It appears that neglecting recombination causes a higher and much longer current pulse and that suppressing detachment by conversion to stable hydrated ions causes a current which is significantly lower.

Fig. 2.34 shows the total energy dissipated in the streamer as a function of time and the relative contribution of the electrons in the streamer head region E_h/E_t (estimated according to Eq. 2.69 under standard conditions). From an initial value of 100%, the contribution of the electrons in the streamer head decreases very rapidly. At t=25, 50, 100 and 200 ns, E_h/E_t is respectively 11, 7.4, 4.5 and 3.6%.

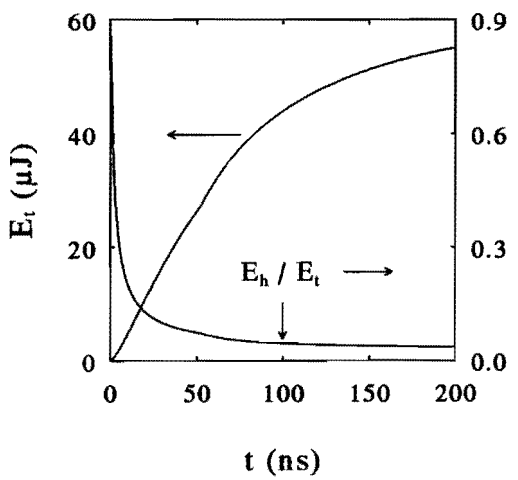

Fig. 2.34 Energy dissipation in the streamer and the relative contribution of electrons in the streamer head region to the total dissipated energy E_h/E_t

2.4.4 Discussion of streamer models

The numerical model for the primary streamer, presented in **2.3**, offers insight in the electric field and charged particle density distributions in the propagating primary streamer front and the residual primary streamer channel, a possibility which the simple analytical model presented in **2.4.2** misses completely. However, because of the considerable differences in the electric field and charged particle density distributions calculated by the different codes (see **2.3.4**), a further check of the numerical procedures is necessary. Because diffusion appears to have a negligible effect on the calculated results, in future numerical calculations a faster implicit FCT algorithm can be used (Steinle and Morrow, 1989).

The main characteristics of positive streamers in dry air, which were predicted by the numerical calculations, are:

1) The primary streamer consists of three separate regions. (a) The streamer head is a region where ionization dominates all other electron gain and loss processes (attachment, detachment, recombination etc.) and where large gradients in the electric field and charged particle densities occur. The characteristic size of the region where both the electric field and the electron density are close to maximum values is very small (~10 μm). (b) The primary streamer channel is a region where attachment and recombination dominate ionization and where the electric field stabilizes at the value where the net attachment frequency possesses a minimum. (c) Close to the anode, an attachment instability causes a region with a comparatively moderate electric field (close to the critical value) and low electron density.
2) The emission intensity and the absorption of photoionizing radiation, providing initial electrons in front of the streamer, strongly influences streamer propagation. This is clearly demonstrated by the simulations of streamer propagation in N_2-O_2 mixtures where a high O_2 concentration may even inhibit streamer propagation in the mid-gap region.

The analytical primary streamer model for air (Gallimberti, 1972) appears to be in reasonable agreement with the numerical results obtained with code I (**2.3.4**): The electron density is in the range 10^{20}-10^{21} m^{-3}, the calculated maximum field strength is in the range 500-1000 Td and the electric field in the streamer channel is close to the stability field: 20-40 Td. In agreement with the analytical model, also the numerical model shows that the charged particle density increases as long as $E_g > E_s$. According to the numerical results obtained with code I with $V_m = 30$ kV and $t_r = 40$ ns (see Figs. 2.21 and 2.27), the charge density, the electric field strength and the propagation velocity of the streamer head reach a maximum at $t = 28$ ns after the start of the voltage pulse and at $x = 5$ mm distance from the anode. At this moment the applied (time-varying) potential is ~15 kV and the geometric field at $x = 5$ mm is ~25 Td. Thus both the numerical and the analytical models clearly demonstrate that the charge density, the electric field and the propagation velocity of the primary propagating positive streamer head increase as long the local geometric (applied) field is higher than the stability field value. Both models also demonstrate that positive streamers can propagate in an electric field which is far below the stability field but with decreasing charge density and velocity.

Extending the analytical streamer model with a simple set of equations which correlate the electric field distribution to the local channel resistivity, it appears to be possible to simulate the secondary streamer phenomenon. According to the calculations, the residual streamer channel is divided into two domains separated

by high gradients of the electric field and the electron density. According to the adopted model, the secondary streamer corresponds to a domain where the electric field is close to the ionization threshold $(E/n)_{crit}$ and where the electron density is comparatively low. In the other part of the residual primary streamer channel the electric field is close to the stability field strength $(E/n)_s$ and the electron density is comparatively high. The length of the secondary streamer l_s is thus determined by:

$$l_s = \frac{V/n - (E/n)_s\, d_g}{(E/n)_{crit} - (E/n)_s} \tag{2.70}$$

The extended analytical streamer model can be used to investigate the influence of basic discharge parameters (coefficients for ionization, attachment, detachment, ion conversion and recombination) on energy dissipation. Electron-positive ion and ion-ion recombination have a major effect on the peak value and the duration of the current pulse. In the presence of 2% water vapour, the effect of detachment is negligible and during the discharge current pulse gas heating by vibrational relaxation plays a minor role because of the comparatively long vibrational relaxation time.

The models for simulation of the primary and secondary streamer possess uncertain input parameters which have been varied in order to obtain optimum agreement between experimental and measured streamer properties. In the numerical model (using $R_s = 100$ μm) the intensity of photoionizing radiation (the factor $f_q\ \omega/\alpha$ in Eq. 2.39) has been varied to fit calculated streamer velocities with measured data (see section **5.3.2**). In the analytical streamer model, the streamer radius R_s (and thus via Eq. 2.50 the energy loss per ion γ) has been adapted to fit calculated and measured streamer velocities (a proper fit has been obtained with $R_s = 50$ μm). A more detailed understanding of the specific mechanism of photo-ionization in positive streamers is desirable. In order to check the quasi-one dimensional electric field approximation (Eq. 2.23), the one-dimensional numerical primary streamer model should be compared with 2-D modelling results. A 2-D model has been realized recently by Kennedy and Wetzer (1994).

In both the primary propagating streamer head and in the secondary streamer, the electric field is high enough for the production of chemical reactive dissociation fragments. Some of the various chemical processes which are possible will be discussed in **2.5**.

Although the calculations of streamer formation and propagation have been limited to (humid) air and N_2-O_2 mixtures, it is possible to discuss qualitatively the influence of the other gas components of flue gases (CO_2 and H_2O) on streamers. Because both CO_2 and H_2O contribute to attachment, these gases tend to reduce the height of the current pulse. In dry air, coal combustion gas (6% H_2O) and in

humid air (10% H_2O), the net attachment frequency (which was calculated by M. Yousfi solving the Boltzmann equation, see Fig. 2.17) possesses a local minimum at respectively ~20, ~40 and ~50 Td. Thus in flue gas and humid air the electric field in the streamer channel is expected to be higher than in dry air and consequently the maximum length of primary streamers will be less than in dry air. It is possible to predict the maximum length of the secondary streamer using Eq. 2.70. In dry air, flue gas B and humid air, where $(E/n)_{crit}$ is respectively ~110, ~115 and ~135 Td, the maximum length of the secondary streamer in a 35 mm gap with V=45 kV is respectively 12, 5 and 0.6 mm.

Experimental investigations of photo-ionizing radiation by Przybylski (1962) and Teich (1967) indicate that the range of the radiation is much influenced by the gases H_2O and CO_2 (see **2.1.3**). However, no sufficient quantitative data for the absorption of photo-ionizing radiation in these particular gases are available to incorporate their influence in the numerical model.

Gas heating influences the time-to-breakdown (increase of E/n by decrease of n) and chemical reaction rates. It is difficult to estimate even qualitatively the effect of CO_2 and H_2O on gas heating. The presence of these gases will limit energy dissipation because of attachment (both 3-body and 2-body) but on the other hand these gases possess large cross sections for elastic scattering and rotational excitation favouring the direct transfer of electron energy to the gas. In addition, the presence of H_2O will reduce the vibrational relaxation time thereby increasing the rate of gas heating after the primary streamer phase.

An experimental investigation of the validity of the streamer models is desirable and possible. Although no experimental methods with sufficient spatial and time resolution are available to check the very large spatial and temporal gradients in the streamer head region, optical methods (presented in Chapter **4**) can been applied to measure integral quantities such as the average streamer velocity (integrating streamer propagation over a small distance) and the time- and spatial integrated light emission intensity of the streamer head.

2.5 Chemical kinetics

In this section we will first present the results of the calculation of initial densities of chemical reactive dissociation products by means of the numerical streamer model. Then we will discuss some of the results obtained by Alekseev et al. (1993) who realized a numerical model for streamer-induced chemical kinetics. Finally we will compare the time scales of the various physical and chemical processes which are likely to play a role in the pulsed corona $deNO_x$ process.

Calculation of initial densities of chemical reactive dissociation products

The local densities of chemical reactive products n_r formed by electron impact dissociation of molecules with density n_h can be calculated by:

$$n_r(t) = \int_0^t n_h \, n_e[t'] \, k(E/n[t'])dt' \tag{2.71}$$

where $k(E/n)$ is the rate coefficient which can be calculated from the solution of the Boltzmann equation $f(E/n, \epsilon)$ and the appropriate cross sections according to Eq. 2.30. Cross sections for dissociative ionization of H_2O and CO_2 have been taken from Orient and Srivastava (1987), for dissociative attachment from Melton (1972) and all other cross sections have been taken from the data compilations of Kieffer (1973), Phelps (1985) and Phelps and Pitchford (1985). Fig. 2.35 shows cross sections for dissociative attachment of O_2, CO_2 and H_2O and for dissociative ionization of H_2O.

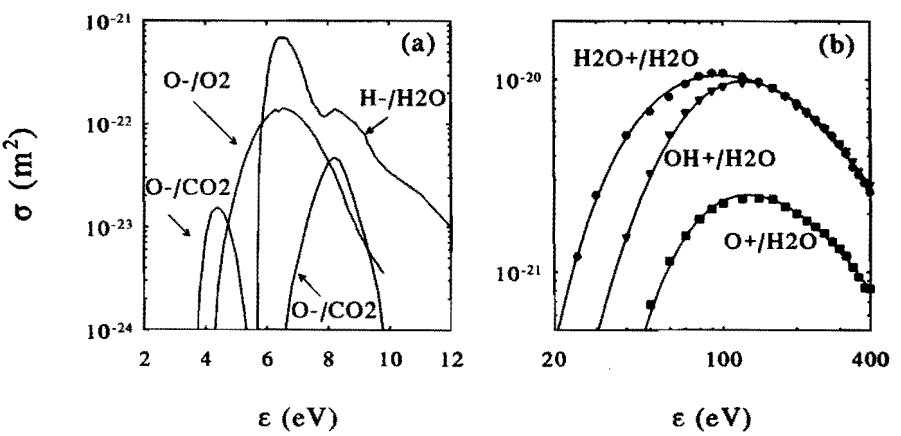

Fig. 2.35 Cross sections for (a) dissociative attachment of O_2, CO_2 and H_2O (compiled by Kieffer, 1973) and (b) dissociative ionization of H_2O (Orient and Srivastava, 1987).

The energy thresholds of cross sections for dissociative attachment are significantly lower than those for dissociative ionization. As a consequence, direct electron-impact dissociation in the secondary streamer will be mainly due to dissociative attachment and in the primary streamer head dissociative ionization will be dominant. In the residual primary streamer channel where $E/n \approx (E/n)_s$ the average electron energy is too low for direct electron impact dissociation.

Fig. 2.36 shows rate coefficients for excitation, dissociation, dissociative attachment and dissociative ionization (the symbols used to indicate ions are explained in Table 2.3).

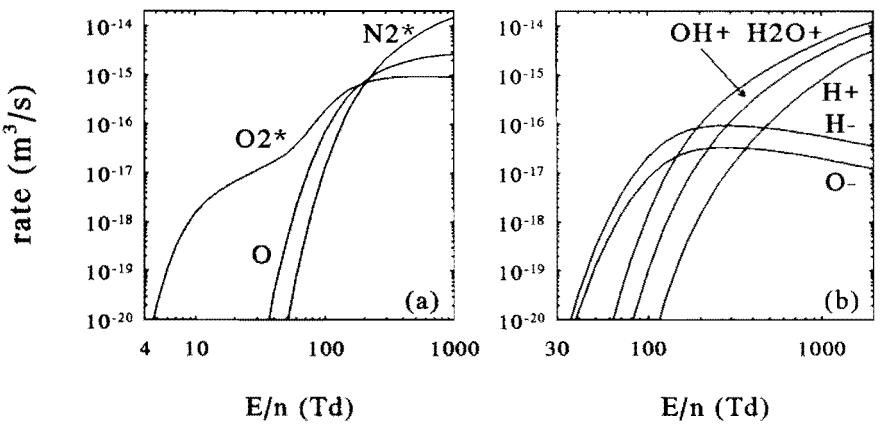

Fig. 2.36 Rate coefficients for (a) excitation, dissociation and dissociative attachment calculated using the solution of the Boltzmann equation by Yousfi (1993).

The following calculations of the concentrations of chemical reactive products in the neutral gas are limited to the effect of the primary streamer head. The calculations have been performed for primary streamers at 10 mm from the anode under three conditions using the different numerical codes I and II (with results presented in respectively Figs. 2.21 and 2.23) and two different values for the streamer radius R_s (see Table 2.3). Because the numerical models of the primary streamer have not yet been applied to flue gas, it has been assumed that the results obtained with the electron transport coefficients of dry air also apply to flue gas. This assumption is justified because:

1) The properties of the streamer head depend almost exclusively on the effective ionization frequency (at high E/n the effective ionization frequency is almost the same in air and flue gas) and on the generation of initial electrons in front of the streamer (which can not be calculated in flue gas with high accuracy because of the lack of photo-ionization data for CO_2 and H_2O).

2) The differences in gas composition between air and flue gas cause less differences in the properties of the streamer head than uncertain model input parameters like the streamer radius R_s and numerical approximations (differences between codes I and II).

An example of concentrations of excited states and ions as a function of time when the primary streamer propagates through the gas is given in Fig. 2.37. The time $t=0$ corresponds to the moment when the E/n reaches its maximum (also indicated in Table 2.3). The characteristic time of the streamer head (the time during which the neutral gas is "exposed" to both high E/n and high n_e) is short (~0.1 ns) compared to the characteristic times of many chemical reactions. The effects of these reactions can thus be studied by numerical modelling of their kinetics assuming a "step increase in time" of the initial reactive ions, radicals and excited states.

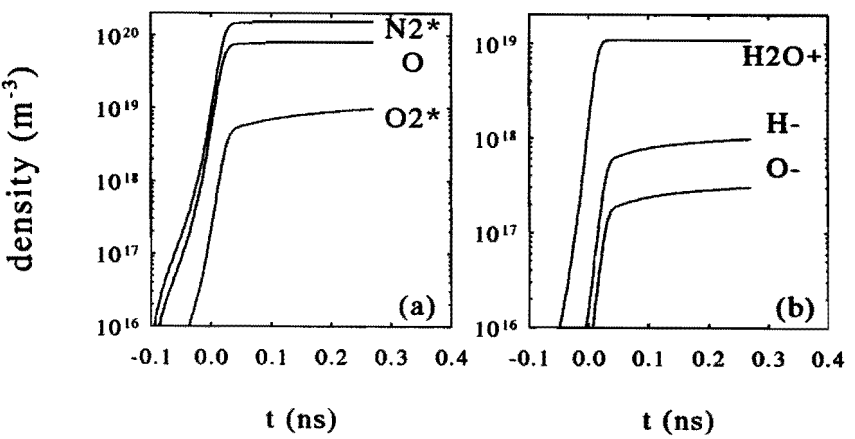

Fig. 2.37 The build-up of chemical reactive dissociation fragments in the neutral gas by a passing primary streamer at 10 mm from the anode (flue gas B, code I, R_s=25 μm). The time t=0 corresponds to the moment when E/n reaches its maximum.

The assumed streamer radius strongly influences the calculated concentrations which have been displayed in Table 2.3. In the case of code I and R_s=25 μm, the calculated electron density and the densities of all dissociation products all considerably higher than in the case of R_s=100 μm. The difference is due to (a) the higher electron energy and (b) the lower streamer velocity (the gas is exposed to high n_e and E/n during a longer time). It is evident that the accuracy of the calculation of concentrations of chemical reactive products is strongly limited by the rough approximation of the electric field in the one-dimensional streamer model. Nevertheless, the calculated results can be used for an evaluation of the main dissociation products and the influence of the field strength on relative concentrations can be investigated. Apart from ions, a relative high concentration is reached by the metastable excited state $N_2(A^3\Sigma_u^+)$.

code		I	I	II
R_s (μm)		100	25	100
$(E/n)_{max}$ (Td)		640	1100	1630
v_s (mm/ns)		0.9	0.7	2.8
n_e (m^{-3})		$1.0 \cdot 10^{20}$	$4.3 \cdot 10^{20}$	$1.1 \cdot 10^{21}$
Ionization				
$e + N_2 \rightarrow N_2^+ + 2e$	N2+	$7.0 \cdot 10^{19}$	$2.6 \cdot 10^{20}$	$6.0 \cdot 10^{20}$
$e + N_2 \rightarrow N^+ + N + 2e$	N+/N	$1.6 \cdot 10^{18}$	$1.1 \cdot 10^{19}$	$4.2 \cdot 10^{19}$
$e + O_2 \rightarrow O_2^+ + 2e$	O2+	$6.3 \cdot 10^{18}$	$2.1 \cdot 10^{19}$	$4.6 \cdot 10^{19}$
$e + O_2 \rightarrow O^+ + O + 2e$	O+/O	$3.9 \cdot 10^{17}$	$2.1 \cdot 10^{18}$	$6.5 \cdot 10^{18}$
$e + H_2O \rightarrow H_2O^+ + 2e$	H2O+	$3.1 \cdot 10^{18}$	$1.1 \cdot 10^{19}$	$2.6 \cdot 10^{19}$
$e + H_2O \rightarrow OH^+ + H + 2e$	OH+/H	$1.3 \cdot 10^{18}$	$5.6 \cdot 10^{18}$	$1.5 \cdot 10^{19}$
$e + H_2O \rightarrow H^+ + OH + 2e$	H+/OH	$2.4 \cdot 10^{17}$	$1.4 \cdot 10^{18}$	$5.0 \cdot 10^{18}$
$e + H_2O \rightarrow O^+ + H_2 + 2e$	O+/H2	$2.8 \cdot 10^{16}$	$2.3 \cdot 10^{17}$	$9.1 \cdot 10^{17}$
$e + CO_2 \rightarrow CO_2^+ + 2e$	CO2+	$2.1 \cdot 10^{19}$	$7.4 \cdot 10^{19}$	$1.7 \cdot 10^{20}$
$e + CO_2 \rightarrow CO^+ + O + 2e$	CO+/O	$6.0 \cdot 10^{17}$	$2.4 \cdot 10^{18}$	$6.1 \cdot 10^{18}$
$e + CO_2 \rightarrow O^+ + CO + 2e$	O+/CO	$6.2 \cdot 10^{17}$	$3.0 \cdot 10^{18}$	$8.2 \cdot 10^{18}$
$e + CO_2 \rightarrow C^+ + O_2 + 2e$	C+/O_2	$4.7 \cdot 10^{16}$	$3.3 \cdot 10^{17}$	$1.2 \cdot 10^{18}$
Dissociative attachment (and dissociation)				
$e + O_2 \rightarrow O^- + O$	O-/O	$1.1 \cdot 10^{17}$	$2.9 \cdot 10^{17}$	$1.6 \cdot 10^{17}$
$e + CO_2 \rightarrow O^- + CO$	O-/CO	$7.4 \cdot 10^{16}$	$1.8 \cdot 10^{17}$	$1.1 \cdot 10^{17}$
$e + H_2O \rightarrow H^- + OH$	H-/OH	$3.7 \cdot 10^{17}$	$9.5 \cdot 10^{17}$	$5.3 \cdot 10^{17}$
$e + H_2O \rightarrow O^- + H_2$	O-/H2	$6.9 \cdot 10^{16}$	$1.4 \cdot 10^{17}$	$1.1 \cdot 10^{17}$
$e + H_2O \rightarrow OH^- + H$	OH-/H	$1.5 \cdot 10^{16}$	$3.5 \cdot 10^{16}$	$2.3 \cdot 10^{16}$
$e + O_2 \rightarrow 2O$	O	$3.6 \cdot 10^{19}$	$8.1 \cdot 10^{19}$	$1.0 \cdot 10^{20}$
Excitation				
$e + N_2 \rightarrow N_2(A^3\Sigma_u^+) + e$	N2*	$7.3 \cdot 10^{19}$	$1.6 \cdot 10^{20}$	$1.8 \cdot 10^{20}$
$e + O_2 \rightarrow O_2(a^1\Delta_g) + e$	O2*	$3.9 \cdot 10^{18}$	$9.1 \cdot 10^{18}$	$7.6 \cdot 10^{18}$

Table 2.3 Calculated initial concentrations of dissociation fragments in flue gas B.

In chemical kinetics studies of ozone generation in air, this metastable is the primary source of oxygen radicals(see e.g. Braun, 1992). Note that in the case of code I and R_s=100 μm, dissociative ionization and dissociative attachment contribute about equally to *OH* formation whereas in the case of code II and R_s=25 μm the contribution of dissociative ionization is about 10 times higher. Also the electron and ion densities in the streamer calculated by code II are about a factor 10 higher than the densities calculated by code I. Note that the considerably higher electric field strength calculated by code II causes higher densities of chemical reactive dissociation products in spite of the higher streamer velocity (short "exposure time" of the gas to high E/n and n_e).

Calculation of streamer-induced chemical kinetics

Calculations of streamer-induced chemical kinetics have been performed by Alekseev et al. (1993) for various conditions using the same set of rate coefficients as previously used by Mätzing (~700 reactions, see **1.5.2** and references therein). Fig. 2.38 shows results obtained by calculations using the typical composition of flue gas formed by natural gas combustion (71% N_2, 16% H_2O, 5% O_2, 8% CO_2, 400 ppm *NO* and 1000 ppm SO_2). Initial conditions of chemical reactive dissociation products have been calculated with code II, wire-cylinder corona gap, V=40 kV, R_s=100 μm, T_g=400 K (see Alekseev et al., 1993, p. 24).

Fig. 2.38 (a) shows the concentrations of some essential oxydizing radicals. *OH* formation by direct-electron impact dissociative ionization and dissociative attachment appears to be relatively unimportant when compared to indirect processes. HO_2 and O_3 are formed some time after the formation of the primary dissociation products in the discharge and are destroyed in oxydation reactions within 10^{-4} - 10^{-2} s.

Fig. 2.38 (b) shows the concentrations of the nitrogen and sulphur oxydes and oxydation products (acids) as a function of time. These results have been obtained assuming a temperature increase of the neutral gas from 400 to 630 K (with τ_{VT}=100 μs). Under constant temperature (T_g=400 K) the *NO* concentration decreases from 400 ppm to 300 ppm while 55 ppm NO_2 is formed (25% *NO* removal, 11% NO_x removal). With increasing temperature (T_g increases from 400 to 630 K) *NO* decreases from 400 to 340 ppm while 20 ppm NO_2 is formed (15% *NO* removal, 10% NO_x removal). Thus the increase of temperature appears to have little effect on the NO_x removal. The calculations indicate inadequate SO_2 removal. At constant temperature (400 K) the SO_2 concentration decreases from 1000 ppm to 975 ppm (only 2.5% is oxydized).

(1) *OH*
(2) *H*
(3) *O*
(4) HO_2
(5) O_3
(6) *N*

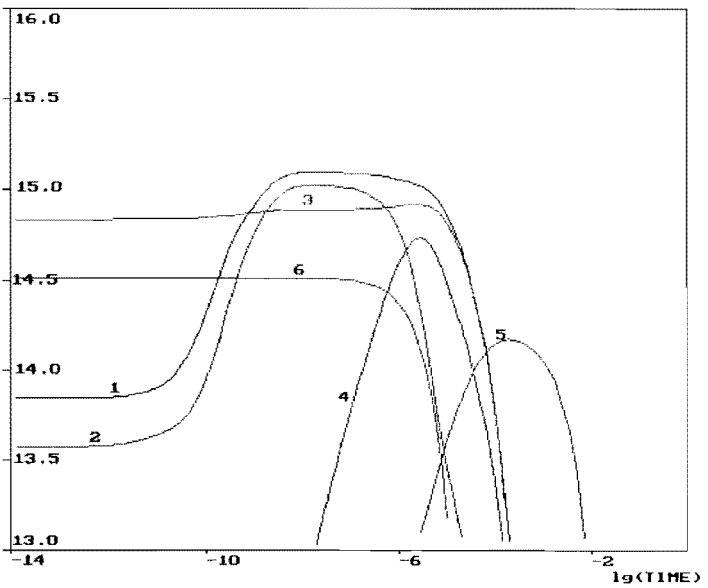

(a) Constant temperature (400 K)

(1) O_3
(2) NO_2
(3) HNO_2
(4) HNO_3
(5) H_2SO_4
(6) *T*
(7) SO_2
(8) *NO*

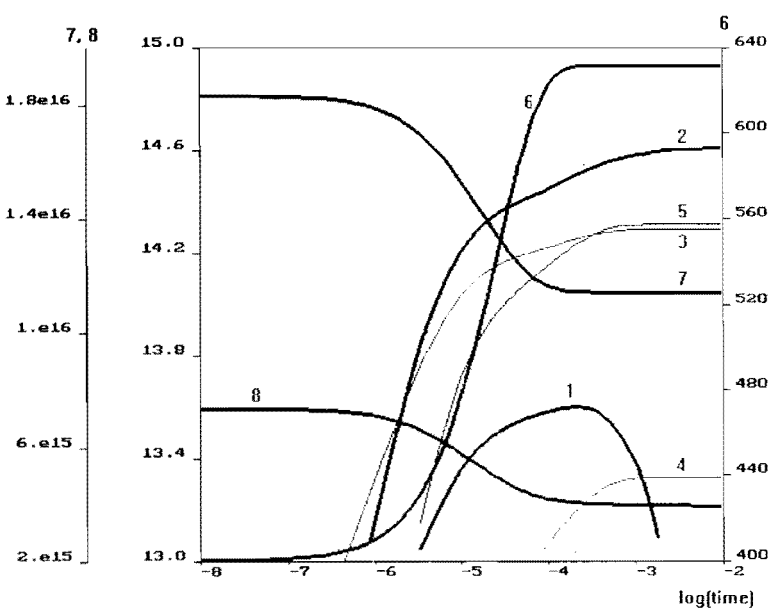

(b) Temperature increase by vibrational relaxation

Fig. 2.38 Densities (in cm^{-3}) of chemical reactants in the gas exposed to the conditions of a primary streamer head, calculated by Alekseev et al. (1993).

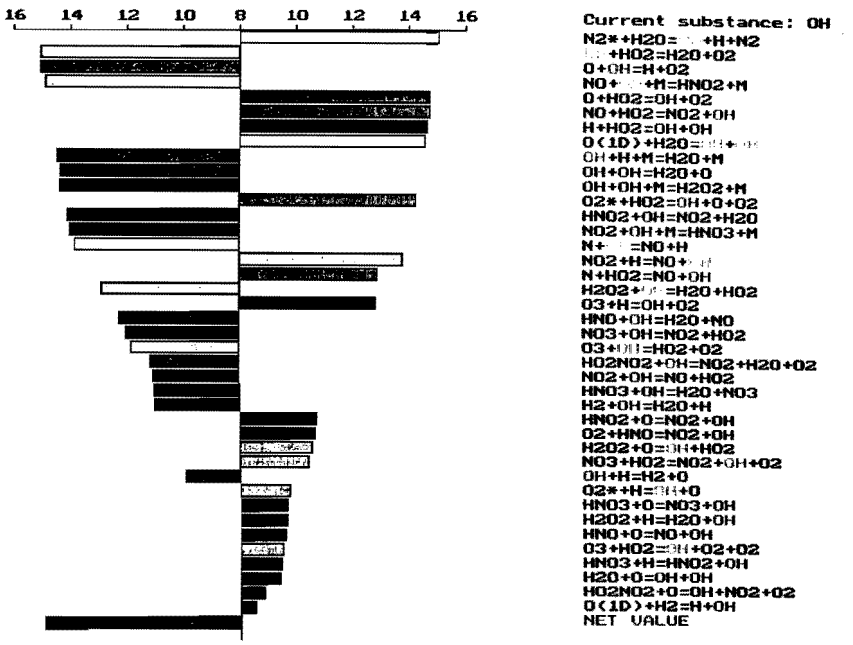

(a) Loss (←) and production (→) of OH radicals by reactions with neutrals.

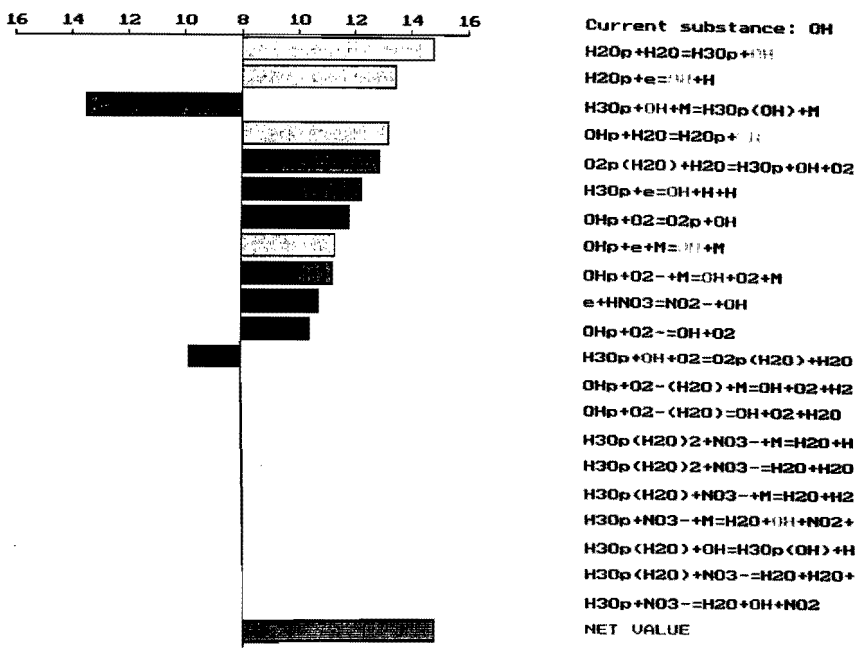

(b) Loss (←) and production (→) of OH radicals by reactions with ions.

Fig. 2.39 Diagrams showing the time-integrated contributions of chemical reactions to the formation and loss of OH and NO (see page 99), unit: log(density[cm^{-3}]), time interval: 0-80 ms, calculated by Alekseev et al. (1993).

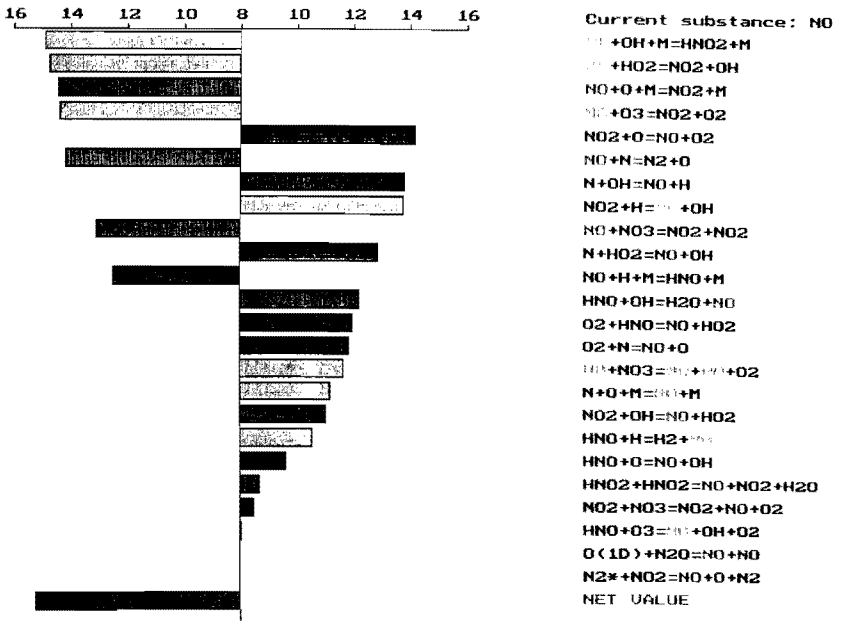

Fig. 2.39 (c) *Loss (←) and production (→) of NO.*

In order to get a clear view of the contributions of specific chemical reactions to the formation or loss of a particular chemical compound, these contributions have been calculated and represented in diagrams like those shown in Fig. 2.39. *OH* radicals are mainly produced by the metastable $N_2(A^3\Sigma_u^+)$ and H_2O^+ ions but also recombination between electrons and H_2O^+ ions plays a significant role, see Fig. 2.39 (a,b). Fig. 2.39 (c) shows that *NO* is mainly oxydized by *OH*, HO_2, *O* and O_3. The radicals *O*, *OH* and *N* play also a significant role in back-reactions: *O* radicals are the main source for the reduction of NO_2 to *NO*. The back-reactions strongly limit the oxydation process from NO_x to acids.

Characteristic time-scales and discussion

The accuracy of the calculations of chemical kinetics in the pulsed streamer corona *de*NO_x reactor is limited by two factors: (a) Not all essential physical and chemical processes have been taken into account (for example by separation of the models for the streamer discharge and streamer-induced chemical kinetics). (b) A second factor is the lack of accuracy of cross sections and rate coefficients used in the electrical discharge and chemical kinetics models. Some of the neglected processes are briefly discussed below:

1) Recombination of electrons with positive ions can play a significant role in radical production (e.g. $H_2O^+ + e^- \rightarrow OH + H$ and $N_2^+ + e^- \rightarrow N + N(^1D)$ followed by $N + NO \rightarrow N_2 + O$. Recombination rates strongly decrease with increasing temperatures of electrons and ions (Mul et al. 1983). However, in the calculations of chemical kinetics these temperatures were assumed to be equal to the gas temperature.
2) Dissociation of N_2 molecules through electron impact proceeds via the formation of electronic excited states which are de-excited by molecular collisions. At present there are no reliable data on the N_2 dissociation cross section at atmospheric pressure (Naidis, 1992; Aurela, 1989).
3) The secondary streamer contributes without any doubt also to the formation of reactive ions and radicals, see for example the calculated distributions of O^- and O in Fig. 2.31 (c).
4) The main direct collision process for energy loss of electrons in the streamer discharge is vibrational excitation of N_2. The possibility of resonant vibrational excitation of H_2O to the dissociation threshold was suggested by Gallimberti (1988). Low energy electrons ($\epsilon < 1$ eV) are of general importance for vibrational excitation of polar molecules (Seng and Linder, 1976) and the possibility of decomposition of H_2O by step-wise vibrational excitation has been demonstrated in laser-fluorescence studies (Vander Wal and Crim, 1989).
5) Diffusion of chemical reactive particles may strongly improve their effectiveness for NO_x removal because diffusion is expected to suppress reactions among radicals (e.g. $O + O_3 \rightarrow 2\ O_2$).
6) Apart from homogeneous gas-phase reactions, heterogeneous gas-liquid or gas-solid phase reactions can also be responsible for NO_x removal. In the corona reactor, solid dust particles and small water droplets (formed at pressures above the water vapour saturation level), commonly referred to as aerosols, can act as condensation nuclei which grow by scavenging of other aerosol (solid and liquid) matter. The modelling of oxidation reactions in the heterogeneous phase is complicated. For example sulfate formation in a droplet (aquous phase oxidation of SO_2 to SO_4^-) depends on the size and acidity (pH) in the drop and the concentrations of dissolved oxydants like O_3 and H_2O_2 (Roelofs, 1992). Salt particles formed by the thermal SO_2-NH_3 reaction in a corona reactor may initiate or catalytically affect $deNO_x$ but no basic data are available of such processes.

Up to now, it seems impossible to include all essential procecces for streamer corona induced $deNO_x$ in computational models. Nevertheless, the modelling results which have been presented in this chapter have given an improved understanding of these processes and their possible interaction. Fig. 2.40 shows schematically the characteristic time-scales of physical and chemical processes.

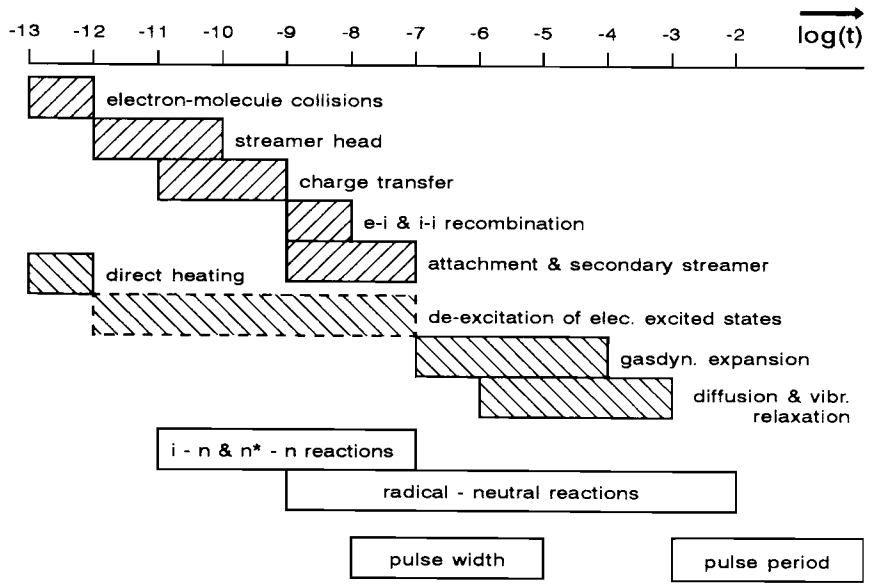

Fig. 2.40 Characteristic time-scales of physical and chemical processes in a pulsed streamer corona reactor.

In principle an improvement of the exactness of the calculation of chemical kinetics can be obtained by the simultaneous calculation of the electrical discharge properties and chemical reactions and/or the simultaneous calculation of hydrodynamics (gasdynamic expansion and diffusion) and chemical reactions. However, the inaccuracy caused by unknown model input data will remain and in order to get a better understanding of essential process parameters it seems more relevant to develop simplified models which can be used to study parts of the total process. For example it is possible to calculate the radial distributions of the electric field and charged particle densities in the residual streamer channel assuming quasineutrality in the direction of the streamer axis and including the effects of electron energy dependent recombination, gasdynamic expansion and diffusion.

Neglecting the above mentionned processes like diffusion of radicals and heterogeneous reactions, it is possible to use the results of this chapter to make a rough estimate of the energy cost per oxidized *NO* molecule. In case of a short (rectangular) 40 kV - 20 ns voltage pulse (avoiding energy dissipation after primary streamer transit) the energy dissipated by a streamer in a 35 mm gap is ~10 μJ (~$6 \cdot 10^{13}$ eV). With $R_s = 100$ μm, the volume of gas which is "treated" by this streamer is 10^{-9} m^3. The results shown in Fig. 2.38 indicate that approximately 2 *NO* molecules are oxydized per electron produced in the streamer head ($n_e = 10^{21}$ m^{-3}, 100 ppm *NO* = $2 \cdot 10^{21}$ m^{-3}), thus ~2.10^{12} *NO* molecules are oxydized. The energy cost per oxidized *NO* molecule is thus approximately 30 eV/*NO*.

Chapter 3 Experimental Set-up for Investigation of Pulsed Corona

3.1 Corona geometries

For a detailed study of corona discharges many types of geometries can be used. The optimal choice of a certain type of geometry will depend on criteria such as:

1) *Electric field distribution:* The conditions for both the formation and propagation of streamers depend strongly on the geometric electric field.
2) *Gas flow conditions:* The chemical performance of a corona reactor depends on the gas residence time and the type of flow (laminar or turbulent).
3) *Applicability of diagnostics:* The geometry can be optimized, for example, for obtaining 2-D optical images of streamers.
4) *Symmetry properties:* These facilitate calculations for particular experimental conditions.

Three different corona configurations are shown in Fig. 3.1.

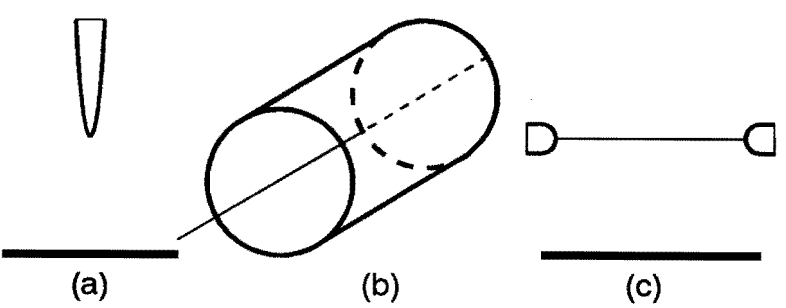

Fig. 3.1 Corona configurations, (a) point-plate, (b) wire-cylinder, (c) wire-plate.

A commonly preferred geometry for the investigation of streamers in DC coronas is the point-plate configuration. Under constant applied potential, streamers can be produced with a high and stable repetition rate and good reproducibility in space which are properties of large interest for diagnostics such as photon counting techniques. Another attractive aspect is, that the axis of symmetry of both the

geometric electric field and the space charge electric field of streamers coincide which makes the comparison of experimental results with 1-D or 2-D model calculations easier. However, when one applies externally generated HV pulses to the anode point, several streamers which may even branch into more streamers are formed simultaneously during each pulse (see **2.2.2**). The advantages of the point-plate geometry with respect to the applicability of diagnostics and the comparison with calculations are lost then.

The most simple electric field distribution is obtained with the wire-cylinder configuration because the electric field depends on radial distance only. The maximum number of streamers and the energy density per unit volume is generally higher than in point-plate configurations. These aspects together make the wire-cylinder configuration suitable as corona-reactor for many applications. For an optical investigation of streamers it is possible to view the discharge in the direction along the central wire in the cylinder. However, when a large number of streamers starting from the wire is formed, it becomes difficult to distinguish between them in the line of sight. This problem is solved with a wire-plate geometry because the development of many streamers, from the formation at the anode-wire up to the arrival at the cathode-plate, can then be viewed along the line of sight perpendicular to the wire.

Table 3.1 gives an overview of geometries which have been used in experimental investigations of pulsed corona discharges in different gas mixtures. More details on the geometry (materials, dimensions) are provided with the description of diagnostic techniques. Experiments demonstrating the removal of NO and NO_2 have been performed in wire-cylinder corona reactors. For optical diagnostics mostly a wire-plate geometry has been used. Also some streamer properties in point-plate and sphere-plate configurations were investigated.

While the electric field in a wire-cylinder configuration depends only on radial distance, the electric field in the wire-plate configuration decreases with increasing distance from the symmetry plane (at fixed distance from the anode surface). The same can be said about the off-axis electric field in a point-plate configuration.

The radial electric field in a wire-cylinder configuration with wire radius r_w and cylinder radius r_{cyl}, is at a distance x from the wire surface:

$$E(x) = E_{max} \frac{r_w}{x + r_w}, \qquad E_{max} = \frac{V}{r_w \ln\left(\frac{r_{cyl}}{r_w}\right)} \tag{3.1}$$

The electric field between a single wire with radius r_w and a plate at constant distance d_g is similar to the electric field between two infinite parallel wires at distance $2d_g$. The electric field in the plane of symmetry through the wire and perpendicular to the plate is (Kuffel, 1984):

$$E(x) = E_{max} \frac{r_w}{x + r_w - \frac{x^2}{2d_g}}$$

$$E_{max} = \frac{V \sqrt{\left(\frac{d_g}{r_w}\right)^2 + \frac{2d_g}{r_w}}}{d_g \ln\left(1 + \frac{d_g}{r_w} + \sqrt{\left(\frac{d_g}{r_w}\right)^2 + \frac{2d_g}{r_w}}\right)} \tag{3.2}$$

Representing the hemispherical needle point of a point-plate configuration as an hyperboloid, the electric field along the symmetry axis can be described in good approximation as (Jacottet, 1974):

$$E(x) = E_{max} \frac{1}{1 - \frac{x^2}{d_g(r_t+d_g)}}$$

$$E_{max} = \frac{V}{\sqrt{d_g(r_t+d_g)} \cdot \ln\left(\frac{\sqrt{r_t+d_g} + \sqrt{r_t} + \sqrt{d_g}}{\sqrt{r_t+d_g} + \sqrt{r_t} - \sqrt{d_g}}\right)} \tag{3.3}$$

where r_t is the minimum radius of curvature of the point.

The geometric field distributions, calculated with Eqs. 3.1, 3.2 and 3.3, are compared in Fig. 3.2. The electric field of an isolated sphere with a plate at far distance ($d_g \gg r_{sp}$) is used to represent the electric field in the sphere-plate configuration. In the critical volume ($r<r_{crit}$, $E>E_{crit}$ =2.5 kV/mm), large differences in the electric field distributions exist. For the example shown in Fig. 3.2 (d_g=35 mm, V=30 kV), r_{crit} (point-plate) = 1.9 mm, r_{crit} (wire-plate) = 2.0 mm, r_{crit} (wire-cylinder) = 2.2 and r_{crit} (sphere-plate) = 3.3 mm. The distance from the anode surface where the geometric electric field equals the stability field (E_s =0.5 kV/mm) is for each geometry in the range 12-13 mm.

configuration	radius (mm)	gap (mm)	wire length (mm)	diagnostics[1]
wire-plate I	0.1, 0.2, 0.3, 0.4, 0.5	35	50	PM, CCD (**4.1.1**)
wire-plate II	0.3, 0.4	50	100	SCH (**4.3.4**)
wire-cylinder I	0.3	35	450	PM (**4.1.4**)
wire-cylinder II	0.4	50	100	SCH (**4.3.4**)
wire-cylinder III	0.3	25	450	NO (**3.3.1**)
wire-cylinder IV	1.5	75-100	800-3500	NO, PM (**3.3.2**)
needle tip-plate	0.3	35		CCD (**4.1.1**)
sphere-plate	4	35		CCD (**4.1.1**)

[1] NO: NO_x removal measurements CCD: 2-D images using CCD-camera
PM: Photomultiplier measurements SCH: Schlieren photography

Table 3.1 Overview of corona geometries and diagnostics.

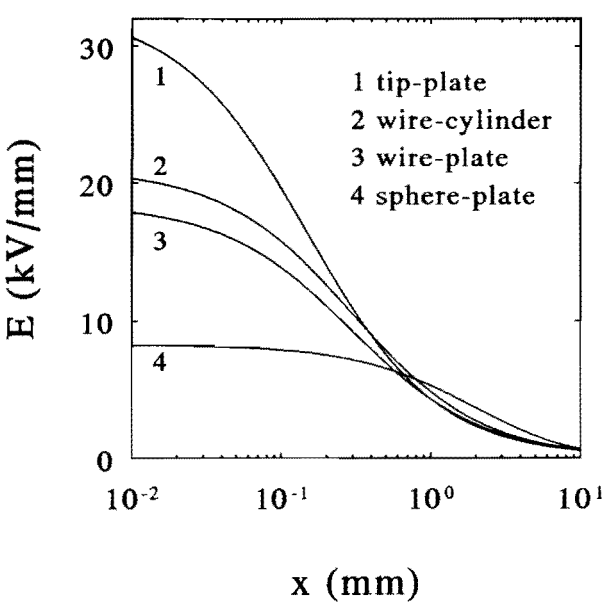

Fig. 3.2 Electrostatic electric fields with d_g=35 mm, V=30 kV (r_w=r_t=0.3 mm), sphere with plate at far distance: $E = V\, r_{sp}/x^2$, r_{sp} =4 mm.

Fig. 3.3 shows alternatives for the wire-plate and point-plate geometries. The main differences in the electric field distribution of these and "simple" geometries can be qualitatively indicated. When an array of sharp pins is substituted for the wire in a wire-plate configuration, the conditions for streamer propagation in the low electric field region are almost unchanged. However, the shape of the critical volume will differ significantly. At least one streamer is expected at each pin except when the mutual influence of electron avalanches and streamers (electrostatic repulsion, removal of initial electrons by drift) would prevent this. When a sharp point is replaced by a sphere, as shown in Fig. 3.3 (b), the electric field in the high field region is decreased and the electric field in the low field region is increased. The sharp protruding pin is needed to satisfy the condition for streamer formation (avalanche growth up to $\sim 10^8$ electrons). In the sphere-plate configuration the cathode has been covered with a dielectric in order to work with small overvoltage ($\sim 10\%$) without breakdown.

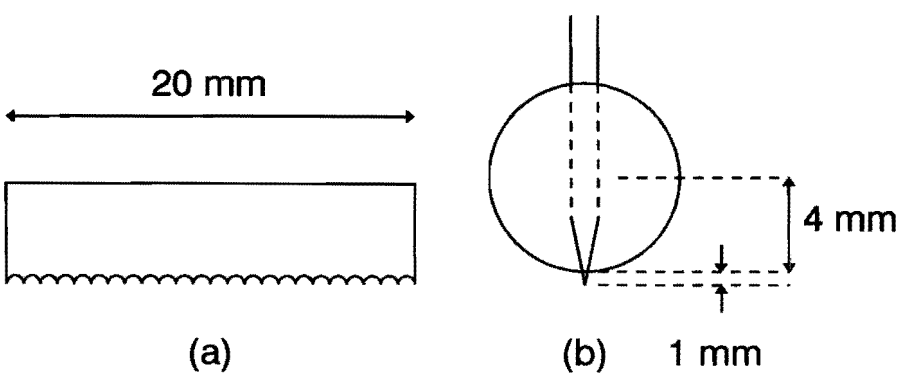

Fig. 3.3 Alternative anode structures: (a) multiple pins, (b) sphere and protruding pin.

3.2 The electrical circuit

A pulsed positive corona reactor for NO_x and SO_2 removal can be operated with a variety of HV pulse shapes. Because of lack of knowledge about the influence of pulse parameters on process efficiency, the possibility of changing pulse parameters independently has been the main criterion for selecting the type of electrical circuit. After a description of the pulse forming circuit in **3.2.1**, the methods for measurement of voltage and current are discussed in **3.2.2**. A simple RCL scheme, presented in **3.2.3**, is used to calculate the main characteristics of the HV pulses.

Circuit parameters (stray capacitance, induction) are determined from voltage measurements in **3.2.4.** Finally, the pulse parameters needed to characterize the shape of the HV pulses are defined in **3.2.5.**

3.2.1 The production of HV pulses

The electrical circuit for production of HV pulses (Fig. 3.4) is based on discharging a capacitor. The energy storage capacitor C_s is negatively charged via a resistor R_{c1}. The negative side of C_s is grounded using a triggered spark gap SG_1 as a switch. This causes a positive pulse at the opposite side of C_s and therefore at the anode of the corona reactor. The spark gap can be exchanged with C_s without changing the main circuit characteristics. The main advantage of a spark gap connected to ground is that the circuit used to trigger the spark gap can be kept at low voltage. Another advantage is that C_s also serves as a coupling capacitor, allowing for the superposition of a HV pulse on a DC bias without the need for another capacitor.

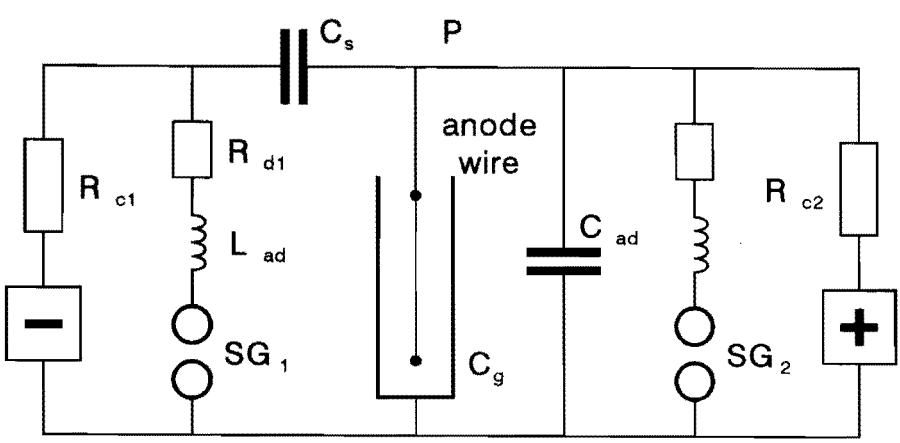

Fig. 3.4 Electrical circuit for the production of steep HV pulses.

The rise time of the voltage is controlled by inserting different damping resistors R_{d1} or inductances L_{ad} in series with the spark gap SG_1. The voltage rise time may also be modified by connecting an additional capacitor C_{ad} parallel to the corona configuration. Without the addition of any component like R_{d1}, L_{ad} or C_{ad}, the pulse rise time depends on the resistance, the stray inductance and the stray capacitance of leads and components in the circuit (**3.2.4**). For the present discussion of the circuit characteristics, the capacitance between the point P in Fig. 3.4 and ground is represented by an equivalent capacitance C_e.

In absence of the corona discharge and in absence of voltage oscillations, the maximum voltage V_m that will be reached at the anode is given by:

$$V_m = V_{DC} + V_0 \frac{C_s}{C_s + C_e} \tag{3.4}$$

where V_0 is the charging voltage at the negative side of C_s. V_m will be maintained at the anode, again in absence of a corona discharge, as long as the low resistivity of the spark gap prevents recharging. The spark gap resistivity varies with time and depends on conditions such as the gap distance, the pressure in the spark gap, the corona discharge current and also on the current delivered via R_{cl}. Under the experimental conditions which have been used (spark gap distance: 5 mm, spark gap air pressure: 2 bar, $R_{cl} = 10$ MΩ), often the voltage at the anode started to decrease after a period in the range 1-10 μs. This is the time needed for quenching, by thermal recovery, of the spark gaps (Portela, 1992). The voltage at the anode decays exponentially with a time constant:

$$t_d = R_{cl} \frac{C_s C_e}{C_s + C_e} \tag{3.5}$$

When the corona discharge displaces a charge Q from cathode to anode, the voltage at the anode will decrease according to:

$$V = V_m - \frac{Q}{C_s + C_e} \qquad i.e. \qquad Q = V_0 C_s + (V_{DC} - V)\cdot(C_s + C_e) \tag{3.6}$$

The maximum charge that can be transferred (obtained from Eq. 3.6 setting $V=0$) depends on C_e only when $V_{DC} \neq 0$. The charge Q is removed again, in between succeeding HV pulses, via the positive power supply (at the right-hand side of Fig. 3.4).

The length of single shot HV pulses can be made short, triggering the second spark gap (SG_2 in Fig. 3.4). C_s is then discharged completely so that the minimum period between two pulses is at least limited to $\sim R_{cl}.C_s$. By this method, the pulse length can not be predetermined with an accuracy higher than 100 ns due to time variations in the trigger moment of spark gap SG_2. Another method for the production of short HV pulses uses fast discharging of C_s and C_e by the discharge itself. For this purpose the value for C_s and C_e must be chosen such, that the displaced charge Q causes a strong voltage reduction, according to Eq. 3.6.

Two similar electrical circuits, suitable for 50 and 100 kV pulsed voltage, have been build up conform the scheme of Fig. 3.4. The design of both circuits is as compact as possible in order to keep stray inductance small. Circuits components,

such as the inductor L_{ad} and the storage capacitor C_s, can be easily exchanged with components having a different value. The used values of various components are given in Table 3.2.

	circuit I	circuit II
V_m (kV)	50	100
C_s (pF)	65, 5000	850
C_{ad} (pF)	0, 100	0
R_{d1} (Ω)	0, 50, 500	0
L_{ad} (μH)	0, 50	0, 18, 55
R_{c1}, R_{c2} (MΩ)	10	10

Table 3.2

Components of circuit I and II for the production of HV pulses.

Circuit I has been used often in combination with wire-plate configuration I, where streamers are produced along an anode-wire with a length of 50 mm. The corona charge is then sufficiently small to consider the circuit, with C_s=5 nF, practically as a voltage source. This property allows for the investigation of the influence of voltage parameters under well defined voltage conditions. Circuit II has been used merely for the production of short HV pulses in combination with wire-cylinder configuration IV which was primarily designed for NO_x and SO_2 removal experiments.

An undesirable effect of the large rate of rise of the current in the pulse-forming circuit, exceeding sometimes 20 A/ns, is strong electromagnetic field generation that will induce currents in measuring cables and in surrounding electronic equipment if no appropriate shielding is provided for. In order to perform accurate measurements and to satisfy regulations for electromagnetic compatibility (EMC), both pulse forming circuits have been surrounded by a Faraday cage. Measuring cables in the cage, for example for the measurement of voltage and current, have been shielded with a surrounding metal tube. In contrast to the current probe, the voltage divider is directly connected to the HV circuit. In the case of sensitive measurements, e.g. photon counting (**4.1.4**), the voltage divider has been disconnected from the circuit.

The electrical circuit described here fits well the requirements of an experimental parameter study. It is emphasized that the requirements of pulsed power supplies needed for large scale $deNO_x$-$deSO_2$ applications differ considerably. Two issues that have not been considered in the design of this circuit but that are of vital importance in applications, are:

1) Minimization of energy losses in the electrical circuit.
2) The life time (and costs) of switching elements.

In industrial application one should minimize circuit resistance and use induction coils (never resistors) to influence rise time, if required. Spark gaps exhibit electrode erosion that, in case of continuous operation at a repetition rate of the order of 100 Hz, limits their life time to several weeks. Reduction of the circuit maintenance requirements is possible, replacing the spark gap by another type of switch with longer life time, for example a thyratron or a stack of thyristors (Kirkman et al., 1993). Alternative circuits for the production of short HV pulses are possible, for example using pulse transformers and magnetic pulse compression techniques as developed for lasers or pulsed e-beams (Keet, 1992).

3.2.2 Voltage and current measurement

The voltage is measured in both circuit I and circuit II with the same type of capacitive-resistive divider (Tektronix, model P6015) with division ratio 1/1000. Rise times in excess of 10 ns are correctly measured, provided that the divider is carefully calibrated. With sub-microsecond pulses and appropriate control of the field stress at the probe tip it is possible to use the divider up to pulse voltages of 100 kV. The DC bias must be kept below 20 kV. In circuit II, where the DC bias can exceed 20 kV, the voltage divider is separated from the anode by a capacitor C_d that is part of the capacitor stack C_s. The DC component at the probe tip is kept zero via a resistor (not shown in Fig. 3.4). In this case, the voltage at the anode can be determined from the measured voltage at the probe V_{meas}, with:

$$V(t) = V_{meas}(t) + \int_{t=0}^{t} \frac{i(t)\,dt}{C_d} \tag{3.7}$$

The current has been measured with Rogowski coils. One of the smallest coils available (Pearson, model 2877, inner diameter 6 mm), with a rise time of 2 ns, has been used in circuit I. For the much higher currents in circuit II a larger coil (Pearson, model 150, inner diameter 50 mm) with a rise time of 20 ns has been used.

The voltage and current signals are both measured with a digital oscilloscope with 300 MHz analog bandwidth and 2 ns sample time (Tektronix, DSA 601). Data are transmitted from the oscilloscope to a computer via a GPIB interface for further analysis.

If corona occurs in a part of the HV pulse where $dV/dt \neq 0$, the total measured current i_t contains a pure capacitive component which must be subtracted in order to obtain the real discharge current i_d:

$$i_d(t) = i_t(t) - C_g \frac{dV}{dt} \tag{3.8}$$

where C_g is the geometric capacitance of the electrode configuration and dV/dt is determined by third order numerical differentiation using 5 samples of $V(t)$, thereby effectively averaging over time periods of 10 ns (2 ns per sample). The energy dissipated in the discharge during a single pulse is calculated by integration of $V.i_d$ in time. Although the capacitive current dissipates no energy in the corona reactor, it is recommendable to reduce this current in applications, because it will contribute to the energy losses in the internal resistance of the circuit and it will reduce the life time of spark gaps or other switching elements.

The discharge current consists of two terms:

$$i_d(t) = \iint_S j_c(t)\, dS + \iint_S \varepsilon_0 \frac{\partial E(t)}{\partial t} \cdot dS \tag{3.9}$$

where $j_c(t)$ is the electron current density and $\vec{E}(t)$ is the electrical field strength at the electrode surface S. The first term, the *conduction current*, corresponds to the transport of electrons through the electrode surface with current density j_c. The second term, referred to as *displacement current*, is due to variations in the electric field strength at the electrode surface that results from moving charges in the electrode gap.

The current, measured at the anode wire during a HV pulse, is made up of the contributions of many streamers. At the cathode it is in principle possible to measure a current which is caused by a single streamer. For this measurement a cathode current probe, similar to the one used by Küchler (1990) and shown in Fig. 3.5, has been used. The probe consists of a central pin of 1 mm in diameter and a surrounding ring with an outer diameter of 4 mm. They are separated from each other and from the surrounding plate with a thin (0.2 mm) insulating cover. The probe is integrated in the flat polished cathode thereby having a negligible influence on the geometric electrical field distribution. The probe and the cathode are made of brass. A Rogowski coil (Pearson 2877, rise time: 2ns) is used to measure the current from both the surrounding ring and the central pin. A signal from the central pin, indicating that a streamer "hits" the probe in its centre, is also separately measured.

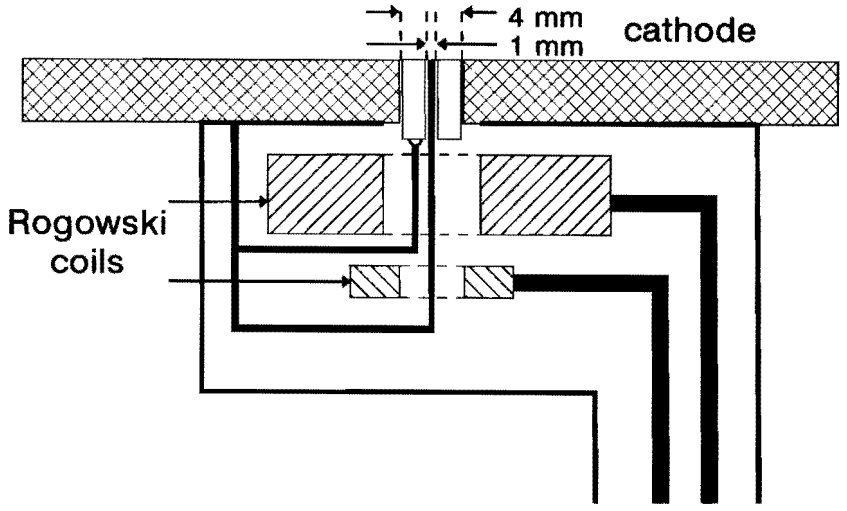

Fig. 3.5 Current probe, integrated in cathode plate.

The analysis of the probe signal is, in general, difficult. In principle, more than one streamer can arrive at the probe during the same HV pulse. Experimental results (2-D pictures of discharge emission in **5.3.1**) will be used to show that the probability that this happens is low. However, even in case of a single streamer, propagating exactly along the symmetry axis through the centre of the measuring probe, the interpretation of the current probe signal is not straightforward. A displacement current may be detected before the moving streamer arrives at the probe surface. A linear dependence of the probe signal on the total displacement current of this streamer can be assumed only if almost the complete electrical flux of the streamer is collected on the circular probe surface. Calculations by Wetzer and van der Laan (1989) show that this condition is fulfilled when the probe diameter is about equal to, or larger than, the gap distance. This condition does not apply here since the gap distance is about 10 times larger than the probe diameter. On the other hand, it may be safely assumed that when a single streamer approaches the probe at small distance, while other streamers are relatively far away, the probe signal is due solely to the displacement current of this streamer.

Measuring optically (**4.1.3**) the moment of streamer "arrival", the probe signal after this moment can be used to measure the current injected from the cathode in a single residual streamer channel. However, also after primary streamer propagation, a non-zero displacement current may exist due to local variations of the charged particle density and field in the residual streamer channel, near the current-probe surface. Only after a redistribution of the electric field in the residual plasma channel, the cathode probe signal can be used to measure the conduction current.

3.2.3 The equivalent circuit

In order to get insight in circuit characteristics, e.g. the maximum rate of rise of the voltage and the minimum width of the voltage pulses, the circuit for production of HV pulses is represented by an equivalent RCL scheme. The inductance and stray capacitance depend on the shape and location of high voltage leads. In principle it is possible to represent the inductance and capacitance of each part of the real circuit with induction coils and capacitors in the equivalent scheme. Although numerical programs are available to calculate the time response of such complicated equivalent scheme, there is still the problem of finding the proper values of the assumed inductors and capacitors. Therefore an equivalent scheme, that is as simple as possible, has been used (Fig. 3.6).

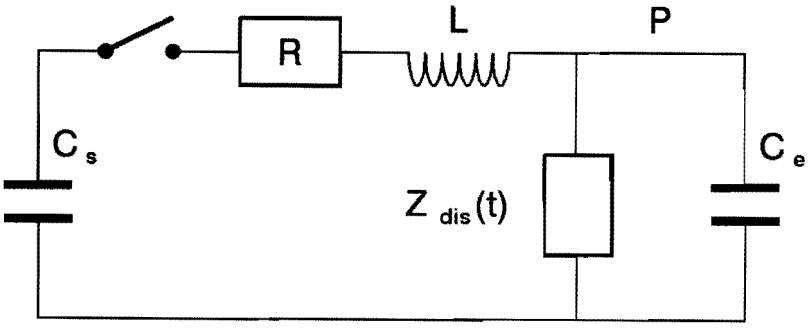

Fig. 3.6 The equivalent circuit.

The spark gap is considered as an ideal switch, i.e. its resistivity is assumed to change instantaneously from infinite to zero. The stray inductance L_s and an added inductance L_{ad} are represented by a single value, $L = L_s + L_{ad}$. The resistance R is taken as the sum of the internal resistance of the circuit R_i and an added damping resistor R_{dl}. Apart from C_s the capacitance between the point P and ground is represented by a single value C_e, that is the sum of the capacitance of the corona geometry C_g, the stray capacitance and a possible added capacitance C_{ad}. The time-dependent discharge impedance is represented by the symbol $Z_{dis}(t)$.

The maximum rate of rise of HV pulses produced by discharging a capacitor is generally reached in the initial rising part of the voltage before corona inception occurs. Thus in order to determine theoretically the maximum rate of rise, the influence of the discharge can often be neglected. Neglecting $Z_{dis}(t)$ the voltage as function of time $V(t)$ at point P in Fig. 3.6 can be calculated by solving the differential equation:

$$L\,C_e\,\frac{d^2V}{dt^2} + R\,C_e\,\frac{dV}{dt} + \left(1+\frac{C_e}{C_s}\right)V = V_0 \tag{3.10}$$

where V_0 is the negative charging voltage of the storage capacitor C_s. There are three different solutions for Eq. 3.10 depending on the damping constant k:

$$k = \frac{R}{2\sqrt{L/C}} \quad , \quad C = C_s C_e \tag{3.11}$$

The voltage is critically damped when $k=1$, less than critically damped when $k<1$ and more than critically damped when $k>1$. From the solutions of Eq. 3.10 (given in Appendix B) it is possible to determine the maximum rate of rise imposing the condition $d^2V/dt^2=0$. For all values of the damping constant k, the maximum rate $(dV/dt)_{max}$ has the form:

$$\left(\frac{dV}{dt}\right)_{\max} = V_0\,\frac{C_s}{C_s+C_e}\,\omega_0\,D(k) \tag{3.12}$$

where ω_0 is the resonance frequency in a damped circuit:

$$\omega_0 = \frac{1}{\sqrt{LC}} \tag{3.13}$$

The damping factor $D(k)$ is given in appendix B and, graphically, in Fig. 3.7.

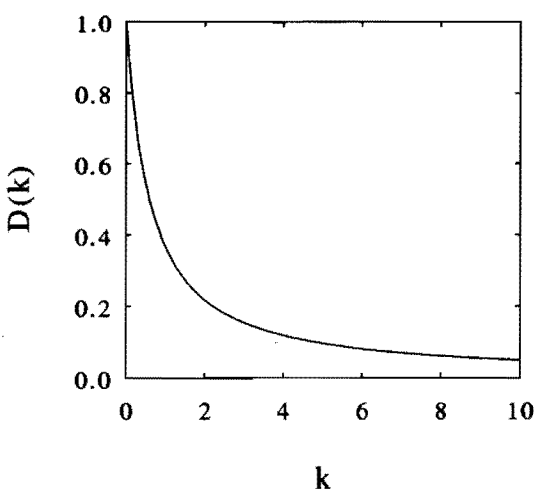

Fig. 3.7

The damping factor D(k) as a function of the damping constant k.

Taking the discharge impedance $Z_{dis}(t)$ into account as a time dependent resistor $R_{dis}(t)$, the differential equation for the equivalent circuit in Fig. 3.6 can be written

as:

$$\frac{d^3V}{dt^3} + a\frac{d^2V}{dt^2} + b\frac{dV}{dt} + c = 0$$

$$a = \frac{R}{L} + \frac{1}{R_{dis}(t)\,C_e}, \quad b = \frac{1}{L\,C_e} + \frac{1}{L\,C_e} + \frac{R}{R_{dis}(t)\,L\,C_e} \tag{3.14}$$

$$c = \frac{1}{R_{dis}(t)\,L\,C_s\,C_e}$$

Also in this case a damping criterion exists. The necessary and sufficient criterion for damping is (Vondenbusch, 1958):

$$K = \left(\frac{b}{3} - \frac{a^2}{9}\right)^3 - \left(\frac{a^3}{27} - \frac{ab}{6} + \frac{c}{2}\right)^2 > 0 \tag{3.15}$$

From Eq. 3.15 follows that for small values of C_s (used for the production of short HV pulses) the circuit will be damped. A solution for the damped case can be derived assuming as initial conditions $V_{t=0}=0$, $(dV/dt)_{t=0}=0$ and $(d^2V/dt^2)_{t=0}=V_0/(LC_e)$ (Vondenbusch, 1958):

$$V(t) = \frac{V_0}{LC_e\left(\omega^2+(P_2-P_1)^2\right)} e^{-P_1 t} - \frac{V_0}{LC_e\omega\sqrt{\omega^2+(P_2-P_1)^2}} e^{-P_2 t}\cos(\omega t - \psi) \tag{3.16}$$

where P_1 and P_2 are given by:

$$P_1 = \frac{a}{3} - \sqrt[3]{\alpha_1} - \sqrt[3]{\alpha_2} \qquad P_2 = \frac{a}{3} + \frac{1}{2}\left(\sqrt[3]{\alpha_1} + \sqrt[3]{\alpha_2}\right)$$

$$\alpha_{1,2} = -\left(\frac{a^3}{27} - \frac{ab}{6} + \frac{c}{2}\right) \pm \sqrt{K} \tag{3.17}$$

and the oscillation frequency ω and phase shift ψ are:

$$\omega = \frac{\sqrt{3}}{2}\left(\sqrt[3]{\alpha_1} - \sqrt[3]{\alpha_2}\right) \qquad \psi = \arctan\left(\frac{P_2 - P_1}{\omega}\right) \tag{3.18}$$

Solution 3.17 is valid only when $V_{DC}=0$. The solution can be used to calculate the shape of the voltage pulse assuming that the discharge impedance is mainly resistive.

3.2.4 Determination of circuit parameters

The equivalent capacitance C_e and the stray inductance L_s can be determined from voltage and current measurements. C_e can be calculated from the exponential decay time of voltage pulses in absence of a corona discharge (Eq. 3.5). It is more accurate to determine C_e from the resonance frequency (Eq. 3.13) when a known inductance L_{ad}, much larger than L_s so that $L \approx L_{ad}$, is inserted into the circuit. Fig. 3.8 (a) shows an example of an oscillating voltage waveform, obtained with circuit I and wire-cylinder configuration I in absence of a corona discharge.

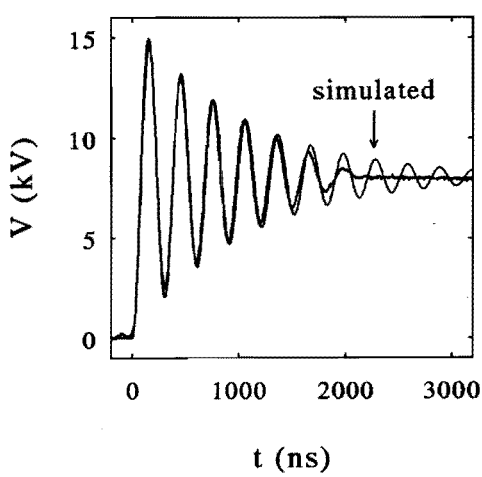

Fig. 3.8 Comparison of between a simulated voltage waveform (Eq. B.5) and a waveform measured in absence of a corona discharge.
Wire-cylinder configuration I and circuit I with C_s=5 nF, R_{dl}=0 Ω and L_{ad}=50 μH.

From the measured resonance frequency (3.35 MHz), the value of C_e has been estimated at 45±2 pF. The best fit between measured and computed waveforms is

obtained adopting an internal resistance with R_i=70 Ω. From this comparison it appears also that after ~2 μs the measured oscillations are damped more rapidly than the calculated oscillations. This effect can be explained by an increase of spark gap resistivity. Values of R_i have been determined for various values of V_m, below the corona onset (~10 kV), by comparison of computed and measured voltage waveforms. The product of R_i (obtained by fitting) and the maximum current is in the range 100-500 Volt. This is roughly the voltage required to sustain an arc discharge in a spark gap with 5 mm gap distance (Portela, 1992).

The oscillation frequency of pulses below the corona onset has also been used to determine the stray inductance L_s. With the combination of wire-cylinder geometry I and electrical circuit I (C_s=5 nF, R_{d1}=0, L_{ad}=0) an oscillation frequency of 29 MHz is measured. Since C_e=45 pF the stray inductance must be L_s≈0.7 μH. The same value is calculated from resonance frequencies obtained with an added capacitor C_{ad}=100 pF. The stray inductance is probably due to the thin corona wire and other parts of the circuit but not to the spark gap because the estimated stray inductance of an arc channel with a diameter in the range 0.1-1 mm and 5 mm length is lower than 0.02 μH (Persephonis, 1992).

The geometrical capacitance C_g has been determined from the charge-to-voltage ratio, measured with voltage pulses below corona onset, i.e. when the current is only capacitive. Values of C_g, C_e and L_s for different circuit-geometry combinations are given in Table 3.3.

Circuit	Geometry	C_g (pF)	C_e (pF)	L_s (μH)
I	wire-plate I	18	30	0.6
I	wire-plate II	22	-	-
I	wire-cylinder I	31	45	0.7
I	wire-cylinder III	33	-	-
II	wire-cylinder IV	43	-	8

Table 3.3 Circuit parameters of several circuit-geometry combinations.

3.2.5 Definition of pulse parameters

In order to characterize the shape of pulses delivered by the HV power supply, the following pulse parameters can be used: DC bias V_{DC}, rise time t_r, peak voltage V_p and pulse width t_w. Only the definition of V_{DC} is unambiguous. For all other parameters various definitions are possible.

The peak voltage V_p is defined as the maximum voltage that is measured. V_p will depend on the bandwidth of the voltage probe and the oscilloscope. Another parameter that is used to characterize the height of voltage pulses, is the maximum voltage that would is reached in absence of corona and in absence of voltage oscillations: $V_m = V_{DC} + V_0 C_s / (C_s + C_e)$.

The rise time t_r is only used here in case of strongly damped voltage pulses that can be represented by the function (Eq. B.9):

$$V(t) = V_{DC} + V_0 \frac{C_s}{C_s + C_e} \left(1 - \exp[-t/t_r]\right) \tag{3.19}$$

In case of HV pulses produced by discharging a capacitor, the moment when the voltage starts to increase is generally seen as a discontinuity in dV/dt. According to Eq. 3.19 the rise time t_r is defined as the time needed to reach $1\text{-}e^{-1}$ (i.e. 63%) of V_m-V_{DC}. Also in case of oscillating voltage pulses a definition of rise time is possible. The time needed to reach 90% of V_p-V_{DC} is widely used. However, this definition can be criticised because, when high frequency voltage oscillations occur, the actual peak voltage is often difficult to determine.

Usually, the maximum rate of rise $(dV/dt)_{max}$ can be easily measured although the measured value will depend on the bandwidth of the voltage probe and the oscilloscope in case of very fast rising pulses. In this case the maximum is generally reached before corona occurs and therefore it will often not depend on the discharge load.

The pulse width t_w is, in the case of short HV pulses, defined as the width at 50% of V_p. The pulse width of HV pulses with a fast rise and an exponential decay, is specified by the exponential decay time constant, t_d (Eq. 3.5).

3.3 Corona reactors for gas cleaning

3.3.1 Bench-scale set-up

The experimental set-up for NO_x removal experiments with simulated flue gas is schematically shown in Fig. 3.9. In this bench-scale set-up, wire-cylinder configuration III (Table 3.1) has been used as corona reactor. The volume of this reactor (25 mm radius, 500 mm length) is 0.98 litre. The wire and the cylinder are made of stainless steel, the walls and gas connections at both ends of the cylinder are made of teflon. The pulse forming circuit (circuit I, Table 3.2) is suitable for pulse voltages up to 50 kV. Instead of the gap distance of 35 mm that has been used for most of the optical diagnostics, a gap distance of 25 mm was chosen in order to work with higher overvoltage.

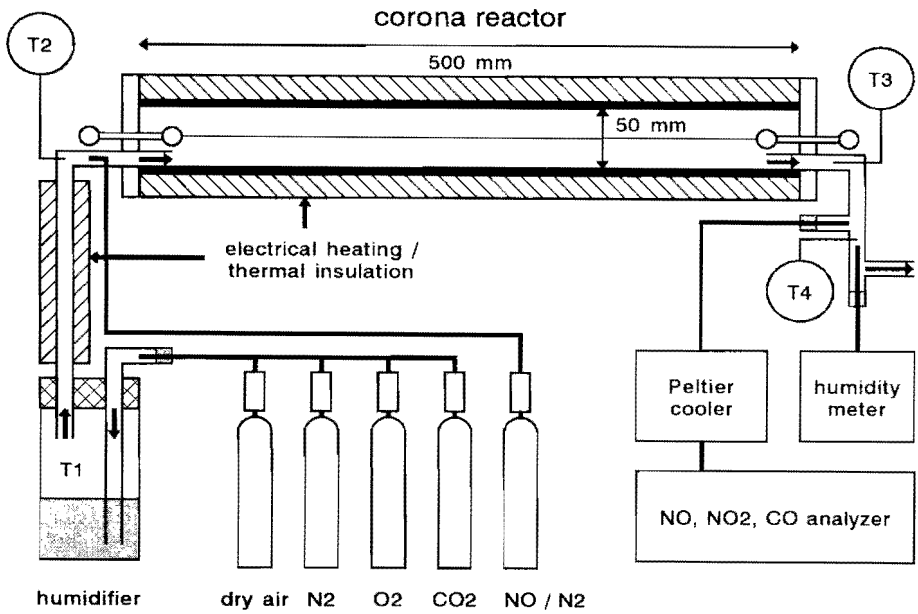

Fig. 3.9 Bench-scale set-up for NO_x removal.

A N_2-O_2-CO_2 gas stream is supplied from cylinders with pure gases (technical grade, 99.9% purity) and using flow controllers for each gas. The gas is humidified by passing it through a bottle filled with water and small glass pearls (4 mm in diameter) that increase the contact surface between the gas and the water. After the humidifier the gas is heated up to the desired temperature passing it through an electrical heating pipe. The gas temperature is measured with thermocouples at four different locations: In the humidifier (T_1), near the gas inlet of the reactor (T_2), in the reactor near the gas outlet (T_3), and downstream of the reactor (T_4). In order to obtain a uniform gas temperature in the reactor, T_2 and T_3 are made equal. Additional heating of the reactor using a surrounding electrical heating jacket appeared necessary. The flow of the dry N_2-O_2-CO_2 mixture is kept constant at 6 litre/min. The flow in the reactor is turbulent with an average residence time of ~10 seconds.

The humidity level of the gas has been varied by changing the temperature in the humidifier and an electronic solid state sensor (Rotronic C80) has been used to measure both the relative humidity RH and the temperature (T_4). The absolute humidity was determined from RH and the saturation pressure p_{sat} as: $AH = RH \cdot p/p_{sat}$ with $p = 1013$ mbar. The saturation pressure p_{sat} was determined at T_4 in the

range 60-80 C°. The humidity levels that have been used are given in Table 3.4. Increasing T_4 from 60 to 80 °C, *AH* increased from 5 to 7 %. An estimation of the error in absolute humidity was made from measurements as function of T_4. The error in the total gas flow, that results from the error in *AH*, is small compared to the accuracy of the gas flow controllers (2-5%). A gas stream of 10% *NO* in N_2 is added to the N_2-O_2-CO_2-H_2O mixture close to the gas inlet of the reactor. The initial *NO* concentration is kept at a constant level of 250 ppm. The addition of N_2 with *NO* causes a negligible change (0.25 %) in the total gas flow. Interlocks at the cover of the Faraday cage, surrounding the reactor and pulsed power supply, provide HV safety control. In order to protect the environment from NO_x the gas stream is finally passed through a 10% peroxide solution.

T_1 (°C), humidifier	AH_{sat} (%) at T_1	AH (%), reactor outlet	gas flow (m^3/hr) (including H_2O)	flow error due to AH error
40	7.3	6 ± 1	0.38	1%
50	12.2	10.5 ± 1.5	0.40	1.25%
60	19.7	18 ± 2	0.42	1.5%

Table 3.4 Humidity conditions in simulated flue gas.

The treated gas is sampled near the outlet of the reactor via a heated, stainless steel pipe, dried in a Peltier-cooler and analyzed with an electrochemical analyzer (SONOX R100-4011) with sensors for O_2, *NO*, NO_2, SO_2 and *CO*. Electrochemical sensors use porous catalytic electrodes in which the gas component to be analyzed reacts with a liquid electrolyte. The concentration can be derived from the current through the electrolyte (Böhm, 1983; Ogink, 1988). The internal microprocessor of the analyzer accounts for the cross-sensitivity of sensors. The maximum error in measured concentrations was specified, after factory calibration, at 5% of concentrations at full scale (for *NO*, NO_2 and SO_2, 5% of respectively 500, 250 and 1000 ppm). The accuracy of the [*NO*] measurement was checked prior to measurements using a mixture of dry air and 250 ppm *NO*. The error in [*NO*] was found to be about 10 ppm, i.e. 5% of the measured concentration.

3.3.2 Pilot-scale set-up

A pilot-scale set-up has been build in order to demonstrate the effectiveness of pulsed positive corona for the combined removal of NO_x and SO_2 from gas streams with a large mass flow (e.g. the flue gas of an electrical power plant, Fig. 3.10). The

gap distance of the corona geometry (100 mm, wire-cylinder configuration IV, Table 3.1) is suitable for large-scale application. The pulsed power supply (circuit II, Table 3.2) offers high flexibility with respect to variation of pulse height, pulse duration and repetition frequency. The length of the anode wire l_a is 3.5 m, the effective volume of the reactor is 110 litre ($l_a\ \pi r_c^2$).

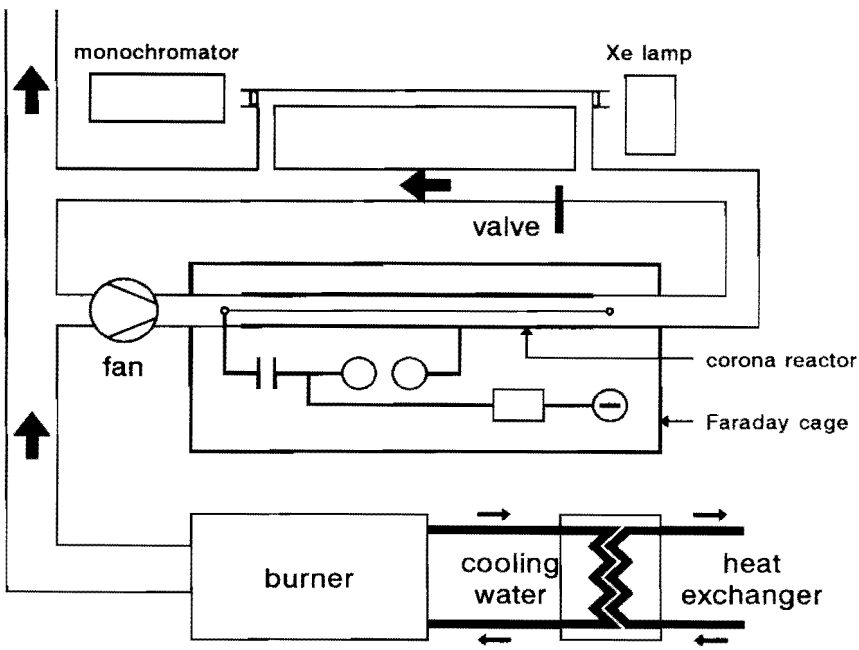

Fig. 3.10 Pilot-scale set-up for NO_x and SO_2-removal.

The set-up is provided with flue gas from a natural gas burner (Klöckner KL.30.1.RG) that can be adapted to burn other gases or oil. The low-NO_x burner has a maximum capacity of 185 kW at a natural gas consumption of ~20 m^3/hr, giving a flue gas output ~300 Nm^3/hr. The capacity can be adjusted down to 25% with an air-to-fuel ratio that is kept constant by mechanical coupling of the air and fuel inlet valves. A boiler and heat exchanger are used to vary the flue gas temperature. A part of the flue gas is lead through a by-pass so that the flow can be varied independently of the temperature. Thermal insulation covering of the flue gas ducts and additional electrical heating of the reactor was necessary to obtain a uniform gas temperature at low gas flow. The lower and upper limits of the gas temperature in the reactor are 60 and 170 °C.

Downstream of the reactor the flue gas passes a straight tube with 25 mm radius and 2 m length that used for both flow and spectroscopic absorption measurements. The flow is determined from a calibrated compression flange half-way the tube and NO and O_3 absorption measurements are performed using a high pressure Xe-band lamp and a monochromator (Jarrell-Ash, f=0.5 m, D=16 Å/mm). The flue gas composition is determined from the measurement of the excess of air in the combustion. Assuming that pure methane is burned, via the reaction $CH_4 + 2\ O_2 \rightarrow CO_2 + H_2O$:

$$[CO_2] = 0.5\ [H_2O] = 21\% - [O_2] \tag{3.20}$$

The O_2 concentration is measured with the electrochemical analyzer. Because of the pressure drop in the flue gas ducts and over the compression flange in particular, fans are required to maintain the gas flow. NO and SO_2 flows are controlled with mass flow controllers with 20 ppm accuracy (Tylan FC 280-S). A programmable logic analyzer (PLC, Siemens S5-100U) is used for safety control. The inputs of the PLC are connected to a SO_2 leakage detector, fans and the cooling water detector of the heat exchanger. The outputs are connected to the NO_x and SO_2 mass flow controllers and the burner.

Chapter 4 Optical Diagnostics

4.1 Optical diagnostic techniques

4.1.1 Experimental arrangement

For most of the optical measurements wire-plate configuration I (Table 3.1) has been used. The configuration is placed in a gas-tight box (150x150x150 mm) made of celeron, see Fig. 4.1. A central wire or needle tip are used as anode and both are made of stainless steel. A corona discharge is produced along a part of the wire, limited to a length of 50 mm, by means of dielectric insulation. The cathode plate is made of brass (10x100x100 mm) with rounded edges. The position of the anode-wire, anode-tip and cathode-plate can be varied. This allows for changing the gap distance and for changing the position of the discharge with respect to the optical axis of the image intensifier-CCD camera system. A second identical cathode plate can be placed facing the first one at the same distance from the wire.

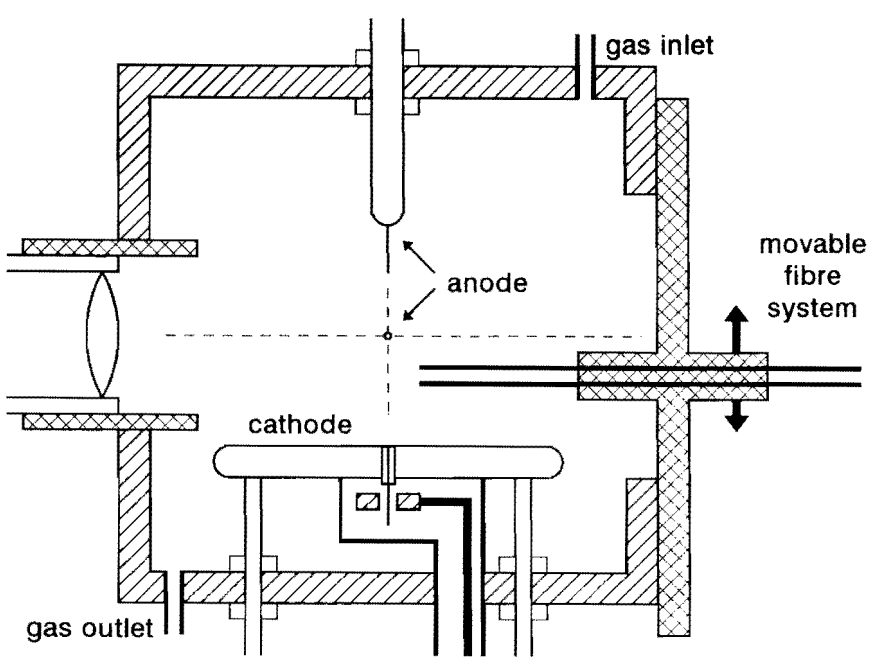

Fig. 4.1 The wire-plate corona configuration for optical diagnostics.

As a standard condition a wire radius of 0.3 mm and a single cathode plate at 35 mm distance are used. The corona discharge is operated in dry air, N_2-O_2 mixtures or in some cases N_2-CO_2 mixtures. The gas supply system is described in **3.3.1**. The gas flow is maintained at 6 l/min giving an average residence time of the gas in the box of ~0.6 min. The inside of the box and the cathode plate have been covered with matt black paint in order to avoid light reflections.

4.1.2 Image intensifier and CCD camera

Two-dimensional images of discharge emission have been made with an image intensifier combined with a Charge Coupled Device (CCD) camera. An image of the discharge region is made on the image intensifier by means of a quartz lens (f_1=50 mm) and a camera lens (f_2=60 mm) is used to form an image of the fluorescence plate of the intensifier on the CCD (Fig. 4.2). The plane through the wire-axis, perpendicular to the surface of the cathode-plate, is the object plane of the camera.

The CCD (EG&G model 1430-P, 13.3x8.8 mm) is made up of 576x384 rectangular pixels of 23x23 μm in size. According to the specifications, the quantum efficiency of the CCD is higher than 20% in the spectral range 450-900 nm. The CCD is equipped with a 14-bit digitizer. Transfer of data from the CCD to a computer occurs via the CCD-detector interface (EG&G model 1430-1) and a parallel bus (GPIB). The CCD pictures are stored on magnetic tape (~1 Mbyte per picture).

The image intensifier (supplied by EG&G as option to the CCD camera) has been used in order to increase the sensitivity for discharge emission at wavelengths below 450 nm, where the CCD camera is not sensitive enough and where the strongest emission lines of nitrogen are situated. The light-sensitive circular surface of the intensifier, with a diameter of 25 mm, is build up of circular pixels, each of them having a diameter of 70 μm. The pixels are sensitive in the spectral range 180-600 nm. The fluorescence plate of the image intensifier re-emits light in the visible part of the spectrum, for which the CCD-camera is sensitive. The intensifier offers the possibility of making time-resolved pictures. It can be activated with a gate pulse during a minimum period of 34 ns. This period is short enough for the investigation of different phases of the discharge. According to its specifications, the intensifier should possess an amplification factor of the order of $\sim 10^4$, that is close to that of photomultipliers. In practice however, the amplification factor was be significantly lower (about 10^3). Relative intensity measurements as function of gate pulse length, using a continuous light source, show that the amplification factor is constant for pulse lengths larger than 100 ns. However, for the minimum pulse length of 34 ns the amplification factor is about a factor 2 lower.

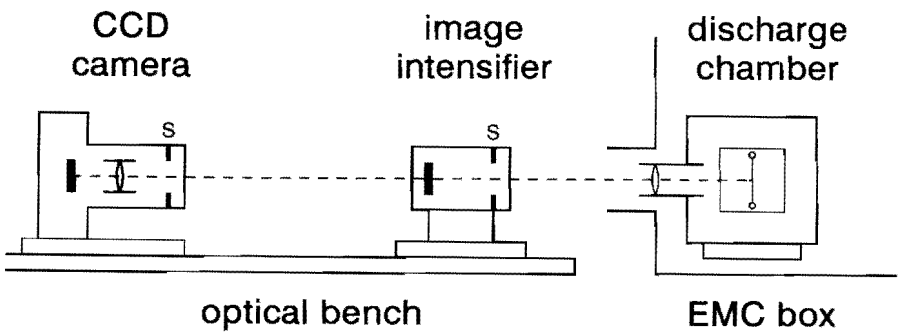

Fig. 4.2 Imaging system with image intensifier and CCD-camera (S=shutter).

The imaging system has been used to produce two types of images:
1) Reduced images of the whole discharge region in between anode and cathode
2) Magnified images of a part of the discharge region in order to study details such as the diameter of a single streamer discharge channel

Magnification factors that have been used are given in Table 4.1. In case of $M_2=0.48$ the circular shape of the intensifier is observed on the rectangular CCD image and in case of $M_2=0.57$ parts of the circular intensifier image are not detected by the CCD. Some pictures of discharge emission have also been made using only the CCD-camera (without image intensifier). This possibility offers better image quality at the expense of time resolution and sensitivity.

M_1 ($f_1=50$ mm)	M_2 ($f_2=60$ mm)	$M=M_1 \cdot M_2$
0.43	0.48	0.21
0.37	0.57	0.21
7.2	0.57	4.10
-	0.25	0.25

Table 4.1 Magnification factors for image intensifier-CCD optical system.

Those streamers, deviating from the object plane on their way to the cathode, will be out of focus. In order to work with a good depth of field a diaphragm with small aperture (4 mm) has been placed in front of the quartz lens. The influence of defocusing was investigated by observation of the image quality of a sharp needle, with a tip radius of curvature of 25 μm and by changing the object distance between this needle and the quartz lens. In case of de-magnification ($M=0.21$) noticeable

defocusing was observed only by changing the object distance by more than 30 mm. In case of magnification (M=4.1) the width of the needle tip image was approximately doubled by changing the object distance over ~2 mm.

The measurements with the image intensifier-CCD camera system have been performed with single shot HV-pulses (the period between two pulses was generally larger than 1 min.). A synchronisation signal of a mechanical shutter, in front of the image intensifier, triggers the CCD controller (EG&G model 1461) that opens the CCD camera shutter. A "shutter-open" signal, indicating that the camera shutter is fully opened, serves as a trigger for both the pulse generator of the intensifier and the HV pulsed power supply of the discharge. For optimum electromagnetic compatibility the HV pulse forming circuit is triggered by means of an optical signal. Statistical variations in time between this trigger signal and the moment when the corona discharge is actually produced are due to jitter in the triggered spark gap and to the statistical time lag for corona inception. Because of both statistical time variations, it is impossible to synchronise the intensifier and the discharge with an accuracy higher than 100 ns. On the other hand, the delay time between the start of the discharge (using integral light emission) and the start of the gate pulse can be measured with 2 ns time resolution. Measuring this statistically varying delay time for a large number of pulses and selecting only those pictures which correspond to different delay times, a series of pictures with ~34 ns exposure time, that shows the evolution of the discharge, is obtained.

4.1.3 Integral and local light emission

Optical fibres have been installed for measuring integral and local light emission. The position of the optical fibres with respect to the corona geometry is shown in Fig. 4.3. The aperture of the fibre measuring integral light emission is ~60 deg., i.e. larger than needed to collect light emission from the entire discharge gap. The integral light emission signal is used to determine the starting moment of the discharge, i.e. the moment when the first streamer(s) is (are) formed.

The measured voltage, current and light emission signals possess relative delay times that are due to the measuring systems (e.g. the delay times of cables with different lengths and the delay times of the photomultipliers). The signals have been calibrated in time using relative low and damped voltage pulses (V_m=20 kV, t_r≈40 ns) when streamer inception occurs after the rising part of the HV pulse, thus when the capacitive and discharge currents are clearly separated in time. The calibration is performed requiring that (a) the maximum in dV/dt and the maximum in the capacitive current coincide in time and (b) the start of the discharge current pulse and the integral light emission signal coincide in time.

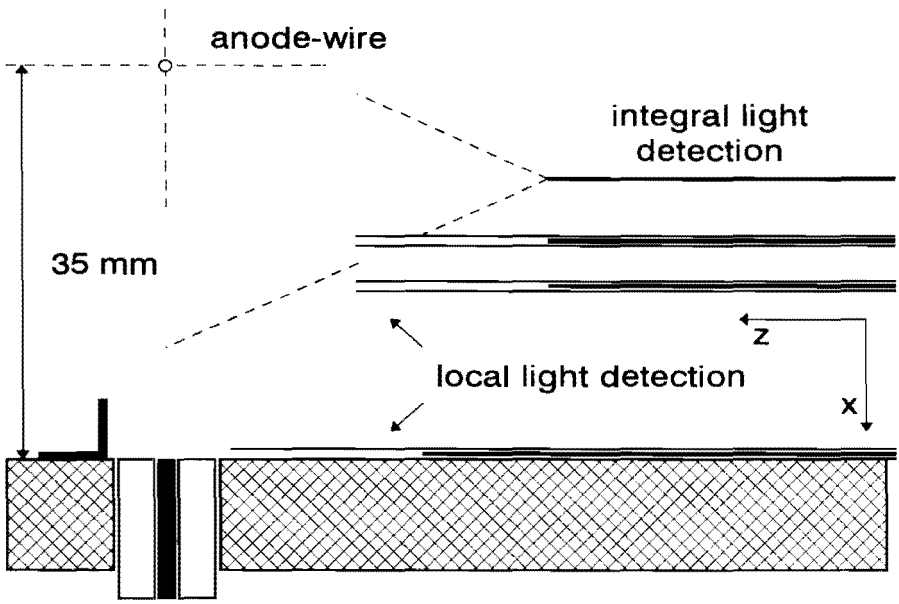

Fig. 4.3 Measurement set-up for integral and local light emission.

Local light emission is measured with fibres (600 μm in diameter), contained in thin tubes (inner diameter: 1 mm) that strongly limit the angle of light rays that may reach the fibres. The inner sides of the tubes, made of aluminium oxide, have been covered with matt black paint to avoid internal reflections. The diameter of the cone-shaped volume, for which the local measurement is sensitive, is 1.8 mm in the plane through the wire-axis and perpendicular to the flat cathode (see Fig. 4.3). Local light emission signals are used for the measurement of:

1) Streamer inception time lag and voltage
2) Streamer inception time difference
3) Streamer propagation velocity
4) Emission close to the cathode current-probe
5) Streamer transit time

Features of each measurement are discussed below:

1) Simultaneous measurements of *local* light emission and voltage are used to determine average values and statistical spread of the *streamer inception time lag* T_i and the *streamer inception voltage* V_i. The streamer inception time lag is defined as

the time difference between the moment when the voltage reaches the minimum streamer inception voltage $V_{i,\,min}$ and the moment when local emission of one or more streamers is detected. For measurements of T_i, the central axis of the cone-shaped volume for which the measurement is sensitive, is positioned at 2 mm distance from the wire surface (in the x-direction, see Fig. 4.3). Light emitted in a region within 1 mm from the wire surface is not detected. Therefore, this local light emission measurement is not sensitive for the possible emission from electron avalanches that do not develop into cathode-directed streamers. Also detection of light reflected at the smooth anode-wire is avoided.

2) Streamers that are produced at the same wire during the same HV pulse, are not always formed simultaneously. The inception time lag (T_i) of separate streamers may be different. The local light emission measurement is sensitive for the emission of a single or only a few streamers. Therefore, the time difference between the start of the integral light emission signal and the start of a local light emission signal, measured at 1-3 mm distance from the wire (in the x-direction), is used to yield information on average values and statistical spread of the *streamer inception time difference*, ΔT_i.

3) A system consisting of two thin tubes 4 mm apart is used to measure the average streamer propagation velocity $<v_s>$. The system can be shifted in position along the gap axis. In fact, only the velocity component in the x-direction normal to the cathode plate is measured. The average streamer velocity is determined from the average delay time between the two local light emission signals.

4) Another optical fibre is positioned close to the cathode current probe (**3.2.2**). This fibre detects only light emitted by streamers that hit the current probe because for this particular measurement light emission from other parts of the cathode surface is obstructed by a small piece of black paper.

5) The average time needed for streamers to cross the gap $<T_s>$ is determined by averaging the delay time between local light emission signals at both the anode and the cathode.

The optical fibres are connected to photomultipliers (Hamamatsu, R666). The photomultiplier pulse response has a rise time of ~2 ns and an exponential decay time of ~10 ns. The photomultiplier signals of integral and local light emission are digitized with the oscilloscope (Tektronix DSA 601) with 2 ns sample time and 300 MHz analog bandwidth.

In order to avoid the dependence on signal amplitude, the start moments of local light emission signals have been determined at 25% of the signal amplitude. At this reference level the signal rate of rise is determined by the photomultiplier only. Data are transferred from the oscilloscope to a computer in real time.

Although the sample time of the oscilloscope and the rise time of photomultiplier signals are limited to a minimum of ~2 ns, shorter delay times can

be determined using linear interpolation of the measured samples neighbouring the reference levels. Average delay times are determined from 1000 separate delay time measurements at 20 Hz repetition frequency of the discharge.

The optical volume of the local light emission measurement may be crossed by more than one streamer during the same HV pulse. Therefore, measured delay times T_i, ΔT_i and T_s may differ from real values valid for single streamers. However, when the spatial resolution of the measurement (1.8 mm in the plane through the wire-axis perpendicular to the flat cathode) is small compared to the average distance between streamers, the measured probability distributions and average values of delay times may be considered as representative for real delay times valid for single streamers.

Also an alternative optical system for measuring the streamer velocity with a small lens has been used, see Fig. 4.4. Streamers, deviating much from the object plane will be out of focus. Therefore, this system is expected to be less accurate than the tube-fibre system (Fig. 4.3).

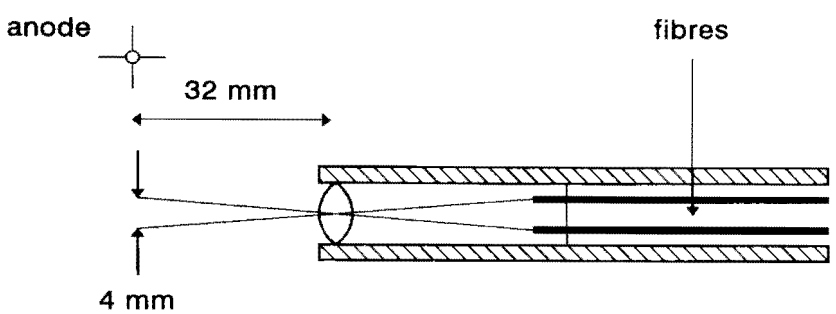

Fig. 4.4 Lens-fibre system for measurement of streamer velocity.

4.1.4 Emission spectroscopy

Optical fibres have also been used for emission spectroscopy. In order to collect enough light at the monochromator entrance slit, 7 quartz fibres, each of them having a diameter of 600 μm, are put in a linear array before the entrance slit of the monochromator. In the wire-plate configuration the 7 fibres are mounted in a tube with an inner diameter of 3.3 mm. The inside of the tube is covered with black paint in order to avoid reflections. This optical system allows for measurements as a function of distance to the anode-wire with a spatial resolution of ~7 mm (Fig 4.5).

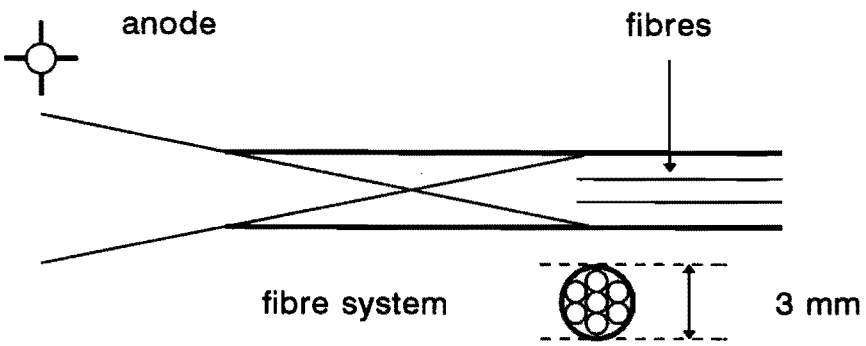

Fig. 4.5 Optical fibres for emission spectroscopy.

More light can be collected with the system of 7 fibres without tube (detecting light from the entire gap) in the wire-cylinder configuration I (wire length: 450 mm). This possibility has been used for the measurement of the rotational spectrum of the 337.1 nm line of N_2 with high spectral resolution ($\Delta\lambda = 0.04$ nm).

The monochromator (Jobin Yvon, $f = 1$ m, dispersion 0.8 nm/mm) is equipped with a holographic grating, blazed at $\lambda = 600$ nm, that can be used in the wavelength range 300-900 nm. Spectral scanning is achieved with a computer-controlled stepper motor. Time-dependent signals of the photomultiplier (Hamamatsu, R666), have been measured using the oscilloscope (Tektronix DSA 601, 2 ns time resolution) with the exception of weak spectroscopic signals which have been measured with a multi-channel analyzer (Lecroy 3001, QVT analyzer). The analyzer has been operated in the charge acquisition mode (Q-mode, 40 ns time resolution). For each monochromator setting, the charge distribution of 3000 spectroscopic signals (300 Hz discharge repetition rate during an acquisition time of 10 seconds) was measured. Data were transferred via a CAMAC-IEEE interface to computer for analysis. The photon counting mode (V-mode) has not been used because the probability of measuring two photons during a single HV pulse was not negligible.

4.1.5 Ozone absorption measurement

The average ozone concentration in wire-cylinder configuration I has been measured by means of absorption measurements (Fig. 4.6). A high pressure Hg-lamp was used as light source and the transmitted intensity was measured using a monochromator. Ozone has a broad absorption spectrum with a well known absorption cross section. The maximum absorption occurs at a wavelength of 254 nm where the absorption cross section at a gas temperature of 298 K is

$\sigma_{max}(O_3) = 1.41\ 10^{-21}$ m^2 per ozone molecule (Finlayson-Pitts, 1986). For a wavelength of 291 nm the cross section is 10 times lower. The ozone concentration $n(O_3)$ is calculated using Beer's law:

$$n(O_3) = \frac{1}{\sigma(O_3)\, l} \ln\left(\frac{I}{I_0}\right) \tag{4.1}$$

where I and I_0 are respectively the light intensity with and without absorption and l is the optical path length. The accuracy of the concentration measurement can be optimized by selecting a combination of wavelength and optical path length with $I/I_0 \approx 0.5$.

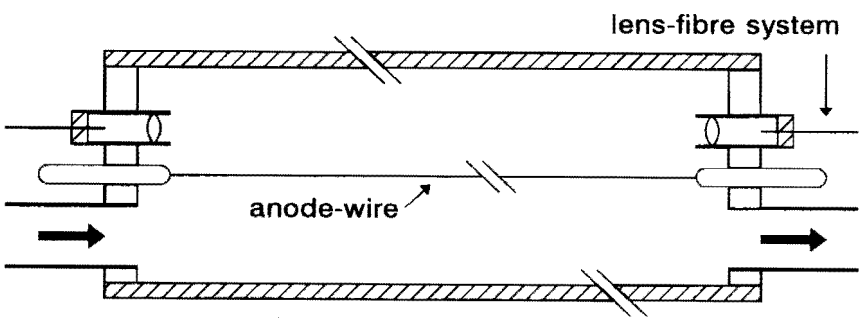

Fig. 4.6 Optical scheme of ozone absorption measurement.

4.2 Emission spectroscopy

4.2.1 Spectroscopic investigations of corona discharges

For spectroscopic investigations of the light emitted by corona discharges, preferentially self-repetitive DC coronas in tip-plate configurations were used in the past. The excellent reproducibility in both space and time of positive streamers or Trichel discharges under these conditions, offers the possibility to measure relative weak emission lines with high wavelength resolution using photon counting techniques. A detailed study of the N_2 emission spectrum was performed by Hartmann (1977) who used a positive streamer corona in a tip-plate configuration (10 mm gap) in air at 1 bar and a monochromator (Jarrel-Ash) with a focal length

of 3.4 m. The high wavelength resolution of the spectra enabled him to determine the gas temperature from individual rotational emission lines. In spite of the high repetition rate of the streamers (for d_g=12 mm and V=9.5 kV: f=10 kHz) the gas temperature appeared to be close to the room temperature: T_g=300-400 K (Hartmann, 1977). The vibrational structure of the emission spectrum was used to determine the vibrational temperature T_v. When raising the voltage from 9.5 kV to 12.3 kV, T_v increased from 300 to 1200 K (the average current from 35 to 70 μA, streamer speed from 2.3 to $4.6 \cdot 10^5$ m/s and repetition frequency from 10 to 12.6 kHz, Hartmann, 1974). Measurements of the relative intensity of N_2^+ and N_2 emission lines revealed a high average electron energy in the light emitting streamer head: $\epsilon_h = \sim 10$ eV (Hartmann, 1974, 1977).

Spyrou and Manassis (1989) performed similar but spatial resolved measurements (positive DC corona, tip-plate configuration with 20 mm gap distance, filled with ambient air at 1 bar). These measurements show that, during streamer propagation, ϵ_h first increases from ~5 eV to a maximum of ~9 eV at 2 mm distance from the tip and then decreases to ~7 eV before arrival at the cathode. Also measurements of the rotational (gas) temperature have been made as a function of the position along the gap axis (Spyrou et al., 1992). These measurements show that in positive DC corona discharges the gas temperature may be much higher near the anode-tip than near the cathode plate.

Also for the measurement of the electron density in coronas, emission spectroscopy has proven to be a useful tool. Bastien al. (1976, 1977, 1979) calculated the electron density from the line broadening of H_α and H_β emission lines (Stark effect) in a corona discharge in oxygen with minute concentrations of hydrogen. Under the conditions of the experiments (p=300 Torr, aborted spark regime) the maximum electron density in the streamer head region is determined at 10^{21} m^{-3}. Gravendeel (1987) investigated the negative corona discharge in the Trichel regime where the much higher discharge repetition frequency (about 1 MHz) is even more suitable for photon counting techniques. He determined from continuum radiation measurements (free-bound radiation from electron-ion recombination) that during a Trichel pulse the electron density increases from 10^{21} m^{-3} to 10^{24} m^{-3} within approximately 1 ns.

Time-resolved photon counting spectroscopy with a negative corona in the Trichel regime, has recently been used to identify molecular species that are formed in air and flue gas (Teich, 1992, 1993). Rate coefficients for the formation and decay of species like NO and N_2O have been measured under conditions which are close to those used in corona induced $deNO_x$ (weakly ionized plasma, atmospheric pressure).

In this section the methods for determination of the average electron energy ϵ_a, the vibrational temperature T_v, and the gas temperature T_g, previously applied to self repetitive positive streamer corona by Hartmann (1977), are discussed. A new

investigation of these quantities in coronas produced with externally applied pulses is justified because the conditions under which streamers are formed and propagate are different from those in DC coronas. The energy of electrons in a streamer discharge is an essential parameter that directly influences the quantity and type of radicals and ions that are formed in binary electron-molecule collisions. Hartmann's study was primarily directed to the understanding of electronic and vibrational excitation processes of N_2 when the streamer front passes through the gas. Emphasis will be given here to the accuracy of the method for determination of the average electron energy.

The structure of the N_2 emission spectrum will be discussed first in **4.2.2.** Then electronic excitation and de-excitation (quenching) and vibrational excitation and de-excitation (relaxation) are discussed in respectively **4.2.3** and **4.2.4**. The method for the determination of the average electron energy in a streamer is described in **4.2.5.** Finally in **4.2.6**, the theory needed for determination of the rotational temperature will be presented.

4.2.2 The structure of the N_2 emission spectrum

The spectrum of light emitted by primary streamers in air is dominated by emission lines originating from electronic excited states of the N_2 molecule and the N_2^+ ion. The conventional spectroscopic notation of the main electronic excited states, indicating angular momentum, spin and also symmetry properties of molecules (Herzberg, 1955), is replaced here by a simpler notation. In the following, the electronic states of neutral nitrogen molecules $N_2(X^1\Sigma_g^+)$, $N_2(A^3\Sigma_u^+)$, $N_2(B^3\Pi_g)$, $N_2(C^3\Pi_u)$ and $N_2(E^3\Sigma_g^+)$ will be denoted as respectively $N_2(X)$, $N_2(A)$, $N_2(B)$, $N_2(C)$ and $N_2(E)$. Similarly, the electronic states nitrogen ions $N_2^+(X^2\Sigma_g^+)$ and $N_2^+(B^2\Sigma_u^+)$ will be denoted as respectively $N_2^+(X)$ and $N_2^+(B)$. The main radiative electronic transitions are indicated in the (simplified) potential energy diagram of N_2 and N_2^+, shown in Fig. 4.7.

According to the quantum theory of electronic motion in molecules, the vibration of the nuclei causes discrete vibrational energy levels, denoted with quantum number v, that are superimposed on the electronic energy levels (Herzberg, 1955). There are no strict selection rules for the change of vibrational quanta v in electronic transitions. Thus, many transitions from any vibrational level v' of an electronic excited state to any vibrational level v'' of another electronic state are allowed. Accordingly, for each electronic transition a number of emission lines with different wavelengths $\lambda(v',v'')$ can be detected. All the emission lines together, belonging to the same electronic transition, form a system of spectral lines.

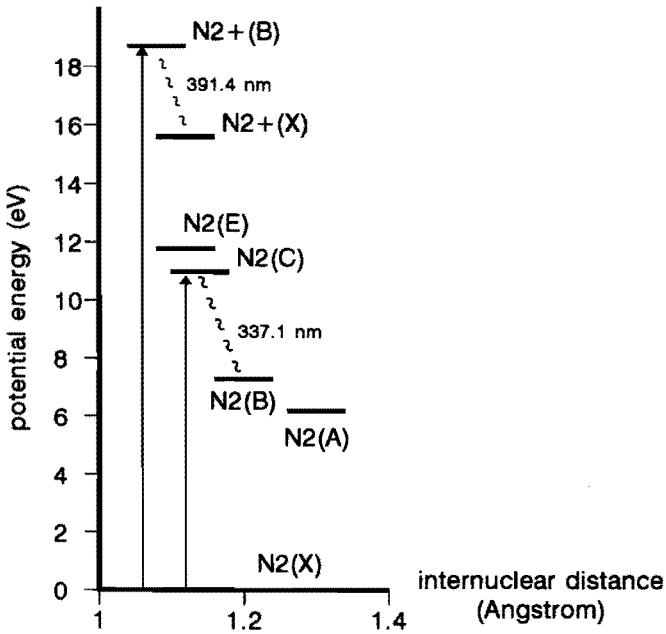

Fig. 4.7 Part of the potential energy diagram of N_2 and N_2^+ (after Gilmore, 1965).

The Franck-Condon principle states that "vertical" transitions between electronic states, i.e. transitions with a small change in relative position and velocity of the nuclei, have a high probability. The minima of the potential energy curves of the excited states $N_2(C)$ and $N_2^+(B)$ are at about the same value of internuclear distance as the minimum of ground state $N_2(X)$. Therefore, according to the Franck-Condon principle, very favourable conditions exist for direct electron impact excitation to these states:

$$N_2(X)_{v=0} + e(>11.0eV) \rightarrow N_2(C)_{v'} + e$$
$$N_2(X)_{v=0} + e(>18.7eV) \rightarrow N_2^+(B)_{v'} + 2e \qquad (4.2)$$

Because of their relative high intensity, the most interesting systems, with respect to diagnostics, are the *Second Positive System* (SPS) of N_2 and the *First Negative System* (FNS) of N_2^+:

$$SPS: \quad N_2(C)_{v'} \rightarrow N_2(B)_{v''} \quad \lambda(v'=0, v''=0) = 337.1\ nm$$
$$FNS: \quad N_2^+(B)_{v'} \rightarrow N_2^+(X)_{v''} \quad \lambda(v'=0, v''=0) = 391.4\ nm \qquad (4.3)$$

The SPS of N_2 accounts for more than 95% of the total light intensity of streamer discharges in air and is therefore the most easy to detect. The strongest emission lines belong to the transitions between the levels $v' = 0$ and $v'' = 0$. The rotation of the N_2 molecule also causes discrete energy levels that are superimposed on the vibrational energy levels (not shown in Fig. 4.7) and denoted with the quantum number J. High wavelength resolution ($\Delta\lambda < 0.05$ nm) is usually required to resolve the rotational line structure of an electronic-vibrational transition (v', v'').

4.2.3 Electronic excitation and quenching

In electrical discharges, in general, the concentration of molecules in an excited state depends on a large number of collisional and radiative processes for production and loss of this specific state. Sometimes, the balance equation for production and loss can be numerically solved, for instance in an inductively coupled plasma with power interruption (Fey, 1993). In a streamer discharge, where both the electric field and the electron density vary strongly as function of both position and time, drawing up the balance of excitation and de-excitation seems, at first sight, an impossible task.

However, as pointed out previously by Hartmann (1977), a number of excitation and de-excitation processes can be neglected. The collisional-radiative balance in the fast propagating streamer head is, for any vibrational level v' of $N_2(C)$ and $N_2^+(B)$, dominated by four processes:

1) Direct electron impact excitation and ionization
2) De-excitation by collisions with neutrals (quenching)
3) Spontaneous emission
4) Vibrational excitation and relaxation

According to Hartmann (1977) the following processes play a minor role in light emission from the streamer front:

5) Indirect excitation and ionization via an intermediate excited or ionized state
6) (Auto-) absorption of photons
7) Energy transfer between electronic excited molecules
8) Recombination of atoms (e.g. $N + N \rightarrow N_2(C)$)

Examples of process 5 are (a) ionization forming the nitrogen ion ground state $N_2^+(X)$ followed by excitation to $N_2^+(B)$ and (b) excitation of $N_2(C)$ via the metastable $N_2(A)$. The processes 5 up to 8 have in common that they involve collisions between two particles that must previously have been produced in the

discharge. These processes, referred to as *indirect processes*, can be neglected when compared to the *direct processes*, 1 up to 4, because all particles produced in the discharge (electrons, ions, excited states, photons, dissociation fragments) have a density that remains far below the neutral gas density. This assumption is affirmed by results of the numerical streamer model (**2.3.4**) and is associated with the very short time for excitation and ionization in the streamer head, $\tau_h = \delta_h / v_s \approx 50\mu m / 5 \cdot 10^5$ m/s $\approx$ 0.1 ns. In such a short period, the probability that a molecule undergoes more than one inelastic collision (leading to excitation in two steps) is very small.

The arguments mentioned above for neglecting completely the indirect excitation processes ignore the possibility that, in a streamer corona reactor with low gas flow and high pulse repetition rate, metastable vibrational or electronic excited states may reach a much higher density than in a single streamer. Although no direct proof for dominant direct excitation is available, Hartmann's (1978) measurements of relative transition probabilities for a large number of combinations (v',v'') of the SPS of N_2, confirm the assumption of direct excitation: these transition probabilities, which are determined from measured line intensities of a DC corona discharge assuming excitation from the electronic ground state to $N_2(C)$, compare very well with data that have been determined with basically different methods. An indirect excitation process of $N_2(C)$, e.g. via the metastable $N_2(A)$, was unlikely to occur in Hartmann's experiments because it would have resulted in a large modification of the measured vibrational distribution in $N_2(C)$. In the DC corona used by Hartmann, streamers follow exactly the same path as previous ones with a frequency of about 10 kHz. Because the repetition rate of pulsed corona streamers is generally lower (of the order of 100 Hz) and streamers will often propagate along different paths, the probability that electronic excited metastables influence the excitation processes in pulsed corona streamers is even much lower.

It is assumed that after direct excitation (process 1), the population density of an excited state depends only on collisional quenching (process 2) and spontaneous emission (process 3). The problem of vibrational excitation and relaxation will be dealt with separately in **4.2.4**.

In air at 1 bar the decay of the $N_2(C)$ state and the $N_2^+(B)$ state is mainly due to non-radiative collisional quenching (de-excitation) in two-body collisions with N_2 and O_2 molecules. The rate of loss of excited molecules with density n^*, after the source of excitation is removed, is given by:

$$\frac{dn^*}{dt} = -\frac{n^*}{\tau_0} - (k_1 p_1 + k_2 p_2 + \ldots) \qquad (4.4)$$

where τ_0 is the natural life time of the excited state, k_1, k_2 are the quenching

coefficients and p_1, p_2 the partial pressures of the different molecules that constitute the gas. The fraction of molecules g that radiates, is given by the ratio of the life time τ to the natural life time τ_0. According to Eq. 4.4 this fraction can be expressed as:

$$g = \frac{\tau}{\tau_0} = \frac{1}{(1 + k_1 p_1 + k_2 p_2 + ...)} \tag{4.5}$$

Table 4.1 gives an overview of the quenching coefficients for $N_2(C)$ and $N_2^+(B)$, obtained in several experimental investigations. Some authors give quenching rate coefficients (unit $m^{-3}s^{-1}$) that have been converted to quenching coefficients (unit m^{-3} or bar^{-1}) using the values of natural life times mentioned by these authors.

excited state	k_{N2} (bar^{-1})	$k_{O2}^{(1)}$ (bar^{-1})	$k_{air}^{(2)}$ (bar^{-1})	Δk (%)	τ_0 (ns)	ref.
$N_2(C)_{v'=0}$	12	334.5	76.5	13	44.5	(3)
	8.4	214	49.5	5	30.3	(4)
$N_2(C)_{v'=1}$	25	278	75.6	6	37	(4)
$N_2^+(B)_{v'=0}$	720	810	1170	13	65.8	(3)
	1225			15	61	(5)
$N_2^+(B)_{v'=1}$	2242			15	60	(5)

1) Determined from N_2-O_2 mixtures
2) 80% N_2 - 20% O_2 mixture
3) Mitchell, 1970
4) Millet et al., 1973
5) Jolly and Plain, 1983

Table 4.1 Collisional quenching coefficients k with accuracy Δk and natural life times τ_0 for $N_2(C)$ and $N_2^+(B)$

The data in Table 4.1 show that quenching of $N_2^+(B)$ in air is about 15 times stronger than quenching of $N_2(C)$. It also appears that the quenching coefficients of the $v'=1$ levels are about twice larger than the coefficients of the $v'=0$ levels. This will be further discussed in **4.2.4.** Recent accurate measurements of the natural life times of the $v'=0$ levels yield:

$N_2(C)_{v'=0}$ $\tau_0 = 41 \pm 2$ ns (Carr and Dondes, 1977)
$N_2^+(B)_{v'=0}$ $\tau_0 = 60 \pm 1$ ns (Smith et al., 1975)

According to Mitchell's (1970) data and Eq. 4.5 the fraction of excited molecules that radiate and the life time of the excited states are in air at 1 bar:

$N_2(C)_{v'=0}$	$g_C = 1.3\ 10^{-2}$	τ_C = 0.52 ns
$N_2^+(B)_{v'=0}$	$g_B = 1.2\ 10^{-3}$	τ_B = 0.07 ns

τ_C is larger than the characteristic time for direct excitation of the gas in the active region of the primary streamer (0.1 ns), whereas τ_B is smaller. The calculated value $\tau_C = 0.5$ ns is close to the value (0.8 ns) which was measured using time-resolved single photon spectroscopy by Kondo and Ikuta (1980).

4.2.4 The influence of vibrational relaxation

In streamer discharges in air and flue gas a predominant part of the energy of electrons will be transformed to molecular vibrations of N_2 (see **2.4.3**). As a consequence of vibrational excitation of the electronic ground state, the vibrational distribution of electronic excited states will be modified. A schematic representation of vibrational and electronic excitation processes and de-excitation processes (quenching and relaxation), is given in Fig. 4.8. Vibrational excitation and relaxation of $N_2(X)$ in a streamer discharge in (humid) air or flue gas involves a large number of processes. Even if these processes can be properly incorporated in a model, the lack of accurate data for vibrational relaxation prevents one from calculating a realistic distribution among the vibrational states.

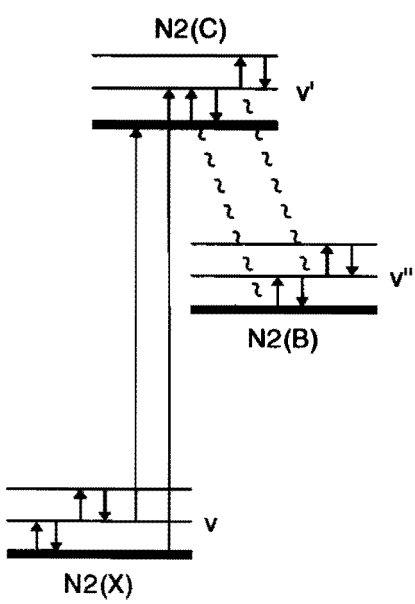

Fig. 4.8

Vibrational and electronic excitation and de-excitation processes which influence the relative intensities of the emission lines of the SPS of N_2.

In order to investigate the influence of vibrational excitation of $N_2(X)$ on the emission lines of the SPS, the vibrational distribution of $N_2(X)$ is characterized by a Boltzmann distribution with vibrational temperature T_v. The relative number of molecules $\Pi(v)$ in vibrational excited state v is:

$$\Pi_X(v) = \frac{1}{Q_v} \exp\left(\frac{-\omega_v}{T_v}\right) \tag{4.6}$$

where ω_v is the vibrational quantum of N_2 (ω_v=3360 K) and Q_v the state sum:

$$Q_v = 1 + \exp\left[\frac{-\omega_v}{T_v}\right] + \exp\left[\frac{-2\omega_v}{T_v}\right] + \ldots \tag{4.7}$$

The concept of a vibrational temperature T_v is applicable when thermal equilibrium exists between vibrational excitation and de-excitation processes. Although thermal equilibrium for vibrational states is probably not reached during the period of light emission by a streamer discharge (~0.1 ns for the primary streamer, ~100 ns for the secondary streamer), T_v is used here as a variable input parameter to investigate theoretically the influence of vibrational excitation in the ground state on the emission spectrum.

Assuming only direct electronic excitation and neglecting transitions in between vibrational levels of $N_2(C)$, this distribution can be calculated as (Herzberg, 1955):

$$\Pi_C(v') = \sum_v \Pi_X(v)\, q(v\text{-}v') \tag{4.8}$$

where $q(v\text{-}v')$ are the Franck-Condon factors that are well known for transitions in N_2. Those for the lowest vibrational levels of the transition $N_2(X) \rightarrow N_2(C)$ are given in Table 4.2:

	$v'=0$	$v'=1$	$v'=2$
$v=0$	0.546	0.306	0.107
$v=1$	0.347	0.0797	0.267
$v=2$	0.0918	0.361	0.00261

Table 4.2 Franck-Condon factors $q(v\text{-}v')$ for the transition $N_2(X) \rightarrow N_2(C)$ (McCallum et al., 1972).

The relative numbers of molecules in the two first excited states v' of $N_2(C)$ have been calculated with Eqs. 4.6 and 4.8 for T_v=300, 600 and 1200 K, see Table 4.3.

T_v (K)	$\Pi(v=1)/\Pi(v=0)$	$\Pi(v=2)/\Pi(v=0)$	$\Pi(v'=1)/\Pi(v'=0)$	$\Pi(v'=2)/\Pi(v'=0)$
300	$1.3\ 10^{-5}$	$1.8\ 10^{-10}$	0.5604	0.1960
600	$3.4\ 10^{-2}$	$1.2\ 10^{-3}$	0.5540	0.2082
1200	$1.9\ 10^{-1}$	$3.4\ 10^{-2}$	0.5431	0.2553

Table 4.3 Normalized distribution of the lowest excited states of $N_2(X)$ and $N_2(C)$ assuming different vibrational temperatures T_v.

The vibrational distribution $\Pi_C(v')$ in the electronic state $N_2(C)$ can also be measured from the relative intensities of emission lines of the SPS of N_2:

$$\Pi_C(v') = \sum_{v''} I(v',v'') \tag{4.9}$$

where $I(v',v'')$ are the intensities of all detectable emission lines according to the same upper level v' of the SPS of N_2. In principle T_v can be calculated from the measured distribution $\Pi_C(v')$ (Mnatsakanyan and Podlubnyi, 1972). Table 4.3 shows that $\Pi_C(v')$ is only weakly dependent on $\Pi_C(v)$. The consequence of this weak dependence is that the accuracy of the measured intensities $I(v',v'')$ must be very high in order to determine which value for T_v fits best with experimental results.

So far, transitions in between vibrational levels of $N_2(C)$ have not been considered and those of $N_2(X)$ have been assumed to be in equilibrium. The quenching coefficient for $N_2(C)_{v'=1}$ (Table 4.1) is several times larger than for $N_2(C)_{v'=0}$. Also for $N_2^+(B)$ a stronger quenching of $v'=1$ than for $v'=0$ is observed. According to Calo and Axtmann (1971) the decay of $N_2(C)_{v'}$, for $v'>0$, is not only due to transitions to lower electronic states (quenching) but also to transitions to $v'=0$, i.e. vibrational relaxation. They were able to determine, though with low accuracy, the coefficients for quenching and relaxation of $N_2(C)_{v'=1}$ in N_2 separately.

quenching of $v'=0$ $\quad k_0 = 13.6 \pm 4\%$ bar^{-1}
quenching of $v'=1$ $\quad k_1 = 10.3 \pm 50\%$ bar^{-1}
relaxation $v'=1 \rightarrow v'=0$ $\quad k_{10} = 18 \pm 30\%$ bar^{-1}

The probability that electrons "cascade" from the $v'=1$ level to the $v'=0$ level is even higher than the quenching of the $v'=0$ level. Data for vibrational relaxation of $N_2(C)_{v'>0}$ by O_2 molecules are not available. The data for N_2 can be used for a rough estimation of the relative amount of excited states with $v'=0$ that produced

via relaxation from $v' = 1$:

$$\frac{\Delta\Pi_C(v'=0)}{\Pi_C(v'=0)} = \frac{\Pi_C(v'=1)}{\Pi_C(v'=0)} \frac{k_{10}}{1 + k_1 + k_{10}} \tag{4.10}$$

Inserting the ratio $\Pi(v'=1)/\Pi(v'=0)$ for T_v=300 K, given in Table 4.3, and the coefficients k_{10} and k_1 given above, an increase of $\Pi_C(v'=0)$ by 35% can be calculated. Calo and Axtmann suggest that the fast vibrational relaxation of $N_2(C)_{v'>0}$ occurs by collisions with $N_2(X)$ through the formation of an intermediate N_4 molecule. The details of vibrational relaxation of $N_2(C)_{v'}$ are still obscure and no data are available for vibrational relaxation of the excited ion state $N_2^+(B)$.

4.2.5 The intensity ratio of the N_2^+(391.4) and the N_2(337.1 nm) emission lines.

The emission lines corresponding to the $v'=0$ to $v''=0$ transition of the FNS of N_2^+ and the SPS of N_2 are designated here as the N_2^+(391.4) and the N_2(337.1 nm) emission lines. Experimental cross sections σ_B and σ_C for the production of these lines by direct excitation from the ground state $N_2(X)$, published by different authors, are compared in Fig. 4.9. The cross sections of Cartwright (1977), originally for the total emission of the SPS, have been normalized to fit the peak value of cross sections of Burns (1969). This peak value is also close to that of Aarts (1969).

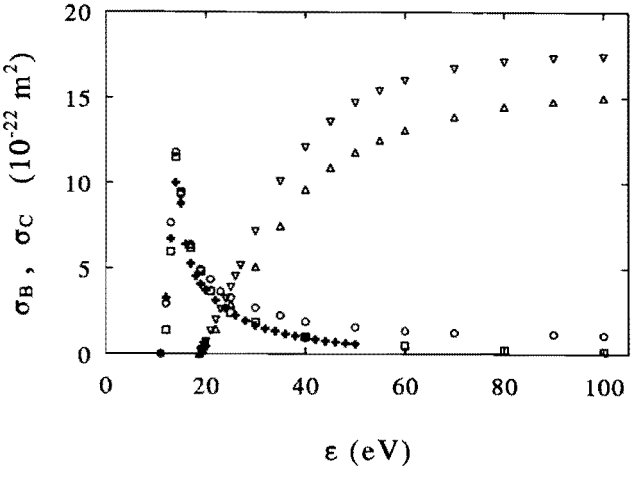

Fig. 4.9 *Experimental cross sections for $v'=0$ to $v''=0$ transitions of: N_2 SPS: (○) Burns (1969), (□) Aarts (1969) and (+) Cartwright (1977). N_2^+ FNS: (▽) Borst (1970), (△) Mc Conkey (1971).*

The threshold electron energies for the production of the $N_2^+(391.4)$ and the $N_2(337.1\ nm)$ emission lines, are respectively 18.7 and 11.0 eV. Because of the large difference between these thresholds the intensity ratio of the $N_2^+(391.4)$ and the $N_2(337.1\ nm)$ emission lines depends strongly on the average electron energy ϵ_a in the streamer.

The intensity ratio of the $N_2^+(391.4)$ and the $N_2(337.1\ nm)$ emission lines can be calculated from integrations of the appropriate cross sections over the electron energy distribution function $f(E/n, \epsilon)$:

$$\frac{\Pi_B}{\Pi_C} = \frac{\int_0^\infty f(E/n,\varepsilon)\ \sqrt{\varepsilon}\ \sigma_B(\varepsilon)\ d\varepsilon}{\int_0^\infty f(E/n,\varepsilon)\ \sqrt{\varepsilon}\ \sigma_C(\varepsilon)\ d\varepsilon} \tag{4.11}$$

The ratio Π_B/Π_C has been calculated as a function of E/n using solutions of the Boltzmann equation for $f(E/n, \epsilon)$ (see **2.3.3**) and cross sections of McConckey (1971) for σ_B and cross sections of Burns (1969) for σ_C, see Fig. 4.10. Also the average electron energy ϵ_a and the characteristic electron energy D_T/μ_e are shown as functions of E/n. The average electron energy has been used to calculate also the ratio Π_B/Π_C from Maxwell electron energy distribution functions.

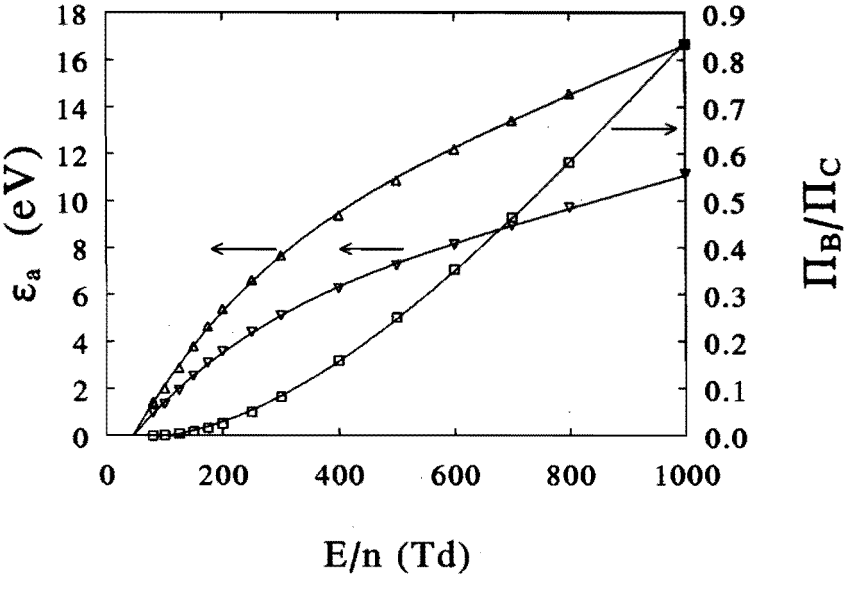

Fig. 4.10 *(□) Ratio Π_B/Π_C calculated with Boltzmann solution of eedf's (see 2.3.3), (△) average electron energy ϵ_a, (▽) characteristic electron energy D_T/μ_e.*

In principle, the strong correlation between the intensity ratio Π_B/Π_C and E/n can be used to determine E/n or (without the use of Boltzmann calculations and assuming a Maxwell eedf) ϵ_a in the discharge from the measured intensity ratio I_B/I_C:

$$\frac{\Pi_B}{\Pi_C} = \frac{I_B}{I_C} \cdot \left[\frac{g_B\, C(\lambda = 391.4\ nm)}{g_C\, C(\lambda = 337.1\ nm)} \right]^{-1} \tag{4.12}$$

where $C(\lambda)$ is the transmission factor of the optical system (fibres, monochromator, photomultiplier). Three limitations for the application of this "relative line intensity method" to a (primary) streamer discharge exist:

1) The most serious limitation of the method is due to the fact that in the propagating primary streamer head E/n and n_e are strongly varying function of both space and time. However, because models (see **2.3.4**) show that almost all electrons are produced in a electric field which is close to the maximum field strength, it is reasonable to assume that the light emitted by primary streamers is dominated by radiation from excited states produced at the maximum field strength.
2) The method is also limited by the spatial and temporal resolution of the measuring method (see **4.1.4**). The spatial resolution is about 10 mm so that a streamer propagating with a velocity of 1 mm/ns through the detection volume causes a light emission signal with a duration of about 10 ns. The photomultiplier pulse response has a rise time of ~2 ns and a decay time of ~10 ns. The signal is measured with the multi channel analyzer integrating over 40 ns in time. The pulse response of the photomultiplier is thus short enough when compared to the integration time of the signal. The measured integrated signal is proportional to the average light emission of streamers propagating over a length of ~10 mm.
3) Finally, the relative line intensity method is limited by the uncertainty in experimental data. Errors in the calculation of the ratio Π_B/Π_C as function of E/n are made because of the lack of accuracy of collisional quenching coefficients and cross sections. It is better not to take vibrational relaxation of the $N_2(C)$ state into account because no data for a possible vibrational relaxation in the $N_2^+(B)$ state are available. The quenching coefficients of Mitchell (1970), giving $g_B/g_C \approx 0.1$, possibly include the effect of vibrational relaxation in both states.

The *measured ratio* Π_B/Π_C involves two different integrations: (a) An integration of light within the streamer head region and (b) an integration within the detection volume. For this reason, the measured "integrated" ratio will be denoted as $<\Pi_B>/<\Pi_C>$. It is possible to evaluate the influence of limitation (1) using results of the numerical streamer model. Assuming that the characteristics of the streamer

do not change while propagating through the detection volume, the measured ratio $<\Pi_B>/<\Pi_C>$ may be calculated with:

$$\frac{<\Pi_B>}{<\Pi_C>} = \frac{n_B(t)}{n_C(t)} = \frac{\int_0^t k_B(E/n)\, n_e(t')\, n\, dt'}{\int_0^t k_C(E/n)\, n_e(t')\, n\, dt'} \qquad (4.13)$$

$$\text{with} \quad k_{B,C}(E/n) = \int_0^\infty f(E/n,\varepsilon)\, \sqrt{\varepsilon}\, \sigma_{B,C}(\varepsilon)\, d\varepsilon$$

where n_B and n_C are local densities along the streamer axis of the radiative excited states $N_2^+(B)$ and $N_2(C)$. In order to investigate the influence of large changes in the maxima of E/n and n_e on the measured ratio $<\Pi_B>/<\Pi_C>$, the model results obtained with code I and code II, where the maximum space charge fields are respectively 640 and 1630 Td (see **2.3.4**), have been used. Fig. 4.11 shows E/n, n_B and n_C as a function of time for a streamer head at 10 mm distance from the anode. Because of the different electric field gradients and velocities of the streamer heads calculated with code I and code II, the time needed for the densities of the excited states to growth two orders of magnitude is respectively ~0.1 and ~0.02 ns. The influence of molecular quenching on n_B and n_C is shown. The ratios n_B/n_C that can be calculate with numerical codes I and II, are respectively 0.2 and 0.7. If these ratios are set equal to the ratio Π_B/Π_C in Fig. 4.10, one obtains E/n values of respectively ~500 and ~900 Td, i.e. ~90% and ~55% of the field maxima.

We have shown that the relative line intensity method is not accurate for the determination of maxima in E/n or ϵ_a in a primary streamer. Nevertheless, the measured ratio $<\Pi_B>/<\Pi_C>$ can be used for a rough estimation of these values. In spite of difficulties encountered in determining the maximum electric field in the streamer from the measured ratio $<\Pi_B>/<\Pi_C>$, qualitative measurements of this ratio are useful because it depends strongly on the E/n maximum in the streamer. The relative line intensity method can be applied to detect possible changes in the space charge field of propagating primary streamers as function of their position in the gap or as function of HV pulse parameters. Because quenching coefficients are known for collisions with N_2 and O_2 molecules separately (Table 4.1), also a qualitative investigation of possible changes in E/n, when the relative O_2 content in a N_2-O_2 mixture is varied, can be performed.

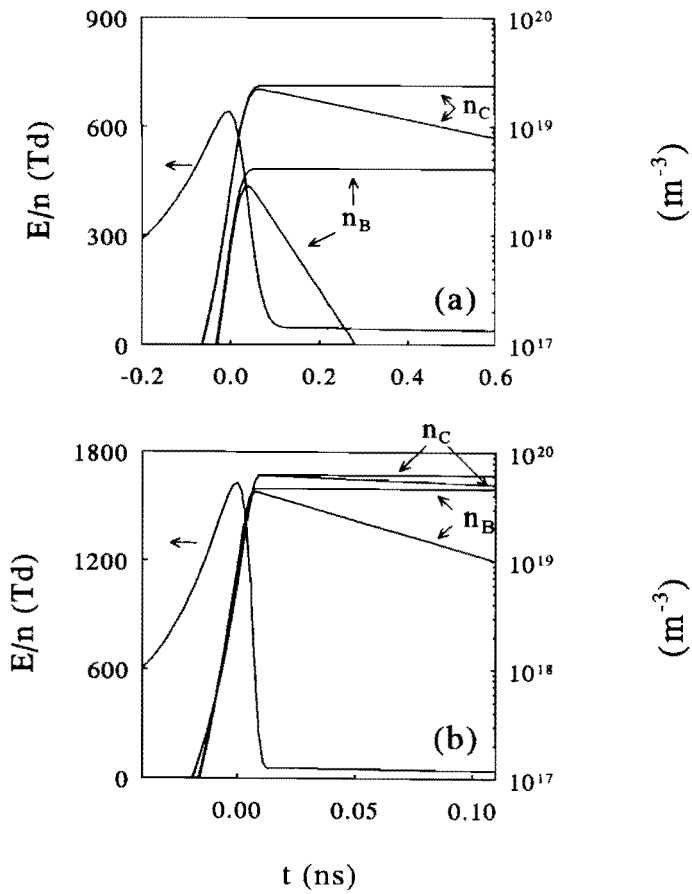

Fig. 4.11 The densities n_B, n_C in a streamer at 10 mm from the anode, (a) calculated with code I, (b) with code II (see Figs. 2.21 and 2.23).

4.2.6 Simulation of the rotational band structure

Owing to the small energy difference between rotational energy levels (10^{-4}-10^{-3} eV), the transfer between translational and rotational energy is a fast process. In principle, the rotational temperature T_r (that equals the gas temperature T_g) can be determined from relative line intensity measurements of rotational emission lines. However, in a pulsed corona discharge in air at 1 bar, even the emission intensity of the strongest vibrational band, the (0,0) band of the SPS, is too weak to resolve the rotational line structure entirely. In an alternative method, the rotational temperature T_r is obtained by parameter fitting, comparing the shape of the

measured band with the shape of a simulation of the band (e.g. Phillips, 1975; Czernichowski, 1987). This method is applied here.

In air at 300 K, about 5 collisions between molecules are sufficient to cause a Boltzmann distribution among the rotational levels at the same temperature as the neutral gas temperature and the rotational relaxation time τ_R is about 0.6 ns (Lambert, 1977). This time is long when compared to the characteristic time of the primary streamer (0.1 ns) but short when compared to the characteristic time of the secondary streamer (100 ns). Therefore the rotational temperature obtained from the emission of secondary streamers can be used to determine the neutral gas temperature in the discharge.

N_2 molecules in the electronic ground state $N_2(X)$ are principally in the $v=0$ level (**2.4.4**). Excitation to the $N_2(C)$ state mainly occurs by direct excitation (**2.4.3**). In electron impact excitation no large change in the angular momentum J of N_2 molecules occurs and therefore the rotational distribution in the $N_2(C)$ state is practically the same as the distribution in the ground state. In case of thermal equilibrium between the rotational energy levels, the rotational distributions in $N_2(X)$ and $N_2(C)$ are given by the Boltzmann law:

$$f_{J'} = (2J' + 1) \exp\left[-J'(J'+1)\frac{hcB_x}{kT_r}\right] \tag{4.14}$$

where $B_x = 1.9898$ cm^{-1}.

According to the selection rule for the change of angular momentum J in transitions between electronic states ($\Delta J = 0, \pm 1$), the rotational spectrum of a vibrational band $v' \rightarrow v''$ consists of three branches.

$$\begin{aligned} &P: \quad J'-1 \rightarrow J'' \\ &Q: \quad J' \rightarrow J'' \\ &R: \quad J'+1 \rightarrow J'' \end{aligned} \tag{4.15}$$

The upper and lower electronic states of the transition $N_2(C) \rightarrow N_2(B)$ are $^3\Pi$ states. This notation indicates that the quantum number for angular momentum Λ, equals 1 and that the total spin of the molecules Σ can take the three values -1, 0 and 1. Two different cases can be distinguished with respect to the total angular momentum $\Omega = \Lambda + \Sigma$. For low values of the rotational quantum number J the molecular spin Σ is strongly coupled to the internuclear axis ($\Delta\Sigma = 0$). This case is referred to as Hund's case (a). With increasing quantum number J the spin becomes uncoupled. When complete uncoupling occurs, the quantum number of total angular momentum Ω, is not defined. This case is generally referred to as Hund's case (b). First the simulation of the rotational spectrum, assuming Hund's case (a), is considered. Then the correctness of this assumption will discussed.

The total angular momentum $\Omega = \Lambda + \Sigma$ of each $^3\Pi$ state can take the values 0, 1 and 2. The *P* and *R* branches are split in three sub-branches: $^3\Pi_0 \rightarrow {}^3\Pi_0$, $^3\Pi_1 \rightarrow {}^3\Pi_1$ and $^3\Pi_2 \rightarrow {}^3\Pi_2$. On account of the selection rule $\Delta\Sigma = 0$ (a transition with $\Delta J = 0$ is not allowed when $\Omega = 0$) only two sub-branches exist for the Q-branches: $^3\Pi_1 \rightarrow {}^3\Pi_1$ and $^3\Pi_2 \rightarrow {}^3\Pi_2$.

The wave numbers of the rotational lines are obtained from the rotational energy levels (also referred to as term values) $F_{\Omega,J}$. For the band v'-v'' the wave numbers for the different branches P, Q and R are:

$$
\begin{aligned}
P: &\quad \nu^P_{\Omega,J} = \nu_0 + F_{\Omega,J-1} - F_{\Omega,J}\,, \quad \Omega = 0,1,2 \\
Q: &\quad \nu^Q_{\Omega,J} = \nu_0 + F_{\Omega,J} - F_{\Omega,J}\,, \quad \Omega = 1,2 \\
R: &\quad \nu^R_{\Omega,J} = \nu_0 + F_{\Omega,J+1} - F_{\Omega,J}\,, \quad \Omega = 0,1,2
\end{aligned}
\tag{4.16}
$$

where ν_0 is the band origin. The term values $F_{\Omega,J}$ for rotational triplet states may be expressed by semi-empirical formulae (Herzberg, 1955):

$$
\begin{aligned}
F_{0,J} &= B_v \left(J(J+1) - \sqrt{Z_1} - 2Z_2 \right) - D_v \left(J - \tfrac{1}{2} \right)^4 \\
F_{1,J} &= B_v \left(J(J+1) + 4Z_2 \right) - D_v \left(J + \tfrac{1}{2} \right)^4 \\
F_{2,J} &= B_v \left(J(J+1) + \sqrt{Z_1} - 2Z_2 \right) - D_v \left(J + \tfrac{3}{2} \right)^4 \\
Z_1 &= Y_v \left(Y_v - 4 \right) + \tfrac{4}{3} + 4J(J+1) \\
Z_2 &= \frac{\left(Y_v(Y_v - 1) - \tfrac{4}{9} - 2J(J+1) \right)}{3\,Z_1}
\end{aligned}
\tag{4.17}
$$

where B_v and D_v are rotational constants and Y_v is a spin-axis coupling constant that accounts for the transition from Hund's case (a) to Hund's case (b) with increasing *J*. The values of these constants for $v' = 0$ and $v'' = 0$ are given in Table 4.4.

state	B_v (cm^{-1})	Y_v	D_v x 10^6 (cm^{-1})
$N_2(C)_{v'=0}$	1.8149	21.5	6.7
$N_2^+(B)_{v'=0}$	1.62849	25.9	6.4

Table 4.4 Rotational constants for $N_2(C)_{v'=0}$ and $N_2^+(B)_{v'=0}$ (Lofthus, 1960).

On emission, the intensity of each upper rotational level J', is distributed over the P, Q and R branches according to the following line strength factors (also referred to as Hönl-London factors, Herzberg, 1955):

$$S^P = \frac{(J'+1+\Omega)(J'+1-\Omega)}{(J'+1)}$$

$$S^Q = \frac{(2J'+1)\Omega^2}{J'(J'+1)} \qquad (4.18)$$

$$S^R = \frac{(J'+\Omega)(J'-\Omega)}{J'}$$

The semi-empirical term values (Eq. 4.17), originally derived by Budo and given in Herzberg (1955), take the transition from Hund's case (a) to Hund's case (b) into account (spin-axis coupling constant Y_v). Also general theoretical expressions for the line intensities, that apply to both cases, exist (e.g. Kovacs, 1966). However, the use of these complicated expressions is not needed. For low values of J, Hund's case (a) applies and Eq. 4.18 can be used. For high values of J, the intensities calculated with Kovac's (1966) expressions are little different from intensities calculated with Eq. 4.18.

Examples of the simulated band structures, using Eqs. 4.16, 4.17 and 4.18, are given in Fig. 4.12. The wavenumbers have been converted to wavelengths. The Q branche has been neglected because its intensity is very weak with respect to the intensities of the P and R branches (Eq. 4.18). In order to account for the apparatus profile of a monochromator, the simulated bands have been convoluted with a Gaussian profile (0.02 nm, FWHM). A considerable difference in band shapes is shown for T_r=300 and T_r=600 K. By comparison of experimentally measured rotational band shapes with calculated shapes, gas heating by the discharge can be evaluated.

The determination of the slit function of the monochromator is another reason for simulating the rotational band structure. The slit function $S(\lambda_0, \Delta\lambda)$ is the fraction of the total vibrational band intensity I_0 which is transmitted by the monochromator with transmittance $T(\lambda)$ and resolution $\Delta\lambda$:

$$S(\lambda_0, \Delta\lambda) = \int_{-\infty}^{+\infty} \frac{I(\lambda, \lambda_0)\ T(\lambda, \Delta\lambda)\ d\lambda}{I_0} \tag{4.19}$$

The measured line intensity ratio $<I_B>/<I_C>$ (Eq. 4.12 in **4.2.5**) should be corrected for the slit functions of the monochromator for both the 337.1 nm SPS (0,0) band of N_2 and the 391.4 nm FNS (0,0) band of N_2^+. In order to calculate the slit functions of both bands also the rotational structure according to the transition $N_2^+(B) \rightarrow N_2^+(X)$ has been simulated. The upper and lower states of this transition are both states with angular momentum $\Lambda = 0$. Therefore the spin is completely uncoupled and Hund's case (b) strictly applies. Rotational term values and line intensities for this transition are given in Herzberg (1955) and not mentioned here. The slit functions of both bands, $S_C(\Delta\lambda)$ and $S_B(\Delta\lambda)$ have been calculated for $\Delta\lambda = 0.2$ nm (assuming a triangle shaped apparatus profile for the monochromator). For two temperatures, $T_r = 300$ K and $T_r = 600$ K, S_C is respectively 0.47 and 0.35, S_B is respectively 0.48 and 0.42, thus S_B/S_C is respectively 1.02 and 1.2. Neglecting the influence of the slit function in the determination of $<I_B>/<I_C>$ causes a negligible error when compared to other uncertainties that have been discussed in **4.2.5.**

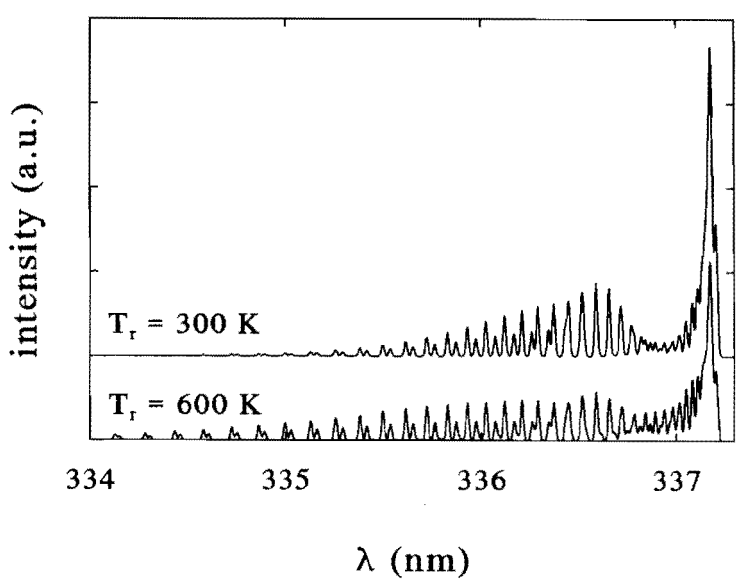

Fig. 4.12 Simulated rotational structure of the 337.1 N_2 SPS (0,0) emission band with $\Delta\lambda = 0.02$ nm, $T_r = 300$ K and 600 K.

4.3 Schlieren photography

Schlieren methods are based upon the detection of minor changes in the refractive index that occur as a result of the variation in the density of a transparent medium. The principle of different Schlieren methods, that have previously been applied to corona discharges, is discussed first (**4.3.1**). Then, the influence of a streamer discharge on the neutral density is considered (**4.3.2**). The knife-edge Schlieren method, that is the most suitable for the pulsed corona discharge, will be evaluated with respect to its sensitivity for small density gradients (**4.3.3**). The experimental arrangement that has been applied to visualize heat transfer from streamers to the gas, is described in **4.4.4**.

4.3.1 Schlieren methods

The basic principle of a Schlieren method has been illustrated in Fig. 4.13. When a ray of light, moving in the z-direction, passes through a cylindrical symmetric density perturbation (caused by a streamer), at a distance y from the central x-axis, and normal to the x-axis, the ray undergoes a deflection angle δ which for small δ is given by (Kogelschatz, 1972):

$$\delta(y) = 2y \int_{y}^{R} \frac{1}{\tilde{n}(r)} \frac{d\tilde{n}}{dr} \frac{dr}{\sqrt{r^2-y^2}} \tag{4.20}$$

where $\tilde{n}$ represents the refractive index, r the radial coordinate and R is the radial extent of the channel where $d\tilde{n}/dr \approx 0$.

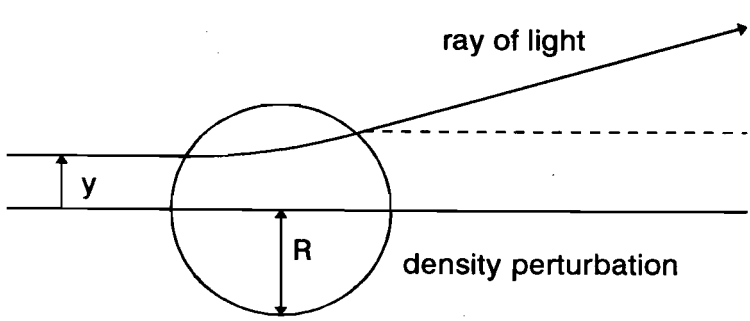

Fig. 4.13 Deflection of a light ray passing through a cylindrical symmetric density perturbation.

Variations in refractive index $\tilde{n}$ may affect the ray of light in three ways:

(1) The ray of light may be deflected through an angle δ. This angle can be detected with a *knife-edge Schlieren method* and depends, according to Eq. 4.20, on $d\tilde{n}/dr$.

(2) As a consequence of its deflection, the ray of light may be displaced laterally. The lateral displacement in an uniform beam of light causes changes in the beam intensity that can be visualized with the *shadow Schlieren method*. The contrast on shadowgraphs depends on the variation of δ, thus according to Eq. 4.20, on $d^2\tilde{n}/dy^2$.

(3) Finally, the ray of light may experience a phase lag that can be measured by means of *Schlieren interferometry*. The shift of fringes in an interferogram is directly proportional to the change in the refractive index $(\tilde{n}\text{-}\tilde{n}_0)$.

A distinction is made between qualitative and quantitative Schlieren methods (Merzkirch, 1974). Qualitative methods are used to visualize neutral gas density gradients and quantitative methods allow for the absolute determination of the neutral gas density.

The knife-edge Schlieren method has often been used for the investigation of filamentary discharges with significant heat production like leader channels where the gas temperature may reach 4000 K (Domens et al., 1988) and arc boundary regions (Kogelschatz, 1972). Woolsey et al. (1986) applied a shadow Schlieren method for time-resolved measurements of neutral density variations of streamers in air. Averaging of the time-dependent signals was possible because of the very good reproducibility of DC corona streamers in both space and time. Kurimoto and Farish (1980) measured density variations in a negative DC corona discharge by means of Schlieren-interferometry. The technique enabled quantitative estimates of gas density to be made. Also this study took advantage of the good reproducibility of DC corona discharges in a tip-plane geometry (Trichel regime).

It is important to recognize that in case of pulsed corona discharges the starting position and propagation path of streamers is unpredictable, thus excluding any averaging procedure. Due to the stochastic nature of the pulsed streamer discharge, it is desirable to obtain a two-dimensional Schlieren picture of the whole discharge region with a good spatial resolution and using a single HV-pulse. The rather low energy content of single streamers requires a high sensitivity of the method.

For visualization of small density gradients with high spatial resolution the knife-edge Schlieren method is more suitable than shadow or interferometric methods. The resolution does not depend on the lateral displacement of rays of light as in the case of shadowgraphy. Small details can be made visible and will not be masked by an interference pattern as in the case of interferometry.

4.3.2 Neutral density variations in a streamer

At voltages near the static breakdown voltage, energy transfer to the gas in the residual streamer channel (see section **2.4**) can be large enough for causing a radially propagating shock wave. During the channel expansion phase, the temperature T, the pressure p and the neutral density n are all changing. After channel expansion, neutral density variations $(n_0-n)/n_0$ are directly proportional to temperature variations $(T-T_0)/T_0$. If the refractive index differs only slightly from unity, which is the case in experiments with air, the relationship between the refractive index $\tilde{n}$ and the neutral density n is given by the Gladstone-Dale formula:

$$\tilde{n} - 1 = Kn \tag{4.21}$$

where K is called the Gladstone-Dale "constant" which is different for each type of gas. In reality K is weakly dispersive for wavelengths far away from resonant absorption: in dry air and in the visible part of the spectrum K varies slightly from $1.187\ 10^{-29}$ m^3 at 300 nm to $1.128\ 10^{-29}$ m^3 at 600 nm. Because K is approximately constant, the refractive index varies for small density variations as:

$$\frac{\tilde{n} - 1}{\tilde{n}_0 - 1} = \frac{n}{n_0} \tag{4.22}$$

where $\tilde{n}_0$ is the refractive index of the non-perturbed gas.

In principle all constituents of an ionized gas (electrons, ions, excited molecules and dissociation fragments) have a contribution to the refractive index. The contribution caused by free electrons can be calculated as (Merzkirch, 1974):

$$\tilde{n} - 1 = -4.46\ 10^{-16}\ \lambda^2 n_e = K_e(\lambda) n_e \tag{4.23}$$

with wavelength λ in m and n_e in m^{-3}. For $\lambda = 600$ nm, $K_e \approx 1.6\ 10^{-28}$ m^3. Because the residual streamer channel is weakly ionized ($n_e K_e < 10^{-4}\ n\ K_e$), the contribution of electrons to the refractive index is negligible in spite of the fact that $K_e > K$. Similar arguments are valid to neglect the contributions of ions, excited species and dissociation fragments to the refractive index.

4.3.3 Principle and sensitivity of the knife-edge Schlieren method

The knife-edge or standard Schlieren method normally involves the formation of a parallel beam of light, passing through the discharge region where the neutral density has been disturbed. The beam is formed by placing a light source (often a narrow slit) in the focal plane of a lens or mirror L_1 (Fig. 4.14). A second lens or

mirror L_2 forms two images: (a) An image of the light source in the knife edge plane and (b) an image of the density perturbation in the image plane. The knife edge is positioned in the focal plane of L_2 parallel to the slit of the light source so that 50% of the total light intensity is allowed to pass. Any refraction of a light ray that arises in the discharge channel will cause a lateral movement of the ray in the knife edge plane but no movement of the image of the density perturbation. The system is sensitive for density gradients in one direction, perpendicular to the knife edge and perpendicular to the optical axis. The intensity variation in the image plane is directly proportional to the deflection angle in the object plane. Bright and dark regions on a Schlieren photograph correspond to density gradients with opposite signs.

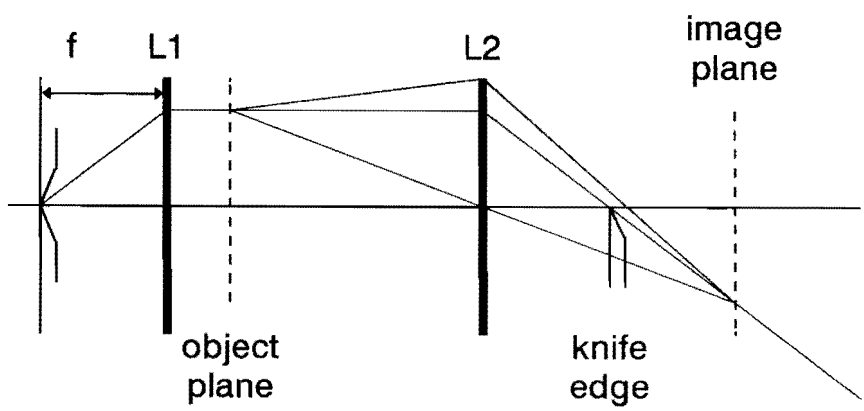

Fig. 4.14 Optical scheme of the knife-edge Schlieren method.

When lenses with equal focal lengths are used and when optical aberrations are neglected, the width of the slit image w is equal to the width of the slit. The relative intensity change or contrast $\Delta I/I$ recorded in a Schlieren picture is described by:

$$\frac{\Delta I}{I} = \frac{2\Delta w}{w} = \frac{2\delta f}{w} \tag{4.24}$$

The maximum deflection angle δ_{max}, causing a partially obscured image ($\Delta I = I$) is:

$$\delta_{max} = \frac{w}{2f} \tag{4.25}$$

The sensitivity of the Schlieren arrangement for the detection of small density

variations can be expressed as the minimum deflection angle δ_{min} that can be recorded. This angle depends on the number of grey tints N_g that can be distinguished on a Schlieren picture, according to:

$$\delta_{min} = \frac{\delta_{max}}{N_g} \tag{4.26}$$

The sensitivity for small density gradients, i.e. small δ, can be improved by reducing the width of the slit image w, i.e. making the slit width smaller. However, this reduces the dynamic range of sensitivity (δ_{min}, δ_{max}). In other words, sensitivity and range of sensitivity are inversely proportional.

The sensitivity of the Schlieren method does not only depend on geometrical optics but also on diffraction. The "width" of a Fraunhofer diffraction pattern is given by the distance between the position of the central maximum and the first minimum in the fringe pattern:

$$w_F = \frac{\lambda f}{D} \tag{4.27}$$

where λ is the wavelength and D the diameter of the imaging lens or mirror.

4.3.4 The Schlieren set-up

In the Schlieren set-up, schematically shown in Fig. 4.15, a flash lamp (with UV bulb) is used as light source. The half width of the flash lamp light pulse duration is 5 μs. A quartz fibre with a diameter of 600 μm transmits the light of the flash lamp to the Schlieren optical arrangement. The fibre is positioned in front of a slit with a width of 60 μm. The imaging system consists of two identical parabolic mirrors (f=0.9 m, D=0.1 m) which are operated at the same small off-axis angle (~0.17 rad) in order to minimize optical errors (coma, astigmatism). The knife edge is positioned precisely parallel to the slit in the image plane of the slit source. With this set-up, the maximum angle that causes a partially obscured image δ_{max} is 33.3 μrad.

In order to verify the correct position of the knife edge, the transmitted light as a function of the knife edge position is measured in the image plane using a photodiode as detector. Fig. 4.16 shows that the intensity changes linearly from 5% to 95% of its maximum value by translation of the knife-edge over 60 μm. The width of the non-linear boundaries of the slit image is ~5 μm. This value corresponds well with the diffraction fringe which can be estimated with Eq. 4.27. For wavelengths in the range 300-600 nm, a mirror diameter of 0.1 m and a focal length f=0.9 m the width of the diffraction pattern is in the range 2.7-5.4 μm.

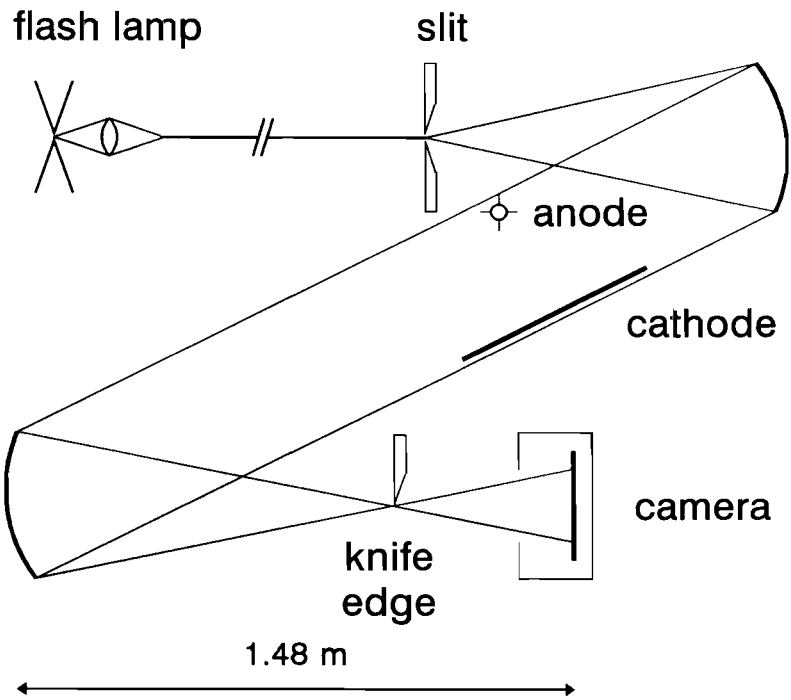

Fig. 4.15 Schlieren set-up.

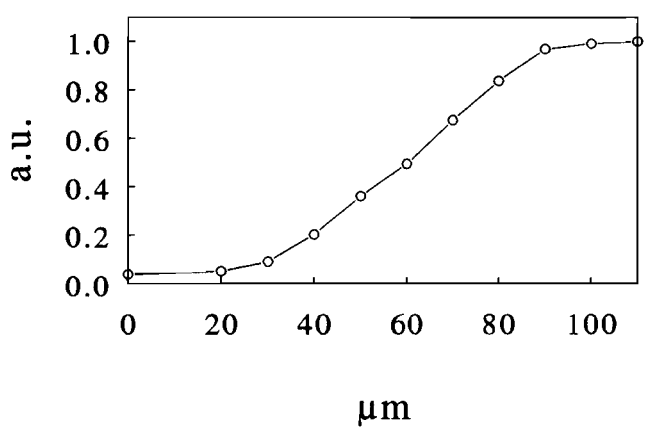

Fig. 4.16 Measured transmitted light intensity as function of knife edge position.

A black-and-white photographic film (Kodak TMY 400) is contained in the camera body without camera lens. The sensitivity of the film has been upgraded to 4000 ASA. The camera shutter serves as the trigger of the HV-pulse forming circuit and the light emitted by the triggered spark gap (measured with a photodiode) is used to trigger the flash lamp. The delay between the start of the discharge and the start of the flash lamp light pulse has been varied from a minimum of 2 μs up to 1 ms. It was possible to study qualitatively the transfer of heat from streamers to the gas with a time resolution corresponding to the width of the light pulse (~5 μs).

Chapter 5 Experimental Results

This chapter starts presenting measurements of voltage and current waveforms (in **5.1**) which condition all the other results. Section **5.2** presents electrical measurements using discharge light emission as a trigger which yield information on the streamer inception time lag and the streamer inception voltage. Section **5.3** covers various results of optical diagnostics where discharge light emission is used to determine basic streamer properties. The development of the light emission intensity of primary and secondary streamers in space and in time is investigated using pictures obtained with the image intensifier-CCD camera system. This section also includes streamer velocity measurements and data obtained by emission spectroscopy yielding estimates of the maximum field strength in propagating primary streamers and the neutral gas temperature in the residual streamer channel. Schlieren pictures which visualize heat transfer from streamers to the gas are shown in **5.4** and the last section (**5.5**) presents measurements of the NO and NO_2 oxidation efficiency.

5.1 Voltage and current measurements

In the presentation of different types of voltage and current pulses, the type of corona geometry and the values of components in the electrical circuit are given in the captions below the figures. In the description of experimental results throughout this chapter, the type of voltage and current pulses will be indicated by referring to these figures. Only single shot, non-averaged signals (300 MHz analog bandwidth and 2 ns sample time) are displayed. In order to indicate the type of corona geometry and electrical circuit, references will be made to Tables 3.1 and 3.2. In a majority of cases, the wire diameter r_w is 0.3 mm and the gap distance d_g is 35 mm. Gas conditions are: dry air at 1 bar and 20 °C with a gas flow rate of 6 l/min, unless otherwise mentioned. The HV pulse experiments are divided into two groups:

1) Fast rising HV pulses with a shape that is little influenced by the discharge current. After reaching its maximum, the voltage is either slowly decreasing or "switched off" by the second spark gap.
2) Short HV pulses with a shape depending strongly on the discharge current.

Voltage and current measurements with fast rising HV pulses will be described in **5.1.1** and voltage and current measurements with short HV pulses in **5.1.2.** In **5.1.3,** the measured rate of rise of voltage pulses and the measured width of voltage and current pulses will be compared with calculated values. Current measurements with the current probe at the cathode side of the corona configuration are presented in **5.1.4.**

5.1.1 Measurements with fast rising HV pulses

The HV pulses of the type shown in Fig. 5.1 and 5.2 have been used to investigate the influence of voltage pulse parameters V_{DC}, V_m, t_r, f and wire radius r_w on electrical and optical properties of the discharge. Fig. 5.1 (a) shows HV pulses with short rise time, produced with circuit I and wire-plate configuration I (the length of the anode wire is 50 mm). Different rise times, $t_r \approx 40$ ns and $t_r \approx 135$ ns, have been obtained with $C_{ad}=0$ pF and $C_{ad}=100$ pF respectively. The voltage waveform with $t_r \approx 135$ ns is compared with a computed waveform with an exponential shape, according to Eq. 3.19, for a strongly damped circuit. The corresponding current, shown in Fig. 5.1 (b), exhibits two main peaks corresponding to the displacement (capacitive) and the conduction (discharge) currents. After corona inception at $t \approx 260$ ns, thus during the discharge current pulse, a voltage drop over R_{dl} (500 Ω) is visible in the measured voltage pulse. From repeated measurements, it has been observed that the corona inception voltage varied statistically. In the case with $t_r \approx 135$ ns shown here in Fig. 5.1, corona inception clearly occured before the voltage reached its maximum value.

With wire radius $r_w=0.3$ mm and gap distance $d_g=35$ mm the breakdown probability in air at 1 bar becomes non-zero for $V_m>30$ kV, and the probability is 100% for $V_m>34$ kV. In order to avoid breakdown with HV pulses higher than 30 kV, the HV pulses have been limited in time duration by triggering the second spark gap. Fig. 5.2 shows examples of measured voltage and current signals and the derived energy. The capacitive current does not contribute, as expected, to the dissipated energy.

In order to collect sufficient light for the measurement of weak spectroscopic signals the larger discharge volume of wire-cylinder configuration I (wire length: 450 mm) has been used. Examples of voltage and current measurements are shown in Fig. 5.3 (a) and (b) respectively. Voltage oscillations have been reduced with a damping resistor $R_{dl}=50$ Ω that is still small enough for a fast rising pulse. Because the rise time is shorter than the corona inception time lag, the corona discharge starts at the maximum voltage. This is demonstrated by the measured current where the capacitive and corona contributions are clearly separated in time. The discharge impedance, calculated from the measured voltage and current, is shown

in Fig. 5.3 (c). Similar HV pulses and current pulses have been used for NO_x removal experiments with wire-cylinder configuration III.

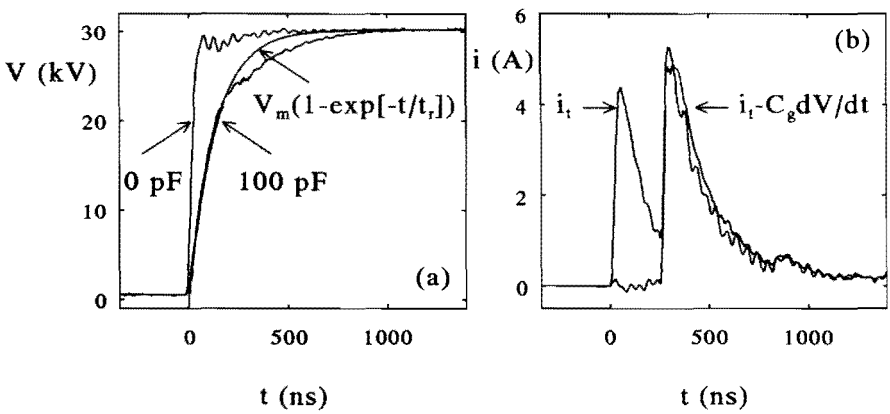

Fig. 5.1 *(a) Voltage waveforms obtained with $t_r \approx 40$ and $t_r \approx 135$ ns.*
(b) Current measurements with $t_r \approx 135$ ns.
Wire-plate configuration I and circuit I with $C_s = 5$ nF, $R_{dl} = 500$ Ω, $L_{ad} = 0$ μH, $C_{ad} = 0$, 100 pF, $f = 10$ Hz.

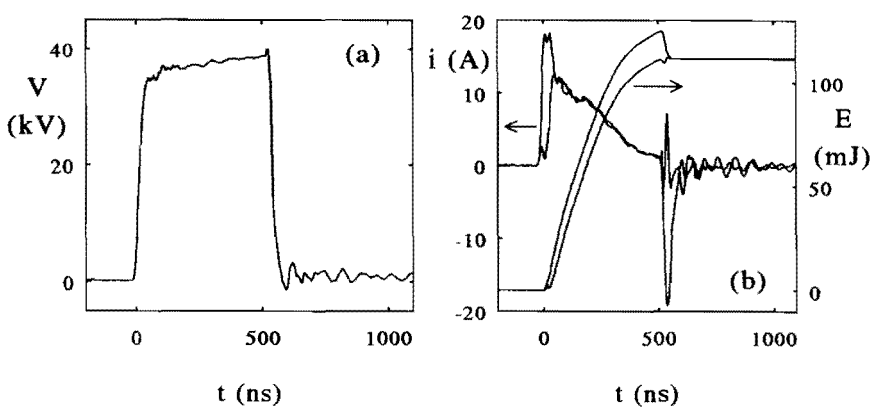

Fig. 5.2 *(a) Short HV pulse obtained by triggering the second spark gap.*
(b) Current and energy with corrections for the capacitive component.
Wire-plate configuration I and circuit I with $C_s = 5$ nF, $R_{dl} = 500$ Ω, $L_{ad} = 0$ μH, $C_{ad} = 0$ pF, single shot.

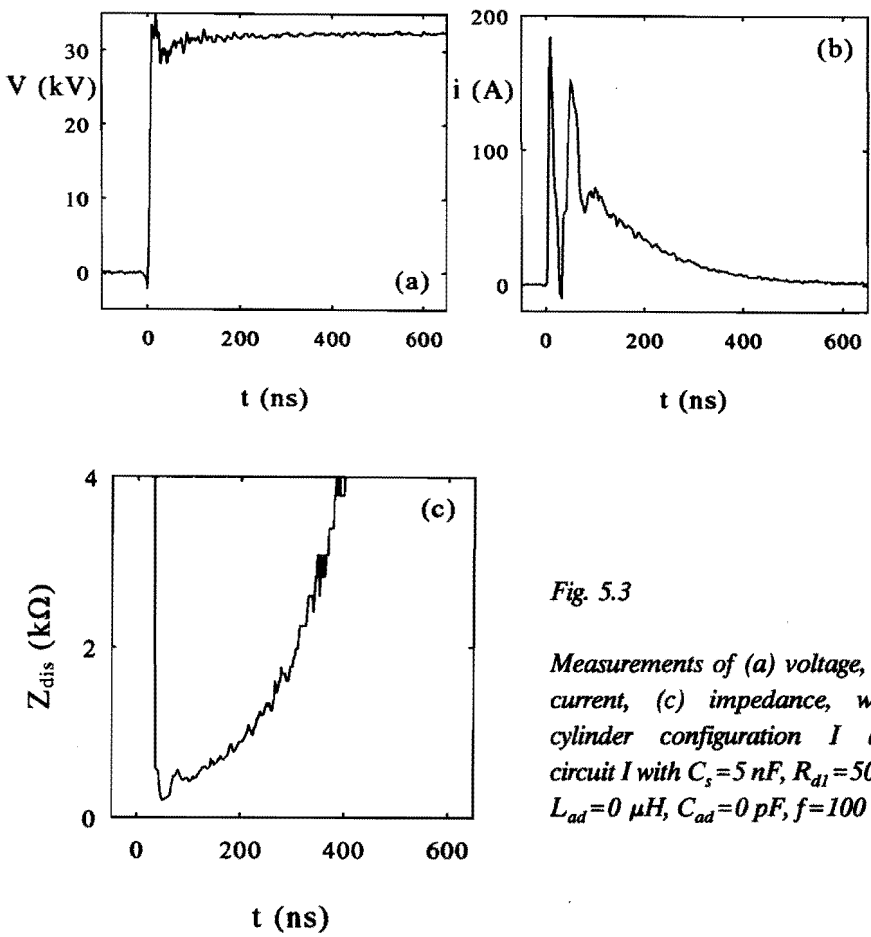

Fig. 5.3

Measurements of (a) voltage, (b) current, (c) impedance, wire-cylinder configuration I and circuit I with C_s=5 nF, R_{dl}=50 Ω, L_{ad}=0 μH, C_{ad}=0 pF, f=100 Hz.

The current pulses shown in Figs. 5.1-5.3 are made up of the contributions of many streamers produced along the same wire (their number density will be determined in **5.3.1**). Possible differences between the shape of measured current pulses and calculated ones (e.g. Fig. 2.25 and 2.33) do not invalidate the streamer models because the streamers can be formed along the wire at different moments during the same discharge current pulse. However, even in case of a wire length of 450 mm (Fig. 5.3), the measured current pulses possess a similar shape as calculated by the model which includes the secondary streamer phase (Fig. 2.33): a short rise time (~10 ns) and a much longer exponential decay time (~200 ns). This result indicates that streamers are formed almost simultaneously along the anode-wire.

Sometimes, more than one peak is discernable in the measured discharge current. A second or more current peaks can be due to (a) oscillations in the electrical circuit, (b) new primary streamer formation or (c) the discharge phase following primary streamer arrival at the cathode. During repeated measurements,

current peaks like the one in Fig. 5.1 (b) at ~650 ns occured with large statistical spread in time and amplitude. These peaks can be caused by new primary streamer formation. Following the first formation of primary streamers, space charge distortion by ions in the vicinity of the anode wire is probably the cause of unfavourable conditions for new primary streamer formation. The current peak at ~50 ns after the start of the discharge current in Fig. 5.3 (b) was observed only at voltages near or higher than the static breakdown voltage. It is probably associated with the discharge phase following primary streamer arrival at the cathode (redistribution of the potential of the streamer head along the residual primary streamer channel, see **2.4.3**).

Fig. 5.4 shows voltage and current measurements, obtained with an added inductance. The inductance (L_{ad}=50 μH) is much larger than the stray inductance (L_s=0.7 μH). A voltage measurement under the same conditions, but with a voltage below the streamer corona inception voltage, was shown before in Chapter **3** (Fig. 3.8) in order to demonstrate the damping of voltage oscillations by the resistance of the spark gap. For V_m=20 kV and V_m=30 kV the maxima of the corona current are respectively ~35 A and ~70 A, thus the minima of the discharge impedance are respectively ~570 and ~430 Ω. According to the damping criterion (Eq. 3.15) damping *by the discharge* should occur and this damping is indeed observed.

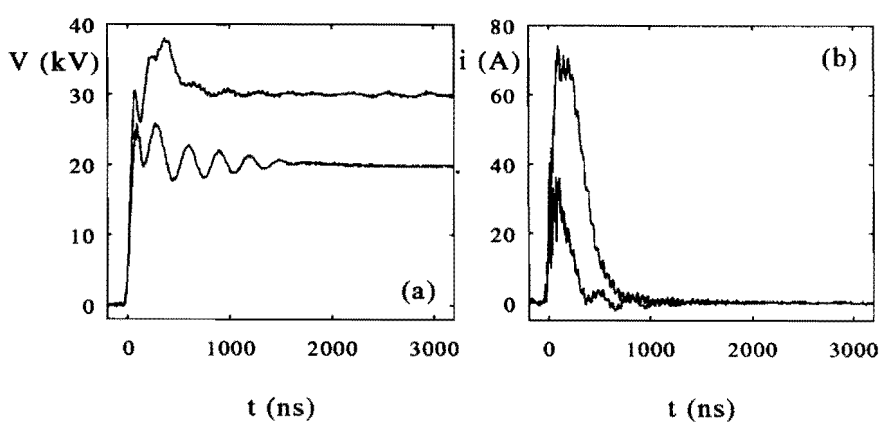

Fig. 5.4 Measurements of (a) voltage and (b) total current obtained with L_{ad}=50 μH, wire-cylinder configuration I and circuit I with C_s=5 nF, R_{dl}=0 Ω, single shot.

The presence of water vapour in air has a large influence on the corona discharge. This is illustrated by Fig. 5.5 showing measurements of the charge per pulse during repetitive operation of a discharge at 4 Hz using HV pulses of the type shown in Fig. 5.3 (wire-cylinder configuration I, no gas flow). In dry air (20 °C), the charge per pulse decreases with a typical time constant of ~50 s. In humid air (2.3% H_2O, 20 °C), however, de charge per pulse decreases much faster. In this case, 4 HV pulses are sufficient to obtain an almost constant charge per pulse.

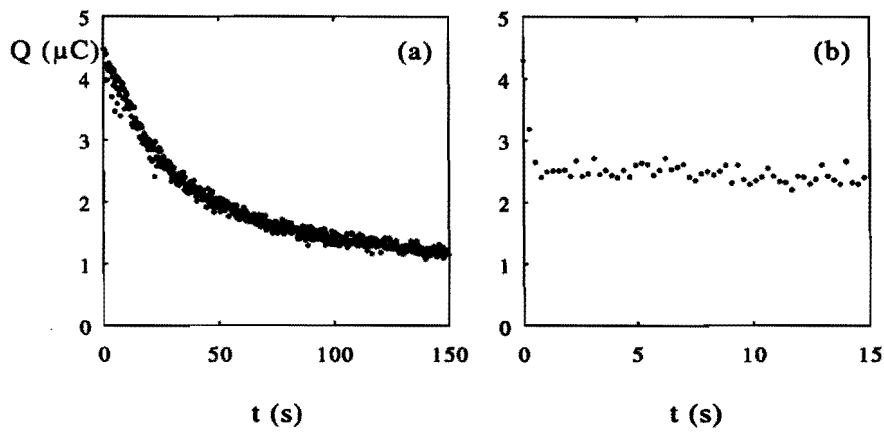

Fig. 5.5 Charge per HV pulse, (a) dry air, (b) humid air, HV pulses similar to those in Fig. 5.3 (wire-cylinder configuration I, V_m=30 kV, no gas flow).

5.1.2 Measurements with short HV pulses

Reducing the pulse width to a value much smaller than the breakdown time is profitable because energy dissipation during the discharge phases following primary streamer propagation (expected to be less energy-efficient for the production of chemical reactive dissociation fragments, see **2.4.4** and **2.5**) can be reduced or even avoided. Fig. 5.6 shows very short voltage and current pulses, obtained with a small energy storage capacitance C_s. The current pulse width ($t_w \approx 20$ ns) is close to the time needed for streamers to cross the gap (see **5.3.2**). In the positive edge of the measured pulse the voltage rises from 21 to 45 kV within 6 ns, i.e. the voltage rate of rise *dV/dt* reaches a value of ~4 kV/ns. In reality, *dV/dt* can be higher because of the bandwidth limitation of the voltage divider. According to Eq. 3.12, *dV/dt* can reach 8.0 kV/ns. The accuracy of the determination of the capacitive current is reduced because the bandwidth of the voltage probe (25 MHz) is less than the bandwidth of the current probe (125 MHz).

In the case of the example shown in Fig. 5.6, the charge determined from integrating the current pulse is 4.36 μC and the voltage that remains at the anode after the current pulse is ~11 kV. According to the relation between the transferred charge and the residual anode voltage (Eq. 3.6), the measured charge Q=4.36 μC yields V=11.3 kV, that is close to the measured value. The maximum transferable charge, that would reduce the voltage to zero, is 5.62 μC. Not all the available charge appears to be used by the discharge.

By raising the bias voltage V_{DC} up to corona onset (~15 kV), while the peak voltage V_p (i.e. the sum of DC bias and pulsed voltage) is kept constant, the peak current increases.

The influence of DC bias may be understood in the following way. A consequence of raising the bias voltage is that streamer inception will occur in a lower part of the superimposed pulse, thus in a part of the pulse where dV/dt is larger. The increase of dV/dt may result in streamer formation at a higher inception voltage (due to the finite formation time of a critical avalanche, see Fig. 2.26) and it results in a higher average voltage during the streamer propagation phase. The highest peak current is thus obtained in case of a bias voltage that is just below the minimum streamer inception voltage (~17 kV). The effects of an increase of dV/dt on the discharge are discussed in more detail in **5.2.3** with pulses having a larger rise time.

The peak voltage V_p has been varied, while V_{DC} was kept constant at 15.5 kV. When V_p is raised from the static breakdown voltage up to 45 kV, the peak of the current pulse becomes larger but the width of the current pulse becomes smaller. The reduction of the current pulse width is even so strong that, in spite of the higher peak current, the charge and energy per current pulse decrease with increasing V_p. This fact has also consequences for the breakdown probability. With V_p in the range 30-40 kV, breakdown often occurs but at still higher peak voltage the breakdown probability becomes zero again.

When V_p is increased and the streamer inception voltage remains unchanged, the average voltage during streamer propagation will still be higher. Increasing V_p also raises the voltage rate of rise dV/dt that may increase the (average) streamer inception voltage. By means of the higher peak current, a faster discharging of the capacitor is achieved which results in a larger negative slope of the voltage after the voltage maximum. As a result of the fast collapse of the voltage, the width of the current pulse is strongly reduced. The observation that the breakdown probability becomes first non-zero and than zero again with higher voltage and less energy dissipation, is well explained by the theory which claims that, after the transit of streamers, the main criterion for streamer-induced breakdown is the total amount of energy dissipated in the primary and secondary streamer channel (section **2.4.3**).

Fig. 5.7 shows voltage and current waveforms which have been measured for the determination of the NO_x removal efficiency in hot moist air (100 °C, $[H_2O]$=5%, see section **5.5**) with wire-cylinder configuration III. In this case, the streamer inception voltage was ~8 kV and the static breakdown voltage ~17 kV. With increasing pulse repetition rate *f*, the residual voltage after the peak increased because of a reduction of the transferred charge per pulse. The reduction of transferred charge is probably due to stable negative ion clusters, e.g. $O^-(H_2O)_n$ and $O_2^-(H_2O)$, which are collected close to the anode lowering locally the electric field. The current shape was little influenced by the changes in the residual voltage after the peak. In the calculation of the dissipated energy per pulse, the influence of the capacitive current has been taken into account. However, this influence is small because $(V_p\text{-}V_{DC}) \cdot C_g$ is small compared to the total charge.

It is emphasized that, apart from electrical circuit parameters (V_{DC}, V_0, *f*), the shape of the short voltage and current pulses depends much on gas conditions. With increasing gas temperature (increase of *E/n* by decrease of *n*) the peak current increases and the voltage and current pulses become shorter. An increase of the water vapour concentration (i.e. increase of both three-body and two-body attachment, see **2.3.3**), has an opposite effect.

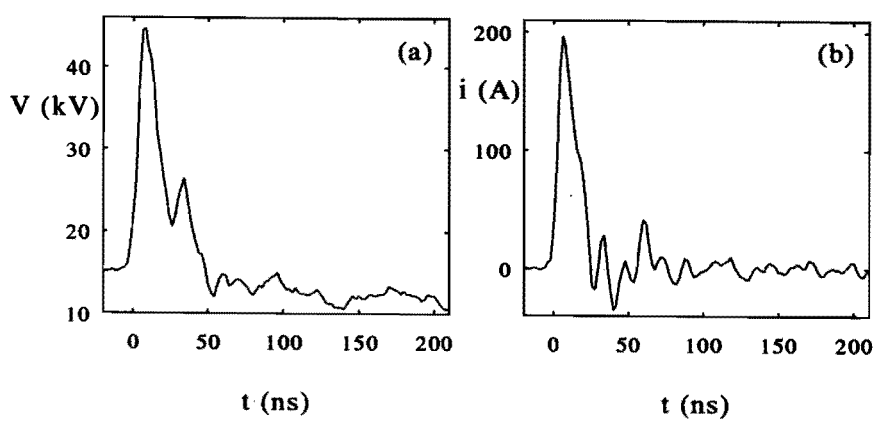

Fig. 5.6 *Voltage and current measurements in dry air at 20 °C. Wire-cylinder configuration I and circuit I with C_s=67 pF, R_{dl}=0, L_{ad}=0 μH, C_{ad}=0 pF, V_0=58 kV, V_{DC}=15.5 kV, f=100 Hz, T=20 °C, Q=4.36 μC, E=105 mJ.*

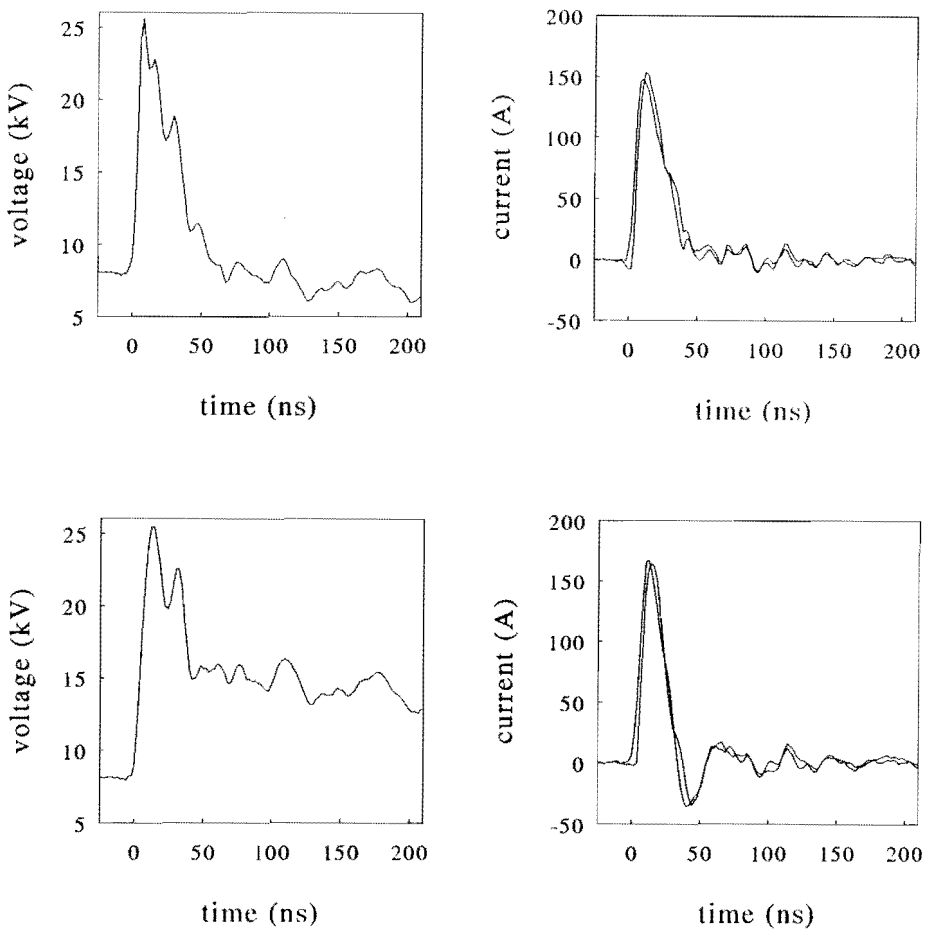

Fig. 5.7 *Voltage and current measurements in air with 5% H_2O at 100 °C. Wire-cylinder configuration III and circuit I with C_s=67 pF, R_{d1}=0, L_{ad}=0 μH, C_{ad}=0 pF, V_0=52 kV, V_{DC}=8.0 kV (top) f=20 Hz, T=100 °C, Q=3.47 μC, E=61 mJ. (bottom) f=300 Hz, T=100°C, Q=2.86 μC, E=44 mJ.*

5.1.3 Comparison with calculated HV pulses

For the various measured voltage waveforms shown in **5.1.1** and **5.1.2**, the measured values for the rate of rise $(dV/dt)_{max}$ have been compared with values predicted by Eq. 3.12 (Table 5.1). A good agreement between measured and computed values is found, except in case of the highest rates of rise. The bandwidth limitation of the HV capacitive-resistive divider is evident for dV/dt>4 kV/ns.

Geometry	wire-plate I	wire-plate I	wire-plate I	wire-cyl. I	wire-cyl. I	wire-cyl. I
C_s (pF)	5000	5000	5000	5000	5000	67
C_{ad} (pF)	0	0	100	0	0	0
$V_0\ C_s/(C_s+C_e)$ (kV)	30	30	30	30	32	35
R_{dl} (Ω)	0	500	500	0	50	0
$L=L_s+L_{ad}$ (μH)	0.6	0.6	0.6	50	0.7	0.7
D(k), Eqs. B.11, B.12	1	0.13	0.067	1	0.60	1
$(dV/dt)_{max}$ (kV/ns) Eq. 3.12	7.1	0.94	0.23	0.64	3.5	8.0
$(dV/dt)_{max}$ (kV/ns), measured (± 25 %)	4	1	0.2	0.6	4	4

Table 5.1 Computed and measured values of the maximum rate of rise, using electrical circuit I.

Measurements of fast rising HV pulses below the corona inception voltage compare well with calculated voltage waveforms using solutions for Eq. 3.10, given in Appendix B. An example of such comparison has been shown in Chapter 3, Fig. 3.8. When a series resistor R_{dl} is used to produce strongly damped HV pulses, the corona current causes a difference between the measured voltage and the exponential shape, expected in absence of a discharge, see Fig. 5.1 (a). No analytical solution is available to calculate the damping influence of the discharge on the oscillating voltage waveforms, shown in Fig. 5.4.

Eq. 3.16 only applies to the undamped case with $V_{DC}=0$ (no pre-charging of capacitors). It can not be applied to calculate the shape of the short pulses with $V_{DC}\neq 0$, shown in Fig. 5.6. Nevertheless this equation can be used to investigate, qualitatively, the influence of induction in the electrical circuit on the shape of the pulse. Assumptions need to be made for the impedance of the spark gap and the discharge. The discharge is represented by a time-varying resistance. Fig. 5.8 (a) shows the assumed function $R_{dis}(t)$. It decreases exponentially with a time constant of 2 ns from 100 kΩ to a minimum of 200 Ω after corona inception and subsequently increases exponentially with a time constant of 400 ns. The corona inception voltage V_i is assumed to be 20 kV. Fig. 5.8 (b) and (c) show voltage and current waveforms which have been calculated using two different values for the inductance L. It is possible to simulate short voltage and current pulses similar to those shown in Fig. 5.6 and 5.7 without the effect of DC-bias taken into account. The minimum width of the voltage and current pulses is $2\pi\sqrt{(LC)}$.

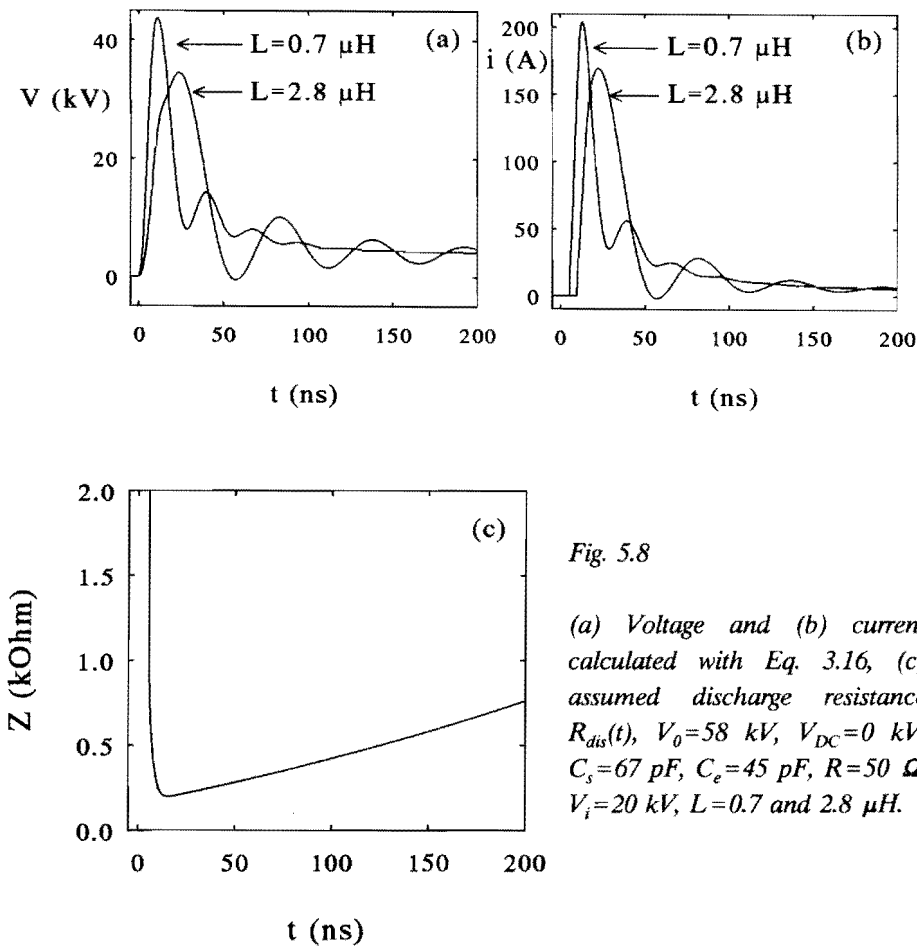

Fig. 5.8

(a) Voltage and (b) current calculated with Eq. 3.16, (c) assumed discharge resistance $R_{dis}(t)$, V_0=58 kV, V_{DC}=0 kV, C_s=67 pF, C_e=45 pF, R=50 Ω, V_i=20 kV, L=0.7 and 2.8 μH.

5.1.4 Cathode current probe measurements

The current probe (see Fig. 3.5) has been used to investigate the current at the cathode, induced by a single streamer. Wire-plate configuration I and HV pulses of the type shown in Fig. 5.1 (a) and Fig. 5.2 (a), with V_{DC}=0 kV and t_r≈40 ns, have been applied. The maximum voltage V_m was the only parameter varied. Signals from the current probe could be detected only with V_m higher than ~20 kV. At lower voltage, the geometrical field is probably not sufficient for streamer propagation up to the cathode surface.

Fig. 5.9 shows typical examples of current signals obtained with respectively V_m=20 kV and V_m=35 kV. In addition Fig. 5.9 (a) shows the charge, obtained from integration of the current signal and Fig. 5.9 (b) shows a signal of local light emission collected simultaneously near the cathode probe (set-up shown in Fig. 4.3).

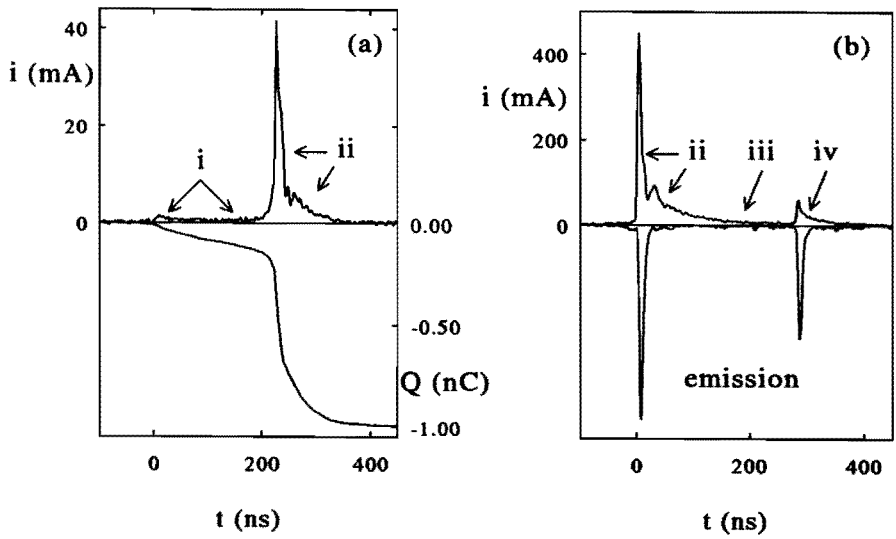

Fig. 5.9 *(a) Measured probe current and calculated charge with V_m=20 kV. (b) Measured probe current and light emission near the cathode probe with V_m=35 kV.*

Several phases, which were recognized before by Marode (1975), are indicated in Fig. 5.9:

i) the primary streamer phase
ii) the compensation phase
iii) the resistive phase

The *primary streamer phase* is seen in Fig. 5.9 (a) as an initial low current, that can be detected starting from the moment of streamer inception at the anode. It is a displacement current resulting from the moving net positive charge of a group of streamers (see Eq. 3.9). One or maybe more streamers, approaching the probe at short distance, are observed as an increase of this current just before the sharp edge in the signal. This edge occurs when a streamer "makes contact" with the probe (see **2.4.3**). Note that the time between the moment of streamer formation at the anode and the arrival of a streamer at the cathode can be estimated from Fig. 5.9 (a) at ~220 ns (at V_m=20 kV the average streamer velocity is ~1.6 mm/ns).

Introducing the term *compensation phase*, Marode alluded to the negative charge needed to neutralize the net positive charge of the streamer. When it is assumed that the sharp increase of charge (~0.5 nC), during the period of the sharp

current peak in Fig. 5.9 (a), is used to compensate the positive charge of a single streamer head, this streamer head must have contained $\sim 3.10^9$ positive ions. This value is large compared to the charge in the positive streamer head that is predicted by Gallimberti's model (see Fig. 2.29, at $V_m = 20$ kV, $N_p \approx 2 \cdot 10^8$). It is possible that the current flowing after the sharp negative edge of the current peak, is used to compensate net positive charge in the residual streamer channel. A period of ~200 ns after streamer arrival, the current becomes less than the detection limit, 0.5 mA. The charge contribution of a *resistive* current through the residual streamer channel is relatively small in this case.

When the current probe signal that has been obtained with $V_m = 20$ kV is compared with the signal that has been obtained with $V_m = 35$ kV (see Fig. 5.9), several changes can be noticed:

1) The peak current is about 10 times higher.
2) A second (local) maximum, immediately following the peak current, is observed.
3) A current of about 20 mA (more than 40 times larger than in the previous case) can now be measured during the resistive phase (iii).
4) A third separate peak (iv in Fig. 5.9) is detected and the shape of this peak is similar to the shape of peaks caused by primary streamers.

It appeared from repeated measurements (at $V_m = 35$ kV) that the second local maximum occurs always within 40 ns following streamer arrival. The time between the first and the second current peaks varies statistically, with a minimum of ~100 ns. Sometimes even more peaks are observed.

The shape of the second separate peak (iv) and the local optical signal indicate that this current peak is caused by the arrival of a new primary streamer. It is possible, but not necessary, that this streamer followed exactly the same path as the previous streamer. The current peaks possess a larger decay time than the optical signals. In particular, the second current peak is not observed in the optical signal. In reality, the optical emission may be even much shorter in time because the measured decay time is close to the apparatus decay time of the photomultiplier signal (~10 ns). The fact that the light emission signal is much shorter than the current signal indicates that, if changes in the local charge density distribution occur close to the cathode probe, these changes do not lead to a field that is high enough for emission to be detected.

As recognized earlier by Marode (1975), after streamer "arrival", during the compensation phase, local charge density variations in the residual streamer channel may still cause a displacement current. The current probe is sensitive for the displacement current that occurs as a result of charge density variations close to the probe surface. However, charge density variations at relative large distance from the probe (more than 4 mm) are only partly measured.

In spite of the limitations in the possible interpretation of cathode probe current signals, the average charge contained in current pulses has been measured as function of V_m. Because of statistical variations, 300 charge measurements were performed for each value of V_m using the signal of the central probe disk (1 mm in diameter) as trigger. The probability distribution of charges for V_m=30 kV is given in Fig. 5.10 (a). The dependence of the average measured charge per streamer $<Q_s>$ on V_m is given in Fig. 5.10 (b). The total charge per HV pulse Q_t measured at the anode is also given in this figure.

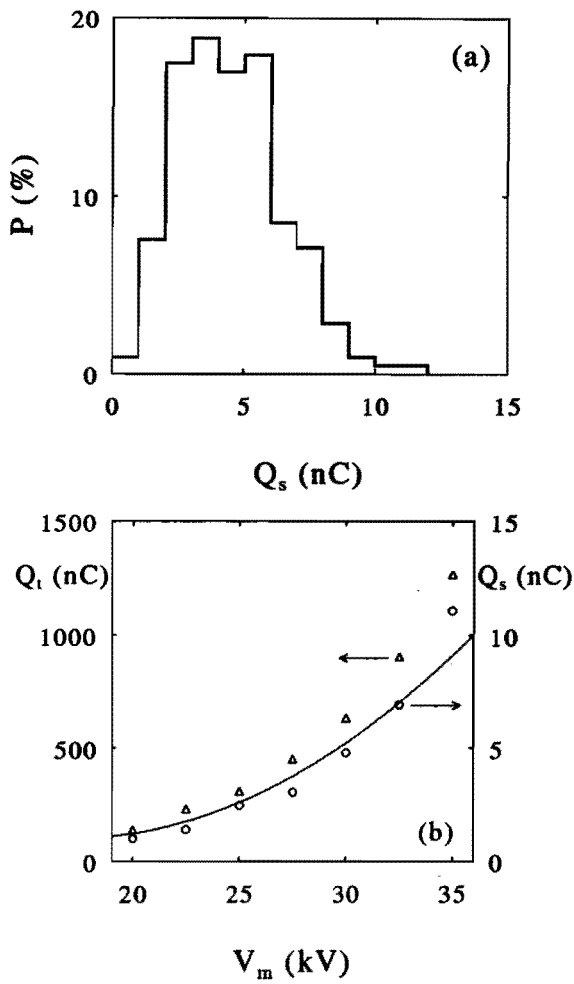

Fig. 5.10 Cathode current probe measurements.
(a) Probability distribution of the charge Q_s for V_m=30 kV.
(b) Average charge $<Q_s>$ and average total charge measured at the anode $<Q_t>$ as a function of V_m.

The line through the measured points $<Q_s>$ in Fig. 5.10 (b), corresponds to the functional dependence:

$$<Q_s> = 1 + 0.025 \cdot (V_m - 17)^2 \qquad (5.1)$$

with $<Q_s>$ in nC and V_m in kV. Fig. 5.10 shows that $<Q_s>$ and $<Q_t>$ depend in a similar way on V_m. The ratio $<Q_t>/<Q_s>$ is approximately independent on the applied voltage ~100. It is not expected that this ratio equals the number of streamers, because the displacement current caused by streamers has been partly measured. Nevertheless, two conclusions can be drawn from the measurements:

1) Since the ratio $<Q_t>/<Q_s>$ is approximately independent of V_m, it is expected that the number of streamers produced at the wire per HV pulse is not strongly dependent on the anode voltage.
2) Since $<Q_s>$ is less than the average charge that is transferred by a single streamer, the ratio $<Q_t>/<Q_s> \approx 100$ indicates an upper bound for the average number of streamers that is produced.

The wire length in the experiment is 50 mm, thus the measurements indicate that not more than 2 streamers per mm wire length are produced.

5.2 Measurements using discharge emission as trigger

5.2.1 Measurements of integral and local emission

For all measurements in this section wire-plate geometry I and electrical circuit I, with voltage and current pulses similar to those shown in Fig. 5.1, have been used (bias voltage $V_{DC} = 0$ kV, decay time $t_d \approx 0.3$ ms). The standard pulse repetition frequency f is 20 Hz and the standard wire radius r_w is 0.3 mm.

Raising V_m in steps of 1 kV, integral light emission is detected only for $V_m = 16$ kV and above. Local light emission measurements, as function of distance to the anode, indicate that at this voltage, streamers with a maximum length of ~10 mm are formed. In case of sub-millisecond HV pulses, the only type of corona discharge that can be observed from light emission is the streamer type. Therefore we will not use the term *corona inception voltage* but only the term *streamer inception voltage*. The measured minimum streamer inception voltage $V_{i,\,min}$ is in the range 16-17 kV. This is close to the value predicted by the Raether-Meek criterion (16.8 kV, see **2.2.3**). V_m must be raised up to ~19 kV in order to observe local emission near the cathode, indicating streamers that cross the entire gap.

Fig. 5.11 (a) shows a typical example a current signal and a simultaneously measured integral light emission signal. Fig. 5.11 (b) shows a typical example of a current signal and a local light emission signal that has been measured simultaneously at the anode. In the current signal statistical variations occur. A high frequency oscillation is sometimes seen in the current and voltage signals (in Fig. 5.11 (a) just before $t=0$ ns and in Fig. 5.11 (b) at $t\approx300$ ns) but not in light emission signals. The cause of this oscillation is not understood. The integral and local light emission signals show no emission before the start of the discharge current. The local emission signal from a region close to the anode shows an emission peak which results from a passing primary streamer, followed by the much longer emission of the secondary streamer. The width of the primary streamer emission peak depends on the time needed for the streamer to pass the optical volume (~4 ns assuming a velocity of 0.5 mm/ns) and on the decay time of the photomultipliers (10 ns). It is emphasized that the estimated duration of the light emission of the primary streamer is much less, namely ~0.5 ns (**4.2.3**).

Fig. 5.11 (c) and (d) show examples of integral light emission and local light emission measured at the cathode. Note the short rise times (90% in 6 ns) of the integral light emission signals. After the initial sharp rise, the signal is slowly varying until local light emission measurements at the cathode indicate the arrival of primary streamers. Then, the integral light emission signals decay within a time of about 500 ns. The signals decay not directly to zero. A relative weak emission signal is detectable during approximately 1 μs. The shapes of the integral light emission signals seem to correspond to the three discharge phases that were mentionned in **5.1.5**: (i) Primary streamer propagation, (ii) secondary streamer and (iii) resistive phase.

Sometimes, during repeated measurements, local emission is not detected near the anode. This observation indicates that the average distance in between streamers along the anode wire is of the order of the spatial resolution of the measurement (1.8 mm in the plane through the wire, perpendicular to the cathode plate). The local light emission signal from the cathode region in Fig. 5.11 (c) shows two separate peaks, thereby indicating that different streamers reach the cathode surface at different moments. The differences in arrival times may have several causes:

1) Streamers have different inception time lags
2) Streamers follow different paths with different lengths
3) Streamer possess different propagation velocities

Streamer inception time differences are the subject of **5.2.2**. 2-D measurements showing the paths followed by streamers will be presented in **5.3.1** and streamer propagation velocity measurements will be presented in **5.3.2**.

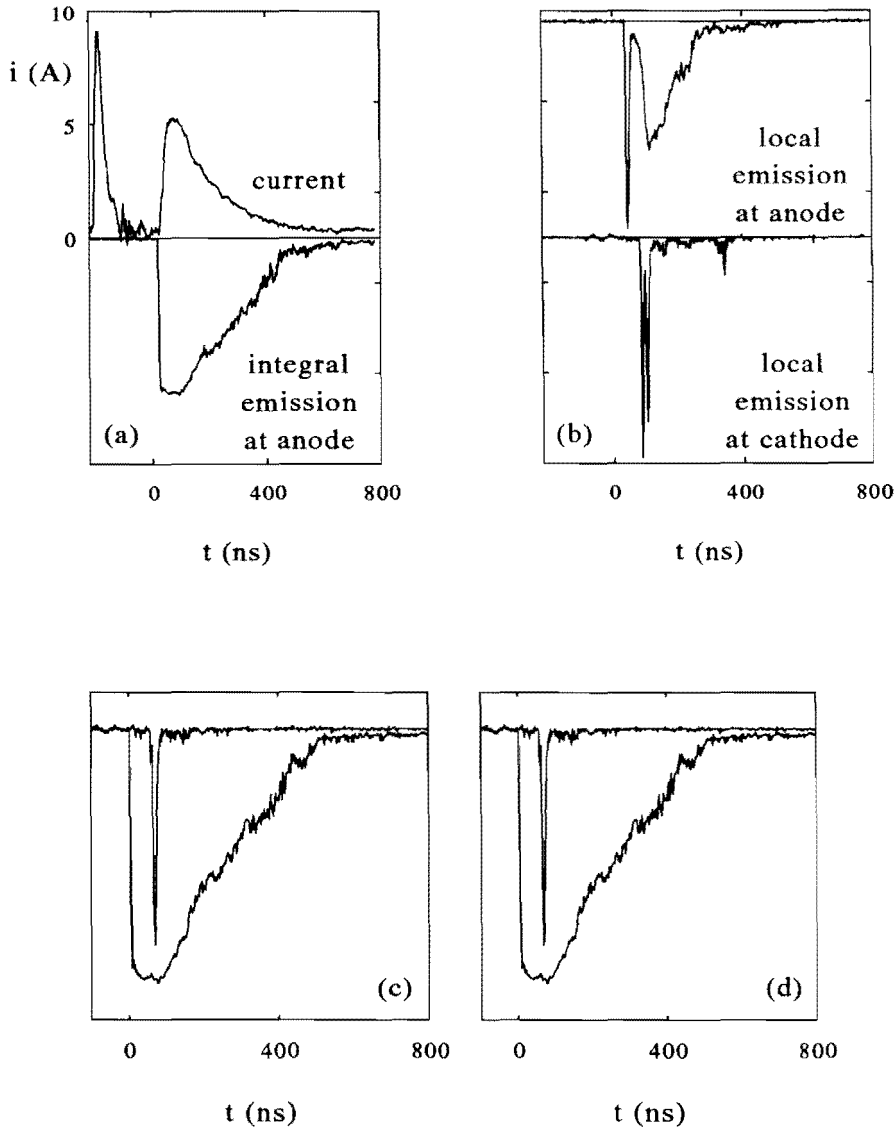

Fig. 5.11 *Current, integral and local light emission. Each graph shows simultaneously measured signals (V_m=30 kV, t_r≈40 ns).*
(a) Current and integral light emission.
(b) Current and local light emission at x=1-3 mm from the anode-wire.
(c,d) Integral and local light emission at the cathode.

5.2.2 Measurements of streamer inception time differences

Streamer inception time lags T_i and *streamer inception time differences* ΔT_i have been measured according to the method described in **4.1.3**. Fig. 5.12 (a) shows probability distributions of ΔT_i for voltage maxima V_m of 20 and 30 kV, measured with 1000 HV pulses with a rise time of ~40 ns. In both cases, the measured streamer inception time differences appear to be always less than 13 ns. The main part of streamers is formed within a period of 3 ns at each location (~2 mm spatial resolution) along the wire of 50 mm length. The measured probability distributions show a relative low probability of streamer formation in the period 3-13 ns following the formation of the first streamer(s). Increasing V_m from 20 to 30 kV, the relative number of streamers formed within the first period of 3 ns becomes larger. Repeating the measurement of local light emission at different locations along the smooth wire (at x=2 mm, z=-2 mm and displacing the tube-fibre system in the y-direction, see Fig. 4.3 for the definition of coordinates) gave similar distributions.

With V_m=20 kV streamers are formed after the rising part of the voltage, thus the average streamer inception voltage $<V_i>$ is 20 kV. The streamer inception time lag T_i varies statistically from ~100 ns upto a maximum of several μs, thus T_i values are very large compared to ΔT_i values. With V_m=30 kV streamer inception occurs during the rise of voltage but close to the maximum. The average streamer inception voltage is ~25 kV.

The probability distribution of ΔT_i in Fig. 5.12 (b), measured with a longer rise time $t_r \approx 135$ ns, shows a different structure. The spread in ΔT_i is now larger but still streamers are formed along the wire length of 50 mm within a short period, $\Delta T_i < 20$ ns.

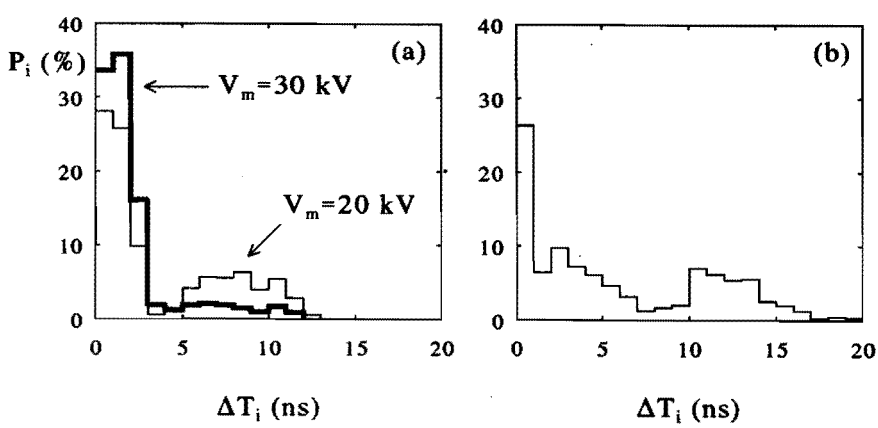

Fig. 5.12 (a) Probability distribution of ΔT_i *with* $t_r \approx 40$ *ns,* V_m=*20 kV and* V_m=*30 kV (b) Probability distribution of* ΔT_i *with* $t_r \approx 135$ *ns and* V_m=*30 kV.*

The fact that streamer inception time differences ΔT_i are very small when compared to streamer inception time lags T_i demonstrates evidently the influence of the first formed streamer(s) on conditions favouring the formation of streamers at other locations along the wire. The photoionization mechanism can be responsible for this influence.

5.2.3 Measurements of streamer inception time lags, inception voltages and energy dissipation

The influence of voltage parameters and anode wire radius on the streamer inception voltage and the influence of the streamer inception voltage on energy dissipation has been investigated. The following parameter variations have been applied: V_m=25, 30 kV, V_{DC}=-5, 0, 5 kV, t_r=~40, ~135 ns, f=1-1000 Hz, r_w=0.1-0.5 mm.

The average streamer inception time lag $<T_i>$, the average streamer inception voltage $<V_i>$ and the average energy per pulse $<E>$ have been determined as function of V_m, see Fig. 5.13. For each value of V_m 1000 measurements of local light emission (used as trigger), voltage and current were performed and analyzed in real time to determine average values and probability distributions.

Fig. 5.13 (a) shows the average streamer inception time lag $<T_i>$. With increasing voltage V_m, streamers are formed more frequently during the rising part of the voltage. For V_m>25 kV, $<T_i>$ is less than the rise time of the HV pulse (t_r≈40 ns). At V_m=30 kV, $<T_i>$=25 ns. This average value is still larger than the maximum streamer inception time difference (ΔT_i<13 ns, see Fig. 5.12 (a).

Fig. 5.13 (b) shows that for low V_m, the average inception voltage $<V_i>$ is about equal to V_m. When V_m approaches the static breakdown voltage (~30 kV), $<V_i>$ becomes significantly lower than V_m. The influence of V_m on $<V_i>$, at constant rise time t_r, can be due to an increase of the rate of rise dV/dt.

Fig. 5.13 (c) shows that the energy dissipation per pulse increases strongly with increasing V_m. With considerable overvoltage ($\Delta V/V_b$>10%), a significant current continues to flow after the "normal" exponential decay. When the pulse width is increased from ~800 to ~1600 ns, the dissipated energy increases because of this "after current".

Some measurements of $<V_i>$ and $<E>$ with a positive and negative DC bias are also shown in respectively Fig. 5.13 (b) and (c) (triangle symbols). Increasing the bias voltage from 0 kV to 5 kV (keeping V_m at 30 kV), the average inception voltage decreases from ~26 kV to ~19 kV, and the average energy per pulse from ~20 mJ to ~17 mJ. With a negative bias the changes are in the opposite direction but smaller: The average inception voltage is increased from ~26 kV to ~28 kV and the average energy per pulse from ~20 mJ to ~22 mJ.

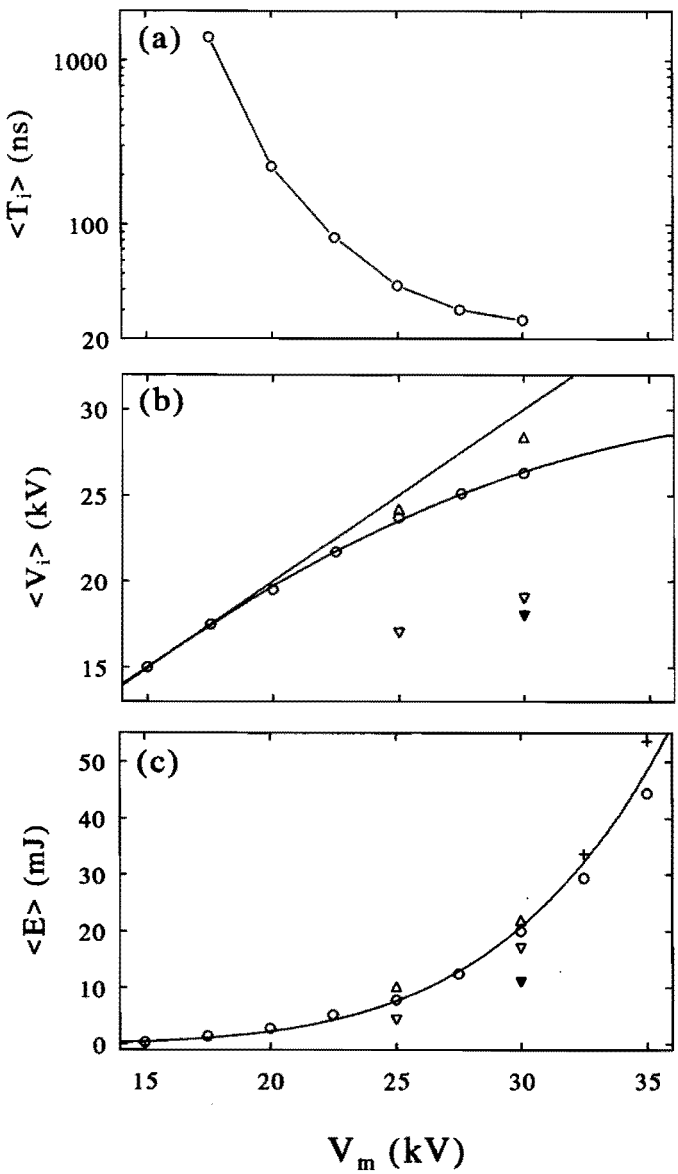

Fig. 5.13 *The influence of V_m on average values of (a) inception time lag $<T_i>$, (b) inception voltage $<V_i>$ and (c) energy per pulse $<E>$. Measurements with t_r = ~40 ns, $<E>$ integrated over 800 ns:*
(○) V_{DC}= ~0 kV, (▽) V_{DC}=5 kV, (△) V_{DC}=-5 kV.
(▼) V_{DC}=5 kV, t_r= ~135 ns, $<E>$ integrated over 800 ns.
(+) V_{DC}= ~ 0 kV, t_r= ~40 ns, $<E>$ integrated over 1600 ns.

The measurements with $V_{DC} \approx 0$ kV, shown in Fig. 5.13, were performed without knowledge about the influence of V_{DC} on the average streamer inception voltage. In fact, due to AC coupling in the electrical circuit, V_{DC} may have been slightly lower than 0. In order to investigate the influence of the *DC* bias voltage on streamer inception in more detail, streamer inception probability distributions have been measured. The streamer inception probability distribution is dramatically changed when a bias voltage is applied. Fig. 5.14 (a) shows the probability distribution P_i of the streamer inception voltage V_i for $V_m = 30$ kV, $V_{DC} \approx 0$ and $t_r \approx 135$ ns. For each interval of V_i, the average dissipated energy E has been calculated. The inception voltage V_i fluctuates in a range from 17 to 28 kV. A strong correlation exists between the inception voltage and energy dissipation. Fig. 5.14 (b) shows distributions obtained with $V_{DC} = +5$ kV and $V_{DC} = -5$ kV. The lowering of the inception voltage in case of a positive bias can be due to the collection of negative ions in the critical volume. Detachment from these negative ions provides initial electrons for streamer formation, reduces the (average) streamer inception time lag and reduces the (average) streamer inception voltage.

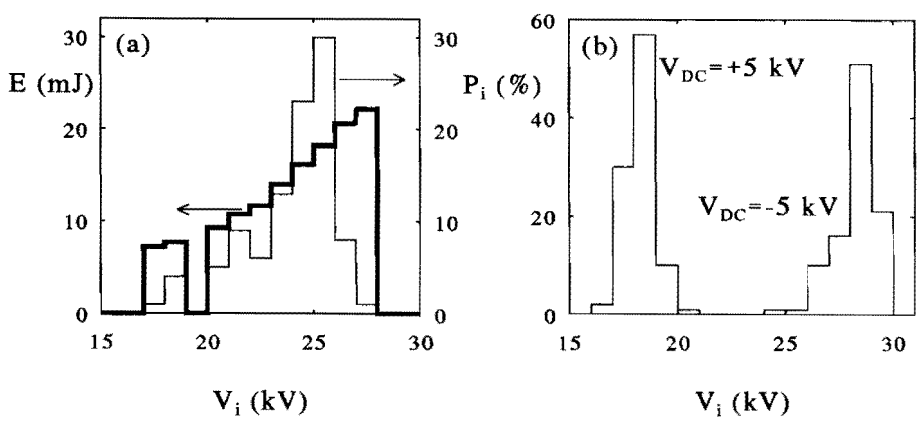

Fig. 5.14 *(a) The dissipated energy per pulse E and the inception probability P_i as a function of the inception voltage V_i, $V_m = 30$ kV, $V_{DC} = 0$ kV, $t_r = \sim 135$ ns. (b) Inception probability distribution P_i as a function of the inception voltage, $V_m = 30$ kV, $V_{DC} = -5$ kV, 5 kV, $t_r = \sim 40$ ns.*

For $V_m = 30$ kV and $t_r \approx 40$ ns, an increase of V_{DC} from 0 to 5 kV, has a large influence on $\langle V_i \rangle$ (~30%) but a relative small influence on $\langle E \rangle$ (~15%). However, with longer rise time, $t_r = \sim 135$ ns, an increase of V_{DC} from 0 to 5 kV, has a much larger influence on $\langle E \rangle$ (~50%, symbol ▾ in Fig. 5.13). This effect can be understood comparing the length of the current pulse with the rise time. The

current decays exponentially with a time constant t_d of ~200 ns (e.g. Fig. 5.11 (a)). In the case $t_r \approx 40$ ns, even if V_i is far below V_m, the major part of the energy will be dissipated at a voltage close to V_m. In other words: The influence of the streamer inception voltage on the energy dissipation will be limited if the voltage rise time is small compared to the length of the current pulse.

When the repetition rate f of HV pulses ($t_r \approx 40$ ns) is varied from 1 up to 1000 Hz, the breakdown voltage is lowered from ~30 to ~27 kV. The influence of f on $<V_i>$ and $<E>$ was investigated with HV pulses with $V_m = 25$ kV and $t_r \approx 40$ ns. At high repetition rate, a negative bias is formed in between the pulses as a result of AC coupling in the electrical circuit. Fig. 5.15 (a) shows an example of a series of HV pulses with $f = 1000$ Hz. An approximately zero bias voltage has been achieved here using the positive DC power supply to compensate for the AC coupling effect.

Fig. 5.15 (b) shows the dependence of average energy per pulse $<E>$ on repetition rate f, for $V_{DC} \approx 0$ and $V_{DC} = 5$ kV. In both cases $<E>$ is inversely proportional to the logarithm of f. With $V_{DC} = 5$ kV, raising the frequency from 1 to 1000 Hz, $<E>$ decreases by ~35%. As a result of the positive bias, the average inception voltage (not shown in Fig. 5.15) remains approximately constant at $V_i = V_{i,min} \approx 16$ kV. The reduction of $<E>$ with increasing f can thus be attributed exclusively to a lowering of the field with increasing average ion density in the anode region. With $V_{DC} \approx 0$ kV, raising the frequency from 1 to 1000 Hz, $<E>$ decreases by ~60%. In this case both the increase of the average ion density in the gap and the decrease of inception voltage due to detachment from negative ions in the anode region play, probably, a role. At $f = 1$ kHz, the period between the HV pulses is close to the width of the HV pulses so that the time-averaged voltage at the anode reaches a value of about 5 kV. The average streamer inception voltage decreases from ~23 kV at $f = 10$ Hz to ~20 kV at $f = 1000$ Hz.

Finally, the influence of the anode-wire radius r_w has been investigated using HV pulses with $t_r \approx 135$ ns, $V_{DC} \approx 0$ kV. The average streamer inception voltage $<V_i>$ and the average energy dissipation per pulse $<E>$ increase with r_w. In Fig. 5.16 (a) with $r_w = 0.5$ mm and $V_m = 25$ kV, the average streamer inception voltage $<V_i>$ is close to V_m.

The minimum inception voltage $V_{i,min}$ has been obtained from the minimum value of V_i appearing in histograms of streamer inception distributions, e.g. Fig. 5.14 (a). Therefore, the accuracy in $V_{i,min}$ is limited to ± 1 kV. The minimum inception voltage has also been calculated using the Raether-Meek criterion, see **2.2.3**. For different values of r_w the measured values of $V_{i,min}$ compare well (within 2 kV) with values predicted with this criterion.

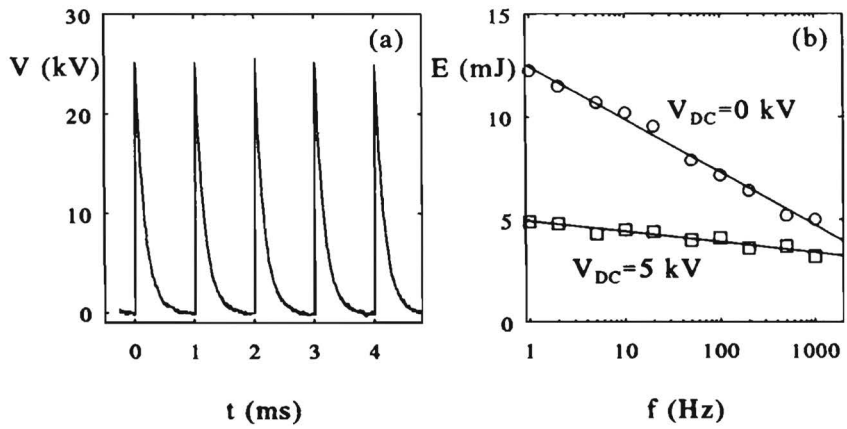

Fig. 5.15 *The influence of repetition rate f with V_m=25 kV and t_r=40 ns.*
(a) HV pulses with f=1 kHz.
(b) Average dissipated energy <E>, (○) V_{DC}=0, (□) V_{DC}=5 kV.

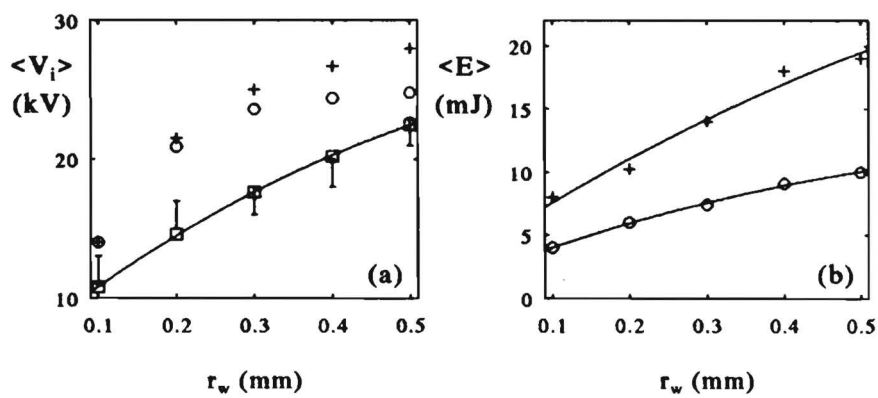

Fig. 5.16 *The influence of anode wire radius r_w with t_r=~135 ns and V_{DC}=0.*
(a) Average inception voltage <V_i>, (b) average energy per pulse <E>.
(○) V_m=25 kV, (+) V_m=30 kV.
(vertical bars) $V_{i,\,min}$ from measurements.
(line, □) $V_{i,\,min}$ according to the Raether-Meek criterion.

5.3 Optical investigation of streamer properties

In this section, pictures obtained with the gated image intensifier and CCD camera, visualizing the spatial structure and the various phases of the discharge in time, will be displayed (**5.3.1**). Photomultiplier measurements will be presented to show the local velocity of streamers with higher time resolution than can be achieved with the image intensfier. According to the methods presented in **4.2,** measurements of the intensity ratio of emission lines of N_2^+ (391.4 nm) and N_2 (337.1 nm) will be used to show that electrons reach a high average energy in propagating primary streamer heads and the rotational structure of the N_2 (337.1 nm) emission line is analyzed to show that the neutral gas temperature in the streamer channel is little affected. The experiments have been performed in wire-plate configuration I with HV pulses similar to those shown in Fig. 5.1 (a) and with a rise time t_r of ~40 ns. If not otherwise mentionned, a maximum voltage V_m of 30 kV and dry air have been used as standard conditions.

5.3.1 Discharge structure

A series of pictures has been made with the gated image intensifier and the CCD camera and with the smallest possible exposure time (gate pulse width: $\tau_g = 34 \pm 2$ ns). At $V_m = 30$ kV (just below the static breakdown voltage) this time is smaller than the average transit time of streamers (50 ± 5 ns). The start and finish of the gate period with respect to the moment of corona inception has been determined measuring the integral discharge emission and the gate pulse simultaneously. An example of such measurement is shown in Fig. 5.17.

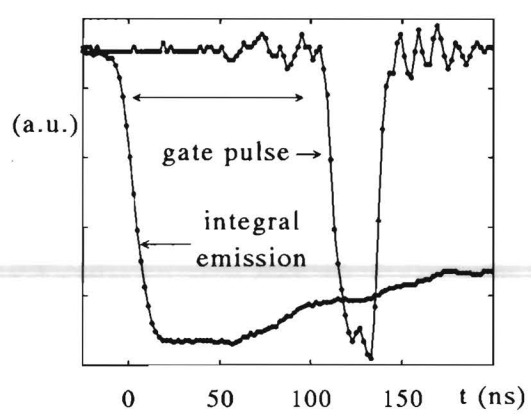

Fig. 5.17

Integral light emission signal and the gate pulse for activation of the image intensifier.

Fig. 5.18 shows 6 pictures obtained during different periods of the discharge. The detected light emission intensity is shown by means of 4 gray tones which, together with the white background of the paper, correspond to a distribution over 5 equal intensity intervals. Black is used for all pixel intensities above a predetermined threshold level. The threshold level, which is the same for all pictures, has been fixed at about 50% of the maximum observed intensity in order to visualize also the structure of weakly luminous streamers. The exposure time, indicated in each picture, refers to the start and the finish of the gate pulse with respect to the start of the discharge.

Pictures (a) and (b) of Fig. 5.18 show the advance of primary streamers before arrival at the cathode. In case of picture (a) the image intensifier has been activated 10 ns before the discharge occurs. According to the numerical streamer model (see sections **2.3** and **4.2.5**) and confirmed by the local emission measurements (**5.2.1**, Fig. 5.11), only the primary streamer head (with a characteristic size $\delta_h \approx 10$ μm) is light emitting while the primary streamer channel remains dark. Thus, the intensity of a trace that is seen on picture (a) or (b), shows the spatial emission intensity distribution of the primary streamer head while propagating from the anode towards the cathode. On these pictures, no large differences in the lengths of primary streamer traces are observed. This fact indicates that the primary streamers have been formed within a period that is small compared to the transit time, in agreement with the results from streamer inception time measurements (**5.2.2**).

The stochastic nature of the primary streamers is evident: streamers propagate not always along straight lines and also branching is sometimes observed. It happens that traces of streamers on the pictures cross each other. In reality, the corresponding streamers will cross at some distance without intersection. In principle however, it is also possible that a primary streamer front joins the quasineutral channel of another streamer that was formed earlier, possessed a higher velocity or followed another path. The average number density of streamers, that is observed along the wire, is in the range 500-700 per meter length.

Fig. 5.18 (c) shows the discharge during a period (20-54 ns) in which a part of the primary streamers reaches the cathode surface (the average transit time is ~50 ns). Incipient secondary streamers are observed in the anode region. Note that secondary streamers are not formed close to the anode-wire but at some distance (~ 2 mm). The intensity distribution of streamer traces at the cathode side of the gap shows that the intensity becomes much stronger with shorter distance to the cathode. This distribution may have two different causes: (a) the intensity of the primary streamer increases when approaching the cathode, (b) a secondary streamer is formed in the cathode region, after primary streamer arrival. The time resolution of the image intensifier is not sufficient to distinguish between these possible causes.

In picture (d), covering a period starting after the moment when the majority of the primary streamers has reached the cathode (50-84 ns), the secondary streamers in the anode region have grown out to a length of about 5 mm but also relative strong emission in the cathode region is still present. This emission may have been caused partially by some delayed primary streamers but this emission is probably dominated by a "secondary streamer phenomenon" in the cathode region.

In the period covered by picture (e), starting only 10 ns after the period of picture (d), the emission intensity from residual streamer channels in the cathode region has strongly diminished while the emission intensity near the anode has almost not changed.

Picture (f) shows that, 100 ns after the start of the discharge, the measured total light intensity of the discharge is almost completely due to secondary streamer emission near the anode. Nevertheless, also weak emission from residual streamer channels in the mid-gap region is still observed.

Summarizing, the pictures (c), (d) and (e) indicate that secondary streamers (i.e. residual primary streamer re-illuminations) are formed in both the anode and cathode regions but that a short time after primary streamer arrival (less than 10 ns) the secondary streamer emission is concentrated in the anode region. Secondary streamer formation in the cathode region was not predicted by the numerical model in **2.4.3** but is in principle possible (the re-distribution of the primary streamer head potential was taken into account in a simplified way and the cathode-fall formation was neglected). The maximum observed secondary streamer length near the anode (~5 mm) is in close agreement with the simulations of the residual streamer channel (Fig. 2.30).

Spatial and temporal gradients of E/n and n_e in the streamer head region (in the direction along the streamer axis) can not be resolved, neither in space nor in time. On the other hand, the spatial resolution of the CCD along the streamer axis (x-direction) is sufficient for detecting intensity changes of the light emitted by the total streamer head region. It is reasonable to assume that the properties of a streamer head change little when it propagates over a distance of ~1 mm, corresponding to about 10 pixels on the CCD image. This assumption is confirmed by numerical simulations (**2.3.4**).

A computer program has been written, that integrates the intensity of CCD pixels in the y-direction. After graphically drawing a closed curve around the contours of a single primary streamer trace on the computer screen, the program calculates the radially integrated emission intensity of the selected streamer as function of the distance x to the anode wire.

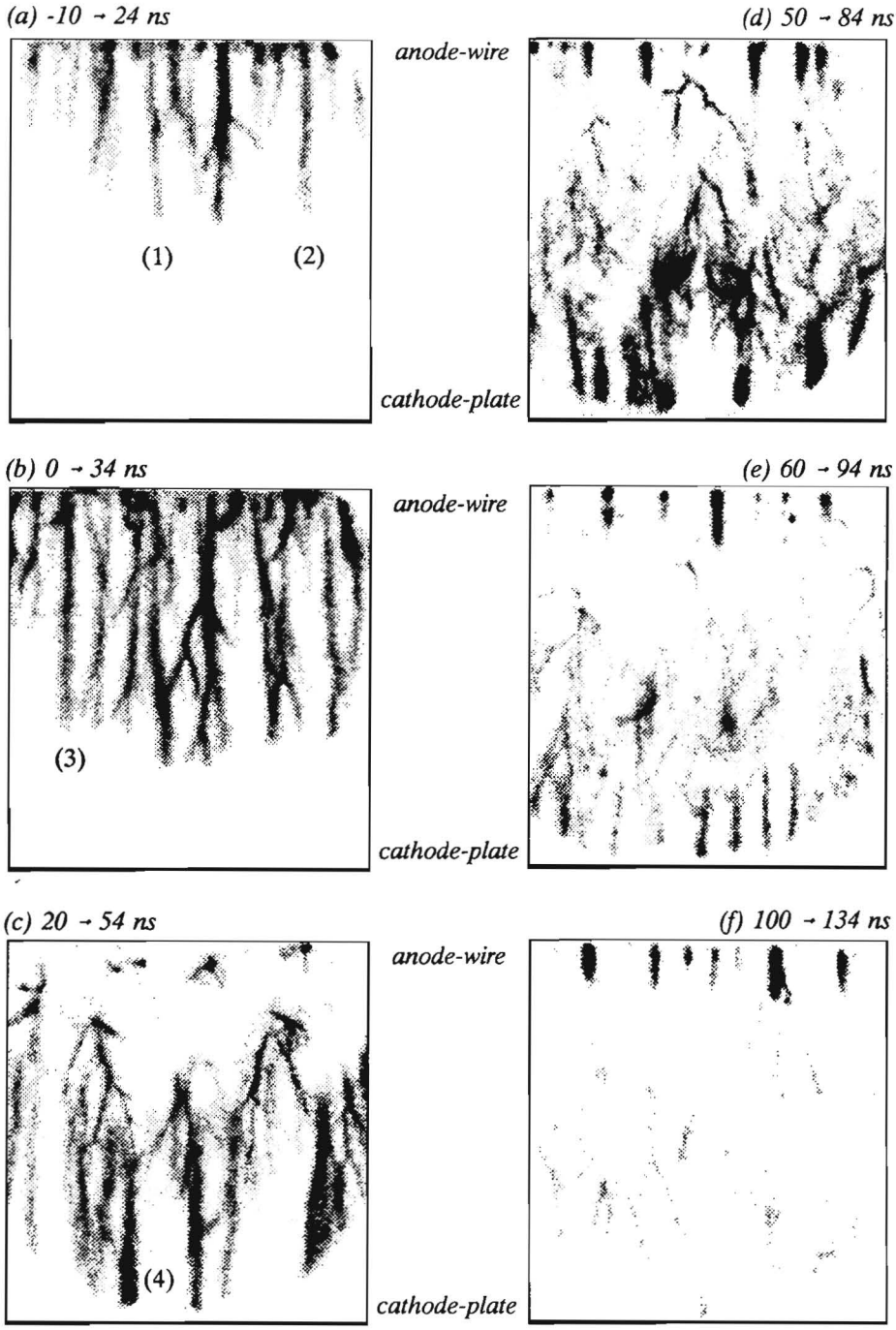

Fig. 5.18 2-D time-resolved discharge emission (object plane dimensions: 35 mm // wire, 38 mm ⊥ wire, M_1=0.43, M_2=0.48, M=0.21, τ_g=34 ns).

In pictures (a), (b) and (c) of Fig. 5.18, 4 streamer traces labelled with numbers (1) up to (4), have been analyzed with the program. The radially integrated intensity (expressed in arbitrary units) as a function of distance x, is shown in Fig. 5.19. In the mid-gap region (x = 10-25 mm), the intensities of the primary streamers (1), (2) and (3) are about equal and slightly decreasing as a function of position x. A sharp peak in trace (1), at x = 10 mm, is probably due to a second crossing primary streamer.

In general, intensity variations of primary propagating streamer heads which are seen on a CCD camera picture, can have a number of causes: (a) Changes in the space charge field distribution $E/n(x')$ (with x' as "streamer coordinate": $x' = x + V_s t$), (b) changes in the electron density distribution $n_e(x')$, (c) changes in the propagation velocity v_s and (d) changes in the radial structure of the streamer. The fact that the emission intensity in the mid-gap region is not a strongly varying function of x indicates that the quantities $E/n(x')$, $n_e(x')$, v_s and the radial streamer structure, are not strongly varying functions of x.

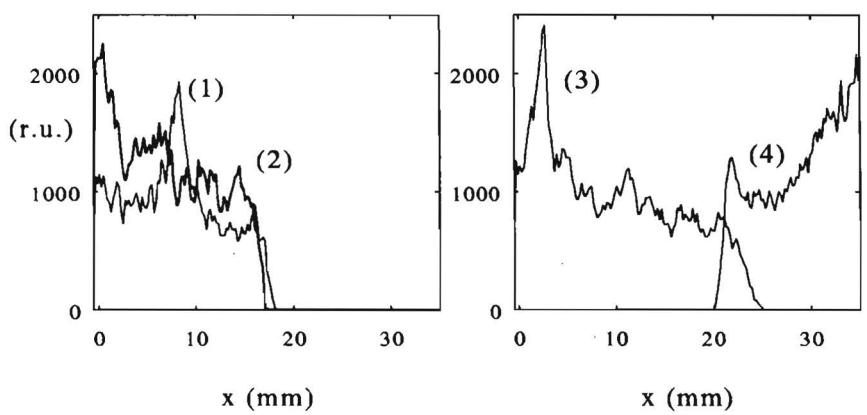

Fig. 5.19 Primary streamer trace intensity, radially integrated and as a function of distance x to the anode-wire. Intensity scales in the left and right pictures are the same. Numbers refer to traces in pictures of Fig. 5.18.

Fig. 5.20 shows examples of pictures, obtained with gate pulses which are long enough to integrate total discharge emission in time. The average streamer number density along the wire at V_m = 30 kV, determined from 20 pictures which are similar to picture 5.20 (a), is 600 m^{-1}. It appeared from a large number of pictures, obtained at different voltages ($20 < V_m < 30$ kV), that the average streamer number density along the wire is independent on the applied voltage.

Fig. 5.20 (b) has been taken with the optical axis in the direction of the anode-wire and shows that streamers deviate from the plane through the wire-axis perpendicular to the cathode surface. Most of the streamers propagate within a cone-shaped volume with a solid angle of 60 deg. In pictures (a) and (b), the threshold level, above which all intensities are shown in black, is the same. This level is chosen at about 50% of the maximum intensity observed in picture (a). At $V_m = 30$ kV, about 80% of the total light intensity, integrated in time, is due to the secondary streamer emission near the anode-wire.

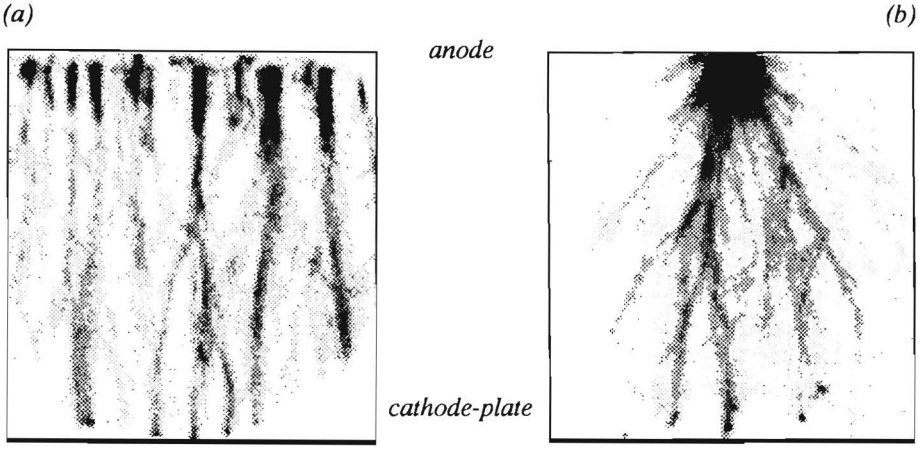

Fig. 5.20 Pictures of discharge emission integrated in time, (a) optical axis ⊥ wire-axis, (b) optical axis // wire-axis, wire length = 50 mm, $M_1 = 0.43$, $M_2 = 0.48$, $M = 0.21$, $\tau_g = 2$ μs, vertical $\Delta x = 2.1$ mm, horizontal $\Delta y = 2.0$ mm.

Magnified pictures of discharge emission are displayed in Fig. 5.21, 5.22 and 5.23. In order to increase sensitivity, the intensity of pixels in the x-direction has been summed. Vertically, the pictures show 24 groups of 16 summed intensities. Horizontally, the highest possible resolution of 1 pixel has been maintained. The spatial resolution (in the object plane) is 6 μm in horizontal direction and 90 μm in vertical direction. In pictures which have been obtained close to the anode, the axis of the anode-wire ($r_w = 300$ μm) is at the top of the picture and the boundary of the wire has been indicated as a horizontal line.

Fig. 5.21 (a) shows a picture obtained with the smallest possible gate pulse width ($\tau_g = 34$ ns). The image intensifier was activated before streamer inception (the inception time was measured with the fiber-tube-photomultiplier system) and de-activated before primary streamer arrival. A streamer, probably a cathode-directed streamer, is clearly seen. Two much weaker dots of light emission may be due to electron avalanches with insufficient space charge field for the initiation of cathode-directed streamers.

Fig. 5.21 (b) shows radial intensity profiles obtained from the data of picture (a) by averaging of 64 pixels in the y-direction (360 μm in the object plane). The "relative units" (r.u.) along the vertical axis are used for comparison with other pictures but not for quantitative determinations. The profiles do not show the radial emission intensity of streamer channels for which a de-convolution will be necessary. Nevertheless, it can be ascertained that at ~1 mm distance from the anode wire, the *optical streamer radius*, measured at 50% of the intensity maximum of the un-convoluted intensity profile, is ~200 μm. The broader profile at $x = \sim 2$ mm distance from the wire, can be due to the streamer being out of focus.

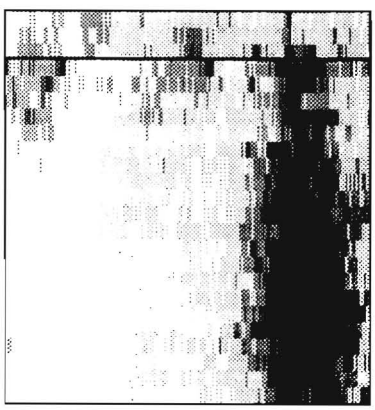

(a) Object plane dimensions:
vert. $\Delta x = 2.1$ mm, horiz. $\Delta y = 2.0$ mm.

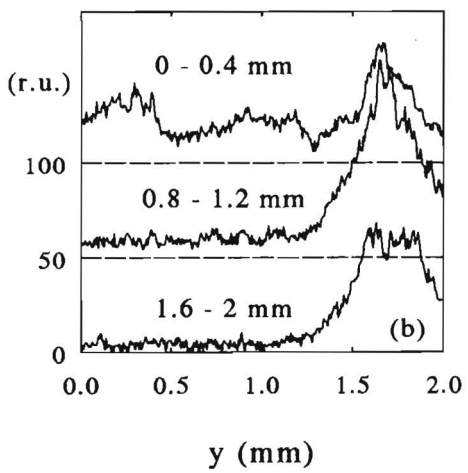

Fig. 5.21 (a) Magnified picture of discharge emission ($M = 4.1$, $\tau_g = 34$ ns).
(b) Radial intensity profiles for data integrated in x-direction of picture (a), dotted lines show zero emission levels corresponding to the different profiles.

Fig. 5.22 (a, b, c) shows examples of pictures obtained close to the anode wire with a gate pulse width of 2 μs. With this relative long gate pulse, the position of streamers is better observed. Fig. 5.22 (c) shows streamers formed close to each other. The two streamers, that flank the central streamer, propagate under an angle with the field direction. This fact may be caused by electrostatic repulsion of the electron avalanches in the streamer fronts. Fig. 5.22 (d, e) shows radial intensity profiles corresponding to Fig. 5.22 (a, b). Note the different scale, in relative units, along the vertical axis of intensity profiles in Fig. 5.21 and 5.22. The difference in emission intensity is mainly due to the contribution of the secondary streamer but also partly to increased sensitivity (increasing the gate pulse width from 34 ns to 2 μs, the sensitivity of the image intensifier increases by about a factor 2).

(a) (b)

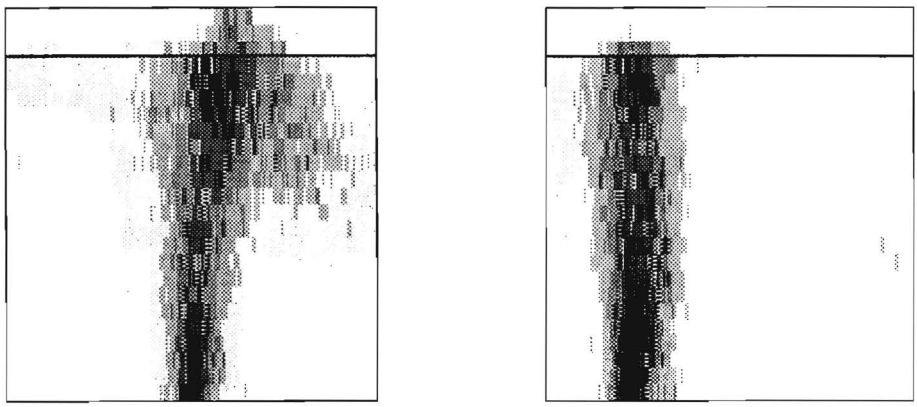

(c)

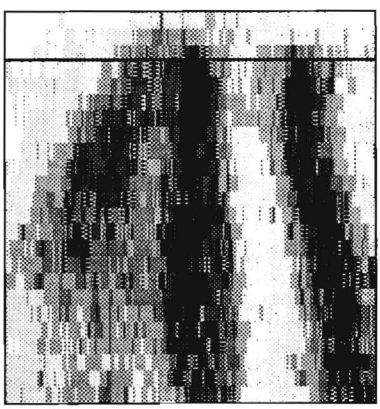

Fig. 5.22

(a, b, c) Magnified pictures of discharge emission, $M=4.1$, $\tau_g=2$ μs, object plane dimensions: vertical $\Delta x=2.1$ mm, horizontal $\Delta y=2.0$ mm.

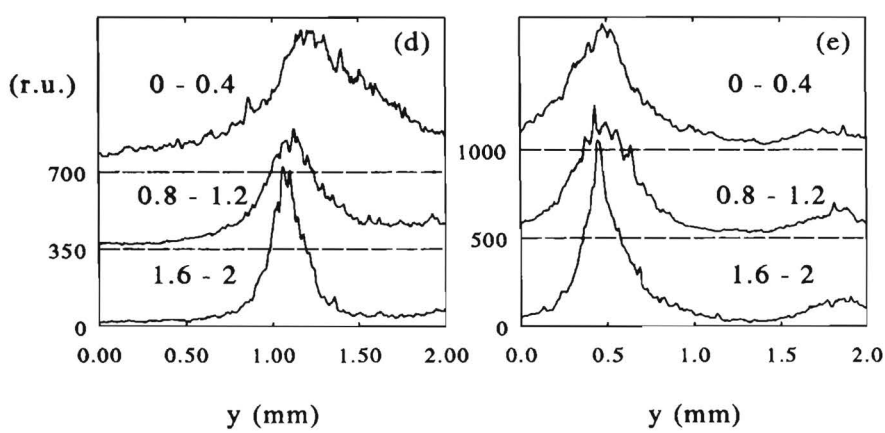

Fig. 5.22 (d, e) Radial intensity profiles for data of pictures 5.22 (a, b).

The radial emission profiles at x=1.6-2 mm, shown in pictures (d) and (e), indicate a relative small optical streamer radius (~120 μm) when compared to data in Fig. 5.21. It is conceivable that this difference is caused by different optical radii of primary and secondary streamers. In front of the primary streamer, the electron drift will in general have a radial component except for those avalanches which are directed along the central axis of the streamer (**2.2.2**). According to 2-D streamer models and current concepts about the secondary streamer phenomena in residual primary streamer channels (**2.4**), most of the electrons are enclosed in the central quasineutral part of the channel. The radial component of the electron drift velocity is relatively small in the streamer channel.

At a distance x larger than 1-2 mm from the anode, the magnified pictures of the discharge are often out of focus. Fig. 5.23 shows an example of one of the narrowest among the observed images at 5-7 mm from the anode. The picture shows the extremity of a secondary streamer. The optical radius of the secondary streamer is ~150 μm, close to the value measured at the anode.

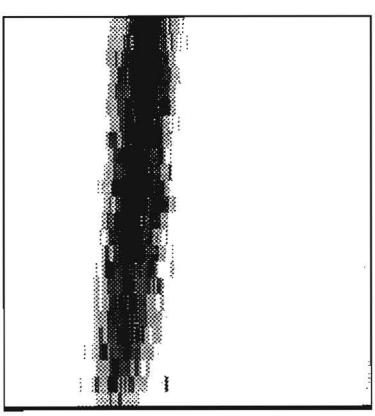

(1 anode)

Fig. 5.23

Magnified picture of discharge emission at distance x=5-7 mm from the anode wire (Δx=2.1 mm, Δy=2.0 mm, M=4.1, τ_g=2 μs).

Fig. 5.24 shows one of the narrowest intensity profiles of primary streamers that has been observed in the region x=30-32 mm. Because the primary streamer emission in this region is relatively weak, the profile has been calculated by summing of all (384) CCD pixels in the x-direction. It appears that the smallest measurable value of the optical streamer radius, in this part of the gap, is ~200 μm, thus also close to the values measured at the anode side of the gap. In principle, it is possible that different streamers possess different radii. However, in the experiment no discrimination could be made between possible larger streamer radii and streamers that were out of focus.

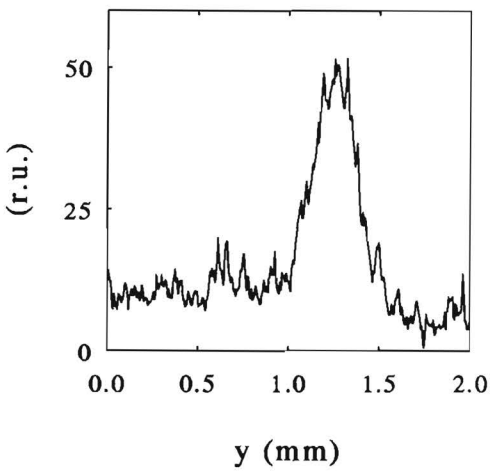

Fig. 5.24

Radial emission profile of a primary streamer at x=30-32 mm (τ_g=34 ns).

From streamer inception delay measurements (**5.2.2**) it appeared that, when a fast rising HV pulse (with long decay time) is applied, after an initial production of streamers along the wire within ~20 ns, no more streamers are formed. A possible explanation for this limited production in time is the distortion of the geometrical field that results from the collection of negative ions near the anode by the maintained high voltage. In order to investigate this possibility, a short HV pulse followed by a second HV pulse, was produced with electrical circuit I, see Fig. 5.25. The first HV pulse was limited in duration by switching the second spark. The second HV pulse was produced by quenching this spark gap. This was achieved by insertion of a resistance in series (R_{d2}=2kΩ, see Fig. 3.4) thereby lowering the spark gap potential. Simultaneously measured integral light emission, also shown in Fig. 5.25, indicates that during the second pulse, a second group of streamers is formed. During the first HV pulse the streamer inception voltage is 28 kV, during the second HV pulse streamer inception occurs at the minimum inception voltage $V_{i,\,min}$=16 kV.

Discharge emission during a first HV pulse and a following HV pulse (similar to pulses shown in Fig. 5.25), is shown in respectively pictures (a) and (b) of Fig. 5.26. It is clearly demonstrated that during the second HV pulse new primary and secondary streamers are produced, but their average number density (number per unit length of the wire) is less.

In section **5.2** was demonstrated that the dissipated energy per HV pulse decreases when the repetition rate is raised. The influence of repetition rate on energy dissipation and the limited production of streamers in time are likely to be both due to the collection of negative ions in the vicinity of the anode. Although in

between the HV pulses shown in Fig. 5.25 the voltage is still a third of the maximum, this lowering of the voltage and the time period of ~500 ns are apparently enough for partly restoring the geometrical field so that new streamers can be formed. Presumably, the streamers shown in Fig. 5.26 (b) followed the paths of the streamers that were produced 500 ns earlier because this also happens in self-repetitive positive streamer corona with a period of 0.1-1 ms.

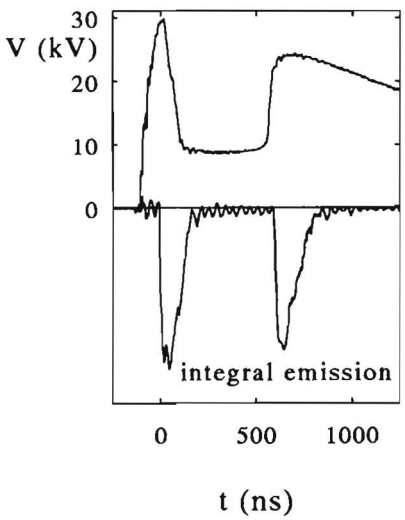

Fig. 5.25

HV pulses with short delay, for the investigation of streamer production as function of time.

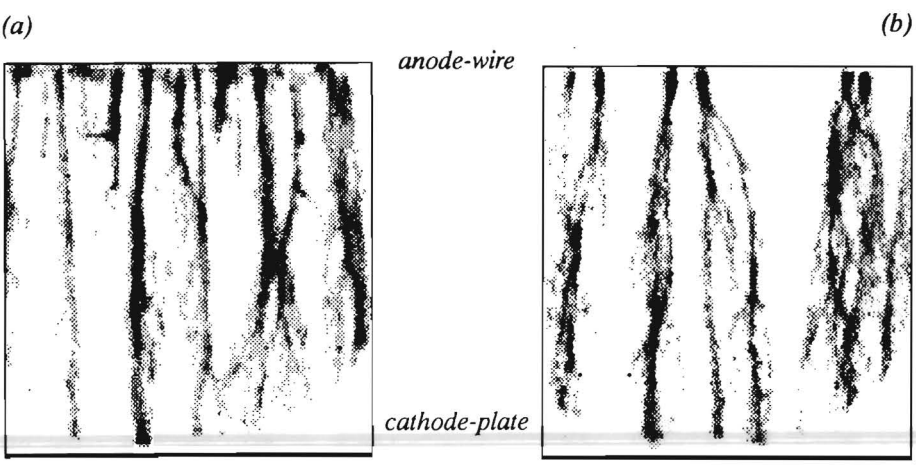

Fig. 5.26 *Pictures of discharge emission during two HV pulses, separated ~0.5 μs in time ($\Delta x = 37$ mm, $\Delta y = 35$ mm, $M_1 = 0.43$, $M_2 = 0.48$, $M = 0.21$, $\tau_g = 0.5$ μs) (a) During first HV pulse, (b) during second HV pulse.*

Fig. 5.27 shows remarkable differences between pictures obtained with tip-plate and sphere-plate configurations (Fig. 3.3 (b), Table 3.1). The intensity intervals, that correspond with gray tones on the pictures, are for both pictures the same. Streamers appear with much higher intensity in the sphere-plate configuration. The pictures have been obtained with V_m=34 kV. Breakdown in the sphere-plate configuration was avoided covering the cathode with a glass plate with 2 mm thickness. Some signs of spreading of the discharge on the dielectric surface are seen. The static breakdown voltage in the tip-plate configuration is higher ($V_b \approx 35$ kV) so that no dielectric was required.

The emission shown on the pictures in Fig. 5.27, is probably dominated by emission from secondary streamers. Time resolved pictures have not been obtained with these configurations. The field in the sphere-plate configuration is lower in the anode region but higher in the cathode region (Fig. 3.2). The lower divergence of the field is a probable cause of more favourable conditions for both primary streamer formation and primary streamer propagation. The formation of primary streamers in the critical volume close to the needle-tip, where $E/n > (E/n)_c$, is probably more hindered by "competition" (electrostatic repulsion) between avalanches and streamers. Propagation of primary streamers in the low field region, where $E/n < (E/n)_c$, can be favoured because the part of the gap volume where the geometrical field is higher than the stability field, $E/n > (E/n)_s$, is larger.

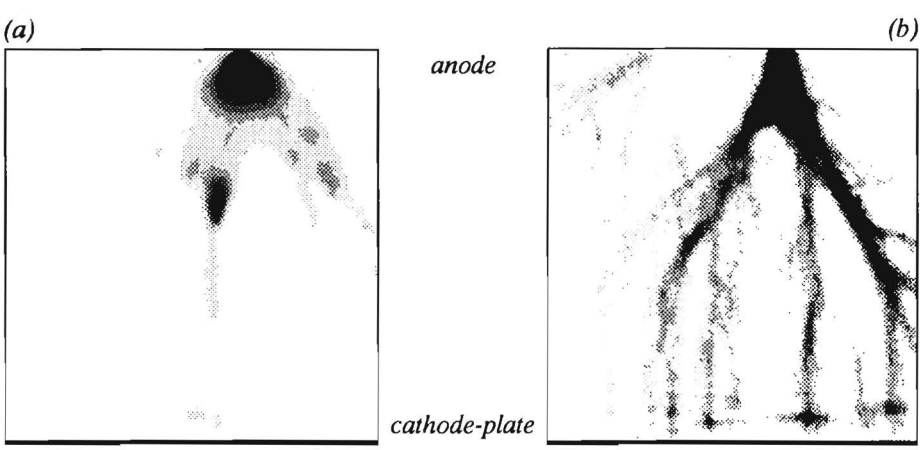

Fig. 5.27 Pictures of discharge emission (M_1=0.37, M_2=0.57, M=0.21, τ_g=2 μs).
(a) Tip-plate configuration I (r_t=0.1 mm, d_g=35 mm).
(b) Sphere-plate configuration (r_s=4 mm, d_g=35 mm).

Fig. 5.28 shows two pictures of discharge emission which have been obtained without the image intensifier and under identical conditions. Although mainly secondary streamer emission is seen, this emission shows the paths that were

ionized by strongly branching primary streamers. Repeated measurements showed large statistical variations in the discharge structure, integral emission intensity and the current. These variations may depend on small differences in time and position of initial primary avalanches that will influence their mutual electrostatic interaction. In wire-plate and wire-cylinder configurations, the mutual influence and the branching of streamers have less influence on the streamer properties.

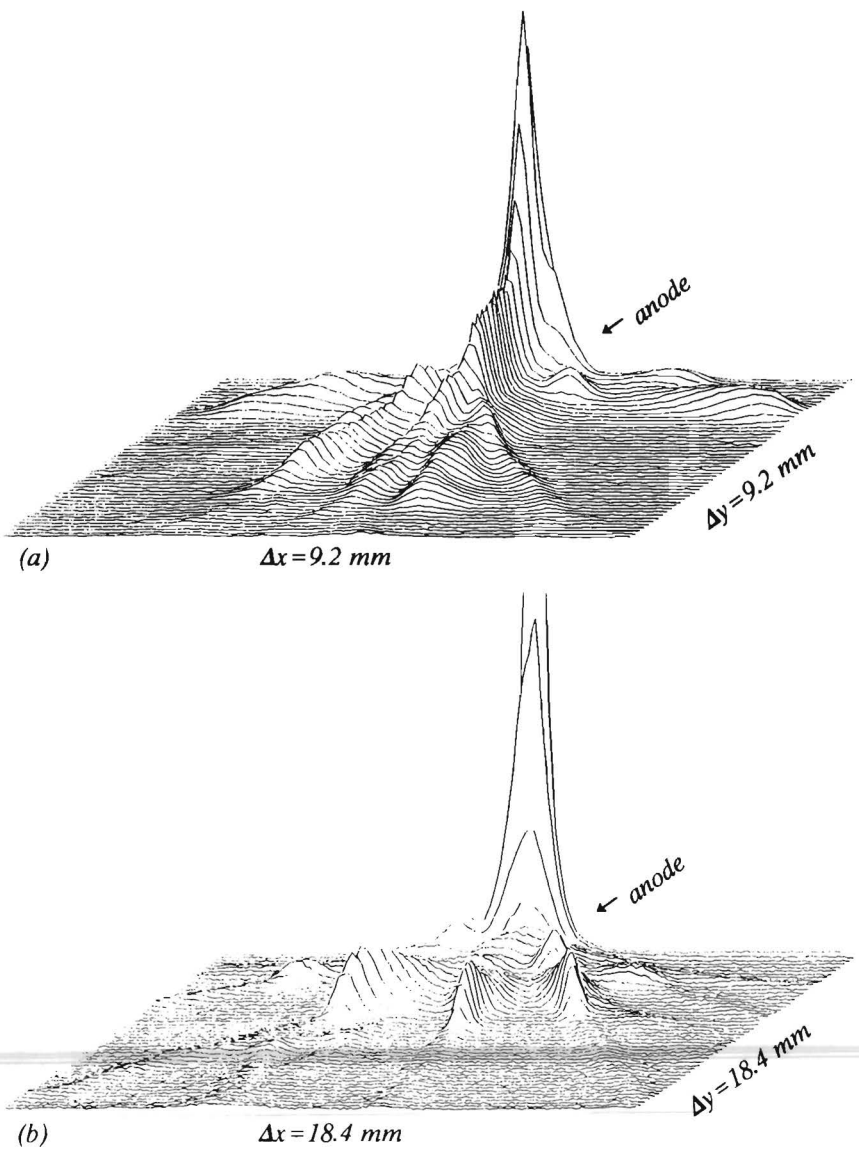

Fig. 5.28 CCD-pictures obtained without the image intensifier, needle tip-plate configuration with 35 mm gap, $V_m = 34$ kV, $M = 0.48$.

The existing theoretical concepts of secondary streamers in air (**2.4**) attribute a predominant role to the attachment properties of oxygen (i.e. the local minimum in the attachment coefficient at $E/n \approx 40$ Td). The influence of attachment to oxygen was investigated, by making pictures of streamers in N_2-O_2 mixtures with much lower oxygen concentration than in air and in N_2-CO_2 mixtures. Fig. 5.29 shows examples of pictures made of streamers in a 5% O_2 - 95% N_2 mixture and in a 20% CO_2 - 80% N_2 mixture. The voltage (V_m=20 kV) was close to the static breakdown voltage in the N_2-O_2 mixture. Although no time-resolved pictures have been made, some conclusions can be drawn from the observation of time-integrated pictures. The pictures can be compared to time-integrated pictures of streamers in air (Fig. 5.20).

In the 5% O_2 - 95% N_2 mixture, secondary streamers are apparently formed because local intensity maxima of residual streamer channel emission are seen in the mid-gap region. A concentration of the secondary streamer emission in the anode region, as in dry air, is not observed. Close to both electrodes, the spatial extend of regions with relative high intensity (probably due to the secondary streamer and the cathode fall) is approximately equal. In the 20% CO_2 - 80% N_2 mixture, the emission is even more concentrated in regions close to both electrodes. Still, secondary streamers may be formed but are not clearly seen. It can be noticed that in the 5% O_2 - 95% N_2 mixture, bending and branching of (primary) streamers occurs more often than in dry air. Streamers in the 20% CO_2 - 80% N_2 mixture propagate almost along straight paths.

Summarizing the results obtained with the image-intensifier CCD system. In the case studied, the average streamer number density is ~600 m^{-1} and independent on the applied voltage. Three discharge phases are observed: (i) primary streamer propagation, (ii) secondary streamer phenomena (re-illumination of otherwise dark primary streamer channels) and (iii) a "resistive" phase, characterized by secondary streamers with constant length and diminishing light emission intensity. Primary streamer channel re-illuminations (probably secondary streamers) are not only observed in the anode region but also (during a period of ~50 ns) near the cathode and mid-gap. The optical radius of primary streamers near the anode is ~200 μm. Similar (minimum) values of streamer radii have been measured mid-gap and close to the cathode. The minimum optical radius of the secondary streamer appears to be ~150 μm. Experiments with "double" HV pulses indicate that during a HV pulse primary streamer formation is limited as a result from negative ion accumulation in the vicinity of the anode.

Results obtained with tip-plate and sphere-plate corona configurations show that conditions for both streamer formation and streamer propagation can be favoured with a more homogeneous distribution of the geometrical field. Experiments with N_2-O_2 and N_2-CO_2 mixtures show that primary streamer properties, like branching and bending, are much influenced by the gas composition.

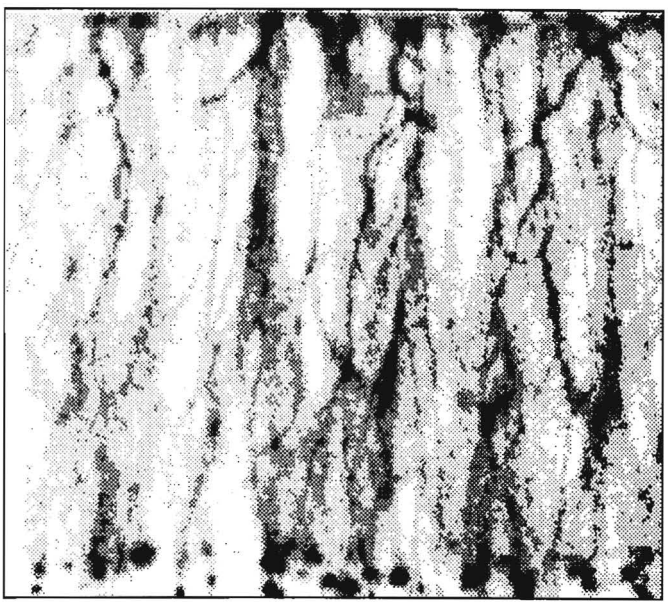

(a) 5% O_2 in N_2-O_2 mixture (anode at top)

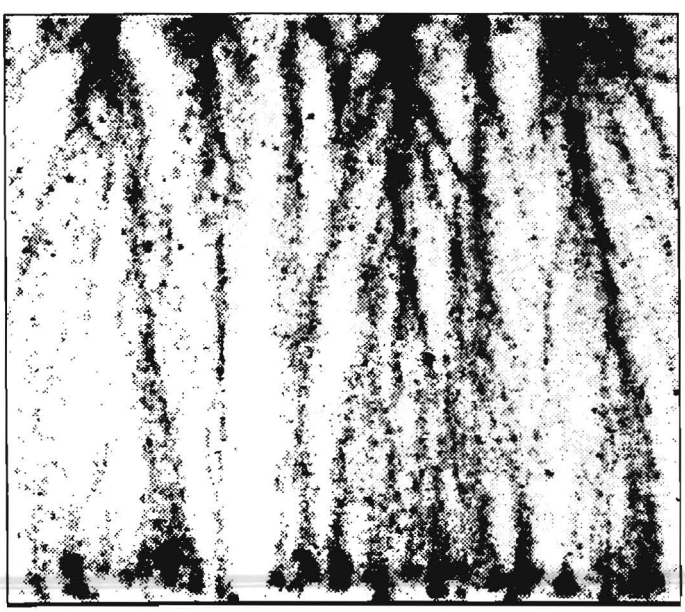

(b) 20% CO_2 in N_2-CO_2 mixture (anode at top)

Fig. 5.29 Discharge emission in N_2-O_2 and N_2-CO_2 mixtures (V_m=20 kV, M_1=0.37, M_2=0.57, M=0.21, τ_g=2 μs).

5.3.2 Streamer velocity

The streamer velocity has been measured according to the methods for the detection of local emission, described in **4.1.3**. HV pulses of the type shown in Fig. 5.1 (a), with $t_r \approx 40$ ns and $f = 20$ Hz, have been used. Fig. 5.30 shows an example of two local light emission signals, detected at respective 3 and 5 mm distance from the anode-wire, with the system of two fibres contained in tubes. The delay time between the primary streamer emission signals (3.8 ns) has been determined from interpolation of measured samples close to the reference level (dotted line in Fig. 5.30). The corresponding streamer velocity is 0.5 mm/ns ($V_m = 25$ kV, $x = 4$ mm). The secondary streamer velocity is ~0.1 mm/ns.

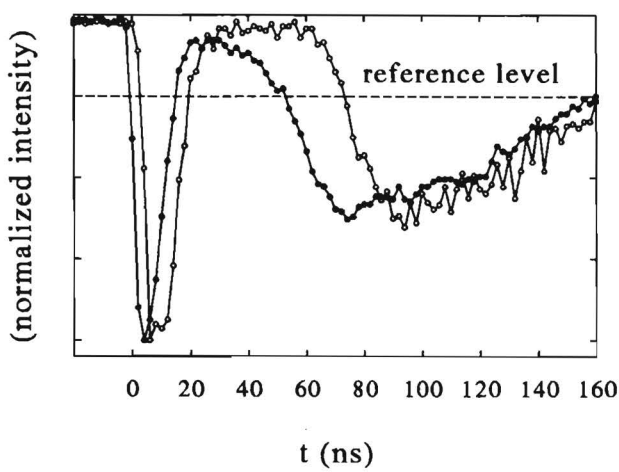

Fig. 5.30 Local light emission measurements at 3 and 5 mm distance from the anode wire (wire-plate configuration I, $V_m = 25$ kV).

The measured average streamer velocities, which will be presented below, have been determined with fibres at 4 mm and 5 mm relative distance. The larger distance (for Fig. 5.30 a relative distance of 2 mm was used) provides a higher reproducibility of results at the expense of spatial resolution. The average delay time has been calculated in real time from 1000 delay time measurements, using for each measurement interpolation of samples at 25% of the signal amplitude. Examples of delay time distributions are shown in Fig. 5.31. The spread in the measured delay times can be due to (a) real differences in the velocities among streamers, (b) the propagation angle with respect to the x-axis and (c) measuring errors. Systematic measuring errors have been minimized requiring that the measured average delay time remains unchanged when the two measuring fibres in the tubes are exchanged. When a streamer propagates under an angle of 30° with the x-axis, a maximum error of 13% can be made.

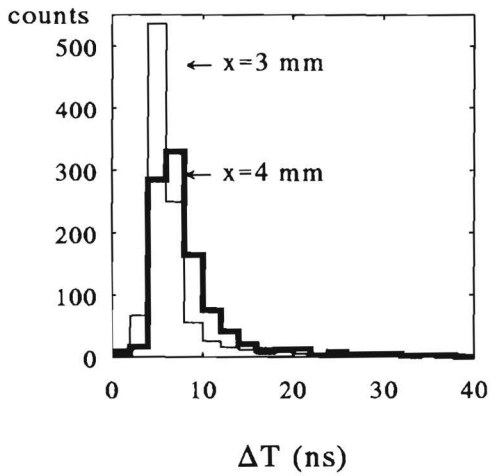

Fig. 5.31

Distribution of delay times for streamer velocity measurements at 3 and 4 mm distance from the anode-wire (wire-plate configuration I, V_m=25 kV).

Fig. 5.32 shows measurements of streamer velocities in wire-plate configuration I, as a function of the distance to the anode. In dry air, the streamer velocity increases with increasing voltage and in N_2-O_2 mixtures it decreases with increasing O_2 concentration. A relative strong decrease in velocity is measured close to the boundary of the critical volume (x_c=2.1 mm at V_m=25 kV). The spatial gradient of the streamer velocity may be even steeper in reality because, in the measurement, velocities are averaged over a distance of 4 mm. At the distance from the anode wire where the geometrical field equals the stability field (x_s=10.5 mm at V_m=25 kV) the streamer velocity is approximately constant.

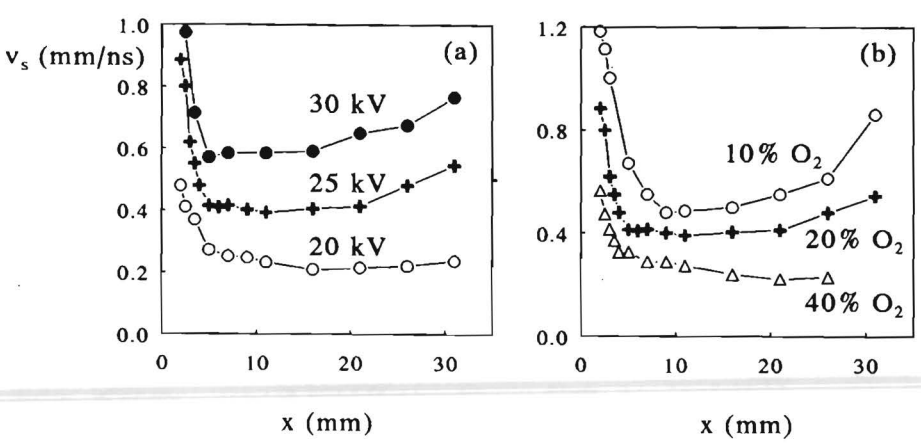

Fig. 5.32 The average streamer velocity $<v_s>$ in wire-plate configuration I, (a) $<v_s>$ for different V_m (in dry air), (b) $<v_s>$ for different $[O_2]$ in a N_2-O_2 mixture (V_m=25 kV), r_w=0.3 mm, d_g=35 mm.

In air, the minimum voltage for streamers reaching the cathode is ~20 kV. The streamer velocity is then remarkable constant for $x>x_s$. At $V_m=25$ kV and $[O_2]=40\%$, streamers stop before reaching the cathode. The streamer propagation velocity appears to be bound to a minimum value of ~0.2 mm/ns. At relative high voltage or low oxygen concentration, streamers appear to propagate faster when approaching the cathode.

The influence of the voltage and oxygen concentration on the measured streamer velocity is in good qualitative agreement with the model results obtained by using numerical code I (**2.3.4**). The observation that streamers stop before reaching the anode in air at $V_m<20$ kV and in N_2-O_2 mixtures with $V_m=25$ kV and $[O_2]>40\%$ is in agreement with the calculations (Fig. 2.27). However, also significant differences between measured and calculated streamer velocities, exist. The numerical model predicts that the streamer velocity first increases and decreases in the region of the gap where where $E/n<(E/n)_s$ (20 Td). However, at the distance from the wire where the model predicts a velocity maximum (~10 mm) a minimum velocity is measured. It is possible that an initial increase of the streamer velocity is not measured due to lack of spatial resolution (the measurement integrates 4 mm in the x-direction and the measurement point closest to the anode is at 2 mm distance). The much faster measured decrease of the streamer velocity can be due to the electrostatic repulsion of simultaneously propagating streamers which was not included in the calculations. The numerical streamer model shows an increase of the streamer velocity when it approaches the cathode at ~2 mm, due to the influence of image-charges at the cathode surface. This effect appears to be insufficient to explain the measured increase of the streamer velocity, starting already in the mid-gap region for high applied voltages.

Fig. 5.33 shows results of streamer velocity measurements using the tip-plate configuration ($r_t=0.1$ mm, $d_g=35$ mm, Table 3.1) and the lens-fibre system (Fig. 4.4). An initial increase of the streamer velocity as a function of distance has been measured in this geometry. The velocities are much higher than those measured in the wire-plate configuration.

The average time needed for streamers to cross the gap, can be determined by averaging of the delay time between local light emission signals at both the anode and the cathode. The average streamer transit time and the spread in the delay time measurements (width at 50% of the maximum in probability distributions), are given in Fig. 5.34. The average streamer transit time has also been calculated from from the sum of locally measured delay times (used for local velocity determinations). A comparison with direct measurements of the streamer transit time (Fig. 5.34) shows that both methods give similar data. The measured average transit time at $V_m=45$ kV has been obtained from local emission measurements in wire-cylinder configuration I with HV and current pulses of the type shown in Fig. 5.5. In this case the local streamer velocity was not measured.

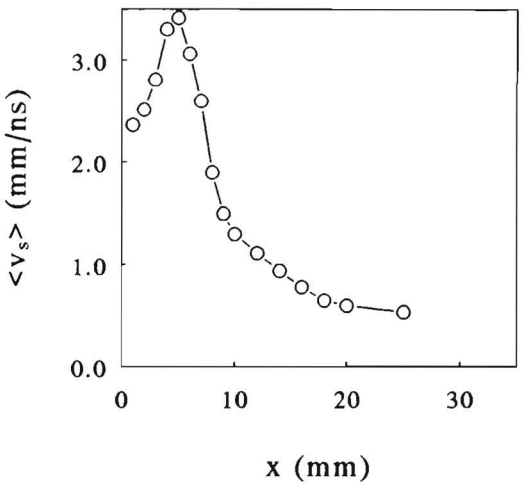

Fig. 5.33

The average streamer velocity $<v_s>$ as a function of distance x to the anode (needle tip-plate configuration, r_t=0.1 mm, d_g=35 mm, V_m=25 kV).

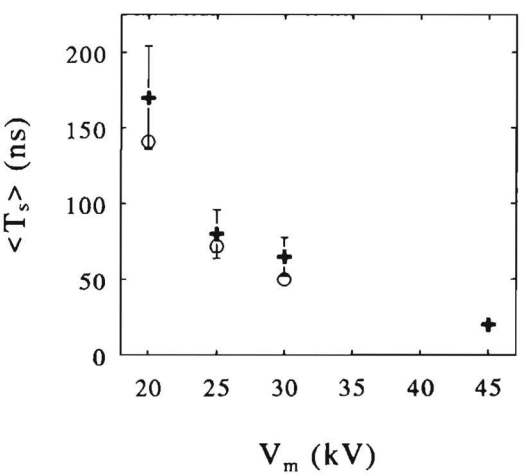

Fig. 5.34

The average streamer transit time as a function of V_m (wire-cylinder configuration I, d_g=35 mm).
(+) from local emission measurements at the electrodes.
(O) sum of local delay time measurements (used for local streamer velocity measurements).

5.3.3 Measurements of N_2^+(391.4 nm) and N_2(337.1 nm) emission lines

Spectroscopic measurements of light emission were performed with the system of optical fibres, described in **4.1.4**, offering a minimum spatial resolution of ~7 mm. Fig. 5.35 (a) shows an example of the emission spectrum in the wavelength range 370-410 nm, obtained with a wavelength resolution of 0.2 nm and the multi-channel analyzer for data acquisition. Fig. 5.35 (b) shows, on enlarged scale, the part of the spectrum with the N_2^+(391.4 nm) emission line. The intensity of this relative weak emission line has been measured as the difference between the intensity maximum at 391.4 nm and the intensity at 391.8 nm, thus accounting for the contribution of neighbouring emission lines of the SPS of N_2 and continuum emission.

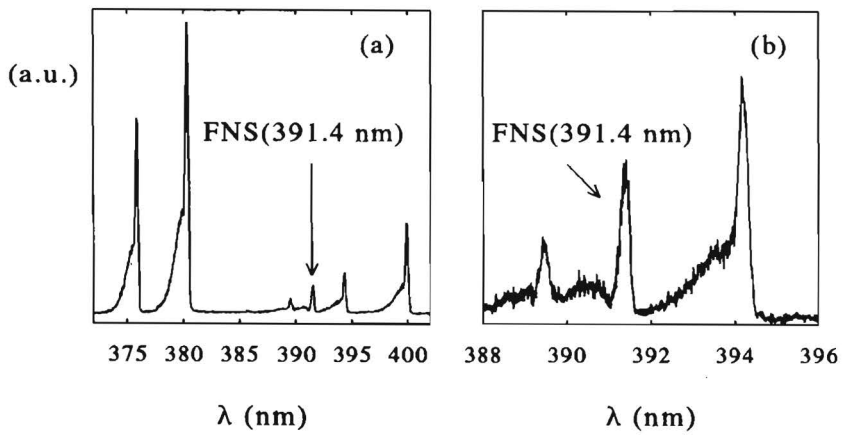

Fig. 5.35 (a) Emission spectrum of the SPS of N_2 and the FNS of N_2^+ (V_m=25 kV, f=100 Hz), (b) the N_2^+(391.4 nm) line and neighbouring lines on enlarged wavelength scale, wavelength resolution $\Delta\lambda$=0.2 nm.

Spectroscopic signals as a function of time were measured with the oscilloscope. In Figs. 5.36 and 5.37 averaged signals are displayed, which have been obtained by measuring 100 signals with a discharge repetition rate of 20 Hz and using integral light as trigger. Fig. 5.36 shows the intensity of the N_2(337.1 nm) emission line for four positions of the central axis of the system of optical fibres. Secondary streamer emission, concentrated in the anode region, is clearly seen. The (average) intensity of primary streamer emission increases when these streamers approach the cathode, see peak (4) in Fig. 5.36. The increase of the primary streamer emission intensity is even stronger at V_m>25 kV. This observation proves that the increased intensity of streamer traces seen on CCD camera picture (c) of Fig. 5.18 (obtained at V_m=30 kV) is, at least partly, caused by primary streamers. Moreover, also an increase of primary streamer velocity has been observed in the cathode region, see Fig. 5.32 (a).

Fig. 5.37 (a) shows that emission of the N_2(337.1 nm) emission line, by both primary and secondary streamers, is strongly suppressed when the oxygen concentration is increased. The decrease of primary streamer light emission is mainly due to the increased collisional quenching of $N_2(C)$ by O_2 molecules. According to Eq. 4.5 and Mitchell's quenching coefficients (Table 4.1), when $[O_2]$ increases from 20 to 40%, the relative number of $N_2(C)$ states that decays by radiation decreases from $1.3 \cdot 10^{-2}$ to $0.7 \cdot 10^{-2}$. The reduction of secondary streamer emission is much stronger. Thus it is evident that, increasing $[O_2]$ from 20 to 40%, secondary streamer emission diminishes by two causes: (a) Increased collisional quenching and (b) less excitation to $N_2(C)$ because of lower E/n.

Fig. 5.37 (b) shows the intensity of the $N_2^+(B)$ emission line as function of time. The displayed signals have been obtained by subtracting two signals at 391.4 nm and 391.8 nm. The intensity of the N_2^+(391.4 nm) line during secondary streamer emission is almost zero. This fact, that was earlier observed by Marode (1972), indicates that the electric field and the average electron energy in the secondary streamer are very low in comparison with values of these quantities in the primary streamer.

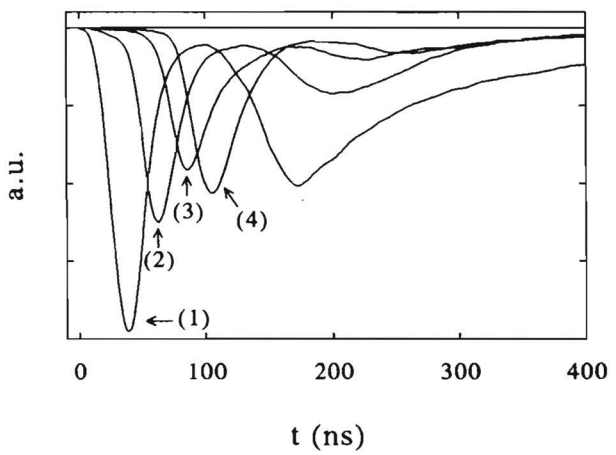

Fig. 5.36 *N_2(337.1 nm) emission as function of time, distance from anode: (1) 0-10 mm, (2) 8-18 mm, (3) 16-26 mm, (4) 25-35 mm (V_m=25 kV, f=20 Hz).*

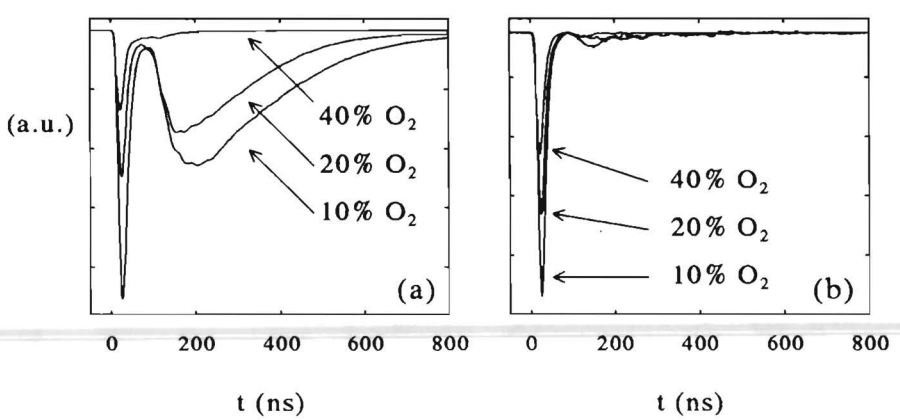

Fig. 5.37 *Line emission as function of time and $[O_2]$, (a) N_2(337.1 nm), (b) N_2^+(391.4 nm), V_m=25 kV, 0-10 mm from anode wire.*

The light emitted by primary streamers is dominated by radiation from excited states which have been produced by electrons in a field close to the E/n maximum because the bulk of the electrons are produced in fields close to this maximum, see **4.2.5.** Therefore, the intensity ratio of the N_2^+(391.4 nm) and N_2(337.1 nm) emission lines, can be used to estimate the maximum values of E/n and the average electron energy ϵ_a in the primary streamer head. According to the discussion in **4.2.5**, even assuming that only direct excitation occurs and that excitation cross sections and collisional quenching coefficients are correct, the measurement yields no exact values of the maxima of E/n and ϵ_a because not all measured light is emitted by electrons at the E/n maximum and the properties of primary streamer heads may change during propagation in the detection volume (~10 mm). Therefore, mean values, e.g. $<\Pi_B>/<\Pi_C>$, $<E/n>$ and $<\epsilon_a>$, which have been defined in **4.2.5**, are used. The ratio $<\Pi_B>/<\Pi_C>$ is determined from spectra, like the spectra shown in Fig. 5.35, which have been measured by means of the multi-channel analyzer with a time resolution of 40 ns which is small enough to separate primary and secondary streamer emission in time.

Fig. 5.38 (a) shows the intensity ratio $<\Pi_B>/<\Pi_C>$ as a function of position in the gap. The position corresponds to the distance of the central axis of the optical fibre system to the anode. The relative line intensity method (see **4.2.5**) is applied to estimate the maximum E/n in the streamer head region from the measured ratio $<\Pi_B>/<\Pi_C>$ (Fig. 4.10). The experimental results are compared in Fig. 5.38 (b) with calculated maxima of E/n (using the numerical streamer model presented in **2.3**). With increasing distance to the anode, the measured ratio $<\Pi_B>/<\Pi_C>$ (and thus E/n in the streamer head) first decrease, remain approximately constant in the region x = 10-20 mm and increase again for x > 20 mm. Close to the cathode (region 25-35 mm) $<\Pi_B>/<\Pi_C>$ decreases again. Because of the limited time resolution of the multi-channel analyzer (40 ns) it is probable that the light measured close to the cathode is partly due to the residual channel re-illuminations observed on CCD camera pictures, see Fig. 5.18 (d). From a comparison with the measured streamer velocity (Fig. 5.32) it can be concluded that the streamer propagation velocity and the maximum field strength in the streamer head are strongly coupled. At V_m = 30 kV, both quantities decrease when streamers propagate from the high geometric field region toward the low field region, are almost constant in the mid-gap region and increase again when approaching the cathode.

Fig. 5.39 shows that when the applied voltage is increased, a considerable increase of $<E/n>$ occurs: increasing V_m from 20 to 35 kV, $<E/n>$ increases by 50%.

Fig. 5.40 shows the influence of $[O_2]$ in a N_2-O_2 mixture on the measured ratio $<\Pi_B>/<\Pi_C>$. By increasing the oxygen concentration from 5 to 40%, $<E/n>$ decreases almost by a factor 2.

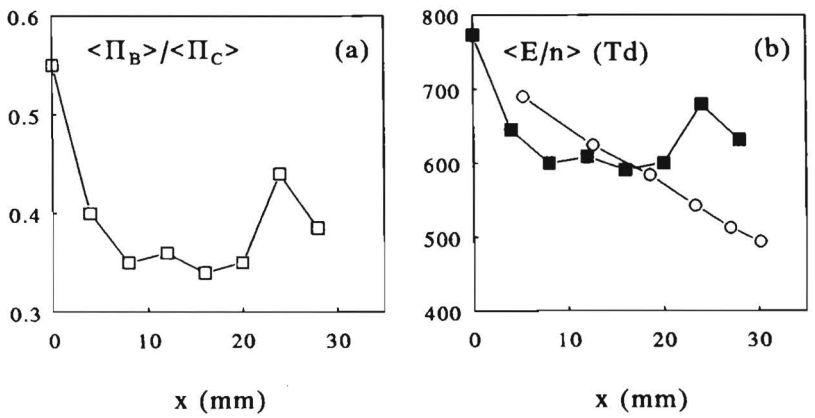

Fig. 5.38 *(a) $<\Pi_B>/<\Pi_C>$ measured as a function of position in the gap.*
(b) $<E/n>$ measured (■) and calculated with the numerical streamer model (○).
(dry air, V_m=25 kV, spatial resolution is ~10 mm, $\Delta\lambda$=0.2 nm)

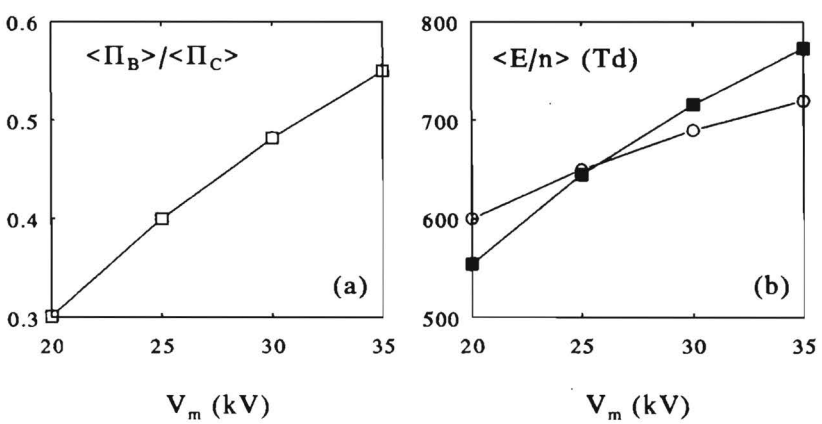

Fig. 5.39 *(a) $<\Pi_B>/<\Pi_C>$ measured as a function of V_m.*
(b) $<E/n>$ measured (■) and calculated with the numerical streamer model (○).
(dry air, 0-10 mm from the anode, $\Delta\lambda$=0.2 nm)

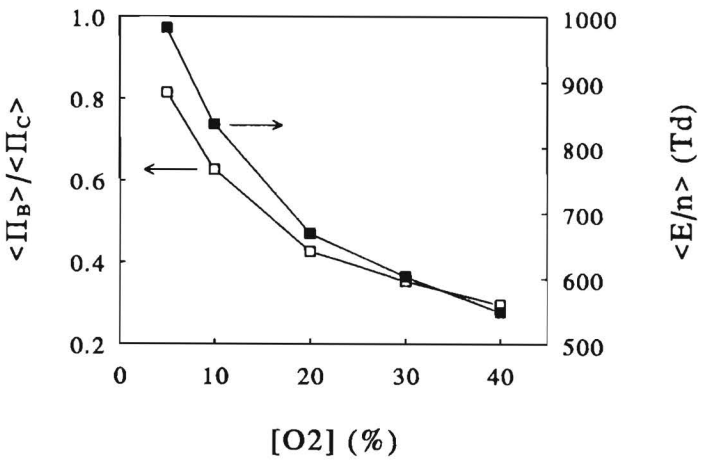

Fig. 5.40 Measured $<\Pi_B>/<\Pi_C>$ and $<E/n>$ as function of $[O_2]$ (V_m=25 kV, 0-10 mm from the anode).

A measurement of the rotational spectrum of the N_2(337.1 nm) emission line is shown in Fig. 5.41. The spectrum has been obtained using wire-cylinder configuration I, without spatial resolution. HV pulses with V_m=30 kV and f=300 Hz were applied. The multi-channel analyzer (time resolution ~40 ns) was activated 50 ns after the start of the discharge, i.e. mainly light emitted by secondary streamers in residual primary streamer channels was detected. The measured spectrum is similar to a simulated spectrum using a rotational temperature of 300 K and a Gaussian convolution profile with 0.04 nm halfwidth. The accuracy of the rotational temperature determination from a comparison of measured and simulated spectra is about 100 K (see the simulated spectrum at 600 K in Fig. 4.12).

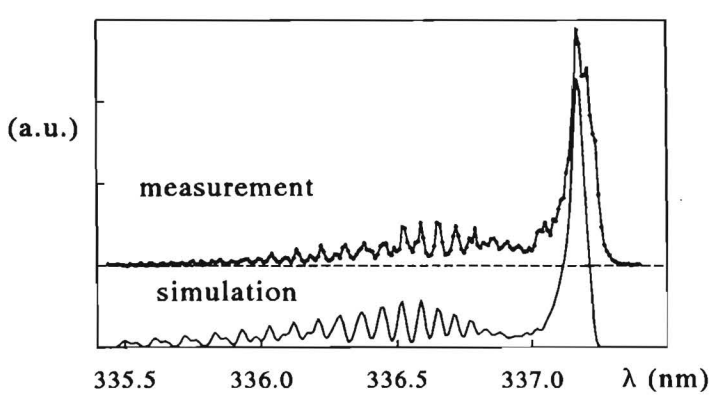

Fig. 5.41 Measured and simulated rotational spectra of secondary streamer light emission ($\Delta\lambda$=0.04 nm, V_m=30 kV).

5.4 Schlieren photography

Schlieren photographs have been made with wire-plate geometry II and wire-cylinder geometry IV (both with d_g=50 mm) in ambient air. The HV pulses were similar to the HV pulses shown in Fig. 5.1 (a) with a rise time of ~40 ns and with the corona inception voltage close to the voltage maximum V_m. The breakdown probability becomes non-zero for V_m>42 kV and practically 100% at V_m>46 kV. Residual streamer channels with relative large density gradients caused by relative high energy dissipation in the channels, are most clearly visualized. Therefore all photographs on pictures presented in this section have been obtained with V_m in the range of 40-45 kV. In any picture the anode is at the top.

Picture (a) in Fig. 5.42 shows that density gradients in residual streamer channels can be visualized when the light pulse of the flash is terminated ~2 μs after the start of the discharge (the flash lamp with a light pulse duration of ~5 μs was triggered before the start of the discharge). Although streamers cross the entire gap (obvious from optical emission), only close to the anode enough energy is dissipated for making density gradients visible with the Schlieren set-up. Pictures (b) and (c) in Fig. 5.42 have been obtained 100 μs after the start of the discharge. In this period, a relative large part of the total dissipated energy appears to be transfered to the gas. Note that the period of 100 μs is close to the vibrational relaxation time in air with 1% H_2O (see references given in **2.4.3**, p. 83). Besides the relaxation of energy contained in (vibrationally) excited states, also ion drift in the streamer channel may contribute to delayed energy transfer. This possibility was recently proposed by Lamb and Woolsey (1992, reference of Chapter **4**) to explain their results obtained with time-resolved Schlieren measurements with self-repetitive DC positive streamer corona. Vibrational relaxation, however, is probably the main contribution because the current of the discharge has principally been carried by electrons in the streamer channel at a field E/n in the range 20-40 Td at which vibrational excitation is the dominant electron energy loss process. It is noted that energy dissipation is the highest in the part of residual streamer channels where also secondary streamers are formed.

The number of (visible) streamers per unit length of wire can be determined from the photographs. The average number, 5-7 streamers per 10 mm wire, is the same as observed from CCD camera pictures of light emission in a 35 mm gap. Residual streamer channels can still be visualized after delay times of several ms but the channels then become less visible because of gas and heat diffusion. All other photographs presented in this section have been obtained with a delay of 100 μs.

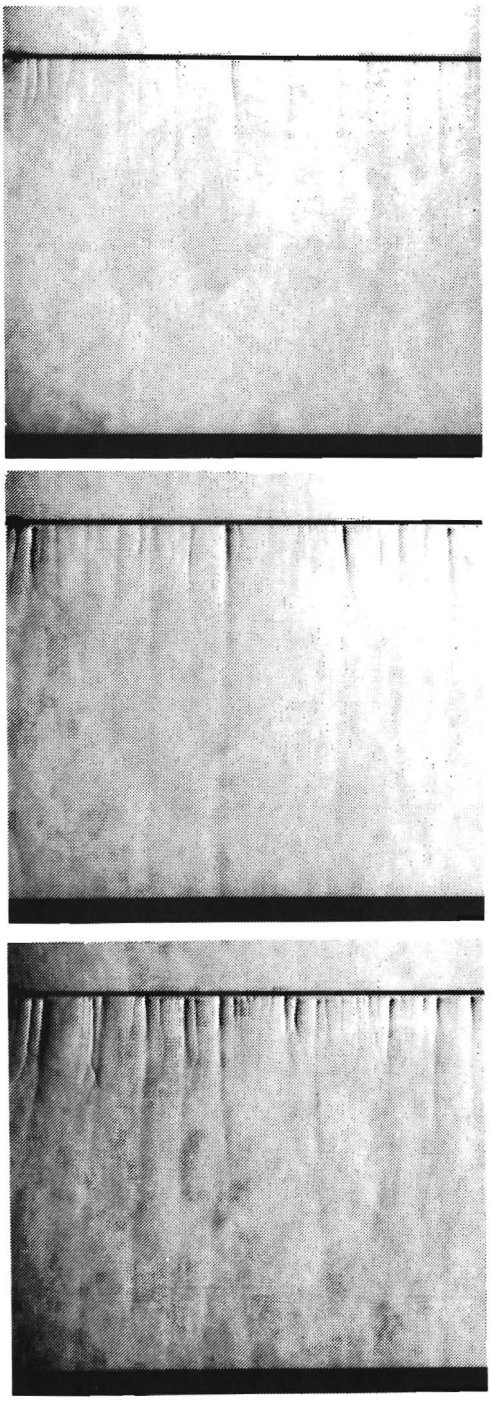

(a) delay time: 2 μs

(b) delay time: 100 μs

(c) delay time: 200 μs

Fig. 5.42 Schlieren photographs made at different moments after the start of the discharge. (wire-plate geometry II, V_m=40 kV).

Fig. 5.43 shows a photograph that has been made using an alternative anode structure with multiple pins (12 per 10 mm length), see Fig. 3.3 (a). At (almost) every pin a streamer channel is seen, thus the number density of (visible) channels has almost been doubled when compared to the number density at a smooth wire. Comparing this picture with the pictures shown in Fig. 5.42, it appears that the differences in energy dissipation between separate streamers are less. Fig. 5.44 shows a photograph obtained with wire-cylinder geometry II, viewing the gap in the direction along the wire. Streamers are produced along 50 mm length of the wire. The photograph shows that the streamers have propagated almost along straight paths in radial direction. During the repetitive discharge, the gas in any part of the gap will be treated although, obviously, the azimuthally averaged density of chemical reactive dissociation fragments will be much higher in the anode-region than in the cathode-region.

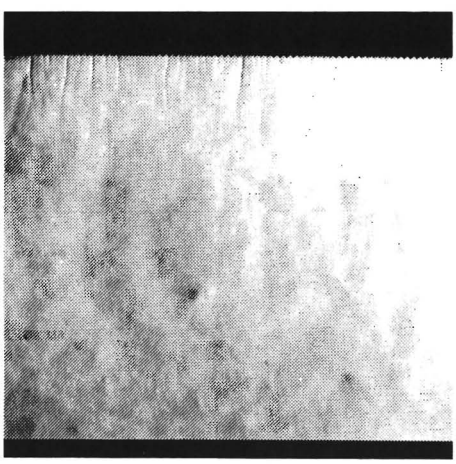

Fig. 5.43

Schlieren photograph of residual streamer channels at an anode consisting of multiple pins (Fig. 3.3, $V_m = 40$ kV).

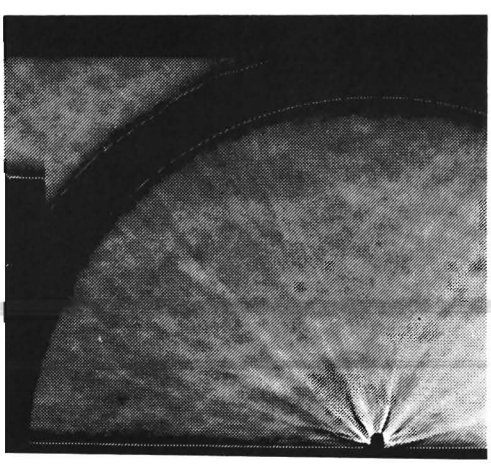

Fig. 5.44

Schlieren photograph of residual streamer channels in wire-cylinder geometry II ($V_m = 40$ kV).

Fig. 5.45 shows two examples of photographs obtained when breakdown occurs. Residual streamer channels are visualized together with the spark which is clearly seen, not only as a result of the Schlieren effect but mainly as a result of its strong light emission. At $V_m = 45$ kV (primary) streamer branching, as shown in Fig. 5.45 (a), is more frequently observed than at $V_m = 40$ kV. Very strong branching of streamers is often observed close to spark channels.

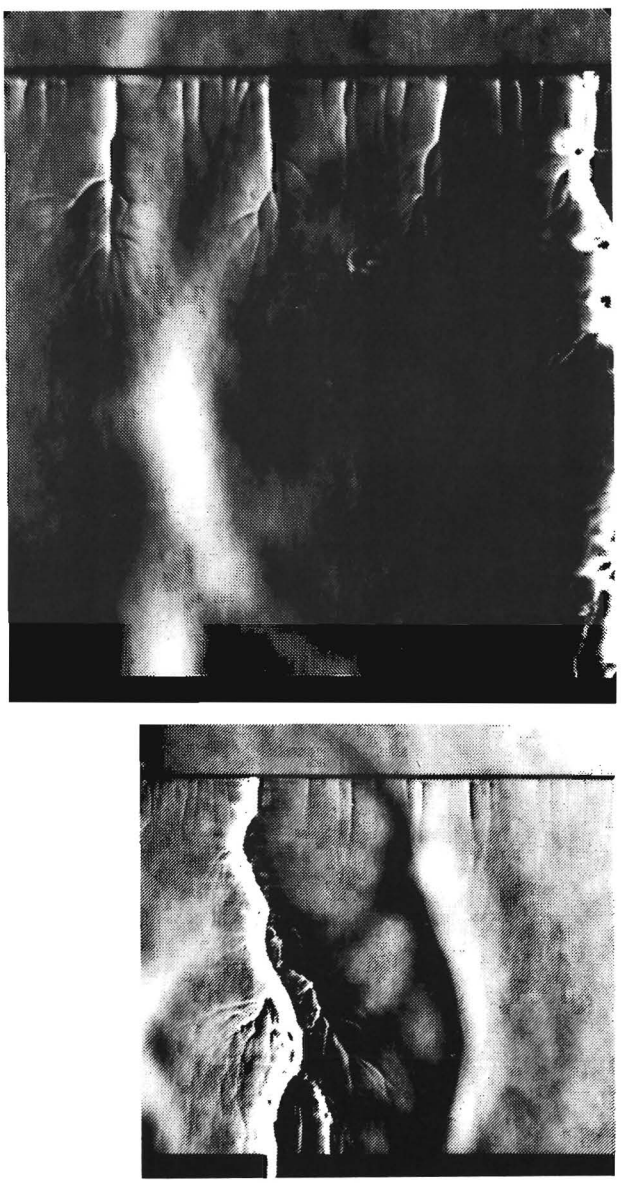

Fig. 5.45 Schlieren photographs obtained when breakdown occurred ($V_m = 45$ kV).

The particularly strongly branched streamer structure which is seen on Fig. 5.45 (b), may have been caused in two different ways:

1) A vigorous primary streamer may have been branched *before primary streamer arrival* at the cathode. Because of the strong branching, much energy is dissipated in a common channel connecting the streamers to the anode. The relative strong decrease of the neutral density n in this common channel causes an increase of the local E/n and increases therefore the probability for spark formation.

2) A vigourous primary streamer reaches the cathode, however, without significant branching. Because of the relative high energy dissipation by vibrational excitation in the secondary streamer (see calculated results in Fig. 2.32), the density n is lowered. When the neutral density n is sufficiently lowered for recombination and attachment being dominated by ionization, the secondary streamer becomes an ionization region with high conductivity so that it is virtually an extension of the anode with a very small radius of curvature. At the extremity of this ionization region a strong non-uniform electric field causes new cathode-directed streamers similar to streamer formation in a tip-plate overvolted gap.

In fact, the second interpretation is close to that of the *leader channel* which is often observed propagating continuously or stepwise in large (>1 m) gaps in air (Gallimberti, 1979, reference of Chapter **2**; Renardières Group, 1986). The Schlieren results obtained here indicate that the thermalized leader channel can also be formed in a small gap after primary streamer arrival.

5.5 Gas treatment

5.5.1 Experiments with bench-scale set-up

NO_x removal experiments have been performed using simulated flue gas in wire-cylinder corona reactor III (Table 3.1, Fig. 3.9) with a flow rate of 0.4 Nm^3/hr. Humid air at 100 °C with 6% H_2O, 250 ppm NO and ~10 ppm NO_2 has been used as a standard condition. Two types of HV pulses have been applied: (a) fast rising HV pulses with long decay time (similar to those shown in Fig. 5.3) and short HV pulses (Fig. 5.7). The average power dissipated in the reactor was varied by changing the HV pulse repetition rate from 20 to 300 Hz. Experimental results are shown in Fig. 5.46.

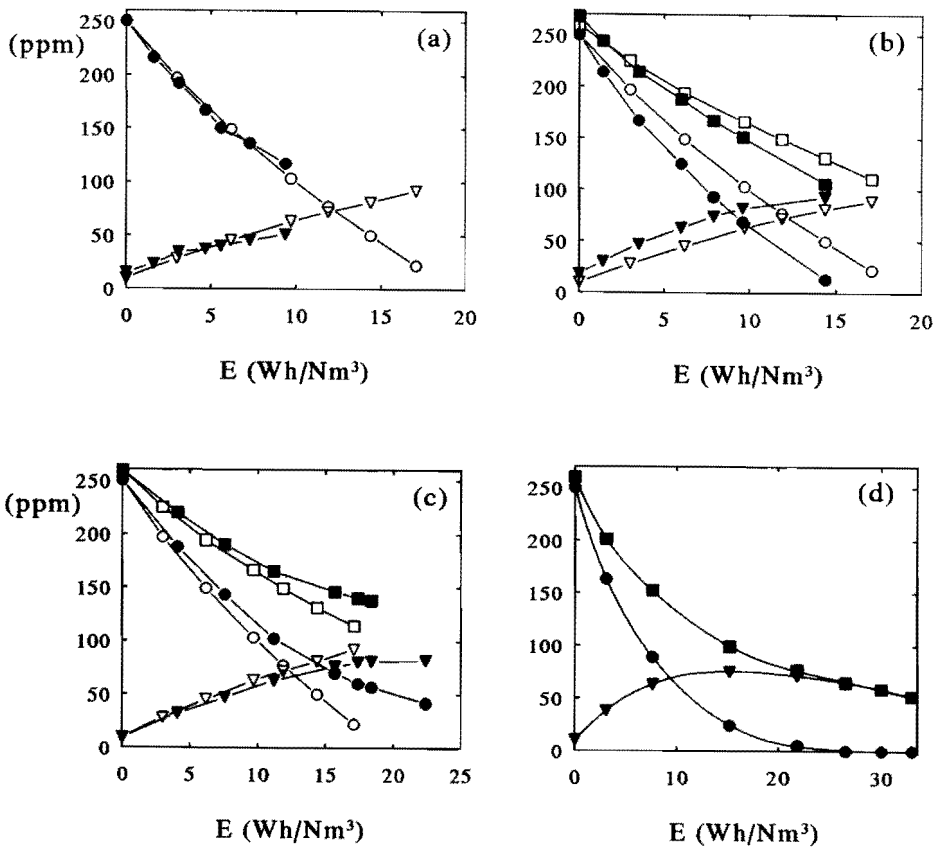

Fig. 5.46 *NO_x removal in simulated flue gas.*
(○) *NO*, (▽) *NO_2*, (□) *NO_x: concentrations at standard condition (HV pulses with $t_r \approx 40$ ns, $t_d \approx 500$ μs, 6% H_2O and $T=100$ °C).*
Influence of parameter variation on (●) *NO*, (▼) *NO_2 and* (■) *NO_x:*
(a) Flue gas B (74% N_2, 5% O_2, 15% CO_2, 6% H_2O)
(b) Humid air with 10.5% H_2O
(c) Increased gas temperature $T_g=150$ °C
(d) Short HV pulses (shown in Fig. 5.3)

Fig. 5.46 (a) shows that no large difference in removal efficiency and energy cost occurs between the flue gas of a coal-fired power plant and humid air with the same water vapour concentration. For oxidizing 50% of an initial concentration of 250 ppm *NO* an energy density of 7.5 Wh/Nm³ is required so, according to Eq. A.2 in Appendix A, the required energy per *NO* molecule appears to be 50 eV/*NO*. The energy required to remove 50% NO_x is 110 eV/NO_x (15.5 Wh/Nm³ is required).

The energy cost for NO and NO_x oxidation is improved by increasing the water vapour concentration. When $[H_2O]$ is increased from 6 to 10.5%, the energy cost for 50% NO_x removal is reduced from 110 eV/NO_x to 90 eV/NO_x, see Fig. 4.46 (b). A higher gas temperature results in a higher energy cost, see Fig. 5.46 (c). Increasing the gas temperature from 100 to 150 °C, the energy cost for 50% NO_x removal increases from 110 eV/NO_x to a least 180 eV/NO_x.

The results in Fig. 5.46 (b, c) show that improvements in the NO_x removal efficiency which can be obtained by either increasing the water vapour concentration or decreasing the gas temperature, are partly offset by higher NO_2 levels.

Fig. 5.46 (d) shows results which were obtained with short HV pulses. By using the HV pulses shown in Fig. 5.7 instead of HV pulses with a long tail, the energy cost for 50% NO_x removal decreases from 110 eV/NO_x to 80 eV/NO_x. Fig. 5.46 (d) in particular shows that the NO concentration can be reduced from 250 ppm practically to zero.

The measured minimum energy cost for 50% NO_x removal can be further reduced by combining a short HV pulse, a low gas temperature and a high water vapour concentration. Also the addition of NH_3 is expected to improve the results. Note in Fig. 1.2 the large effect of NH_3 on e-beam treatment results obtained by Tokunaga and Suzuki (1984). It was not possible to measure NO and NO_2 concentrations in presence of NH_3 because the electrochemical sensors in the gas analyzer (see **3.3.1**) appeared to be strongly sensitive for NH_3.

In order to compare the performance of the pulsed corona reactor with the dielectric barrier discharge for ozone production and to provide a possible check for the chemical kinetics model, a measurement of the energy cost of ozone generation in dry air at 20 °C was performed. Wire-cylinder configuration I with a wire length of 450 mm was used as corona reactor. The ozone concentration was determined from absorption measurements using the optical scheme which is shown in Fig. 4.6. The HV pulses were similar to those used in Fig. 5.3 (V_m=30 kV, t_r≈40 ns, t_d≈0.5 ms). At a flow rate of 0.4 Nm^3/hr and a power consumption of 4 Watt (energy density w=10 Wh/Nm^3) the measured ozone concentration was $2.2 \cdot 10^{21}$ m^{-3} (i.e. 0.18 g/m^3) and thus the ozone yield was 18 g/kWh. This yield corresponds to an energy cost per produced O_3 molecule of ~100 eV/O_3. Experimental optimization studies of ozone generation in dry air (Küchler, 1990) show maximum values for the ozone yield of about 100 g/kWh (at low O_3 concentration). The results obtained here with pulsed corona can probably be improved by using short HV pulses and/or by covering the cathode cylinder with a dielectric (thereby reducing energy dissipation after primary streamer transit). The ozone absorption measurement offers the possibility of a simple investigation (using only dry air as gas) of the influence of HV pulse parameters on the efficiency for the production of oxygen radicals.

5.5.2 Experiments with pilot scale set-up

These experiments were performed using the flue gas produced by a natural gas burner (72% N_2, 4% O_2, 8% CO_2, 16% H_2O) see **3.3.2**, Fig. 3.10) and were directed to optimize the NO_x removal efficiency in a system with gas flow rate and electrode structure which are applicable in a coal-fired power plant. Electrical circuit II (see Table 3.2) has been used to produce short HV pulses which are superimposed on a DC bias. Positive results have been obtained at a gas temperature of 60 °C, i.e. close to the condensation temperature (at 56 °C 16% water vapour is saturated). The gas flow rate was 15 ± 1 Nm^3/hr and the HV pulses possessed a DC bias component of 30 kV and a peak voltage of 110 kV. The width at half maximum of the current waveforms was 30 ns and the dissipated energy per pulse was ~3 Joule. The repetition rate was limited to 30 Hz (the power to 100 Watt), therefore only a small part (5%) of the total gas flow that the burner produces, was treated in the reactor. At the energy density of ~6.7 Wh/Nm^3, an initial concentration of 300 ppm NO decreased to 85 ppm while 70 ppm NO_2 was formed. Thus the energy cost for the removal of 72% NO was ~28 eV/NO and the energy cost for the removal of 50% NO_x was ~42 eV/NO_x.

Chapter 6 Conclusions

The conclusions which can be drawn only from the modelling results are presented first (**6.1**). Conclusions which can be based on experimental results and sometimes on both experimental and modelling results are subdivided in the following items: (**6.2**) spatial structure and time-phases of the discharge, (**6.3**) primary streamer formation, (**6.4**) primary streamer propagation, (**6.5**) residual channel and secondary streamer, (**6.6**) streamer current and energy dissipation and (**6.7**) NO_x removal.

6.1 Modelling

Numerical primary streamer model

The absence of experimental electron transport coefficients at low reduced field strength ($E/n < 50$ Td) in flue gases and the lack of experimental data for photo-ionization in flue gases makes it necessary to limit the numerical modelling of the streamer discharge to simple gas mixtures (e.g. N_2-O_2).

The calculated axial electric field and electron density distributions in the streamer head strongly depend on the input parameter R_s of the 1-D model which accounts for the finite streamer radius and which can be fitted to obtain optimum agreement between calculated and experimental streamer properties. A comparison of 1-D modelling results with a 2-D model is desirable.

The characteristic size of the primary streamer head where both the electric field and the electron density are close to their maximum values, is only ~10 μm. The maximum electric field in the streamer head is in the range 500-2000 Td. The electric field in the primary streamer channel is almost independent on time and position close to the value where the effective attachment frequency possesses a minimum. This value is also close to the empirical applied field for stable streamer propagation (stability field, in dry air ~20 Td).

According to the model results, electron impact ionization and excitation to the excited states $N_2^+(B^2\Sigma_u^+)$ and $N_2(C^3\Pi_u)$ radiating respectively at *391.4 nm* and *337.1 nm* mainly occurs by electrons produced at values of the electric field which are close to the maximum value. This is an essential argument for using the relative intensity of N_2^+*(391.4 nm)* and N_2*(337.1 nm)* emission lines to

estimate experimentally the maximum field strength reached in primary streamers.

Electrons produced in a streamer head possess initially an average electron energy in the range 10-20 eV. This value is very well suited for the production of chemical reactive products by dissociative attachment and dissociative ionization. However, in the streamer channel the average electron energy is about 1 eV. This value is too low for direct electron impact dissociation processes with a threshold electron energy of ~5 eV.

The streamer velocity is of the same order of magnitude but not equal to the electron drift velocity corresponding to the electric field maximum. Nevertheless, these quantities are strongly coupled: increasing the applied voltage, the maximum field, the corresponding electron drift velocity and the streamer propagation velocity increase.

The model calculations confirm the analytical streamer model where the empirical stability field is an essential parameter: the ionization region is limited to the streamer head and the net positive charge in this head increases as long as the geometric electric field exceeds the stability field.

Secondary streamer model (extended analytical streamer model)

The results calculated with the secondary streamer model show that the formation of secondary streamers is due to an instability of E/n which occurs because the effective attachment frequency increases with E/n (in air in the range of 20-50 Td).

The extended analytical streamer model has been used to calculate the contributions of electrons in the streamer head and in the streamer channel to energy dissipation. The main contribution is caused by electrons in the streamer channel where the average electron energy is about 1 eV. Because at this electron energy resonant vibrational excitation of N_2 is the dominant electron loss process, it is expected that the main part of energy dissipated during the propagation of the primary streamer is transformed into vibrational energy.

Chemical kinetics model

The radicals OH, HO_2, O and O_3 are essential for the oxidation of NO and NO_2 to HNO_2 and HNO_3. However O radicals also play a role in back-reactions reducing NO_2 to NO. These back-reactions strongly limit the oxidation process.

The *OH* radical is formed by direct electron-molecule collision processes (dissociative attachment and dissociative ionization) and by indirect processes: reactions involving the metastable molecule $N_2(A^3\Sigma_u^+)$ and H_2O^+ ions. According to the chemical kinetics model *OH* is mainly formed by the indirect processes.

6.2 Spatial structure and time-phases of the pulsed positive corona discharge

The wire-plate geometry is well suited to investigate optically streamers which are produced under application of positive HV pulses along the wire because in the entire gap separate streamers can be distinguished from each other.

Using both photomultiplier measurements of local light emission and pictures of light emission obtained with a gated image intensifier and CCD camera, three phases of the development of a streamer in time can be distinguished:
i) The primary streamer head propagates with high velocity ($>2\cdot10^5$ m/s) from the anode wire to the cathode plate while the residual plasma channel which is left by the primary streamer head remains dark.
ii) Upon the arrival of a primary streamer head at the cathode, light emission is again observed in parts of the dark residual primary streamer channel, mainly near the anode wire. The prolongation of the light emitting region in a residual primary streamer channel near the anode wire corresponds to the phenomenon which is commonly referred to as secondary streamer.
iii) A decay phase which is characterized by light emission mainly concentrated in a region close to the anode with constant length and diminishing intensity.

It was established from CCD camera pictures that, in case of an anode-wire and a single cathode-plate, the average streamer number density along the wire is about 600 m^{-1} and independent on the magnitude of the applied voltage. In case of a central wire in between two plates, the streamer number density is about 600 m^{-1} at both sides of the wire. Similar values for the average streamer number density have been obtained from Schlieren photographs visualizing neutral gas heating in residual discharge channels in the gas. The streamer number density can be increased from about 600 m^{-1} to about 1200 m^{-1} by replacing the smooth anode-wire by an array of multiple pins.

Magnified and time-resolved pictures obtained with the image intensifier - CCD camera system can be used to measure the optical radius of primary streamers (determined at 50% of the maximum emission intensity). The optical

radius of primary streamers close to the anode wire is about 200 μm. The optical radius of secondary streamers appears to be smaller: 120 - 150 μm. The theoretical evaluation of the measured optical streamer radius requires the development of a 2-D model where the radial structure of the streamer is calculated self-consistently.

6.3 Primary streamer formation

Simultaneous measurements of voltage and local light emission can be used to determine average values and spread of the (primary) streamer inception voltage. Measured values of the minimum streamer inception voltage as function of anode wire radius are close to values predicted by the Raether-Meek criterion.

Streamer inception time differences are much smaller than streamer inception time lags. This observation clearly demonstrates the influence of a streamer or streamers, which are formed first, on the formation of streamers at other positions along the wire. Ionizing radiation from highly excited states in streamers can be responsible for this influence.

The differences in the streamer inception voltage which are measured changing the polarity of the bias voltage (on which positive HV pulses are superimposed) indicate that detachment from negative ions is the principal source of initial electrons forming the first electron avalanches and streamers after application of a HV pulse.

6.4 Primary streamer propagation

Spatially resolved photomultiplier measurements of light emission are an effective means to determine the maximum length of primary streamers. Under the conditions of the experiments, using positive HV pulses with a short rise time (~40 ns) and a long decay time (~0.5 ms), the voltage range for streamers not reaching the cathode plate is small (16-20 kV) when compared to the voltage range for primary streamers reaching the cathode but not leading to breakdown (20-30 kV).

Measurements of delay times between local light emission signals caused by propagating primary streamers can be used to measure their average local velocity. When streamers propagate from the critical volume toward the low field

region their velocity strongly decreases. In the mid-gap region, the streamer velocity is approximately constant. At voltages close to the breakdown value, streamers increase their velocity again when approaching the cathode. In the entire gap, the streamer velocity increases with increasing voltage and decreasing oxygen concentration.

The measured streamer velocity is close to calculated values in the mid-gap region. The influence of the applied voltage and the relative O_2 concentration on the measured primary streamer velocity is in good qualitative agreement with model calculations. However, a serious discrepancy exists between measured and calculated velocities as a function of distance to the anode.

Measurements of the intensity ratio of $N_2^+(391.4\ nm)$ and $N_2(337.1\ nm)$ emission lines can be used for a rough estimate of the maximum field strength in the primary streamer head. The maximum field strength in the streamer head varies with its distance from the anode wire in a similar way as the streamer velocity: when streamers propagate from the critical volume toward the low field region the maximum field is lowered, in the mid-gap region it is approximately constant and when streamers approach the cathode it increases again. The intensity ratio measurements show that the maximum field increases with increasing applied voltage and decreasing oxygen concentration.

The measured maximum field strength is close to calculated values in the mid-gap region. Similar to the comparison between measured and calculated streamer velocities, measurements of the intensity ratio as function of the applied voltage and the relative oxygen concentration are in good qualitative agreement with computed values. The measured variation of the maximum field strength as a function of the distance to the anode is not as predicted by the calculations.

6.5 Residual streamer channel and secondary streamer

CCD camera pictures show that the secondary streamer phenomenon not only occurs near the anode but also near the cathode and in the mid-gap region. Prolonging secondary streamers with strong light emission intensity are mainly formed in the anode region.

Measurements of the intensity ratio of $N_2^+(391.4\ nm)$ and $N_2(337.1\ nm)$ emission lines show that the electric field, and therefore the ionization rate in the secondary streamer is low.

Measurements of the rotational spectral structure of the $N_2(337.1\ nm)$ emission line show that during secondary streamer emission (a period of ~100 ns following the transit of primary streamers) the neutral gas in the residual streamer channel is not much heated (the measured temperature is close to the ambient gas temperature).

The model describing the secondary streamer phenomenon as an attachment instability (caused by a local minimum in the attachment rate as a function of E/n) that divides the residual streamer channel in regions with a field close to the stability field (20-40 Td) and a field just below the critical field (~100 Td) is in agreement with the limited secondary streamer length observed from CCD camera pictures.

The average electron energy corresponding to the electric field in the secondary streamer ($E/n \approx 100$ Td, $\epsilon_a \approx 3$ eV) is well suited for the formation of both O and OH radicals by dissociative attachment to O_2 and H_2O and for the formation of the metastable molecules $N_2(A^3\Sigma_u^+)$ which are also effective for both O and OH production. However, the production will be limited by the relative low electron density.

6.6 Streamer current and energy dissipation

The numerical primary streamer model and the extended analytical streamer model have been used to calculate the characteristic shape of single primary-streamer induced current. The rise time of measured current signals is close to the rise time of calculated current signals which again shows that all streamers are formed almost simultaneously at the anode-wire.

The secondary streamer is generally not seen as a separate peak in the smoothly decaying current signal measured at the anode. At a voltage close to the breakdown voltage, however, current measurements at the anode and current-probe measurements at the cathode sometimes show a separate peak coinciding in time with the formation of the secondary streamer.

Schlieren photographs show that relative high energy dissipation occurs in a part of residual primary streamer channels where also secondary streamer emission is observed. The main part of the total dissipated energy is transferred to the neutral gas by vibrational relaxation with a characteristic time of ~100 μs.

It has been demonstrated that the (average) dissipated energy per pulse is strongly dependent on the (average) streamer inception voltage. The inception voltage can be increased to the voltage maximum by either reducing the rise time of the HV pulse or by increasing the anode radius of curvature.

6.7 NO_x removal

A considerable improvement of the NO and NO_x removal efficiency is obtained by reducing the HV pulse width to a value corresponding to the primary streamer transit time. Using HV and current pulses with a width of ~30 ns, the energy cost for removing 50% of an initial concentration of 300 ppm NO_x in natural gas combustion gas is ~42 eV/NO_x.

NO_x removal measurements show that the energy cost for NO and NO_x removal can be improved by decreasing the gas temperature and increasing the water vapour concentration. The NO_x removal efficiency is strongly limited by back-reactions from NO_2 to NO.

The addition of NH_3 is expected to increase the oxidation of NO_2 thereby limiting reduction of NO_2 to NO. Similar to results obtained by multiple e-beam treatment, the treatment of the gas by pulsed corona in two or more stages may lead to a reduction of the energy cost: NO_2 and HNO_2 can be further oxidized by slow reactions, before radicals, produced in the electrical discharge, cause back-reactions.

A more detailed analysis of reaction products, such as N_2O, NO_3 and HNO_2, with methods such as gas chromatography, mass spectrometry and infrared absorption spectroscopy is necessary.

Appendix A Definitions and unit conversion

Normal Pressure and Temperature (NPT):

p = $1.013 \cdot 10^5$ Pa, T = 293 K
Molar volume: V_m = $2.404 \cdot 10^{-2}$ Nm^3
1 Nm^3 gas contains: N_A/V_m = $2.505 \cdot 10^{25}$ molecules

Concentrations by volume n(ppm) and weight (mg/m^3) at NPT:

$$n(mg/m^3) = 10^{-3} \cdot n(ppm) \cdot \frac{M(g)}{V_m(m^3)} \tag{A.1}$$

Examples: NO (M=30 g): 1 ppm ≡ 1.248 mg/Nm^3
NO_2 (M=46 g): 1 ppm ≡ 1.914 mg/Nm^3
SO_2 (M=64 g): 1 ppm ≡ 2.662 mg/Nm^3
O_3 (M=48 g): 1 ppm ≡ 1.997 mg/Nm^3

Energy consumption

The energy consumption per molecule, W_m (eV/molec.) is determined from the energy density w and the difference between concentrations Δn:

$$W_m(eV/molec.) = \frac{w(J/Nm^3)}{q_e \, \Delta n(molec./Nm^3)} = \frac{w(J/Nm^3)}{4.01 \cdot \Delta n(ppm)} = \frac{897 \cdot w(Wh/Nm^3)}{\Delta n(ppm)} \tag{A.2}$$

with q_e = $1.6022 \cdot 10^{-19}$ J. In the electron-beam irradiation studies it is common to use the dose D in units of Mrad (1 Mrad = 10 kJ/kg):

$$W_m(eV/molec.) = \frac{D(J/kg)\ \rho(kg/Nm^3)}{q_e \, \Delta n(molec./Nm^3)} = \frac{D(Mrad)\ \rho(kg/Nm^3)}{4.01 \cdot 10^{-4}\ \Delta n(ppm)} \tag{A.3}$$

where ρ is the mass density. For dry air: ρ(293 K) = 1.205 kg/m^3, ρ(373 K) = 0.947 kg/m^3. The energy yield Y (mg/kJ or g/kWh) depends on W_m(eV/molec.) according to:

$$Y(g/kWh) = \frac{3600 \cdot M(g)}{q_e . N_A . W_m(eV/molec.)} = \frac{37.31 \cdot M(g)}{W_m(eV/molec.)} \qquad (A.4)$$

For example: $W_m(O_3) = 50$ eV/molec. corresponds to $Y = 36$ g(O_3)/kWh.

Appendix B Electrical circuit equations

The differential equation for the RCL network shown in Fig. 3.6 is:

$$L\,C_e \frac{d^2V}{dt^2} + R\,C_e \frac{dV}{dt} + \left(1 + \frac{C_e}{C_s}\right) V = V_0 \qquad (B.1)$$

Three different solutions are possible, depending on the damping constant k:

$$k = \frac{R}{2\sqrt{L/C}} \quad , \quad C = \frac{C_s C_e}{C_s + C_e} \qquad (B.2)$$

When $k = 1$ the circuit is *critically damped*:

$$V(t) = V_{DC} + V_0 \frac{C_s}{C_s + C_e} \left[1 - \exp[-t/\tau] \, (1 + t/\tau) \right] \qquad (B.3)$$

with the time constant τ given by:

$$\tau = 2L/R = RC/2 \qquad (B.4)$$

When the circuit is less than critically damped ($k < 1$) the solution is:

$$V(t) = V_{DC} + V_0 \frac{C_s}{C_s + C_e} \left(1 - \sqrt{1 + \frac{1}{(\omega\tau)^2}} \exp(-t/\tau) \cos(\omega t - \psi) \right) \qquad (B.5)$$

with

$$\tau = \frac{2L}{R} \quad , \quad \omega = \sqrt{\omega_0^2 - (1/\tau)^2}$$

$$\omega_0 = \frac{1}{\sqrt{L\,C}} \quad , \quad \psi = \arctan\frac{1}{\omega\tau} \qquad (B.6)$$

When the circuit is more than critically damped ($k>1$):

$$V(t) = V_{DC} + V_0 \frac{C_s}{C_s+C_e} \cdot \left(1 + \frac{\tau_1}{\tau_2-\tau_1} \exp(-t/\tau_1) - \frac{\tau_2}{\tau_2-\tau_1} \exp(-t/\tau_2) \right) \tag{B.7}$$

with

$$\frac{1}{\tau_{1,2}} = \frac{R}{2L} \mp \sqrt{\frac{R}{2L} - \frac{1}{LC}} \tag{B.8}$$

For very strong damping $k \gg 1$ Eq. (B.7) will be reduced to:

$$V(t) = V_{DC} + V_0 \frac{C_s}{C_s+C_e} \left(1 - \exp[-t/\tau_2] \right) \tag{B.9}$$

For all values of the damping constant k, $(dV/dt)_{max}$ has the form (Kärner, 1967):

$$\left(\frac{dV}{dt}\right)_{max} = V_0 \frac{C_s}{C_s+C_e} \omega_0 D(k) , \quad \omega_0 = \frac{1}{\sqrt{LC}} \tag{B.10}$$

For $k<1$ the function $D(k)$ is:

$$D(k) = \left(k-\sqrt{k^2-1}\right)^{\frac{k}{\sqrt{k^2-1}}} \tag{B.11}$$

For $k>1$:

$$D(k) = \exp\left(-\frac{k}{\sqrt{1-k^2}} \arccos k \right) \tag{B.12}$$

For the critically damped circuit ($k=1$) and $D(k)=1/e$.

References of Chapter 1

Alekseev G.Yu., Levchenko A.V., Bityurin V.A. (1993), *Flue Gas Cleaning by Pulse Corona. Part II: The Chemical Kinetics and Heat- and Mass Transfer in NO/SO_2 Removal*, IVTAN Analytical & Numerical Research Association, Moscow, Research Report IVTAN-ANRA #93/2, 77 p.

Ando J. (1989), *Recent developments in SO_2 and NO_x abatement technology for stationary sources*, in: *Man and his Ecosystem*, Eds. L.J. Brasser and W.C. Mulder, Proc. of the 8th. World Clean Air Congress, The Hague, The Netherlands.

Baulch D.L., Cox R.A., Hampson R.F., Kerr J.A., Troe J., Watson R.T., *Evaluated kinetic and photochemical data for atmospheric chemistry*, CODATA Task Group on Gas Phase Chemical Kinetics,
J. Phys. Chem. Ref. Data, **9**, p. 295-471 (1980).
Supplement I: J. Phys. Chem. Ref. Data, **11**, p. 327-497 (1982).
Supplement II: J. Phys. Chem. Ref. Data, **13**, p. 1259-1381 (1984).

Boonekamp P.G.M., van Hilten O., Kroon P., Rouw M. (1992), *Nationale energie verkenningen* (in Dutch), Energieonderzoek Centrum Nederland, rapport ECN-C-92-017, 162 p.

Civitano L. (1993), *Industrial application of pulsed corona processing to flue gas*, in: *Non-Thermal Plasma Techniques for Pollution Control*, 1993, NATO Advanced Series Institute Series G, **34B**, Eds. B.M. Penetrante and S.E. Schultheis, Springer, Heidelberg, p. 103-130.

Civitano L., Sani E. (1993), *DeNO_x-deSO_x process by gas energization*, in: *Plasma Technology: Fundamentals and Applications*, Eds. M. Capitelli and C. Gorse, p. 153-166.

Dinelli G., Civitano L., Rea M. (1990), *Industrial experiments on pulse corona simultaneous removal of NO_x and SO_2 from flue gas*, IEEE Trans. on Ind. Appl., **26**, p. 535-541.

Christophorou L.G., McCorkle D.L., Christodoulides A.A. (1984), *Electron attachment processes*, in: *Electron-Molecule Interactions and their Applications*, Vol. 1, Chap. 6, p. 477-617.

Couch G.R. (1991), *Advanced Coal Cleaning Technology*, IEA (International Energy Agency) Coal Research, London, Report No. IEACR/44, 95 p.

Creyghton Y.L.M., van Veldhuizen E.M., Rutgers W.R. (1993), *Electrical and optical study of pulsed positive corona*, in: *Non-Thermal Plasma Techniques for Pollution Control*, 1993, NATO Advanced Series Institute Series G, **34A**, Eds. B.M. Penetrante and S.E. Schultheis, Springer, Heidelberg, p. 205-230.

Davidson R.M. (1993), *Organic Sulphur in Coal*, IEA (International Energy Agency) Coal Research, London, Report No. IEACR/60, 79 p.

Frank N., Hirano S. (1993), *The history of electron beam processing for environmental pollution control and work performed in the United States*, in: *Non-Thermal Plasma Techniques for Pollution Control*, 1993, NATO Advanced Series Institute Series G, **34B**, Eds. B.M. Penetrante and S.E. Schultheis, Springer, Heidelberg, p. 1-26.

Harter P. (1989), *Acidic Deposition - Ecological Effects on Soils and Forests*, IEA (International Energy Agency) Coal Research, London, Report No. IEACR/17, 66 p.

Hjalmarsson A.K., Soud H.N. (1990), *Systems for Controlling NO_x from Coal Combustion*, IEA (International Energy Agency) Coal Research, London, Report No. IEACR/30, 240 p.

Jones T. (1992), *Environmental Impact Assessment for Coal*, IEA (International Energy Agency) Coal Research, London, Report No. IEACR/46, 79 p.

Jordan S.J., Paur H.R., Cherdon W., Lindner W. (1986), *Physical and chemical properties of the aerosol produced by the electron beam dry scrubbing of flue gas*, J. Aerosol Science, **17**, p. 669-675.

Keet A.L. (1992), *Magnetic Switching Techniques for High Power Pulse Generation*, Ph.D. thesis, Eindhoven University of Technology, The Netherlands, 112 p.

Kieffer L.J. (1973), *A compilation of electron collision cross section data for modelling gas discharge lasers*, JILA Information Center Report No. 13, University of Colorado, 139 p.

Kimura T. (1991), *Future demand for steam coal in north-east Asian nations*, paper presented at the 4th World Coal Outlook Conference, 14-15 November 1991, Sydney, NSW, Australia.

Landrieu G., Turpin M. (1989), *Perspectives d'avenir pour l'utilisation du charbon / Future Trends in Coal Utilization*, Revue de l'énergie, **413**, p. 792-802.

Levine M.D., Liu F., Sinton J.E. (1992), *China's energy system: Historical evolution, current issues, and prospects*, Annual Rev. Energy Environ., **17**, p. 405-435.

Masuda S. (1988), *Pulse corona induced chemical process: a horizon of new plasma chemical technologies*, Pure & Appl. Chem., **60**, p. 727-731.

Masuda S. (1993), *Report on novel dry $DeNO_x/DeSO_x$ technology for cleaning combustionn gases from utility thermal power plant boilers*, in: *Non-Thermal Plasma Techniques for Pollution Control*, 1993, NATO Advanced Series Institute Series G, **34B**, Eds. B.M. Penetrante and S.E. Schultheis, Springer, Heidelberg, p. 131-147.

Masuda S., Hirano M., Akutsu K. (1981), *Enhancement of electron beam denitrization process by means of electric field*, Radiat. Phys. Chem., **17**, p. 223-228.

Masuda S., Nakao H. (1990), *Control of NO_x by positive and negative pulsed corona discharges*, IEEE Trans. on Industry Applications, **26**, p. 374-383.

Masuda S., Wu Y. (1987), *Removal of NO_x by corona discharge induced sharp rising nanosecond pulse voltage*, Inst. Phys. Conf. Series, No. 85, Electrostatics '87, Oxford, p. 249-254.

Matteson M.J., Stringer H.L., Busbee W.L. (1972), *Corona discharge oxidation of sulfur dioxide*, Environmental Science & Technology, Vol. 6, No. 10, p. 895-901.

Mätzing H. (1989), *Chemical Kinetics of Flue Gas Cleaning by Electron Beam*, Kernforschungszentrum Karlsruhe, Report KfK/4498, Germany, 111 p.

Mätzing H. (1991), *Chemical kinetics of flue gas cleaning by irradiation with electrons*, in: *Advances in Chemical Physics*, Vol. LXXX, Ed. by I. Prigogine and Stuart A. Rice, John Wiley & Sons, p. 315-359.

McLean K.J. (1988), *Electrostatic precipitators*, Review Article, IEE Proc., **135**, p. 347-361.

Mizuno A., Clements J.S., Davis R.H. (1986), *A method for the removal of sulfur dioxide from exhaust gas utilizing pulsed streamer corona for electron energization*, IEEE Trans. on Ind. Appl., **IA-22**, p. 516-522.

Nelson J.K., Salasoo L. (1987), *The impact of pulse energization on electrostatic precipitation performance*, IEEE Trans. on Elec. Ins., **EI-22**, p. 657-675.

Ohtsuka K. (1985), *Electrostatic methods for integrated pollution control of combustion gas*, PhD thesis, Dept. Elect. Eng., University of Tokyo, Japan.

Park C.C. (1987), *Acid Rain, Rhetoric and Reality*, Methuen, London, 272 p.

Patterson W.C. (1993), *Coal-use Technology, New Challenges, New Responses*, Management Report Published by Financial Times Business Information, London.

Person J.C., Ham D.O., Boni A.A. (1985), *A Unified Projection of the Performance and Economics of Radiation-Initiated NO_x/SO_x Emission Control Technologies*, US Department of Energy, Report PSI-TR-259-542.

Person J.C., Ham D.O. (1988), *Removal of SO_2 and NO_x from stack gases by electron beam irradiation*, Radiat. Phys. Chem., 31, p. 1-8.

Sälge J., Labrenz M., Scheibe K. (1983), *Rationelle Ozonerzeugung*, Institut für Hochspannungstechnik der Technischen Universität Braunschweig, Forschungsbericht T 83-226, 50 p.

Scheuermann A., Bloss W.H. (1988), *Verfahren zur Entstickung und Entschwefelung von Verbrennungsabgasen mittels Corona-Entladung* (in German), Kernforschungszentrum Karlsruhe, report KfK-PEF 47, 51 p.

Schobert H.H. (1987), *Coal, the Energy Source of the Past and Future*, Ed. by K.L. McCeney, American Chemical Society, Washington DC, 298 p.

Seinfeld J. (1986), *Atmospheric Chemistry and Physics of Air Pollution*, John Wiley & Sons, New York, 738 p.

Soud H.N. (1991), *Emission Standards Handbook: Air Pollutant Standards for Coal-fired Plants*, IEA (International Energy Agency) Coal Research, London, Report No. IEACR/43, 248 p.

Tokunaga O., Suzuki N. (1984), *Radiation chemical reactions in NO_x and SO_2 removals from flue gas*, Radiat. Phys. Chem., **24**, p. 145-165.

Tokunaga O., Namba H., Hirota K. (1993), *Experiments on chemical reactions in electron-beam-induced NO_x/SO_2 removal*, in: *Non-Thermal Plasma Techniques for Pollution Control*, 1993, NATO Advanced Series Institute Series G, **34B**, Eds. B.M. Penetrante and S.E. Schultheis, Springer, Heidelberg, p. 55-62.

Ulrich B. (1990), *Waldsterben: Forest decline in West Germany*, Environ. Sci. Technol., **24**, p. 436-441.

Verhaart H.F.A. (1992), *Pulse powered corona discharges in flue gas*, Proc. 10th Int. Conf. on Gas Discharges and their Applications, Swansea 1992, Vol. 1, p. 348-351.

Vernon J.L., Jones T. (1993), *Sulphur and Coal*, IEA (International Energy Agency) Coal Research, London, Report No. IEACR/57, 62 p.

Zaengl W., Teich T., Friedrich G., Nasciuti A., Schötzau H. (1991), *Zur Reduktion der gasförmigen Schadstoffe in Abgasen mit Hilfe elektrischer Entladungen* (in German), Bulletin SEV/VSE, **82**, p. 27-35.

References of Chapter 2

Abdel-Salam M., Allen N.L. (1990), *Inception of corona and rate of rise of voltage in diverging electric fields*, IEE Proc., **137-A**, p. 217-220.

Abdel-Salam M., Turky A. (1988), *Breakdown voltage and time-to-breakdown as influenced by the steepness of the applied positive impulse*, IEEE Trans. on Ind. Appl., **24**, p. 1031-1037.

Aleksandrov N.L. (1978), *Electron detachment from O^- and O_2^- ions by excited molecules in a discharge in air*, Sov. Phys. Tech. Phys. **23**, p. 806.

Alekseev G.Yu., Levchenko A.V., Bityurin V.A. (1993), *Flue Gas Cleaning by Pulse Corona. Part II: The Chemical Kinetics and Heat- and Mass Transfer in NO/SO_2 Removal*, IVTAN Analytical & Numerical Research Association, Moscow, Research Report IVTAN-ANRA #93/2, 77 p.

Allen N.L., Berger G., Dring D. (1987), *Positive corona and atmospheric negative ion density under repetitive impulse conditions*, IEEE Trans. on Ind. Appl., **IA-23**, p. 990-994.

Allen N.L., Boutlendj M. (1991), *Study of the electric fields required for streamer propagation in humid air*, IEE Proc. A, **138**, p. 37-43.

Aurela A.M., Punkkinen R., Bilund A. (1989), *Process model for nitrogen oxidation in onset streamers in air*, J. Phys. D: Appl. Phys. **22**, p. 650-658.

Babaeva N.Yu., Kulikovsky A.A., Mnatsakanyan A.Kh., Naidis G.V., Solosobov Yu.M., *Flue gas cleaning by pulsed corona. Part I: The streamer propagation models in N_2-O_2 mixtures and flue gas*, internal report no. EG/93/672, Electrical Energy Systems group, Faculty of Electrical Engineering, Eindhoven University of Technology, 48 p.

Barnett R.N., Landman U., Cleveland C.L. (1988), *Size dependence of the energetics of electron attachment to large water clusters*, Chem. Phys. Lett., **145**, p. 382-386.

Bass H.E., Hottman D. (1980), *Laser induced fluorescence study of the deactivation of N_2* by H_2O, H_2S, and CH_4*, J. Chem. Phys. **72**, p.2113-2119.

Bastien F., Hang R., Lécuiller M. (1975), *Simulation sur ordinateur de l'évolution temporelle des ions négatifs de l'air*, J. Chem. Phys., **1**, p. 105-112.

Bastien F., Marode E. (1977), *Stark broadening of H_α and H_β in ionized gases with space-charge field*, J. Quant. Spectrosc. Radiat. Transfer, **17**, p. 453-469.

Bastien F., Marode E. (1979), *The determination of basic quantities during glow-to-arc transition in a positive point-to-plane discharge*, J. Phys. D: Appl. Phys., **12**, p. 249-263.

Bastien F., Marode E. (1985), *Breakdown simulation of electronegative gases in non-uniform field*, J. Phys. D: Appl. Phys., **18**, p. 377-393.

Boeuf J.P. (1985), *Modelisation de la cinétique electronique dans un gaz faiblement ionisé*, Thèse d'Etat, No. 3043, Université de Paris Sud, Centre d'Orsay, 249 p.

Boylett F.D.A., Edwards H.G.J., Williams B.G. (1970), *Impulse breakdown of positive point-plane gaps in air containing charged particles*, J. Phys. D: Appl. Phys., **3**, p. 1219-1225.

Boris J.P., Book D.L. (1976), *Solution of continuity equations by the method of flux-corrected transport*, in: *Methods in Computational Physics*, Ed. by J. Killeen, Academic Press, New-York, p. 85-129.

Braun et al. (1992), *Two-dimensional modelling of the dielectric barrier discharge in air*, Plasma Sources Sci. Technol., **1**, p. 166-174.

Carter L. (1972), J. Chem. Phys., **56**, p. 4195.

Cartwright D.C., Trajmar S., Chutjian A., Williams W. (1977), *Electron impact excitation of the electronic states of N_2. II. Integral cross sections at incident energies from 10-50 eV*, Phys. Rev. A, **16**, p. 1041-1051.

Christophorou L.G., McCorkle D.L., Christodoulides A.A. (1987), *Electron Attachment Processes*, in: *Electron-molecule interactions and their applications*, Academic Press, London, Vol. 1, p. 477-617.

Cravath A.M. (1935), *Photoelectric effect and spark mechanism*, Phys. Rev. **47**, p. 254.

Davies A.J., Evans C.J., Llewellyn Jones F. (1964), *Electrical breakdown in gases: the spatio-temporal growth of ionization in fields distorted by space charge*, Proc. Roy. Soc., **281**, p. 164-183.

Davies A.J., Evans C.J. (1967), *Field distortion in gaseous discharges between parallel-plate electrodes*, Proc. IEE, **114**, p. 1547-1550.

Davies A.J., Davies C.S., Evans C.J. (1971), *Computer simulation of rapidly developing gaseous discharges*, Proc. IEE, **118**, p. 816-823.

Davies A.J. (1986), *Discharge Simulation* (Review article), IEE Proc., **133**, p. 217-240.

Davies, D.K. (1987), *Measurements of swarm parameters in dry and humid air*, Proc. of the 18th. Int. Conf. on Phenomena in Ionized Gases, Swansea, UK, p. 2-3.

Dawson G.A., Winn W.P. (1965), *A model for streamer propagation*, Zeitschrift für Physik, **183**, p. 159-171.

Dutton J. (1975), *A Survey of Electron Swarm Data*, J. Phys. and Chem. Ref. Data, **4**, p. 577-856.

Elford M.T. (1991), *The behaviour of low-energy electrons in water vapour*, in: *Gaseous Electronics and its Applications*, Ed. by R.W. Crompton et al., Kluwer, Dordrecht, p. 35-49.

Finzi J., Hovis F.E., Panfilov V.N., Hess P., Moore C.B. (1977), *Vibrational relaxation of water vapour*, J. Chem. Phys., **67**, p. 4053-4061.

Friedrich G., Yousfi M., *Time-resolved measurements and Boltzmann equation calculations of H_2O electron swarm parameters: Application to H_2O collision cross section analysis*, 20th. Int. Conf. on Phenomena in Ionized Gases, Pisa, Italy, **1**, p. 90-91 (1991).

Gallagher J.W., Beaty E.C., Dutton J., Pitchford L.C. (1983), *An annotated compilation and appraisal of electron swarm data in electronegative gases*, J. Phys. Chem. Ref. Data, **12**, p. 109-152.

Gallimberti I. (1972), *A computer model for streamer propagation*, J. Phys. D: Appl. Phys., **5**, p. 2179-2189.

Gallimberti I, Gleijeses B. (1978), *The field computation in filamentary gas discharges*.

Gallimberti I. (1979), *The mechanism of the long spark formation*, Journal de Physique, Colloque C7, supplément au n° 7, Tome 40, p. 193-250.

Gallimberti I. (1987), *Breakdown mechanisms in electronegative gases*, Gaseous Dielectrics V, Ed. by L.G. Christophorou and D.W. Bouldin, Knoxville, Pergamon Press Oxford UK, p. 61-79.

Gallimberti I. (1988), *Impulse corona simulation for flue gas treatment*, Pure & Appl. Chem., **60**, p. 663-674.

Goldman M., Goldman A. (1978), *Corona discharges*, in: *Gaseous Electronics*, Vol. 1, Eds. M.N. Hirsh and H.J. Oskam, Academic Press, New York, p. 219-290.

Hartmann G. (1984), *Theoretical evaluation of Peek's law*, IEEE Trans. Ind. Appl., **IA-20**, p. 1647-1651.

Hartmann G., Gallimberti I. (1975), *The influence of metastable molecules on the streamer progression*, J. Phys. D: Appl. Phys., **8**, p. 670-680.

Holst G., Oosterhuis E. (1923), *The sparking potential of gases*, Phil., **46**, p. 1117-1122.

Hudson R.D. (1971), *Critical review of ultraviolet photoabsorption cross sections for molecules of astrophysical and aeronomic interest*, Rev. Geophys. Space Phys., **9**, p. 305.

Hudson G.G. and Loeb L.B. (1961), *Streamer mechanism and main stroke in the filamentary spark breakdown in air as revealed by photomultipliers and fast oscilloscopic techniques*, Phys. Rev. **123**, p. 29-43.

Hunter S.R., Christophorou L.G. (1987), *Electron Motion in Low- and High-Pressure Gases*, in: *Electron-Molecule Interactions and their Applications*, Ed. by L.G. Christophorou, Vol. 2, p. 89-219.

Huxley L.G.H. and Crompton R.W. (1974), *The Diffusion and Drift of Electrons in Gases*, Wiley, New York, 669 p.

Inoshima M., Černák M., Hosokawa T., 1990, *Waveform of prebreakdown primary streamers in a short positive point-plane gap in air*, Japanese Journal of Applied Physics, **29**, p. 1165-1172.

Kennedy J.T., Wetzer J.M. (1994), *Numerical study of the avalanche to streamer transition in N_2 and dry air*, Gaseous Dielectrics VII.

Kieffer L.J. (1973), *A compilation of electron collision cross section data for modelling gas discharge lasers*, JILA Information Center Report No. 13, University of Colorado, 139 p.

Kline L.E. (1974), *Calculations of discharge initiation in overvolved parallel-plane gaps*, J. Appl. Phys., **45**, p. 2046-2054.

Kline L.E. (1975), *Effect of negative ions on current growth and ionizing wave propagation in air*, J. Appl. Phys., **46**, p. 1994-2000.

Kunhardt E.E. (1980), *Electrical breakdown in gases: The prebreakdown stage*, IEEE Trans. Plasma Science, **PS-8**, p. 130-138.

Kunhardt E.E., Wu J., Penetrante B. (1988), *Nonequilibrium macroscopic descriptions of electrons in weakly ionized gases*, Phys. Rev. A, **37**, p. 1654-1662.

Llewellyn Jones F., Parker A.B. (1952), *Electrical breakdown of gases. Part I: Spark mechanism in air*, Proc. Royal Soc., **A 213**, p. 185.

Llewellyn Jones F. (1966), *Ionization and Breakdown in Gases*, Methuen, London.

Loeb L.B. (1965), *Electrical Coronas*, University of California Press, 694 p.

Loeb L.B., Kip A.F. (1939), *Electrical discharges in air at atmospheric pressure*, J. Appl. Phys., **10**, p. 142-160.

Loeb L.B., Meek J.M. (1940), *The mechanism of spark discharge in air at atmospheric pressure*, J. of Appl. Phys., **11**, p. 438-447.

Lowke J.J. (1992), *Theory of electrical breakdown in air - the role of metastable oxygen molecules*, J. Phys. D: Appl. Phys., **25**, p. 202-210.

Marr G.V. (1967), *Photoionization Processes in Gases*, Pure and Applied Physics, Academic Press, New York, 282 p.

Marode E. (1972), *La formation de l'arc entre une pointe positive et un plan*, Ph.D. thesis University of Paris-Sud, No. 1020, 303 p.

Marode E. (1975), *The mechanism of spark breakdown in air at atmospheric pressure between a positive point and a plane. I. Experimental: Nature of the streamer track*, J. Appl. Phys., **46**, p. 2005-2015.

Marode E., Bastien F., Bakker M. (1979), *A model of the streamer-induced spark formation based on neutral dynamics*, J. Appl. Phys., **50**, p. 140-146.

McGowan J.Wm., Mitchell J.B.A. (1984), *Electron-molecular positive ion recombination*, in: *Electron-molecule interactions and their applications*, Ed. by L.G. Christophorou, Academic Press, London, Vol. 2, p. 65-88.

Melton C.E. (1972), *Cross sections and interpretation of dissociative attachment reactions producing OH⁻, O⁻, and H⁻ in H_2O*, J. Chem. Phys., **57**, p. 4218-4225.

Mnatsakanyan A.Kh., Naidis G.V. (1986), *The vibrational-energy balance in a discharge in air*, High Temperature, **23**, p. 640-648 (translated from Teplofizika Vysokikh Temperatur).

Mnatsakanyan A.Kh., Naidis G.V., Solozobov Yu.M. (1992), *Modelling of Impulse Negative Corona Discharge in Nitrogen-Oxygen Mixtures*, Preprint IVTAN-N-1-334, Russian Academy of Sciences.

Moratz T.J., Pitchford L.C., Bardsley J.N. (1987), *Electron swarm behavior in nonuniform fields in nitrogen*, J. Appl. Phys., **61**, p. 2146-2151.

Morrow R. (1985), *Theory of negative corona in oxygen*, Phys. Rev. A, **32**, p. 1799-1809.

Morrow R., Cram L.E. (1984), in: *Computational Techniques and Applications*, edited by J. Noye and C.H.J. Fletcher, North-Holland, Amsterdam, p. 719-730.

Morrow R., Cram L.E. (1985), *Flux-corrected transport and diffusion on a non-uniform mesh*, J. Comp. Phys., **57**, p. 129-136.

Morrow R. (1988), *A parameter study of streamer propagation in SF_6*, J. Appl. Phys., **63**, p. 5171-5174.

Morrow R. (1991), *Theory of positive corona in SF_6 due to a voltage impulse*, IEEE Trans. on Plasma Science, **19**, p. 86-94.

Moruzzi J.L., Price D.A. (1974), *Ionization, attachment and detachment in air and air-CO_2 mixtures*, J. Phys. D: Appl. Phys., **7**, p. 1434-1440.

Mul P.M., McGowan J.Wm., Defrance P., Mitchell J.B.A. (1983), *Merged electron-ion beam experiments: V. Dissociative recombination of OH^+, H_2O^+, H_3O^+ and D_3O^+*, J. Phys. B: At. Mol. Phys., **16**, p. 3099-3107.

Naidis G.V. (1992), *Modelling of plasma chemical processes in stable corona discharges at thin wires*, J. Phys. D: Appl. Phys. **25**, p. 477-480.

Nasser E. and Loeb L.B. (1963), *Impulse streamer branching from Lichtenberg figure studies*, J. Appl. Phys. **34**, p. 3340.

Nasser E. (1968), *Spark breakdown in air at a positive point*, IEEE Spectrum **5**, p. 127.

Nasser E. (1971), *Fundamentals of Gaseous Ionization and Plasma Electronics* (Chapter 9, 10 & 11, p. 251-362), John Wiley & Sons.

Ness K.F., Robson R.E. (1988), *Transport properties of electrons in water vapour*, Phys. Rev. A, **38**, p. 1446-1456.

Odrobina I., Černák M. (1992), *Numerical modelling of the streamer-cathode interaction in a short positive point-plane corona gap*, Czechoslovak Journal of Physics, **42**, p. 303-315.

Odrobina I., Černák M. (1993), *Formation of cathode region of filamentary high-pressure glow discharges*, 4th. Int. Symp. on High Pressure Low Temperature Plasma-Chemistry (HAKONE), Bratislava, Slovakia, p. 165-170.

Orient O.J., Srivastava S.K. (1987), *Electron impact ionization of H_2O, CO, CO_2 and CH_4*, J. Phys. B: At. Mol. Phys., **20**, p. 3923-3936.

Pack J.L., Phelps A.V. (1966), *Electron attachment and detachment. II. Mixtures of O_2 and CO_2 and of O_2 and H_2O*, J. Chem. Phys., **45**, p. 4316-4329.

Penney G.W., Hummert G.T. (1970), *Photoionization measurements in air, oxygen, and nitrogen*, J. Appl. Phys., **41**, p. 572-577.

Phelps A.V. (1985), *Tabulations of collision cross sections and calculated transport and reaction coefficients for electron collisions with O_2*, JILA Information Center Report No. 28, University of Colorado, 11 p.

Phelps A.V. (1987), *Excitation and ionization coefficients*, Gaseous Dielectrics V, Ed. by L.G. Christophorou and D.W. Bouldin, p. 1-9.

Phelps A.V., Pitchford L.C. (1985), *Anisotropic scattering of electrons by N_2 and its effect on electron transport*, Phys. Rev. A, **31**, p. 2932-2949, tabulations of cross sections in: Phelps A.V., Pitchford L.C. (1985), JILA Information Center Report No. 26, University of Colorado, 21 p.

Phelps, C.T., Griffiths R.F. (1976), *Dependence of positive corona streamer propagation on air pressure and water vapour content*, J. Appl. Phys., **47**, p. 2929-2934.

Przybylski A. (1961), *Die gasioniserende Strahlung einer Entladung in N_2-O_2 Gemischen*, Z. Naturforsch., **16a**, p. 1232.

Przybylski A. (1962), *Untersuchung über die gasionisierende Strahlung einer Entlading II*, Z. Physik, **168**, p. 504-515.

Raether H. (1939), *The development of the electron avalanche in a spark channel (from observations in a cloud chamber)*, Zeitschrift für Physik, **112**, p. 464, translation in: *Electrical Breakdown in Gases* (Rees, 1973).

Raether H. (1940), *The development of Kanal discharges*, Archiv für Elektrotechnik, **34**, p. 49, translation in: *Electrical Breakdown in Gases* (Rees, 1973).

Raether H. (1964), *Electron Avalanches and Breakdown in Gases*, Butterworths, London, 191 p.

Raizer Y.P. (1991), *Gas Discharge Physics*, 449 p., original Russian edition: *Fizika gazovogo razryada*, Nauka, Moscow (1987).

Raja Rao C., Govinda Raju G.R. (1971), *Growth of ionization currents in dry air at high values of E/n*, J. Phys. D, **4**, p. 494-503.

Rees J.A., Jory R.L. (1964), *The diffusion of electrons in dry carbon dioxide free air*, Australian J. Phys., **17**, p. 307-314.

Rees J.A. (1973), *Electrical Breakdown in Gases*, The Macmillan Press, London, 294 p.

Renardières Group (1986), *Double impulse tests of long air gaps* (Part I), IEE Proc. A, **133**, p. 395-468.

Roelofs G.J.H. (1992), *Aerosol and Drop Size Dependent Cloud Chemistry*, Ph.D. thesis, University of Utrecht, The Netherlands, 159 p.

Rogowski W. (1928), *Impulse potential and breakdown in gases*, Archiv für Elektrotechnik, **20**, p. 99, translation in: *Electrical Breakdown in Gases* (Rees, 1973).

Ségur P., Yousfi M., Bordage M.C. (1984), *Comparisons between different methods of solution of the Boltzmann equation adapted to the calculation of swarm parameters in a weakly ionised medium*, J. Phys. D: Appl. Phys., **17**, p. 2199-2214.

Ségur P., Yousfi M., Kadri M.H., Bordage M.C. (1986), *A survey of the numerical methods currently in use to describe the motion of an electron swarm in a weakly ionized gas*, Trans. Theory and Stat. Physics, **15**, p. 705-757.

Sigmond R.S. (1983), *Basic corona phenomena: the roles of space charge saturation and secondary streamers in breakdown*, invited paper in: Proc. of the 16th Int. Conf. on Phenomena in Ionized Gases, Düsseldorf, Germany, p. 174-186.

Sigmond R.S. (1984), *The residual streamer channel: Return strokes and secondary streamers*, J. Appl. Phys., **56**, p. 1355-1370.

Smirnov B.M. (1982), *Negative Ions*, McGraw-Hill, New-York, 170 p.

Somerville I.C., Tedford D.J. (1978), *Time-lags to breakdown: the detachment of atmospheric negative ions*, 5th Int. Conf. on Gas Discharges, IEE Conf. Publ., **165**, p. 250-253.

Steinle P. and Morrow R. (1989), *An implicit flux-corrected transport algorithm*, J. Comp. Phys., **80**, p. 61-71.

Teich T.H. (1967), *Emission gasionisierender Strahlung aus Elektronenlawinen*, Zeitschrift für Physik, **199**, p. 378-410.

Teich T.H. (1991), *Detachment of electrons from negative ions in electrical discharges*, Gaseous Dielectrics VI, Ed. by L.G. Christophorou and I. Sauers, Plenum Press, New York, p. 215-229.

Thomson J.J. (1933), *Conduction of Electricity through Gases*, Cambridge.

Townsend J.S. (1910), *The Theory of Ionization of Gases by Collision*, Constable & Co. Ltd., London.

Townsend J.S. (1915), *Electricity in Gases*, Oxford University Press.

Vander Wal R.L., Crim F.F. (1989), *Controlling the pathways in molecular decomposition: the vibrationally mediated photodissociation of water*, J. Phys. Chem., **93**, p. 5331-5333.

Verhaart H.F.A. (1982), *Avalanches in insulating gases*, Ph.D. thesis, Eindhoven University of Technology, The Netherlands, 116 p.

Verhaart H.F.A., van der Laan P.C.T. (1984), *The influence of water vapour on avalanches in air*, J. Appl. Phys., **55**, p. 3286-3292.

Verhaart H.F.A. (1989), *Discharge parameters in flue gas*, Kema Scientific & Technical Reports, **7**, p. 377-383.

Vitello P.A., Penetrante B.M., Bardsley J.N. (1993), *Multi-dimensional modeling of the dynamic morphology of streamer coronas*, in: *Non-Thermal Plasma Techniques for Pollution Control*, NATO Advanced Series Institute Series G, **34A**, Eds. B.M. Penetrante and S.E. Schultheis, Springer, Heidelberg, p. 249-271.

Vostrikov A.A., Dubov D.Yu., Predtechenskiy M.R. (1988), *Absolute cross sections of electron attachment to clusters*, in: *Electronic and Atomic Collisions*, XV Int. Conf. on the Physics of Electronic and Atomic Collisions, p. 793.

Wang M.C., Kunhardt E.E. (1990), *Streamer dynamics*, Phys. Rev. A, **42**, p. 2366-2373.

Wagner K.H. (1966), *Die Entwicklung der Elektronenlawine in den Plasmakanal untersucht mit Bildverstärker und Wischversluß*, Zeitschrift für Physik, **189**, p. 465-515.

Wagner K.H. (1967), *Vorstadium des Funkens, untersucht mit dem Bildverstärker*, Zeitung für Physik, **204**, p. 177-197.

Wagner K.H. (1971), *Ionization, electron-attachment, -detachment, and charge-transfer in oxygen and air*, Zeitung für Physik, **241**, p. 258-270.

Wen C. (1989a), *Determination of swarm parameters in dry air with a fast time-resolved swarm technique*, Proc. 19th. Int. Conf. on Phen. in Ionized Gases, Belgrade, p. 592-593.

Wen C. (1989b), *Time-resolved swarm studies in gases with emphasis on electron detachment and ion conversion*, Ph.D. thesis, Eindhoven University of Technology, The Netherlands, 160 p.

Wen C., Wetzer J.M. (1988), *Electron avalanches influenced by detachment and conversion processes*, IEEE Trans. on Electrical Insulation, **23**, p. 999-1008.

Wetzer J.M., Wen C. (1991), *Different avalanche types in electronegative gases*, J. Phys. D: Appl. Phys., **24**, p. 1964-1973.

Wetzer J.M., van der Laan P.C.T. (1992), *Prebreakdown currents, basic interpretation and time-resolved measurements*, IEEE Trans. on Elec. Insulation, **24**, p. 297-308.

Yousfi M., Gaouar A., Lamrous O., Fassi J. (1992), *Influence of electron-electron interactions on electron distribution function in non-thermal cold plasmas*, Proc. of the 10th. Int. Conf. on Gas Discharges and their Applications (Swansea), Vol. 2, p. 840-843.

Yousfi M., Poinsignon A., Hamani A. (1993), *Electron data base needed for discharge modeling in flue gas treatment*, in: *Non-Thermal Plasma Techniques for Pollution Control*, NATO Advanced Series Institute Series G, **34A**, Eds. B.M. Penetrante and S.E. Schultheis, Springer, Heidelberg, p. 299-329.

Yousfi M., Ségur P. and Vassiliadis T. (1985), *Solution of the Boltzmann equation with ionisation and attachment: application to SF_6*, J. Phys. D: Appl. Phys., **18**, p. 359-375.

Zheleznyak M.B., Mnatsakanyan A.Kh., Sizykh S.V. (1982), *Photoionization of nitrogen and oxygen mixtures by radiation from a gas discharge*, High Temperature, **20**, 1982, p. 423-428 (translated from Teplofizika Vysokikh Temperatur).

References of Chapter 3

Böhm H. (1983), *Elektrochemische Gassensoren und Gasanalysegeräte*, Technisches Messen, **50**, p. 399-406.

Braun D., Küchler U., Pietsch G. (1991), *Microdischarges in air-fed ozonizers*, J. Phys. D: Appl. Phys., **24**, p. 564-572.

Jacottet P. (1974), *Das Elektrische Feld der Spitze-Platte-Funkenstrecke*, Elektrotechnische Zeitschrift (ETZ-A), **95**, p. 402-404.

Kärner H. (1967), *Die Erzeugung steilster Stoßspannungen hoher Amplitude*, Ph.D. thesis, München University of Technology, 178 p.

Keet A.L. (1992), *Magnetic Switching Techniques for High Power Pulse Generation*, Ph.D. thesis, Eindhoven University of Technology, The Netherlands, 112 p.

Kirkman G., Reinhardt N., Jiang B., Hur J., Yampolski J. (1993), *Power conditioning for corona discharge treatment of effluent gases*, in: *Non-Thermal Plasma Techniques for Pollution Control*, NATO Advanced Series Institute Series G, **34A**, Ed. by B.M. Penetrante and S.E. Schultheis, Springer, Heidelberg, p. 379-386.

Küchler U., 1990, *Zur Optimierung luftbetriebener Ozonerzeiger* (in German), Ph.D. thesis, Aachen Technical University, 146 p.

Kuffel E., Zaengl W.S. (1984), *High Voltage Engineering - Fundamentals*, Pergamon Press, Oxford, 498 p.

Neau E.L., Harjes H.C., Reed K.W., Penn K.J., Wavrik R.W., Johnson D.L., McClenahan C.R., Prestwich K.R. (1993), *Initial results from the RHEPP module*, in: *Non-Thermal Plasma Techniques for Pollution Control*, NATO Advanced Series Institute Series G, **34A**, Ed. by B.M. Penetrante and S.E. Schultheis, Springer, Heidelberg, p. 367-378.

Wetzer J.M., van der Laan P.C.T. (1989), *Prebreakdown currents, basic interpretation and time-resolved measurements*, IEEE Trans. Elec. Insulation, **24**, p. 297-308.

Ogink R.A.M. (1988), *NO_x meting op basis van drie meetprincipes*, Gas, **4**, p. 156-165.

Persephonis P., Vlachos K., Georgiades C., Parthenios J. (1992), *The inductance of the discharge in a spark gap*, J. Appl. Phys., **71**, p. 4755-4762.

Portela C.M., Santiago N.H.C., Oliveira O.B., Dupont C.J. (1992), *Modelling of arc extinction in air insulation*, IEEE Trans. Elec. Insulation, **26**, p. 457-463.

Vondenbusch A. (1958), *Ein allgemeines Berechnungsverfahren für Stoßschaltungen mit drei voneinander unabhängigen Energiespeichern*, Ph.D. thesis, Aachen University of Technology, 69 p.

Wetzer J.M., van der Laan P.C.T. (1989), *Prebreakdown currents, basic interpretation and time-resolved measurements*, IEEE Trans. on Electrical Insulation, **24**, p. 297-308.

References of Chapter 4

Calo J.M., Axtmann R.C. (1971), *Vibrational relaxation and electronic quenching of the $C^3\Pi_u(v=1)$ state of nitrogen*, J. Chem. Phys., **54**, p. 1332-1341.

Carr T.W., Dondes S. (1977), *Direct measurement of the radiative lifetime and the collisional quenching of the $C^3\Pi_u$ state of N_2 as studied by pulse radiolysis*, J. Phys. Chem., **81**, p. 2225.-2228.

Czernichowski A. (1987), *Temperature evaluation from the partially resolved 391 nm N_2^+ band*, J. Phys. D: Appl. Phys. **20**, p. 559-564.

Domens P., Dupuy J., Gibert A., Diaz R., Hutzler B., Riu J.P., Rühling F. (1988), *Large air-gap discharge and Schlieren techniques*, J. Phys. D: Appl. Phys., **21**, p. 1613-1623.

Finlayson-Pitts B.J., Pitts J.N. (1986), *Atmospheric Chemistry: Fundamentals and Experimental Techniques*, John Wiley & Sons, New York.

Hartmann G. (1974), *Variations of the mean energy of the electrons responsible for the luminous emission from primary streamers in atmospheric air*, 3th Int. Conf. on Gas Discharges, IEE Conf. Publ., p. 634-638.

Hartmann G., Gallimberti I. (1975), *The influence of metastable molecules on the streamer progression*, J. Phys. D: Appl. Phys., **8**, p. 670-680.

Hartmann G. (1977), *Spectroscopie de la décharge couronne: étude des méchanismes de collisions dans le dard (streamer)*, Ph.D. thesis no. 1783, Université de Paris-Sud, Centre d'Orsay.

Hartmann G., Johnson P.C. (1977), *Measurements of relative transition probabilities and the variation of the electronic transition moment for N_2 $C^3\Pi_u \rightarrow B^3\Pi_g$ second positive system*, J. Phys. B: Atom. Molec. Phys., **11**, p. 1597-1611.

Herzberg G.H. (1955), *Molecular spectra and molecular structure, part I: Spectra of diatomic molecules*, D. van Nostrand Company, Princeton, 658 p.

Hosch J.W., Walters J.P. (1977), *High spatial resolution Schlieren photography*, Applied Optics, **16**, p. 473-482.

Jolly J., Plain A. (1983), *Determination of the quenching rates of $N_2^+(B^2\Sigma_u^+, v=0,1)$ by N_2 using laser-induced fluorescence*, Chem. Phys. Lett., **100**, p. 425-428.

Kieffer L.J. (1973), *A compilation of electron collision cross section data for modelling gas discharge lasers*, JILA Information Center Report No. 13, University of Colorado, 139 p.

Kogelschatz U., Schneider W.R. (1972), *Quantitative Schlieren techniques applied to high current arc investigations*, Applied Optics, **11**, p. 1822-1832.

Kurimoto A., Farish O., Tedford D.J. (1978), *Schlieren studies of impulse breakdown in air gaps*, Proc. IEE, **125**, p. 767-769.

Kurimoto A., Farish O. (1980), *Negative d.c. corona study in atmospheric air using Schlieren and interferometric techniques*, Proc. IEE, **127**, p. 89-94.

Lamb D.W., Woolsey G.A. (1992), *Optical analysis of the post-streamer channel in atmospheric air*, 10th Int. Conf. Gas Discharges and their Applications, Swansea, p. 460-463.

Lambert J.D. (1977), *Vibrational and Rotational Relaxation in Gases*, Oxford University Press, 142 p.

Merzkirch W.M. (1974), *Flow Visualisation*, Academic Press, New York.

Millet P., Salamero Y., Brunet H., Galy J., Blanc D., Teyssier J.L. (1973), *De-excitation of N_2 ($C^3\Pi_u$ $v=0,1$) levels in mixtures of oxygen and nitrogen*, J. Chem. Phys., **58**, p. 5839-5841.

Mitchell K.B. (1970), *Fluorescence efficiencies and collisional deactivation rates for N_2 and N_2^+ bands excited by soft X-rays*, J. Chem. Phys., **53**, p. 1795-1802.

Mnatsakanyan A.Kh., Naidis G.V. (1986), *The vibrational-energy balance in a discharge in air*, High Temperature, **23**, p. 640-648 (translated from Teplofizika Vysokikh Temperatur).

Mnatsakanyan A.Kh., Podlubnyi L.I. (1972), *Change of the vibrational distribution function in transitions between electron states in diatomic molecules due to collisions with electrons*, Sov. Phys. Techn. Phys., **16**, p. 1680-1683.

Phillips D.M. (1975), *Determination of gas temperature from unresolved bands in the spectrum from a nitrogen discharge*, J. Phys. D: Appl. Phys., **8**, p. 507-521.

Smith A.J., Read F.H., Imhof R.E. (1975), *Measurement of the lifetimes of ionic excited states using the inelastic electron-photon delayed coincidence technique*, J. Phys. B: Atom. Molec. Phys., **18**, p. 2869-2879.

Spyrou N., Held B., Peyrous R., Manassis Ch., Pignolet P. (1992), *Gas temperature in a secondary streamer discharge: an approach to the electric wind*, J. Phys. D: Appl. Phys., **25**, p. 211-216.

Spyrou N., Manassis C. (1989), *Spectroscopic study of a positive streamer in a point-to-plane discharge in air: evaluation of the electric field distribution*, J. Phys. D: Appl. Phys. **22**, p. 120-128.

Tajalli H., Lamb D.W., Woolsey G.A. (1989), *Energy transfer in positive streamers*, J. Phys. D: Appl. Phys., **22**, p. 1497-1503.

Teich T.H. (1991), *Determination of reaction data from corona discharge observation*, 3th Int. Symp. on High Pressure Low Temperature Plasma Chemistry (HAKONE III), Strasbourg, France, p. 77-83.

Teich T.H. (1993), *Emission spectroscopy of corona discharges*, in: *Non-Thermal Plasma Techniques for Pollution Control*, NATO Advanced Series Institute Series G, **34A**, Eds. B. M. Penetrante and S. E. Schultheis, Springer, Heidelberg, p. 231-248.

Waters R.T. (1983), *Diagnostic techniques for discharges*, in: *Electrical Breakdown and Discharges in Gases*, NATA ASI Series, **89B**, Eds. E.E. Kunhardt and L.H. Luessen, Plenum Press, New York, p. 203-265.

Waters R.T. (1986), *Double impulse tests of long airgaps*, Les Renardières Group, IEE Proc. A, **133**, p. 395-468.

Woolsey G.A., MacGregor S.J., Farish O. (1986), *A quantitative Schlieren analysis of positive streamers in atmospheric air*, Proc. Royal Society of London, **A 405**, p. 355-367.

Acknowledgements

I want to express my gratitude to all those who contributed to the accomplishment of this work, in particular:

Wijnand Rutgers, my thesis professor. The weekly scientific discussions stimulated new ideas and were particularly encouraging to proceed with the investigations of both fundamental and applied aspects. I also benefitted from his knowledge in many other scientific fields.

Eddie van Veldhuizen. He has much stimulated my initial experiments and I am grateful for his help with the numerical calculations.

Ad Holten. My truly thanks for the important help with electronics, programming and the remarkable fact that computers continued to do their work in spite of the electromagnetic perturbations caused by the experiments.

Nol van Stratum. My truly thanks for the technical assistance with the build-up of the experiments and for always willing to help.

Loek Baede. Thanks for the excellent support in the fields of optics and high voltage engineering.

Mohamed Yousfi. Thanks for kindly providing the results of Boltzmann calculations.

I am much indebted to those who participated in the numerical modelling of streamers and chemical kinetics in the research group headed by dr. V.A. Bityurin at the Institute of High Temperatures in Moscow: G.Yu. Alekseev, A.V. Levchenko, N.Yu. Babaeva, A.A. Kulikovsky, G.V. Naidis and Yu. M. Solosobov. I want to remember prof. dr. A.Kh. Mnatsakanyan. His long experience in the field of electrical discharge modelling has been very profitable for this work.

I wish to thank Margreet Sanders, Hanneke de Smit and Vadim Banin for their practical help.

Finally, the author would like to thank his wife Isabelle who loves him enough to allow him to pursue such a demanding mistress as research.

Curriculum Vitae

27 augustus 1964	geboren te Nijmegen
juni 1982	Diploma gymnasium β, Titus Brandsma Lyceum in Oss
februari 1989	Doctoraal examen Technische Natuurkunde, Technische Universiteit Eindhoven
maart 1989 - juni 1994	promotieonderzoek bij de vakgroep Elektrische Energiesystemen, Faculteit Elektrotechniek, Technische Universiteit Eindhoven

Stellingen

behorend bij het proefschrift

Pulsed Positive Corona Discharges:

Fundamental Study and Application to Flue Gas Treatment

Yves Creyghton

Eindhoven, dinsdag 20 september 1994

I

De positief gepulste corona ontlading is geschikt voor gasreiniging vanwege de mogelijkheid om met hoog energetisch rendement oxydanten te produceren onder atmosferische (normale) druk in een groot volume en met geringe opwarming van het neutrale gas.

II

Gehydrateerde negatieve ionen, die ontstaan in een positieve corona ontlading wanneer deze optreedt in vochtige lucht, hebben een grote invloed op condities welke essentieel zijn voor de vorming van streamers.

III

Corona streamers die gevormd worden onder toepassing van korte hoogspanningspulsen kunnen beter onderzocht worden in een draad-plaat geometrie dan in een draad-cylinder geometrie of in een punt-plaat geometrie.

IV

De streamersnelheid kan hoger zijn dan de maximum driftsnelheid van de elektronen in de streamer.

V

Voor het beperken en zo mogelijk vermijden van energiedissipatie tijdens de secundaire streamerfase dienen hoogspanningspulsen aanzienlijk korter te zijn dan de maximum pulsduur waarbij geen doorslag optreedt.

VI

De hoeveelheid kolen in de wereld vormt meer aanleiding te vrezen voor een milieuprobleem dan voor een energieprobleem.

VII

Het nemen van foto's van door zure regen aangetaste sculpturen van muziekinstrumenten op de gevels van Romaanse kerken is niet alleen van belang voor het onderzoek naar de historische ontwikkeling van deze instrumenten maar eveneens als documentatie waar men zich op kan baseren wanneer voortgeschreden aantasting restauratie noodzakelijk maakt.

VIII

Voor het verbeteren van de luchtkwaliteit in West-Europa zijn West-Europese investeringen voor gasreiniging in industriële installaties meer effectief in Oost-Europa dan in West-Europa.

IX

Uit het onlangs in Genève gesloten akkoord over een verbod van export van giftige afvalstoffen uit industrielanden naar ontwikkelingslanden blijkt dat de vooruitgang op het gebied van internationale milieupolitiek een schildpad is die dringend op de rode lijst van beschermde diersoorten gezet moet worden om haar voor uitsterven te behoeden.

X

Het zou de democratie in Nederland ten goede komen wanneer de kiezers even goed op de hoogte waren van het kleurverschil tussen de partijprogramma's als van de kleur van de ogen van de lijsttrekkers.

XI

Dat in Frankrijk minder vrouwen in de politiek zitten dan in andere West-Europese landen is een voor vrouwen negatief gevolg van het feit dat Franse mannen minder hard zijn dan hun seksegenoten elders.